2018

Characterization of Anisotropic Mechanical Performance of As-Built Additively Manufactured Metals

Sanna Siddiqui
University of Central Florida, Sanna.Siddiqui@knights.ucf.edu

CHARACTERIZATION OF ANISOTROPIC MECHANICAL PERFORMANCE OF AS-BUILT ADDITIVELY MANUFACTURED METALS

by

SANNA F. SIDDIQUI
B.S.A.E. University of Central Florida, 2012
M.S.M.E. University of Central Florida, 2014

A dissertation submitted in partial fulfillment of the requirements
for the degree of Doctor of Philosophy
in the Department of Mechanical and Aerospace Engineering
in the College of Engineering and Computer Science
at the University of Central Florida
Orlando, Florida

Spring Term
2018

Major Professor: Ali P. Gordon

ABSTRACT

Additive manufacturing (AM) technologies use a 3D Computer Aided Design (CAD) model to develop a component through a deposition and fusion layer process, allowing for rapid design and geometric flexibility of metal components, for use in the aerospace, energy and biomedical industries. Challenges exist with additive manufacturing that limits its replacement of conventional manufacturing techniques, most especially a comprehensive understanding of the anisotropic behavior of these materials and how it is reflected in observed tensile, torsional and fatigue mechanical responses. As such, there is a need to understand how the build orientation of as-built additively manufactured metals, affects mechanical performance (e.g. monotonic and cyclic behavior, cyclically hardening/softening behavior, plasticity effects on fatigue life etc.); and to use constitutive modeling to both support experimental findings, and provide approximations of expected behavior (e.g. failure surfaces, monotonic and cyclic response, correlations between tensile and fatigue properties), for orientations and experiments not tested, due to the expensive cost associated with AM. A comprehensive framework has been developed to characterize the anisotropic behavior of as-built additively manufactured metals (i.e. Stainless Steel GP1 (SS GP1), similar in chemical composition to Stainless Steel 17-4PH), through a series of mechanical testing, microscopic evaluation and constitutive modeling, which were used to identify a reduced specimen size for characterizing these materials. An analysis of the torsional response of additively manufactured Inconel 718 has been performed to assess the impact of build orientation and as-built conditions on the shearing behavior of this material. Experimental results from DMLS SS GP1 and AM Inconel 718 from literature were used to constitutively model the material responses of these additively manufactured metals. Overall, this framework has been designed to serve as standard, from which build orientation selection can be used to meet specific desired industry requirements.

This work is dedicated to my parents for their love, guidance, encouragement and unwavering support throughout my every endeavor

ACKNOWLEDGMENTS

It is with utmost gratitude that I would like to express my appreciation to those individuals who have, through their help, guidance and support allowed for the completion of my dissertation. Foremost, I would like to thank my Ph.D. advisor and committee chair, Dr. Ali P. Gordon for his most insightful feedback and guidance throughout the course of my doctoral research. Through his advice, I was able to overcome challenges experienced during this study. Dr. Gordon's time, motivation and support has served as a contributing factor towards the completion of this body of work, for which I am most appreciative.

I would like to acknowledge my co-chair, Dr. Seetha Raghavan for being a continued and motivating supporter of my research work. I would also like to thank my committee members, Dr. Yuanli Bai and Dr. Yongho Sohn for their knowledgeable advice. Dr. Raghavan and Dr. Bai, thank you for use of the MTS LandMark to conduct part of the experiments presented in this dissertation. Dr. Sohn, thank you for the opportunity to participate in the search and purchase of an additive manufacturing system.

Overall, I would like to thank each and every member of my committee for their time and valuable suggestions towards this dissertation.

I would also like to acknowledge the support of our collaborator, Dr. Abiodun A. Fasoro at Central State University, for not only manufacturing the specimens used in this study, but for guiding us during the manufacturing process, and supporting my dissertation studies. Thank you

to Mr. Robert Wong, machinist in the Physics Department at UCF, for machining the specimens used in this study, and for his continued motivation and insightful suggestions throughout the course of this study. I would like to thank my MOMRG research colleagues for their assistance during various stages of my doctoral studies, most especially, Jonathan Torres, Nathan O'Nora, Thomas Bouchenot, Bassem Felemban, Firat Irmak, Calvin Cole, Aaron Santomauro, Casey Perkowski, Matthew Schuler, Dominic Devito, Austin Corella, and Miled Mourad.

Thank you to Dr. Andrew Dickerson, and his students, Md. Erfanul Alam, Hiba Khan, and Nicholas Smith for use of the Keyence VHX Digital Microscope for fracture analysis; and Dr. Robert Peale and Seth Calhoun, for use of the Dektak profilometer in the Micro Device Prototyping Facility for surface roughness measurements. I would like to acknowledge Mohamed Abdelgader and Dr. Yueqian Jia for their assistance with the MTS Landmark. I would also like to thank UCF's College of Graduate Studies for the opportunity to present at their Graduate Fellows Symposium.

Finally, I would like to acknowledge those funding agencies who recognized my potential, and helped to support my doctoral studies: National Science Foundation Graduate Research Fellowship Program Grant No. (1144246), Zonta International Amelia Earhart Fellowship, and the Athena International Emerging Women Leader Fellowship. I would also like to thank the support of UCF's College of Engineering and Computer Science throughout the course of my undergraduate and graduate careers with multiple scholarship awards, including the Boeing Scholarship Fund, EAS/Airbus North American Scholarship, David T. and Jane M. Donaldson Memorial Scholarship and the Frank Hubbard Engineering Endowed Scholarship.

TABLE OF CONTENTS

LIST OF FIGURES

LIST OF TABLES

CHAPTER 1: INTRODUCTION

Additive Manufacturing (AM) has received much acclaim over the past two decade due to its advantages, as compared with conventional manufacturing techniques, such as casting and forging. With the possibility of complex geometric design flexibility coupled with rapid prototyping of components, AM has found application in a wide-variety of disciplines. Commonly known as 3D printing, additive manufacturing can be mainly classified into powder bed, powder feed or wire feed systems [Wohlers, 2014], of which the powder bed systems are comprised of SLS (Selective Laser Sintering), DMLS (Direct Metal Laser Sintering), SLM (Selective Laser Melting) and EBM (Electron Beam Melting) [Siddiqui, 2017]. There are a number of factors that contribute to the anisotropic mechanical behavior observed of AM materials, which includes the processing parameters, build orientation, and post-processing techniques etc. used to manufacture AM parts. Understanding the role of this anisotropic material behavior on the resulting mechanical performance of as-built AM materials can allow researchers in academia and industry to design components that meet a desired applications' requirements, while determining solutions to improve current limitations and pending flaws with the additive manufacturing process.

1.1 Motivation

Aircraft components are subject to extreme operational and environmental service conditions, hence the need to ensure the reliability and durability of these components. The rapid prototyping capability of additive manufacturing aircraft components, both novel and out-of-circulation, with intricate geometric designs has become more realistic, leading to potential savings in manufacturing costs and greater energy efficiency in aircrafts. For example, more complex turbine blade design has allowed for improved aerodynamic performance that can lead

to improved energy efficiency of aircraft gas turbine engines; however, along with the benefits with the additive manufacturing process, there are considerable concerns that must be assessed for AM to replace conventional manufacturing processes. Most importantly, additively manufactured components may exhibit reduced fatigue life due to voids, inclusions, and surface roughness. This is a result of the layer wise powder deposition process that characterizes powder bed additive manufacturing processes. These defects serve as initiation sites for fatigue cracks, leading to a reduction in life (cycles to failure), and it is this fracture response (i.e., ductile or brittle) that can provide insight into component ability to withstand failure during operation. Furthermore, during start up and shut down, these gas turbine engines or components experience high plastic cyclic strains that can lead to a reduction in life of these components. Pulsating tension and progressive amplitude fatigue environments are also encountered by aerospace components. Analyzing and mitigating the flaws that arise during service conditions can lead to longer life of AM aerospace components.

Additively manufactured components are unique, because they exhibit orientation dependence, in that the resulting mechanical performance of these components will vary with build orientation. Yet unexplored are the design limits of these materials with build orientation, which are critical in ensuring the durability of these components under their respective operating conditions. A comprehensive analysis of mechanical performance with build orientation, for materials used in the aviation industry, under experimental conditions experienced by these components, can allow for part designs that meet or exceed the requirements for a desired application. Aircraft components encounter multiaxial loading conditions, in which an understanding of both the axial and shear response of these AM materials is vital, in addition to

determining Poisson's effect exhibited by these parts. Characterizing the hardening (kinematic and isotropic) and softening behavior exhibited by AM materials, and modeling this cyclic response can reduce the need for experimental fatigue testing, resulting in part production cost savings and time. The novelty of this dissertation is that a comprehensive framework is developed to assess and model the mechanical performance (i.e., tension, torsion, low cycle fatigue, torsional fatigue, pulsating tension fatigue, and progessive strain amplitude fatigue) of as-built additively manufactured Stainless Steel GP1 and Inconel 718 with build orientation.

1.2 Objectives of Proposed Research

The proposed research develops a framework to characterize the anisotropic behavior of as-built AM parts manufactured using built-in optimized manufacturer processing parameters, limiting the use of post-processing techniques, which adds time and production cost in part development. Essentially, this study will investigate the impact of build orientation on as-built AM components, for which surface roughness will contribute to experimentally determined monotonic and cyclic performance of these materials. A series of tension, surface roughness, torsion, and fatigue experiments will be used to classify material behavior as orthotropic, tetragonal, transversely-isotropic/or other, in addition to providing a correlation between build orientation and cyclic softening/hardening, plasticity effects on fatigue life, fracture response, design limits of these materials, and much more. The specific aims for this research are presented as follows.

- **Specific Aim 1: To develop a set of uniaxial tension, fatigue and torsion experiments to characterize the anisotropic monotonic, cyclic and shear response of as-built additively manufactured metals.** The proposed project will determine the material behavior exhibited by DMLS SS GP1 and DMLS IN718 manufactured

along varying build orientations, using EOS optimized build parameters, thereby providing an understanding of the material behavior.

- Impact of build orientation on surface roughness of as-manufactured specimens.
- Observe differences in tension, torsion, and fatigue fracture responses (i.e., ductile, brittle) through microscopic observations, and their correlation to surface roughness, internal voids/density, and hardness present within AM specimens.
- Observe differences in microstructures (e.g., presence of voids/internal cracks, un-melted powder, melt arc pools, etc.) of these materials with build orientation.
- Determine hardening/softening response of these materials under varying experimental conditions.
- Examine plasticity effects on observed life for varying build orientations.
- Determine impact of shear loading conditions on these AM materials, and compute Poisson's ratios and Shear Moduli.
- Characterize the anisotropic material behavior based upon observed mechanical properties (e.g. orthotropic, transversely isotropic).
- Compare experimental outcomes with mechanical properties observed for the conventional manufactured counterpart of these materials.

Experimentally-determined anisotropic material behavior, captured through a series of mechanical tests, will then be used to constitutively model anisotropic failure surfaces/design limits through application of Hill's failure theory, as well as the monotonic performance through the Ramberg-Osgood non-linear strain-hardening model/Hahn plasticity discontinuous yielding model. Young's modulus variation with build orientation will be modeled, and correlations

between existing tensile and fatigue properties for non-additively manufactured materials will be explored for applicability with AM materials. The cyclic material response (i.e., first to stabilized hysteresis curves, stress history etc.) under axial and torsional fatigue loading conditions will be modeled using the Chaboche model. Overall, this research will address the following research goals through constitutive modeling.

- **Specific Aim 2: To constitutively model the anisotropic failure surfaces, monotonic and cyclic behavior of as-built additively manufactured metals, and determine connections between tensile and fatigue properties.** Minimal research studies have constitutively modeled the mechanical behavior of these materials, as such there is a need to be able to simulate the response of these materials. This will not only allow for validation of experimental data, but in addition, provide mechanical material behavior at orientations other than those being tested, because of the expensive cost associated with additive manufacturing. Constitutive modeling will be achieved by using experimental data generated through mechanical testing of DMLS SS GP1 and DMLS IN718. The following research goals will be addressed.
  - Extend Hill's/Tsai-Wu failure criterion to model the anisotropic failure surfaces of this class of materials.
  - Model variation in Young's modulus with build orientation.
  - Develop connections between tensile and fatigue properties, and determine if they correspond to generally accepted relations between tensile and fatigue properties for non-additively manufactured materials.
  - Model the cyclic hysteresis behavior of these materials for varying build orientations from experimentally generated cyclic data, through use of the Chaboche model.

- Extend the Ramberg-Osgood, Hahn plasticity discontinuous yielding theory to model the stress-strain curve of each build orientation for these materials.

The outcomes from experimental mechanical testing and constitutive modeling will be used to develop a framework for testing and characterization of samples with a reduced sample size. This will be used to characterize the monotonic and cyclic performance of AM materials, without the need for manufacturing multiple large-volume samples, which increases AM production costs.

- **Specific Aim 3: To identify a reduced test approach for testing and characterizing an as-built additively manufactured metal, based upon leveraging outcomes/findings from research aims 1 and 2.** With the excessive cost associated with additive manufacturing, there is a need to not only understand the anisotropic behavior of these materials (as is being pursued in research aims 1 and 2), but also to develop a framework from which costs can be reduced, while at the same time providing necessary results to fully characterize these materials. The following research goal will be answered.
  - Develop a reduced experimental sample size that can characterize the monotonic and cyclic behavior of these materials, yielding comparable findings with conventional test specimens used in this study, while maintaining ASTM standards for specimen size.

Outlined within this dissertation is a comprehensive literature review of the additive manufacturing process in Chapter 2, along with the material behavior response of AM Stainless Steel 17-4PH/GP1 and Inconel 718 determined by researchers. Chapter 3 presents the experimental design for tension, torsion, surface roughness and fatigue testing, including

conventional specimen geometry, reduced specimen geometry and experimental parameters, in addition to specifications regarding the additive manufacturing process used to manufacture specimens. Chapters 4-6 presents the experimental results and discussion, in addition to constitutive models developed to determine the impact of build orientation on mechanical performance of these as-built additively manufactured materials, as well as experimental findings for reduced specimen size. Conclusions and suggestions for future work to further support and extend findings is presented in Chapter 7. Appendix A presents the additive manufacturing specimen layouts for Stainless Steel 17-4PH and Inconel 718 batches manufactured through the direct metal laser sintering process. Appendix B summarizes the experimental findings for each specimen, subject to tension, low cycle fatigue, pulsating tension fatigue, progressive strain amplitude fatigue, torsion, and torsional fatigue experimental conditions. Also presented in Appendix B are the surface roughness measurements taken on each specimen with respect to build orientation. Finally, Appendix C presents the constitutive modeling codes/process for failure surface development and Hahn discontinuous yielding modeling.

CHAPTER 2: LITERATURE REVIEW[1]

2.1 Additive Manufacturing

Additive manufacturing (AM) is a novel manufacturing technique, in which a component can be developed through a layer by layer deposition and fusion process based upon an inputted computer-aided design (CAD) model. The AM process has provided considerable benefits across a wide variety of industries including the aerospace, biomedical, automobile and tooling industries. Rapid prototyping, complex geometric design development, and savings in part manufacturing costs are a few of the most profound benefits seen with additively manufacturing parts. Additive manufacturing processes can be divided into three distinct areas: wire-feed, powder-feed and powder-bed additive manufacturing [Wohlers, 2014]. This study focuses on metal printing through the powder-bed AM process.

2.1.1 Powder Bed Additive Manufacturing Processes

Powder-bed AM processes can be classified into four common techniques: selective laser sintering (SLS), selective laser melting (SLM), direct metal laser sintering (DMLS), and electron beam melting (EBM), which vary depending upon the power source and process used for powder melting and fusion. For example, the SLS, SLM and DMLS processes use a focused laser beam as the power source in an inert gas build chamber environment, as opposed to the EBM process, which uses an electron beam as the power source in a vacuum build chamber environment [Sing, 2015]. Essentially, the power source is used to selectively melt powder based upon an inputted geometric design, layer by layer, until fusion of these layers, through which the final component

[1] Certain figures and excerpts in Chapter 2 are from my publications: Siddiqui, S.F., Fasoro, A.A., & Gordon, A.P. (2017). Selective Laser Melting (SLM) of Ni-based Superalloys - A Mechanics of Materials Review. Badiru, A.B., Valencia, V. V., & Liu, D. (Eds.), *Additive Manufacturing Handbook: Product Development for the Defense Industry*. CRC Press; Siddiqui, S.F., Fasoro, A.A., Cole, C., & Gordon, A.P. (2017). Mechanical Characterization and Modeling of Direct Metal Laser Sintered Stainless Steel GP1. Manuscript under review. Submitted to the *ASME Journal of Engineering Materials and Technology*; Siddiqui, S.F., O'Nora, N., Fasoro, A.A., & Gordon, A.P. (2017). Modeling the Influence of build orientation on the monotonic and cyclic response of additively manufactured stainless steel GP1/17-4PH. In *Proceedings of the ASME 2017 International Mechanical Engineering Congress & Exposition*.

is developed. The focus of this study is on the DMLS process, which is described in detail in the following section.

The Selective Laser Melting (SLM) / Direct Metal Laser Sintering (DMLS) process, as depicted in Figure 1, occurs in an argon or nitrogen chamber environment in which an ytterbium (Yb) fiber laser is passed through the beam scanner, which selectively laser melts metal powder located within a powder bed that has been supplied from a powder delivery system on a substrate plate [Siddiqui, 2017].

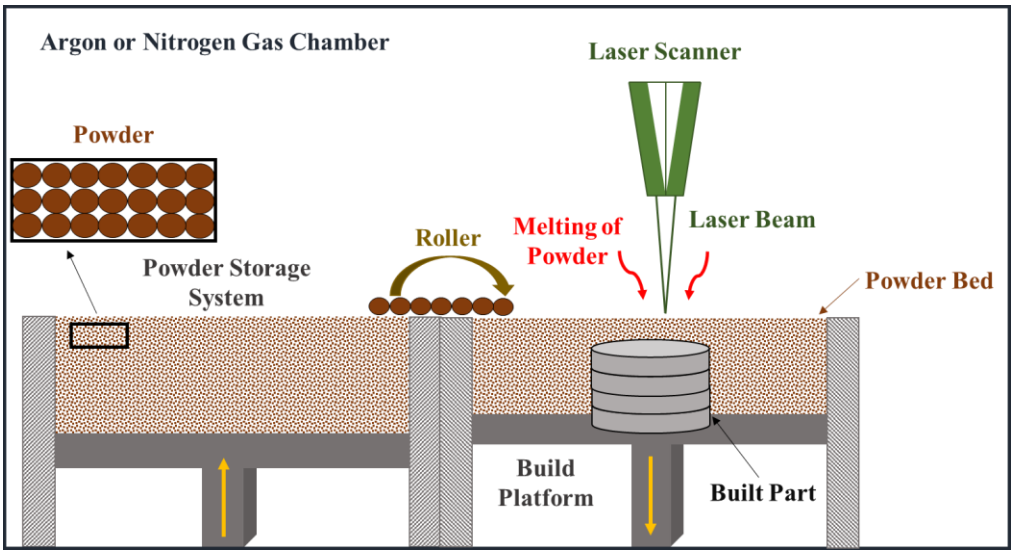

Figure 1: Schematic of powder-bed additive manufacturing processes [Siddiqui, 2017]

For a given candidate 3D component, its associated digital solid model analogy (e.g. STL) file is sliced into 2D layers. To achieve the optimal performance, optimization of SLM processing parameters is necessary in light of a given service condition [Sadowski, 2016]. Studies often use the statistical approach analysis of variance (ANOVA) [Girden, 1992; Torres, 2015] to determine optimal processing parameter sets for manufacturing [Carter, 2015]. These processing parameters together with post processing techniques directly influence the mechanical

performance of the final component. A discussion of these parameters is presented in the following section.

2.1.2 Processing Parameters

A variety of processing parameters during the AM process directly affects the resulting final prototype. Optimization of these parameters is necessary in order to ensure the component developed meets desired application requirements, and to avoid/reduce undesired effects of the AM process (i.e., porosity, warping, surface roughness, residual stress etc.) [Kruth, 2010]. Parameters that also influence the performance and microstructure of powder-bed AM material include the island scanning strategy [Lu, 2015; Carter, 2014; Kudzal, 2017], overlap of melt pools [Cao, 2013], powder particle type/size [Irrinki, 2016], build orientation [Deng, 2017; Chlebus, 2015, Smith, 2016; Yadollahi, 2017; Mahmoudi, 2017; Luecke, 2014], post-build heat treatment processing [Deng, 2017; Chlebus, 2015; Qi, 2009], pre-heating of the substrate plate [Sochalski-Kolbus, 2015; Kirka, 2017], gas chamber environment [Amato, 2012; Murr, 2012], and many more parameters [Hu, 2017; Gu, 2013]. An optimum energy density is favorable in increasing the density of the material and thus reducing the porosity and presence of cracks, and is related to the powder layer thickness or diameter, scanning velocity, laser power, laser spot size and hatch spacing [Gu, 2012; Carter, 2015; Song, 2015; Carter, 2015; Jia, 2014]. A generally accepted optimal density for SLM manufactured parts is greater than 99.5% [Gu, 2012; Chlebus, 2015]; however, too high of an energy density in DMLS and EBM manufactured parts may lead to delamination [Sochalski-Kolbus, 2015]. A depiction of the common processing parameters used during part development is as shown in Figure 2. These include the laser beam spot size, laser power, layer thickness and the laser scanning velocity.

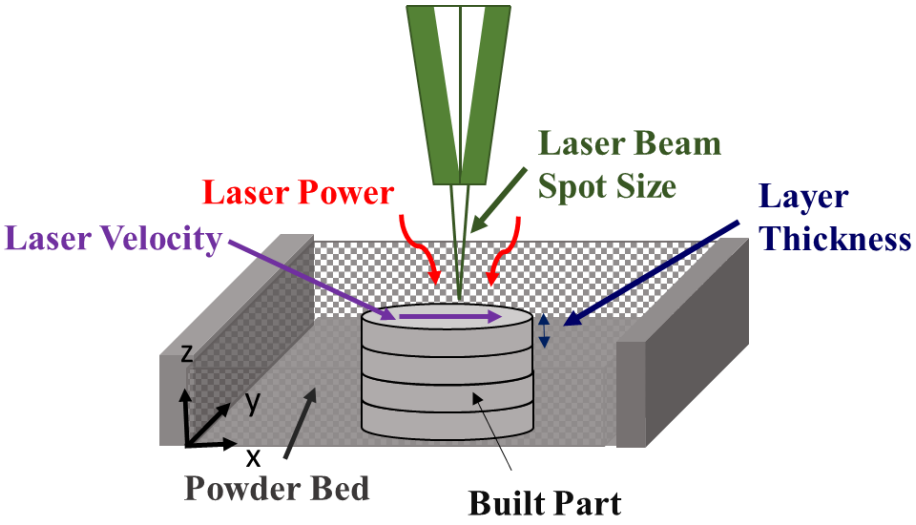

Figure 2: Schematic of most common processing parameters optimized during the powder-bed additive manufacturing process [Siddiqui, 2017]

Manufacturers of additive systems (e.g. EOS, SLM, Renishaw, ARCAM etc.) have optimized these parameters for metal powders to maintain both an optimal density of AM parts, in addition to achieving a reduction in undesirable effects of additive manufacturing (e.g. surface roughness, porosity, residual stress etc. [Watkins, 2013; Song, 2014; Mercelis, 2006; Kruth, 2004; Song, 2015; Zaeh, 2010].

2.2 Material Behavior of Additively Manufactured Stainless Steel 17-4PH/GP1

Stainless Steel GP1, which is also referred to have a chemical composition similar to that of 17-4 Stainless Steel (US convention) or 1.4542 Stainless Steel (European convention) by EOS (Electro Optical Systems) manufacturer [EOS, 2009], is used in a variety of applications at or below 315°C [Cheruvathur, 2015]. Stainless Steel GP1 manufactured parts exhibit high ductility, corrosion resistance and toughness and are also used for parts that require sterilization [EOS, 2009], such as tools for the biomedical industry. A comparison of the chemical composition between SS GP1 and SS 17-4PH can be seen in Table 1, which reveals that besides minor

constituents of certain elements, the chemical composition of both materials are very similar to each another, hence the similitude in naming convention. However, studies have shown that the mechanical performance of these materials vary when additively manufactured [Luecke, 2014; Facchini, 2010; Yadollahi, 2015] due to variation in phase constituents at the microstructure level. Nevertheless, because of the similitude in nominal composition, Stainless Steel 17-4PH is considered the closest material to compare with Stainless Steel GP1 findings. A detailed discussion on these findings along with the mechanical properties reported for SSGP1/17-4PH is presented in the section to follow.

Table 1: Chemical Composition of Stainless Steel GP1 and 17-4PH [EOS, 2009; AK Steel Corporation, 2007; Siddiqui, 2018]

Material	Cr	Ni	Cu	Mn	Si	Mo	Nb	C	P	S	Columbium + Ta	Fe
SSGP1	15-17.5	3-5	3-5	≤1.0	≤1.0	≤0.5	0.15-0.45	≤0.07	-	-	-	bal.
17-4PH	15-17.5	3-5	3-5	≤1.0	≤1.0	-	-	≤0.07	≤0.040	≤0.030	≤0.15-0.45	bal.

2.2.1 Mechanical Properties under Tensile Loading

Tensile testing can provide much needed information about the mechanical behavior of a material (i.e., yielding, strength, ductility etc.), and the suitability of that material for the application in which it is being used, whether that be for turbine blades in gas turbine engines or as surgical tools. Considerable research has been done on determining these mechanical properties through tensile testing, for Stainless Steel GP1/17-4PH. A compilation of these tensile properties across literature are as presented in Table 2. As this research is primarily focused on as-built specimens, the table presents literature findings on as-manufactured stainless steel 17-4PH/GP1.

Table 2: Tensile mechanical properties for as-built AM and conventional SS 17-4PH/GP1

Reference	Condition	Build Orientation	E (GPa)	Y.S. (MPa)	UTS (MPa)	EL%
W. Everhart et al. 2016, J. Mater Sci	Unfinished	Vertical (001)	-	473.7	873.6	41.5
	Unfinished	Vertical (001)	-	479.2	879.1	41.1
	Machined	Vertical (001)	-	535	881.8	51.6
T. Mower et al. 2016, Materials Science & Eng.	Unfinished	Horizontal	165	610	1072	7.2
	Unfinished	45° Orientation	186	737	914	8.6
EOS SSGP1 Material Data Sheet	As-Manufactured	Vertical	170 ± 30	570 ± 50 (Lower), 630 ± 50 (Upper)	960 ± 50	35 ± 5
		Horizontal	170 ± 30	586 ± 50 (Lower), 645 ± 50 (Upper)	930 ± 50	31 ± 5
H. Khalid Rafi et al. 2014, J. of Materials Eng. and Performance	As-Built	-	-	570	944	50
W. E. Luecke et al. 2014, J.of Research of National Institute of Standards and Technology	As-Built	Vertical	-	482, 480, 478 (Lower), 519, 516, 516 (Upper)	996, 994, 947	-
		Horizontal (Hp)		500, 483, 496 (Lower), 550, 542, 545 (Upper)	1068, 1054, 1055	
		Horizontal (Hv)		457, 437, 468 (Lower), 498, 483, 515 (Upper)	1071, 1034, 1068	

Reference	**Condition**	**Build Orientation**	**E (GPa)**	**Y.S. (MPa)**	**UTS (MPa)**	**EL%**
A. Yadollahi et al. 2017, Int. J. of Fatigue	As-Built	Vertical	187.3	580	940	14.5
		Horizontal	187.3	650	1060	5.8
A. Gratton et al.2012, NCUR	No post-process	-		565	1000	30
	No post-process			595	1030	29

Reference	Condition	Build Orientation	E (GPa)	Y.S. (MPa)	UTS (MPa)	EL%
Z. Hu et al. 2017, Optics & Laser Technology	No post-process	-		633.75-666.25	1103.77-1105.75	20.48-21.28
T. LeBrun et al. 2015, Materials and Design	As-Built	Layers oriented in line with loading direction		661+/-24	1255+/-3	16.2+/-2.5
L. Facchini et al. 2010, Advanced Engineering Materials	As-Built	-	-	600 (Upper), 500 (Lower)	1300	28
T. Mower et al. 2016	*Wrought (Rolled-Longit.)*	-	186	898	1085	6.5
Khalid et al. 2014, ASM Handbook	*Wrought (Aged at 482C)*	-	-	1170	1310	10
AK Steel Corporation	*Cold Flattened-Heat Treatment (482C for 1hr)*	-	-	1379	1448	7

Reference	Condition	Build Orientation	E (GPa)	Y.S. (MPa)	UTS (MPa)	EL%
MakeItFrom.Com	Solution Treated (AT) S17400 Stainless Steel	-	190	1080	1120	5.7
MakeItFrom.Com	H900 Hardened S17400 Stainless Steel	-	190	1250	1390	11
MakeItFrom.Com	H1025 Hardened S17400 Stainless Steel	-	190	1060	1140	13
MakeItFrom.Com	H1100 Hardened S17400 Stainless Steel	-	190	890	1100	16

As is evident from Table 2, as-built additively manufactured Stainless Steel 17-4PH yields mechanical properties that are less than conventionally (i.e., wrought) manufactured Stainless Steel 17-4PH. The stress-strain monotonic response of Stainless Steel GP1 has been shown to exhibit both an upper and lower yield strength [EOS, 2009; Luecke, 2014; Facchini, 2010; Clausen, 2017], from which the yield strengths are highest for samples manufactured in the horizontal orientation, but the ultimate tensile strength is highest for samples manufactured in the vertical orientation [EOS, 2009]. Studies have also shown variation in AM versus conventional tensile properties for Stainless Steel 17-4PH because of phases present (i.e., martensitic for conventional and metastable austenite in AM components [Luecke, 2014]). A comparison of tensile properties between unfinished and machined SLM SS 17-4PH revealed a

significant increase in yield strength, with minimal increase in ultimate tensile strength for machined SS 17-4PH [Everhart, 2016]. Displacement-controlled tension tests performed on DMLS SS 17-4PH samples, which were thermally stress relieved at 788°C for 1 hour, revealed lowest yield strength, but the greatest amount of strain hardening for horizontally manufactured specimens [Mower, 2016]. This material was also observed to exhibit discontinuous yielding attributed to the development and movement of Lüders bands, which were suggested to initiate at the end of the gauge length of the sample and propagate to the center of the sample [Luecke, 2014]. Yield and ultimate tensile strengths in heat treated (aged and solution annealed) SLM SS 17-4pH was found to be larger than in non-heat treated SLM SS 17-4PH; however, there was a reduction in the ductility for heat treated SLM SS 17-4PH [Yadollahi, 2015]. This reduction in ductility was attributed to precipitation hardening of Cr-Ni-Co, which essentially limits dislocation movement [Yadollahi, 2015; Wu, 2003]. There is a greater ductility observed in samples as-manufactured vertically (*z*-direction), as opposed to the horizontal direction (*xy*) [EOS, 2009]. Highest level of ductility was observed for thermally stress relieved (788°C for 1 hour) DMLS SS17-4PH samples, manufactured in vertically oriented 45°specimens [Mower, 2016].

An analysis of the Young's Modulus for DMLS SS 17-4PH revealed lower Young's Modulus for horizontally manufactured specimens (E_{horz} = 172.2 GPa) as compared with samples manufactured in the 45° orientation ($E_{vert\ (45°)}$ = 192.9GPa), which approached the Young's Modulus for wrought SS 17-4PH ($E_{wrought}$ = 193.9GPa) [Mower, 2016]. An analysis of Young's modulus from EOS Stainless Steel GP1 material data sheet reveals the same Young's modulus (E = 170 ± 30 GPa) for samples regardless of building in the horizontal or vertical build orientations. This material also exhibits upper and lower yield strengths that are larger for

horizontally built specimens as opposed to vertically built specimens [EOS, 2009]. However, the ultimate tensile strength is larger for samples manufactured in the vertical orientation

While it is well understood that additively manufactured Stainless Steel GP1 exhibits discontinuous yielding behavior with the presence of an upper and lower yield strength, no study to date has applied a constitutive model to fit the monotonic stress-strain behavioral response of this material. Further, in addition to an understanding of the tensile response of these materials, the failure surfaces for these materials can allow designers to tailor component development towards a desired application, which is yet unexplored [Siddiqui, 2017]. Finally, an understanding of the material behavior, such as the variation in Young's Modulus with build orientation is critical in ensuring design limitations when manufacturing along varying build orientations. These knowledge gaps will be answered within this study.

2.2.2 Torsion Performance

An assessment of both the axial and torsional response of AM materials can provide a comprehensive understanding of these materials under tensile and shear conditions. While there are a number of studies that have provided material properties under tensile loading conditions, very few studies have determined material response under shear loading conditions. Studies on the torsional behavior of AM materials have been reported for Ti-6Al-4V [Fatemi, 2017; Fatemi, 2017; Fatemi, 2017], SS 1.4404 [Hitzler, 2017] and PLA [Torres, 2015] materials. A compilation of torsional properties for conventionally manufactured Stainless Steel 17-4PH is as presented in Table 3. Depending upon the form of heat treatment and/or solution annealing, there is a variation in the shear strength of SS 17-4PH, with the shear modulus and Poisson's ratio remaining within the same regardless of processing conditions. While the chemical composition

of DMLS SS GP1 is similar to that of Stainless Steel 17-4PH, the mechanical properties have been seen to vary across literature. Nevertheless, the torsional properties for Stainless Steel 17-4PH will be used as a reference for comparison of results obtained in this study.

Table 3: Torsional properties of Stainless Steel 17-4PH

Reference	Condition	Shear Modulus, G (GPa)	Ultimate Shear Strength (MPa)	Poisson's Ratio, ν
MakeItFrom.com	Solution Treated (AT) S17400 Stainless Steel	**75**	**650**	**0.28**
	H900 Hardened S17400 Stainless Steel	**75**	**830**	**0.28**

No study to date has reported the monotonic torsion and torsional fatigue response of DMLS SS GP1, and the role of build orientation on their material response. Properties such as the shear modulus, ultimate strength in shear and Poisson's ratio are yet undetermined for additively manufactured Stainless Steel GP1. An understanding of torsional fatigue response is also limited for this study, in addition to life assessment under highly plastic shearing conditions and its impact on the exhibited fracture response by this material.

2.2.3 Fatigue Performance

Fatigue life of additively manufactured components is limited, most especially because of the inherent surface roughness/internal voids that is present within as-built components. The presence of surface roughness allows for crack initiation to begin with cyclic loading. Most

fatigue studies on AM SS 17-4PH have focused on determining the stress-life behavior of this material, with limited studies assessing the strain-life behavior.

Strain-controlled, completely reversible (R = -1) fatigue test on SLM as-built and heat-treated SS 17-4PH vertically oriented specimens, were used to develop a strain-life curve, which showed heat-treated specimens yielding higher fatigue strengths in low cycle fatigue regime as opposed to high cycle fatigue regime [Yadollahi, 2015]. A high cycle fatigue study on SLM as-built and machined 1.4542 Stainless Steel (also known as SS 17-4PH), at a stress ratio of R = 0, has shown that higher fatigue strength was found for the machined samples because of lower surface roughness [Stoffregen, 2014]. Completely reversible (R = -1) stress-controlled fatigue tests were performed on DMLS SS 17-4PH samples, horizontally and vertically built, from which it was observed that horizontal specimens performed similar to wrought SS 17-4PH samples, with a fatigue strength 900MPa in LCF regime and an endurance strength near 450MPa, but with considerable scatter in results [Mower, 2016]. It was further observed that 2 batches of vertically built DMLS SS 17-4PH samples, developed using the same optimization parameters, revealed a varying stress-life performance, with the 1^{st} batch exhibiting a fatigue strength 60% of wrought SS 17-4PH, while the 2^{nd} batch exhibited a fatigue strength 25% that of wrought SS 17-4PH [Mower, 2016]. Analysis of fracture surfaces for vertically build samples revealed that the 1^{st} batch had fatigue crack initiation occur from internal defects, whereas the 2^{nd} batch had fatigue crack initiation occur between 2 build planes [Mower, 2016]. There have been other fatigue stress-life studies on SLM SS 17-4PH [Sehrt, 2010; Starr, 2011].

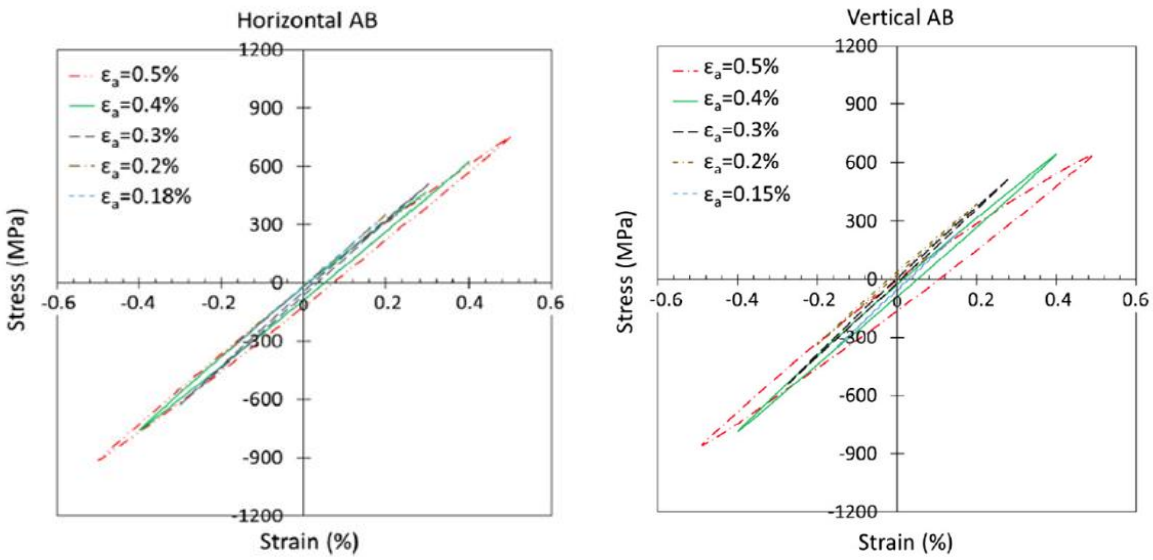

Figure 3: Hysteresis curves from strain ranges tested for as-built additively manufactured SS 17-4PH, horizontal and vertical build orientations reported in literature [Yadollahi, 2016]

While literature findings on additively manufactured Stainless Steel GP1/17-4PH reveal that fatigue studies have been conducted with the aim to determine stress-life and strain-life behavior of these materials, the impact of a variety of fatigue conditions encountered by these materials during application is yet unexplored. During start-up and shut-down of gas turbine engines, material components experience high cyclic plasticity. As Stainless Steel GP1/17-4PH is used in aerospace components, it is necessary to characterize the performance of this material when additively manufactured and subject to low cycle fatigue testing at high plastic strain ranges. With that consideration, this study has evaluated the performance of DMLS SS GP1, manufactured along varying build orientations, and subject to LCF testing at a highly plastic strain range of $\Delta\varepsilon = 1.4\%$.

Understanding the performance of these materials under pulsating tension fatigue conditions, in which repeated tensile mean stresses can be detrimental to the life of a material,

due to the rapid propagation of cracks under these conditions, it is important to ensure that component manufacturing through the AM process does not further contribute to this behavior. As such, research is needed to understand the performance of DMLS SS GP1 under pulsating tension fatigue loading condition.

In addition, aerospace components often encounter progressive amplitude cyclic stresses/strains during operation. Evaluating the role of progressive amplitude fatigue test conditions on additively manufactured materials, such as DMLS SS GP1, can provide insight into the relationship between AM induced defects at the microstructural level and mechanical response of the material. Therefore, this study has conducted preliminary experiments to provide an initial assessment of DMLS SS GP1 under progressive progressive amplitude fatigue loading conditions. Multiple studies have reported the monotonic cyclic stress-strain behavior for this material, as discussed in Section 2.2.1, however, few studies have assessed the cyclic stress-strain response for DMLS SS GP1. A study reported by Yadollahi and coauthors [Yadollahi, 2017], developed an initial cyclic stress-strain curve based upon fatigue tests performed primarily at elastic strain ranges, as shown in Figure 3. The stabilized curves from these experiments will be used to develop a cyclic stress-strain curve for this material, including data points at high plastic strain ranges, which will be compared with those findings reported by Yadollahi and coauthors [Yadollahi, 2017].

2.2.4 Constitutive Models

While considerable number of studies have reported experimental findings on AM SS GP1/17-4PH, limited studies have used constitutive model to replicate and extend findings. Few studies have modeled the monotonic response of these materials through use of a strain-

hardening model, such as the Ramberg-Osgood model [Yadollahi, 2017] or another appropriate theory.

$$\boldsymbol{\varepsilon} = \left(\frac{\boldsymbol{\sigma}}{\boldsymbol{E}}\right) + \left(\frac{\boldsymbol{\sigma}}{\boldsymbol{K}}\right)^{\frac{\mathbf{1}}{\boldsymbol{n}}} \quad (1)$$

$$\boldsymbol{\sigma} = \boldsymbol{K}(\boldsymbol{\varepsilon_p})^{\boldsymbol{n}} \quad (2)$$

The Ramberg-Osgood model, which is defined in Equation (1) can be used to model the monotonic and cyclic stress-strain curve of these materials, in which *K* is the strain hardening coefficient and *n* is the strain hardening exponent. *K* and *n* are determined using a power law regression fit between the 0.2% yield strength and ultimate tensile strain as indicated in Equation (2).

While the Ramberg-Osgood model is commonly employed to simulate the non-linear monotonic stress-strain curve behavior of a number of materials, it is limited in its applicability to model materials that exhibit discontinuous yielding, with the presence of an upper and lower yield strength. This material response is as exhibited in Figure 4, and is attributed to the development of Lüder bands within the material, during tensile testing. After the material yields at point A, these bands of plastic deformation emanate and propagate during region C, as indicated in Figure 4, through the gauge section of the specimen, after which the material begins to encounter strain hardening. This strain hardening initiates after the Lüder bands have propagated through the gauge section of the specimen, immediately after the lower yield strength is reached. It is suggested that the emergence of these Luder bands in certain stainless steel materials is a result of limitation in dislocation movement, causing a sudden drop in the flow stress, as exhibited by the stress-strain response. It has been reported that DMLS SS GP1

exhibits this discontinuous yielding phenomena [Luecke, 2014; Facchini, 2010], thereby necessitating the constitutive modeling of this material behavior.

A plasticity yield-point model, that takes into consideration this discontinuous yielding behavioral response was developed in 1962 by G.T. Hahn, for iron and body centered cubic (BCC) metals that exhibit this material behavior [Hahn, 1962]. This model also takes into consideration the delay-time phenomena [Hahn, 1962].

$$\sigma = q\epsilon_p + 2\tau_0 \left[\frac{\dot{\epsilon}}{0.5bf(\rho_0 + C{\epsilon_p}^a)}\right]^{\frac{1}{n}} \quad (3)$$

As presented in Equation (3), the flow stress, σ, is a function of the macroscopic work hardening coefficient, q, plastic strain, ϵ_p, strain rate, $\dot{\epsilon}$, resolved shear stress for unit velocity, τ_0, average density of unlocked dislocations, ρ_0, Burger's vector, b, fraction of dislocation density, f, dislocation density parameters, C and a, and a constant related to determining dislocation velocity, n [Hahn, 1962]. Currently unexplored is the constitutive modeling of the discontinuous stress-strain response exhibited by DMLS SS GP1, and the applicability of the Hahn model to fit the tensile response of AM materials, as will be presented further on in Chapter 6.

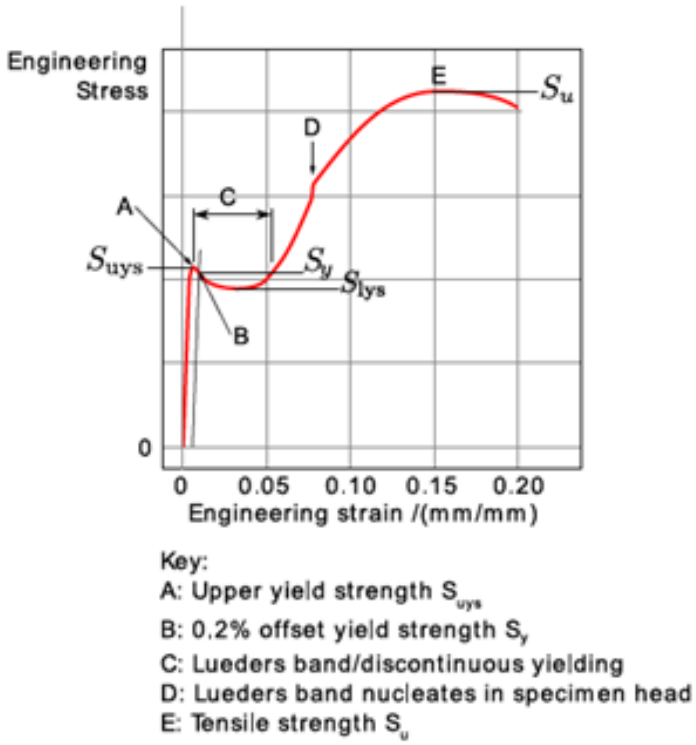

Figure 4: Schematic of discontinuous yielding response exhibited by certain iron-based and body centered cubic (BCC) metals [Luecke, 2014]

In addition to modeling the monotonic stress-strain response of these materials, equally important is addressing the cyclic behavior of AM metal materials, as they have application in a wide number of disciplines in which they are subject to repeated fluctuating stresses.

Most fatigue studies in literature have focused primarily on characterizing the stress-life behavior or strain-life behavior of these materials, as discussed in Section 2.2.3. Cyclic stress-strain behavior of these materials have been experimentally determined for elastic strain ranges [Yadollahi, 2017], and modeled using the Ramberg-Osgood model. However, yet unexplored is the complete cyclic stress strain behavior [Yadollahi, 2017] taking into consideration plastic strain ranges. Given the time and cost associated with fatigue testing of AM specimens, it is vital

that the applicability of current constitutive models to simulate the cyclic hysteresis response, in addition to the kinematic and isotropic hardening behavior of these materials be assessed. Current studies on AM Stainless Steel 17-4PH/GP1 have not yet modeled the cyclic hysteresis response, through application of a viscoplasticity model.

The Chaboche model takes into account the viscoplastic strain rate, kinematic hardening, plastic strain memorization, isotropic hardening, and the time-recovery for kinematic hardening and isotropic hardening [Chaboche, 1989; Chaboche, 1983]. A visual description of the kinematic and isotropic hardening of a material is as presented in Figure 5. With kinematic hardening, there is a shift in the yield surface, whereas with isotropic hardening, the yield surface experiences expansion or contraction, as shown in Figure 5. The kinematic hardening, X, acts as a back stress in the Chaboche Model, which represents movement of the yield surface allowing for directional hardening. For this study, nonlinear kinematic hardening was considered, as shown in Figure 5.

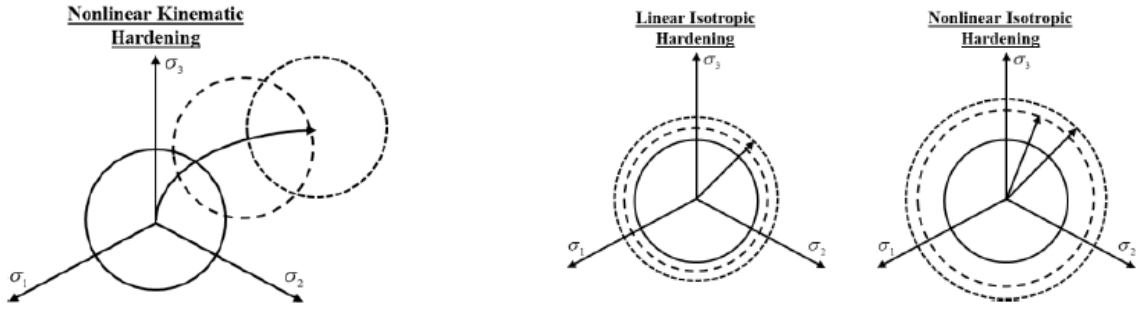

Figure 5: Visual depictions of kinematic and isotropic hardening aspects considered in the Chaboche model **[**O'Nora**,** 2015**]**

The Chaboche model uses the Von Mises yield criterion, which is a function of the predictor stress tensor, σ, kinematic hardening tensor, X, yield stress or proportional limit, k, and isotropic hardening, R, as presented in Equation (4).

$$\boldsymbol{\sigma}_v = J(\boldsymbol{\sigma} - \mathbf{X}) - k - R \quad (4)$$

$$J(\boldsymbol{\sigma} - \mathbf{X}) = \sqrt{\frac{3}{2}(\boldsymbol{\sigma}' - \mathbf{X}'):(\boldsymbol{\sigma}' - \mathbf{X}')}$$

$$\boldsymbol{\sigma}' = \boldsymbol{\sigma} - \frac{1}{3}tr(\boldsymbol{\sigma})\ and\ \mathbf{X}' = \mathbf{X} - \frac{1}{3}tr\mathbf{X}$$

For a given stress space, J (σ-X) is defined as a function of the deviators of σ and X. The Chaboche model is expressed as the plastic strain rate, $\dot{\varepsilon_p}$, which is a function of the norm of the plastic strain rate, $\dot{p}$, stress deviator, σ' and X', the kinematic internal stress tensor/back stress tensor, as shown in Equation (5). The norm of the plastic strain rate is determined as a function of the yield criterion (Von Mises stress), and Z, n material constants, also given in terms of the Norton creep law, as represented in Equation (6).

$$\dot{\boldsymbol{\varepsilon}}_{\boldsymbol{p}} = \frac{3}{2}\dot{p}\frac{\boldsymbol{\sigma}' - \mathbf{X}'}{J(\boldsymbol{\sigma} - \mathbf{X})} \quad (5) \qquad \dot{p} = \left(\frac{J(\boldsymbol{\sigma} - \mathbf{X}) - k - R}{Z}\right)^n \quad (6)$$

Armstrong-Fredrick (Equation (7)) non-linear kinematic hardening terms were used, where in X_i is the i^{th} kinematic hardening term, and C_i and a_i are the associated material constants, corresponding to each kinematic hardening term. For the purpose of this study, 3 non-linear hardening terms were used to essentially obtain a_1, C_1, a_2, C_2, a_3 and C_3.

$$\dot{\mathbf{X}}_{\mathrm{i}} = \frac{2}{3}C_i\dot{\boldsymbol{\varepsilon}}_{\boldsymbol{p}} - a_i\mathbf{X}_{\mathbf{i}}\dot{p} \quad (7)$$

Initial estimates for each of the 3 kinematic hardening constants was determined from plots of plastic strain versus the amount of hardening the material experienced in the early, middle and later portions of the initial quarter cycle. The Chaboche model also takes into consideration isotropic hardening, which is essentially the expansion or contraction of the yield surface, and is attributed to the softening/hardening material response. Direct calibration method has been used to assess both the variation in kinematic and isotropic hardening progression within the "finite plastic deformation region" [Khan, 1999] for non-AM materials, however this study has focused upon localized cycle fits assessing only the kinematic hardening behavior of this material, with future work focused on assessing both the kinematic and hardening response of AM materials. In order to have a significant effect, isotropic hardening takes into account a large amount of plasticity, therefore the effect on the first cycle is negligible. As such, isotropic hardening terms were held at zero.

Conventionally manufactured stainless steels are unique in that tensile properties can be used to predict the hardening/softening material response without the need for long-duration fatigue experiments. As the additive manufacturing process is a costly process, it is important to limit the number of destructive test evaluations, and use models to predict material response. As such, there is a need to determine whether the tensile-fatigue properties that can be applied for non-additively manufactured materials, be applied for these additive class of materials. In fatigue analysis for non-additively manufactured materials, the ratio of UTS to the yield strength can provide insight into the cyclic hardening and softening behavior of the material.

$$\frac{S_u}{\sigma_{0.2\%ys}} > \mathbf{1.4} \ \{\text{Cyclically Hardens}\} \qquad \frac{S_u}{\sigma_{0.2\%ys}} < \mathbf{1.2} \ \{\text{Cyclically Softens}\} \quad (8)$$

This relationship is expressed in Equation (8), from which it can be seen that a material will cyclically harden if this ratio is greater than 1.4 and cyclically soften if this ratio is less than 1.2 [Stephens, 2001]. Tensile properties obtained from experimental testing of DMLS SS GP1 in correlation with these relationships, have been used to predict the hardening/softening response of these AM materials. Findings are used to compare with experimentally observed hardening/softening response from fatigue testing.

Tensile properties, specifically the Young's Modulus, obtained through tension tests or from the first cycle of fatigue experiments can be used to characterize the variation of Young's Modulus with build orientation, of particular importance for AM materials, since they exhibit anisotropic behavior. Few studies have analyzed Young's Modulus variation with build orientation for AM metal materials, such as IN738C [Kunze, 2015], Stainless Steel 1.4404 [Hitzler, 2017], and more recently, this research on IN718 [Siddiqui, 2017] and Stainless Steel GP1 [Siddiqui, 2017]. The Young's Modulus can be found within the LT-plane through use of Equation (9) [Bouchenot, 2014], in which E_L is the Young's Modulus in the *z*-direction (parallel to build axis), E_T is the Young's Modulus in the *x* or *y*-direction (perpendicular to the build axis), and E_{45} is the Young's Modulus 45° from the *z*-direction (build axis) either along the *zx* plane or the *zy* plane. It is important to note that θ is referenced from the *z*-direction (L) build orientation. Equation (9) can be tailored specifically to represent the variation in Young's Modulus across any build plane (i.e., *xy*, *yz* and *xz*), which can contribute to much needed knowledge of exhibited anisotropic Young's modulus variation.

$$\boldsymbol{E(\theta) = \left[\frac{1}{E_L}(\cos\theta)^4 + \left(\frac{4}{E_{45}} - \frac{1}{E_L} - \frac{1}{E_T}\right)(\sin\theta)^2(\cos\theta)^2 + \frac{1}{E_T}(\sin\theta)^4\right]^{-1}} \quad (9)$$

In addition to modeling the anisotropic variation in Young's modulus for these materials, it is also important to model the failure surfaces of these materials. This can provide insight into the failure regime of as-built additively manufactured materials and the role of surface roughness on failure surfaces for these materials. The Hill's criteria is used to model the failure surface for anisotropic materials under multiaxial stress conditions. It assumes the same failure criteria in tension and compression, and considers only the deviatoric stress.

$$\boldsymbol{\sigma_{Hill}} = \sqrt{\boldsymbol{F(\sigma_y - \sigma_z)^2 + G(\sigma_z - \sigma_x)^2 + H(\sigma_x - \sigma_y)^2 + 2L(\tau_{yz}^2) + 2M(\tau_{zx}^2) + 2N(\tau_{xy}^2)}} \quad (10)$$

$$\boldsymbol{F = \frac{1}{2}\left(\frac{1}{R_{yy}^2} + \frac{1}{R_{zz}^2} - \frac{1}{R_{xx}^2}\right)} \quad \boldsymbol{G = \frac{1}{2}\left(\frac{1}{R_{zz}^2} + \frac{1}{R_{xx}^2} - \frac{1}{R_{yy}^2}\right)} \quad \boldsymbol{H = \frac{1}{2}\left(\frac{1}{R_{xx}^2} + \frac{1}{R_{yy}^2} - \frac{1}{R_{zz}^2}\right)} \quad (11)$$

$$\boldsymbol{L = \frac{3}{2}\left(\frac{1}{R_{yz}^2}\right)} \quad \boldsymbol{M = \frac{3}{2}\left(\frac{1}{R_{xz}^2}\right)} \quad \boldsymbol{N = \frac{3}{2}\left(\frac{1}{R_{xy}^2}\right)} \quad (12)$$

The Hill's criteria for multiaxial stress condition is presented in Equation (10) where *F*, *G*, *H*, *L*, *M*, and *N* are Hill's constants [Bouchenot, 2014; Hill, 1998]. These constants are determined by the equations in (11) and (12), which used the strength ratios R_{xx}, R_{yy}, R_{zz}, R_{xy}, R_{yz}, and R_{xz}, which have been normalized with respect to the reference direction/build direction '*z*'. If transversely isotropic conditions are assumed, the plastic anisotropy matrix '*M*' can be described by 3 independent Hill's constants: *F*, *H* and *L* and the strength ratios can be defined as $R_{zz} = R_{LL}$, $R_{xx} = R_{yy} = R_{xy} = R_{TT}$, $R_{xz} = R_{yz} = R_{LT}$. The Hill's criteria can be simplified for a case of plane stress, in which the general equations for plane stress transformation can be used. A first approximation of the failure surfaces for DMLS SS GP1 is developed through use of Hill's criteria, and is presented in Chapter 6.

2.2.5 Microstructure and Fracture Response

For DMLS Stainless Steel GP1, which is suggested to be similar in chemical composition to Stainless Steel 17-4PH [EOS, 2009], a martensitic precipitation hardening stainless steel, it has been found that DMLS as-manufactured SS GP1 was primarily comprised of metastable austenite which transformed to martensite, which is ferromagnetic, when subject to tension testing/plastic deformation [Facchini, 2010; Luecke, 2014]. Other studies have also examined this phase change behavior due to the SLM process [Murr, 2012; Starr, 2012]. As such, it was suggested that classifying DMLS Stainless Steel GP1 as Stainless Steel 17-4PH is not valid, regardless of the similar chemical composition presented in Table 1, because DMLS Stainless Steel GP1 is primarily comprised of metastable austenite phase as opposed to the primarily martensite phase [Luecke, 2014]. In its conventional form, SS 17-4 is in the martensitic phase, with traces of ferrite 'δ' phase that causes embrittlement of the material. In order to counteract this behavior, SS 17-4 undergoes aging heat treatment which introduces austenite phase that improves the mechanical performance of this material [Cheruvathur, 2015; Averyanova, 2010]. The microstructure for N_2 atomized SS 17-4PH used to develop an SLM component in a Nitrogen atmosphere has shown melt arc pools to be present as well as texturing/orientation of grains, with [220] γ and [111] γ texturing in horizontal and vertical planes respectively [Murr, 2012]. Heat treatment of SLM SS 17-4pH was found to result in recrystallization and presence of precipitates at grain boundaries [Yadollahi, 2015]. Microstructure images of as-built DMLS SS GP1 parallel and perpendicular to the build direction is as shown in Figure 6. Melt arc pools are evident parallel to the build direction, while fine grain microstructure and laser scan tracks are evident perpendicular to the build direction. Also clearly evident is the presence of unmelted powder particles perpendicular the build direction.

a.) 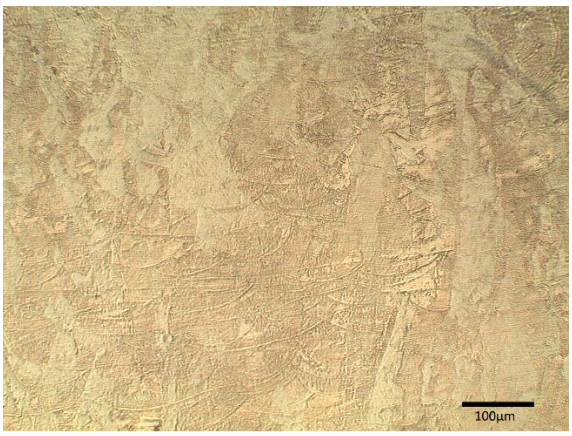

b.) 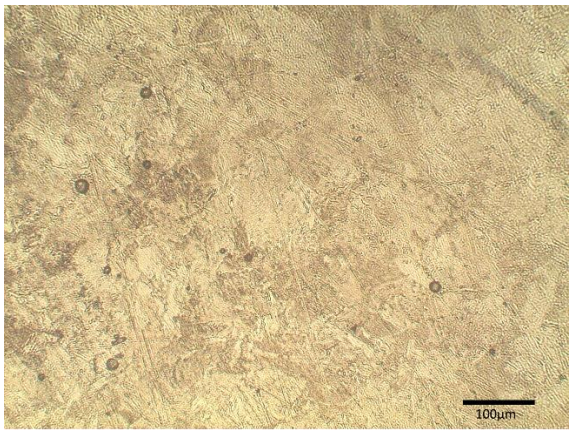

Figure 6: Microstructure of DMLS SS GP1: a.) Parallel to the build direction, b.) Perpendicular to the build direction

Fracture surfaces revealed fatigue crack initiation at un-melted powder locations for low strain amplitudes, as opposed to high strain amplitudes where fatigue crack initiation began at the surface, for strain ranges up to 0.5% tested [Yadollahi, 2015]. It was also found that un-melted locations near the surface of SLM SS 17-4PH were the most damaging, because they cause regions of high stress concentration [Yadollahi, 2017]. For as-built SLM SS 17-4PH, a textured and irregular fracture surface has been observed, for specimens subject to tensile testing [LeBrun, 2015]. SLM as-built and heat-treated SS 17-4PH were observed to exhibit a ductile fracture response [Hu, 2017].

2.2.6 Surface Roughness

Surface roughness, which is characteristic to the additive manufacturing process, is a result of a phenomena referred to as the "stair-stepping" effect [Siddiqui, 2017; Turner, 2015; Strano, 2013]. It essentially is a result of the layer by layer deposition and fusion process that occurs in powder-bed additive manufacturing processes. Surface roughness is of considerable

concern with AM components because it is directly linked to crack initiation during applications in which repeated cyclic stresses are endured by a component. As such, components with high surface roughness can endure pre-mature failure, rendering useless for its intended application.

Average surface roughness "R_a" is defined in Equation (13) in which "$f(x)$" is a function relating the distance between the measurement location at the surface and the reference centerline; here "l" is the distance over which the surface roughness is being measured [Strano, 2013; Siddiqui, 2017].

$$R_a = \frac{1}{l}\int_0^l |f(x)|dx \quad (13)$$

Surface roughness measurements of DMLS SS 17-4pH were found to be 3-5 µm for S_a and 4-7µm for S_{rms} as compared with machined and polished wrought 17-4pH, which was found to be 1µm for both S_a and S_{rms} [Mower, 2016]. A 900µm x 900µm surface profile of DMLS SS 17-4pH fatigue samples revealed surface roughness peak to valley variation of 40µm for a horizontally manufactured sample [Mower, 2016]. After shot-peening, surface roughness values for DMLS SS GP1 have been found to be in the range of 2.5-4.5µm [EOS, 2009]. One study assessed the impact of scanning strategy on surface roughness, and reported average roughness values ranging between 7-11µm [Kudzal, 2017]. Surface roughness for polished SLM 17-4PH on which fatigue experiments were performed were measured to be 0.7µm.

Reduction in the surface roughness (R_a) of SLM manufactured parts by optimization of process parameters is necessary in order to improve the life and performance of these parts. Optimization of SLM process parameters by manufacturers of AM system minimizes R_a. The

research question that needs to be answered is whether or not there is a build orientation that can yield minimal surface roughness to eliminate the need for post-processing techniques, specifically polishing.

2.3 Material Behavior of Additively Manufactured Inconel 718

Nickel-base superalloys are used in high temperature applications due to their excellent oxidation and corrosion resistance at a high temperature of 650°C as well as high strength, and fatigue resistance. Inconel is a trademark name for a Ni-Cr-Fe austenite based superalloy, as represented by its chemical composition in Table 4.

Table 4: Chemical Composition of Inconel 718 [EOS, 2014; Special Metals Corporation, 2013]

Cr	Co	Nb	Mo	Ti	Al	C	Mn	Si	Fe	Ta	B	Ni	P	S	Cu
17-21	≤1.0	4.75-5.5 (with Ta)	2.8-3.3	0.65-1.15	0.20-0.80	≤0.08	≤0.35	≤0.35	B*	Included with Nb	≤ 0.006	50-55 (with Co)	≤ 0.015	≤ 0.015	≤ 0.30

2.3.1 Mechanical Properties under Tensile Loading

The anisotropic microstructural behavior of SLM parts contributes significantly to the mechanical strength observed for these components. Tensile properties across literature for conventionally manufactured Inconel 718 are reported in Table 5, with as-built and/or heat-treated additively manufactured Inconel 718 properties, from select studies, presented in Table 6 and Table 7. Presented in Table 5 are variations in the manufacturing technique used to develop Inconel 718, and include casting, forging, as-rolled, and wrought/annealed conditions. It is clearly evident that additively manufactured Inconel 718 yields tensile properties within range of, or exceeding that of conventionally manufactured Inconel 718.

Table 5: Tensile properties of conventionally manufactured Inconel 718

Source	Type	Young's Modulus, *E* (GPa)	Yield Strength, σ_{ys} (MPa)	Tensile Strength, *Suts* (MPa)	Elongation, *EL* (%) (Strain at Failure)
J.R. Davis, ASM Specialty Handbook	*As-Rolled*	200-211	448-727	896-1014	40-46
SpecialMetals.com	*Wrought (Annealed)*	-	830	1100	3
T. Trosch et al. 2016, Material Letters	*Forged*	-	1192	1380	19.1
T. Trosch et al. 2016, Material Letters	*Cast*		940	950	23.1

Table 6: Tensile mechanical properties of as-built additively manufactured Inconel 718 [Siddiqui, 2018]

Source	Orientation (Millers Indices)	Young's Modulus, *E* (GPa)	0.2% Yield Strength, σys (MPa)	Tensile Strength, *Suts* (MPa)	Elongation, *EL* (%) (Strain at Failure)
Chlebus et al., 2015, Materials Science & Engineering	*L* - (001)	162 ± 18	572 ± 44	904 ± 22	19 ± 4
	T - (010)	193 ±24	643 ± 63	991 ± 62	13 ± 6
	D - (011)- 45°	200 ±23	590 ± 15	954 ± 10	20 ± 1
	(111)- 45°x45°	208 ±48	723 ± 55	1117 ± 45	16 ± 3
Wang et al., 2012,	T- Horizontal	204	889-907	1137-1148	19.2-25.9
Amato et al., 2012,	T- Horizontal		830	1120	25
Strobner et al., 2015,	*L* - Vertical	-	737 ± 4	1010 ± 10	20.6 ± 2.1
	T- Horizontal	-	816 ± 24	1085 ± 11	19.1 ± 0.7
Popovich et al., 2015	-	-	569-646	851-1002	9.8- 31.7
Scott-Emuakpor et al. 2014	L- Vertical	182	868	1162	26
	T- Horizontal	174	789	1059	31
M.E. Aydinoz et al. 2016	L- Vertical		580	845	
P.L. Blackwell 2005			650	1000	38
P.F. Kelley 2016	L- Vertical	72.1 ± 7.31	568.8 ± 5.85	874.3 ± 3.9	55.7
	T- Horizontal	162.7 ± 3.9	640.9 ± 2.44	974.9 ± 4.88	41.6

Table 7: Tensile mechanical properties of heat-treated additively manufactured Inconel 718 [Siddiqui, 2018]

Source	Orientation (Millers Indices)	Young's Modulus, *E* (GPa)	0.2% Yield Strength, *σys* (MPa)	Tensile Strength, *Suts* (MPa)	Elongation, *EL* (%) (Strain at Failure)
Chlebus et al., 2015	*L* - (001)	163 ± 30	1074 ± 42	1320 ± 6	19 ± 2
	T - (010)	199 ± 15	1159 ± 32	1377 ± 66	8 ± 6
	D - (011)- 45°	188 ± 19	1152 ± 24	1371 ± 5	15 ± 5
	(111)- 45°x45°	209± 44	1241 ± 68	1457 ± 55	14 ± 5
Amato et al., 2012	*L* - (001)	-	850	1140	28
	T - (010)	-	890	1200	28
Strobner et al., 2015	*L* - Vertical	-	1136 ± 16	1357 ± 5	13.6 ± 0.2
			1186 ± 23	1387 ± 12	17.4 ± 0.4
	T - Horizontal	-	1227 ± 1	1447 ± 10	10.1 ± 0.6
			1222 ± 26	1417 ± 4	15.9 ± 1.0
Popovich et al., 2015	-	-	1160	1350	17.6
Smith et al. 2016	*L* - (001)	165	1215	-	-
	T - Horizontal	195	1290	-	-
	D - 45°	215	1305	-	-
Trosch et al. 2016	*L* - (001)	-	1180	1400	20.4
	T - Horizontal	-	1186	1440	18.5
	D - 45°	-	1190	1450	16.9

A comparison of these mechanical properties across most studies on SLM IN718, reveal an increase in the 0.2% yield strength and tensile strength with heat treatment [Strøßner, 2015; Chlebus, 2015; Wang, 2012], as opposed to a decrease in the elongation % or ductility with heat treatment [Strøßner, 2015; Wang, 2012]. Anisotropic mechanical properties can also be observed across SLM IN718 studies [Wang, 2015], which finds that the 0.2% yield strength and tensile strength are larger for samples manufactured horizontally, whereas ductility is greatest in samples manufactured vertically [Strøßner, 2015; Chlebus, 2015; Trosch, 2015; Lambert, 2015; Kelley, 2016]. Most studies have examined strength and ductility behavior parallel and perpendicular to the build direction, with few studies examining material behavior at a 45° orientation, within one build plane [Trosch, 2016; Smith, 2016]. One study has assessed the variation in mechanical tensile properties, for samples manufactured in the horizontal, vertical and 45° build orientations at varying temperatures, from which it was found that SLM IN718 properties are improved at room temperature and 450°C, compared with conventional IN718 [Trosch, 2016].

Several findings from literature have reported the tensile response of these materials, however un-reported is the use of these tensile/compression properties towards the development of failure surfaces, that can be used to predict the failure regimes of Inconel 718 when subject to operational conditions. Furthermore, for intermediate build orientations, besides the vertical, horizontal and diagonal orientations tested, it is vital to apply constitutive models to predict the behavioral response at these build orientations. These include Young's Modulus variation with

build orientations and Ramberg-Osgood constant predictions for varying build orientations, all of which are developed in this study.

SLM IN718 samples manufactured in the '*xy*' build plane were found to have slightly higher yield and ultimate tensile strength as compared with samples manufactured in the '*z*' direction [Lambert, 2015]. It was assumed in this study that the material behaves transversely isotropic [Lambert, 2015], but experimentation was not performed to support this finding, nor was the amount of variation in properties along the *x* or *y* direction was determined. A recent study on heat treated and hot isostatic pressing (HIP) DMLS IN718, that were machined to eliminate surface roughness, observed a variation of true yield stress in compression versus tension by 40 MPa [Smith, 2016]. A study by K. Kunze et al. 2015 found anisotropic behavior in IN738LC samples and suggested that this behavior may be attributed to the orientation of the crystals, build orientation variation of the Young's Modulus, and application of stress loading parallel versus transverse to the columnar grains in the build direction for "*z*-specimens" and "*xy* specimens" [Kunze, 2015]. Of considerable interest, and yet unexplored is the anisotropic material behavior of these materials, specifically under torsional loading conditions, exhibited in all three build planes (*xy*, *yz* and *xz*) for classification of material behavior as orthotropic or transversely-isotropic, with some studies assuming transversely-isotropic behavior [Brodin, 2013].

2.3.2 Torsion Performance

In gas turbine engines, where Inconel 718 is often used as the substrate component, a multi-axial stress state is present, in which both an understanding of the axial and torsional material response is necessary. While considerable studies have assessed the axial (tensile/compressive) and fatigue behavior of additively manufactured Inconel 718, no study to

date has assessed the torsional fatigue response of AM Inconel 718. As such, this study explores the impact of build orientation on the completely reversible torsional fatigue response of these materials. A summary of the torsional properties for conventionally manufactured Inconel 718 is listed below in Table 8, and is used as a reference for comparison with the shear modulus and Poisson's ratio determined from this study.

Table 8: Torsional properties for conventionally manufactured Inconel 718

Reference	Shear Modulus, G (GPa)	Poisson's Ratio, ν
Maher.com	**77.2**	**0.294**

2.3.3 Fatigue Performance

Inconel 718 is used considerably in aerospace components, which are subject to cyclic stresses, hence the need to characterize the fatigue performance of these materials when additively manufactured. Considerable research has been done on assessing this behavior. For DMLS Ni-718, it was found that heat treated, HIP and stress relieved samples exhibited a lower fatigue life than samples that were only stress-relieved or samples that were cold-rolled [Scott-Emuakpor, 2015]. Cold rolled and DMLS Ni-718 fatigue life was found to be within the range of $2x10^5$ and $2x10^6$ cycles to failure [Scott-Emuakpor, 2015]. A study on aged SLM IN939 has found that fatigue life was reduced, as compared with fatigue life at room temperature, which was suggested to be attributed to the precipitate formation and presence of pores, resulting in higher sensitivity to crack initiation [Kanagarajah, 2013]. There has been focus on characterizing the life of these materials, primarily in the high cycle fatigue regime leading to determination of the stress-life response of these materials, manufactured along the X/Y and Z orientations

[Kelley, 2016]. Low cycle fatigue testing at strain ranges from 0.6% to 1.4% on DMLS Inconel 718 as-built and heat treated/HIP have been performed for specimens manufactured along the 45° and 90° orientations from the build plane, which was used to develop the strain-life curve using the Coffin-Manson model [Gribbin, 2016]. Low cycle fatigue testing has also been performed at strain amplitudes of 0.35%, 0.5% and 0.85% for SLM Inconel 718 as-built and subject to a variety of heat-treatment conditions [Aydinoz, 2016]. However, yet undeveloped is the complete cyclic stress-strain response, and associated Ramberg-Osgood constants for DMLS Inconel 718 along these build orientations. Crack propagation behavior on SLM Inconel 718 notched specimens has also been assessed along varying build orientations [Konecna, 2016].

2.3.4 Constitutive Models

Considerable studies have presented the monotonic stress-strain curve/properties for DMLS/SLM Inconel 718 of varying build orientations [Smith, 2016; Kelley, 2016; Gribbin, 2016]. Anisotropy in Young's Modulus has been modeled for SLM IN738LC samples based upon tension experiments along *X*, *Y* and *Z* directions [Kunze, 2015], however experimental data has not been presented for intermediary 45° angles within each plane for a complete understanding of material behavior. A crystal plasticity model has been developed for additively manufactured Inconel 718 [Ghorbanpour, 2017]. The stress-life response of DMLS Inconel 718, manufactured along the X/Y and Z orientations has been modeled, yielding an approximation of material constants and the true fracture strength [Kelley, 2016]. The strain-life response, modeled using the Coffin-Manson model has been presented for DMLS Inconel 718, manufactured 45° and 90° from the build orientation [Gribbin, 2016], however a cyclic stress-strain response has not been modeled for this material. Hardening and softening responses have been reported for varying build orientations/heat treatments of AM Inconel 718 [Gribbin, 2016;

Kelley, 2016], however, the applicability of tensile properties in accurately predicting this fatigue response has yet to be ascertained. Further, while it is reported that there is the presence of tensile-compressive asymmetry in additively manufactured Inconel 718 [Smith, 2016], this response has yet to be applied to simulation of failure surfaces for this material. Multiple studies have reported variation in tensile properties with build orientation [Chlebus, 2015; Trosch, 2016; Smith, 2016; Gribbin, 2016], yet no study to date has used experimental tensile/compressive properties towards the development of failure/yielding surfaces for this material. Yield surface development provides both researchers and industries a comprehensive understanding of AM material behavior when manufactured along varying build orientations. These failure surfaces can provide insight about the strength of a material for a desired application. Currently, yield surfaces have been developed for 3D printed plastic polymer materials, with minimal studies presenting yield surface approximations for metal materials, developed through the powder-bed AM process.

As few studies have reported the presence of slight tensile-compressive asymmetry within these materials [Smith, 2016; Mahmoudi, 2017], use of the Tsai-Wu model, which takes into consideration both anisotropic and tensile-compressive asymmetric material behavior, can be used to further enhance the accuracy of failure surfaces developed for AM materials. The Tsai Wu model, simplified for a case of plane stress, assuming transversely isotropic material behavior, is as presented in Equation (14) [Tsai, 1971].

$$\boldsymbol{\sigma_{Tsai-Wu} = F_2\sigma_2 + F_3\sigma_3 + F_{22}\sigma_2^2 + F_{33}\sigma_3^2 + F_{44}\sigma_4^2 + 2F_{23}\sigma_2\sigma_3 \leq 1} \qquad (14)$$

Here, it can be seen that F_2, F_3, F_{22}, F_{33}, F_{44}, and F_{23} represent the strength coefficients, determined through experimental testing. As this study will be assuming transversely isotropic material behavior, with the *xy* plane being the plane of isotropy, the strength coefficients along the '*1*' and '*2*' directions are considered the same. Tension and compression tests are used to determine the failure strengths along each direction, which are then used to calculate the strength coefficients, F_2, F_3, F_{22}, F_{33}. The equations presented in (15) are used to determine these strength coefficients. The strength coefficient, F_{44}, is determined through shear testing, and F_{23}, is determined as a function of F_{22} and F_{33}, and also experimentally through equi-biaxial testing. These equations are presented in (16).

$$\boldsymbol{F_2 = \frac{1}{\sigma_{2t}} - \frac{1}{\sigma_{2c}}} \qquad \boldsymbol{F_3 = \frac{1}{\sigma_{3t}} - \frac{1}{\sigma_{3c}}} \qquad \boldsymbol{F_{22} = \frac{1}{\sigma_{2t}\sigma_{2c}}} \qquad \boldsymbol{F_{33} = \frac{1}{\sigma_{3t}\sigma_{3c}}} \qquad (15)$$

$$\boldsymbol{F_{44} = \frac{1}{{\tau_{23}}^2}} \qquad \boldsymbol{F_{23} = -\frac{1}{2}\sqrt{F_{22}F_{33}}} \qquad (16)$$

The Tsai-Wu criterion is primarily used to model the failure surfaces for composite materials, with limited studies applying the model to simulate the failure surfaces for AM materials. Application of the Tsai-Wu model to AM material failure surface development has been primarily focused on 3D printed plastic materials (i.e., Polylactic Acid (PLA)) [Chen, 2017; Perkowski, 2017]. The failure surface of AM metal materials in compression and tension is critical given the variety of applications and operating environments that these materials experience, and is currently unexplored for DMLS SS GP1 and DMLS Inconel 718. Engineer designers would benefit considerably from an understanding of the failure regions for these

materials. As such, this study has used both experimentally generated data from literature and the current study to present a first approximation of the failure surface for these materials, through application of the Tsai-Wu model and Hill's failure criterion.

In order to model the elastic response of these materials, the elastic compliance matrix [*C*] must be determined. For example, should these materials exhibit transversely isotropic behavior, the elastic compliance matrix would be defined by 5 independent elastic constants: E_T, E_L, ν_{TT}, and ν_{TL}, G_{TL} [Bouchenot, 2014; Moore, 2011], as presented in Equation (17). *E* represents the Young's modulus, ν is Poisson's ratio, *G* is the shear modulus, *L* represents the grain orientation along the longitudinal (*z*-direction), and *T* represents the grain orientation along the transverse (*x* or *y* directions) [Bouchenot, 2014].

$$\boldsymbol{C} = \begin{bmatrix} \frac{1}{E_T} & \frac{-\nu_{TT}}{E_T} & \frac{-\nu_{LT}}{E_L} & 0 & 0 & 0 \\ \frac{-\nu_{TT}}{E_T} & \frac{1}{E_T} & \frac{-\nu_{LT}}{E_L} & 0 & 0 & 0 \\ \frac{-\nu_{TL}}{E_T} & \frac{-\nu_{TL}}{E_T} & \frac{1}{E_L} & 0 & 0 & 0 \\ 0 & 0 & 0 & \frac{1}{G_{LT}} & 0 & 0 \\ 0 & 0 & 0 & 0 & \frac{1}{G_{LT}} & 0 \\ 0 & 0 & 0 & 0 & 0 & 2(\frac{1+\nu_{TT}}{E_T}) \end{bmatrix} \tag{17}$$

E represents the Young's modulus, ν is Poisson's ratio, *G* is the shear modulus, *L* represents the grain orientation along the longitudinal (*z*-direction), and *T* represents the grain orientation along the transverse (*x* or *y* directions) [Bouchenot, 2014]

2.3.5 Microstructure and Fracture Response

The microstructure of SLM Inconel parts contributes significantly to their observed mechanical properties. Multiple studies have shown a characteristic dendritic microstructure in SLM IN718 components, in which arc lines representing melt pools can be observed parallel to the build direction, and series of elongated vectors/tracks representing the repeated laser melt process can be observed perpendicular to the build direction [Kanagarajah, 2013; Amato, 2012; Strøßner, 2015; Chlebus, 2015]. This is clearly evident in Figure 7a and Figure 7b, which are microscopic images of DMLS Inconel 718 taken parallel and perpendicular to the build direction respectively.

a.) 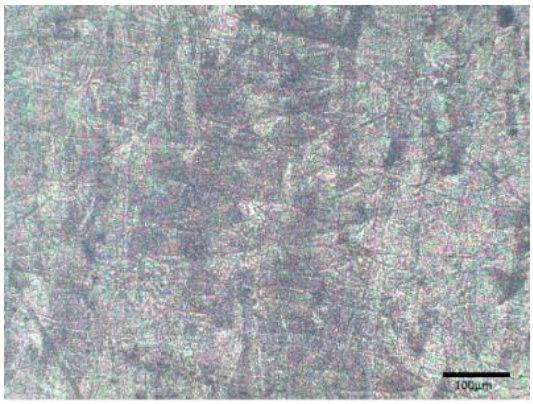 b.) 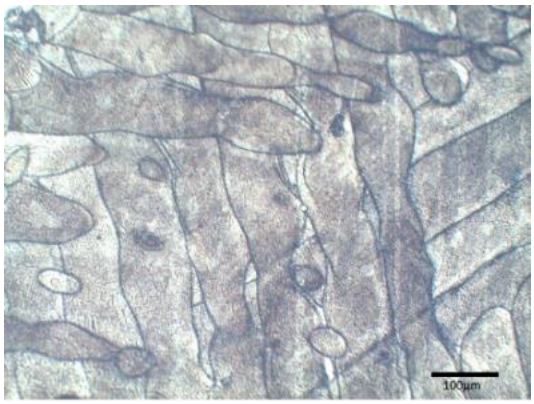

Figure 7: Microstructure of DMLS Inconel 718: a.) Parallel to Build Direction b.) Perpendicular to Build Direction

These columnar dendrites have been observed to grow epitaxially along the (100) crystallographic plane, as well as in the (200) direction [Amato, 2012; Zhao, 2008]. The characteristic dendritic microstructure has been shown to disappear with post-build heat treatment [Wang, 2012]. Recrystallization is often exhibited in SLM parts that have been heat treated [Kanagarajah, 2013; Zhao, 2008; Liu, 2011; Liu, 2011]. Recrystallization for Inconel 718 occurs during the annealing process at temperatures above 1100°C [Amato, 2012; Chlebus,

2015; Liu, 2011], and results in the presence of the strengthening phases γ' and γ", with δ precipitate occurring at grain boundaries [Oradei-Basile, 1991]. The strengthening precipitation phases γ' and γ", are observed to be spherical/cuboidal and lenticular in shape respectively. Brittle phases (e.g. Lave phases) as well as high concentrations of Niobium (Nb) and Molybdenum (Mb) elements occur in overlap areas between adjacent laser tracks and inter-dendritic locations [Chlebus, 2015]. Locations with rich concentrations of the elements Nb and Mb lead to crack initiation and propagation [Zhao, 2008]. Further, low cycle fatigue tests on DMLS Inconel 718 have revealed that porosity impacts are more profound when cycling at higher strain amplitudes [Gribbin, 2016]. Hot isostatic pressing (HIP) was found in 2 studies to deteroriate the fatigue performance of additively manufactured specimens [Aydinoz, 2016; Gribbin, 2016]. Fracture surface analysis of as-built DMLS Inconel 718 specimens, subject to fatigue testing revealed multiple locations with crack initiations, in addition to ductile fracture response [Kelley, 2016]. For SLM Inconel 718, propagation of fatigue cracks has been found to be transgranular [Konecna, 2016]. An analysis of fracture surfaces [Popovich, 2015] for as-built specimens manufactured in varying build orientations can assess whether fatigue crack initiation has occurred at the surface or as a result of internal defects/voids present within the material.

2.3.6 Surface Roughness

Surface roughness in AM components is of critical importance because it is a contributing factor in the fatigue life of materials. With Inconel 718, which is used in high temperature and extreme environmental conditions, ensuring that surface roughness is not the root cause for fatigue failure of a component is vital. Surface roughness analysis for stress-relieved Inconel 718 on top surface has been reported for DMLS specimens manufactured along the X (Ra = 5.42μm, Rq = 6.77μm), Y (Ra = 3.55μm, Rq= 4.79μm) and Z (Ra = 6.24μm, Rq =

7.82μm) build orientations [Kelley, 2016]. Machined surface roughness of DMLS Inconel 718 was reported to be 0.9 μm, which still contributed to high cycle fatigue (HCF) failure observed in specimens [Gribbin, 2016]. Another study that has assessed surface roughness and its relationship to the HCF behavior has reported a surface roughness average for as-built IN718 of 247μm (6.2738μm) [Lambert, 2016]. EOS manufacturers have reported surface roughness values of Ra = 4 to 6.5 μm after shot-peening regardless of build orientation [EOS, 2014].

2.4 Summary of Review

An analysis of literature in the area of additive manufacturing of stainless steel GP1/17-4PH and Inconel 718 reveals considerable knowledge gaps, which need to be further explored in order to ensure that these materials, as developed, meet or exceed the mechanical performance of their conventionally manufactured counterpart. The tensile response for these materials are well understood parallel and perpendicular to the build direction, however few studies have modeled the monotonic response of these materials through a strain-hardening model (i.e., Ramberg-Osgood, Hahn Discontinuous Yielding Model, etc.), nor exhibited a correlation, if any between hardening parameters and build orientation. Most especially, the amount of variation in these monotonic tensile properties along the *x* or *y* build orientations, or at intermediary orientations in the *xy* plane is yet unexplored for as-built specimens. Furthermore, reported tensile properties have not modeled the anisotropic variation in Young's modulus for these materials with build orientation, nor have been used to approximate the failure surfaces of these materials, providing insight into the failure regime of as-built additively manufactured materials and the role of as-built surface conditions on the failure surfaces for these materials. While it is understood that additively manufactured materials exhibit anisotropic material response with respect to the build

orientation, classification of material behavior as orthotropic or transversely isotropic has yet to be conceded.

Most studies have focused on characterizing the life of these materials, primarily in the high cycle fatigue regime and experimentally determined the stress-life response of these materials, with few studies analyzing the strain-life behavior of these materials. The impact of pulsating tension fatigue, completely reversible torsional fatigue, progressive amplitude loading fatigue tests in both elastic and plastic strain ranges, and completely reversible fatigue at a highly plastic strain range has yet to be explored. There is a need to determine whether the tensile-fatigue properties that can be applied for non-additively manufactured materials, be applied for these additive class of materials. Hardening/softening behavior of these additive materials from cyclic data has not been characterized for the varying types of axial and torsional fatigue test presented in this study. The impact of plasticity on life of these materials is yet prematurely understood. Furthermore, the cyclic stress-strain behavior of these materials have not yet been modeled, through a viscoplasticity model, which considers both the kinematic and isotropic hardening response of these AM materials.

To address these knowledge gaps, a combination of experimental mechanical testing and constitutive modeling will be applied, from which a reduced test approach will be developed, providing a comprehensive analysis of these materials, as depicted in the schematic in Figure 8.

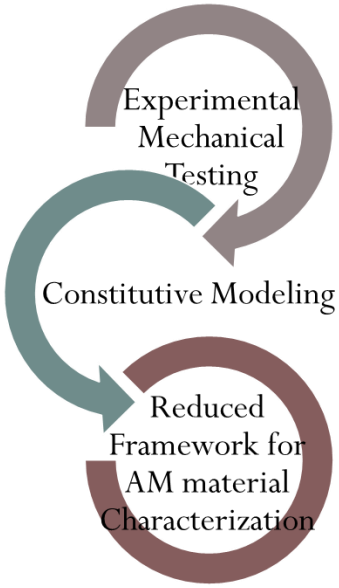

Figure 8: Outcomes of Research

Chapter 3 will present the experimental design, results from mechanical testing for DMLS SS GP1/17-4PH and DMLS Inconel 718 will be presented in Chapters 4 and 5, including a reduced test approach, followed by constitutive modeling results in Chapter 6, and conclusion and future work in Chapter 7.

CHAPTER 3: EXPERIMENTAL DESIGN[2]

The experimental design was developed to address key knowledge gaps presented in Chapters 1 and 2. Experimental testing results along with findings in literature were used to constitutively model the behavioral response of these additively manufactured materials under a variety of testing conditions (i.e., tension, torsion and fatigue) at room temperature, followed by the development of a reduced test specimen to provide a comprehensive assessment of the anisotropic mechanical response of these materials. Manufacturing of as-built DMLS SS GP1/17-4PH specimens was done using the EOS M280 system in the Manufacturing Engineering Department at Central State University in Ohio. Manufacturing of as-built DMLS Inconel 718 specimens was done using the EOS M290 system, through an external additive manufacturing vendor, i3DMFG. Tension and fatigue testing was performed using the MTS LandMark 793 test system, and torsion testing was performed using the MTS EM Bionix test system at the University of Central Florida. Metallurgical observations (i.e., surface roughness, fracture response, etc.) in addition to mechanical testing were also conducted at the University of Central Florida. Scanning Electron Microscopy (SEM) images of fracture surfaces were taken using the Phenom Desktop SEM system. Surface roughness measurements were taken using Veeco's Dektak^{3}ST surface profilometer in the MicroDevice Prototyping Facility in the Physics department at the University of Central Florida.

[2]Certain figures and excerpts in Chapter 3 are from my publications: Siddiqui, S.F., Fasoro, A.A., Cole, C., & Gordon, A.P. (2018). Mechanical Characterization and Modeling of Direct Metal Laser Sintered Stainless Steel GP1. Manuscript under review in *ASME Journal of Engineering Materials and Technology;* Siddiqui, S.F., Fasoro, A.A., & Gordon, A.P. (2018). Axial and Torsional Response of Additively Manufactured Steel under Monotonic and Cyclic Conditions. GT2018-76831. In *Proceedings of the ASME 2018 Turbo Expo Turbomachinery Technical Conference & Expo*; Siddiqui, S.F., Fasoro, A.A., & Gordon, A.P. (2017). Selective Laser Melting (SLM) of Ni-based Superalloys - A Mechanics of Materials Review. Badiru, A.B., Valencia, V. V., & Liu, D. (Eds.), *Additive Manufacturing Handbook: Product Development for the Defense Industry*. CRC Press; Siddiqui, S.F., O'Nora, N., Fasoro, A.A., & Gordon, A.P. (2017). Modeling the Influence of build orientation on the monotonic and cyclic response of additively manufactured stainless steel GP1/17-4PH. In *Proceedings of the ASME 2017 International Mechanical Engineering Congress & Exposition*

3.1 Tension, Torsion & Fatigue Specimen Design

The geometry of the samples used for tension and fatigue testing, was developed as a CAD (Computer Aided Design) model in SolidWorks® and is depicted in Figure 9. The samples were designed with an inner gauge diameter of 0.25" and a gauge length of 1", as suggested by ASTM Standards [ASTM, 2013; ASTM, 2015]. For the final test specimen, the outer gauge diameter of 0.625" was machined down to 0.5" after additively manufacturing the specimens.

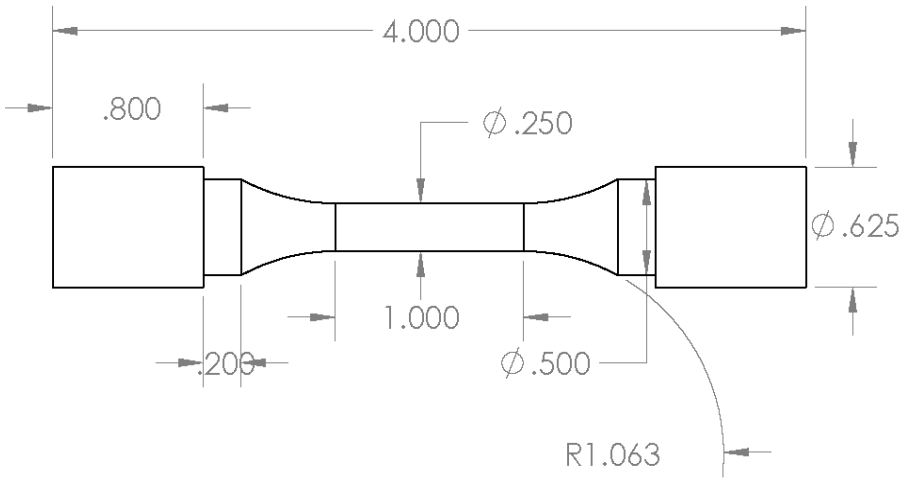

Figure 9: Tension and fatigue sample geometry in inches

The samples used for torsional monotonic and fatigue testing for DMLS SS GP1 is as presented in Figure 10. The samples were designed with an inner gauge diameter of 0.24" and a gauge length of 1.97." The outer shank section was set at 0.51" and reduced to 0.30" at the ends. For the final test specimen, the gripping section was machined from 0.30" at the ends to 0.28".

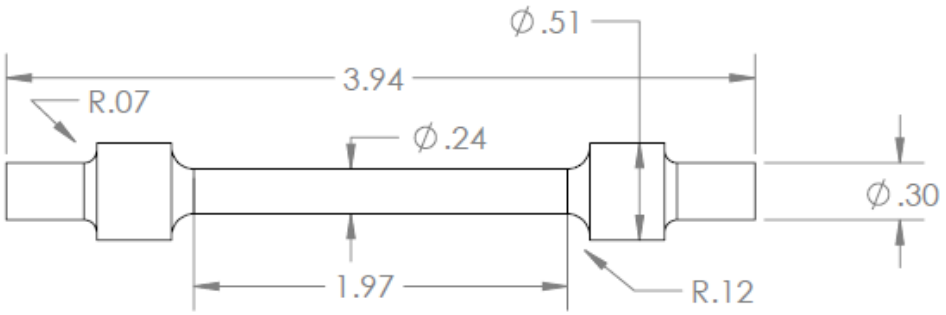

Figure 10: Torsion sample geometry in inches

As this study also explored a reduced framework for complete characterization of additively manufactured materials, a reduced specimen size was developed, which is discussed in detail in Section 3.10.

3.2 Direct Metal Laser Sintering of Specimens

Stainless Steel (SS) GP1/17-4PH specimens were manufactured using the EOSINT M 280-400W Direct Metal Laser Sintering (DMLS) system, shown in Figure 11, which has a build plate size of (9.85" x 9.85" x 12.8") - (x, y, z) [Siddiqui, 2017]. Built-in optimized processing parameters were used to manufacture SS GP1 samples in a nitrogen environment, using a layer thickness of 20µm. The samples were not stress-relieved/heat-treated after manufacturing, in order to investigate the as-built mechanical performance of these materials. The samples were manufactured along the X, Y and XY45° orientations, as depicted in Appendix A. Samples manufactured along the x-axis/(100) direction and y-axis/(010) directions were subject to a -5° offset as suggested by the EOS manufacturer. To limit the level of warping in as-built DMLS samples, specimens were developed using a boxed support structure, between 5 to 10mm in height depending upon the batch manufactured.

Figure 11: EOS M280 DMLS system at Central State University, used to manufacture SSGP1 test specimens [Siddiqui, 2017]

3.3 Sample Preparation Prior to Testing

In order to prepare additively manufactured samples for testing, the samples needed to be removed from the build plate. The layout of samples across the build plate for all batches manufactured is as presented in Appendix A.

Samples were removed from the build plate using a band saw. In order to remove the boxed support structure from each individual sample, small flat-head screwdrivers and other hand tools were used. For certain samples, the band saw was used to remove part of the support structure to allow for ease of removal. Each sample was secured within a vice, before inserting a flat-head screwdriver at the base of the support structure and gently lifting to remove each box support from the sample. Figure 12 shows an image of a sample manufactured in the *xy* build plane, with the boxed support structure attached to the sample. After removal of the support structure, samples were filed using a flat smooth file, in the location where the boxed support structure was originally present. Before experimental testing, the outer gauge section was

machined down to 0.5," and machining marks in the radial section were removed using a sandpaper with a grit size of 3M (300).

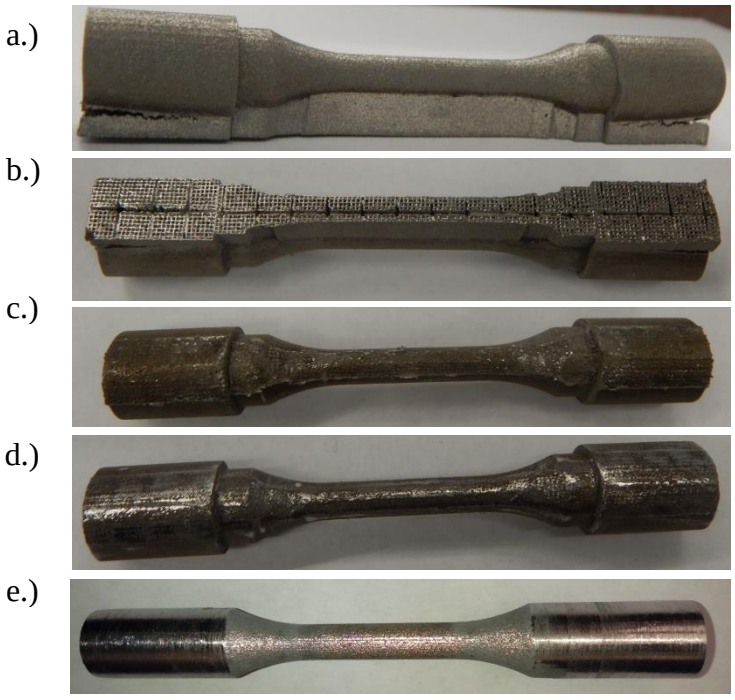

Figure 12: As-built DMLS SS GP1 Sample 12 a.) front view before removal from build plate, b.) bottom view showing boxed support structure, c.) after support structure removal, d.) after filing sample to remove support structure remnants, e.) final sample after machining gripping section and removing machining marks [Siddiqui, 2018]

3.4 Surface Roughness Determination

Surface roughness measurements were taken to provide a comprehensive understanding of how roughness varies with build orientation for these as-built additively manufactured materials, and consequently its role in the fatigue life of these materials. Surface roughness testing was performed using Veeco's Dektak^{3}ST Surface Profile Measuring System. In order to meet the system's requirement for sample size and limit the difficulty associated with surface roughness measurements on cylindrical surfaces, a thin section was sliced from the flat gripping section side of DMLS SS GP1 samples manufactured along the (X), (Y), and (XY45°) build

orientations, maintaining the as-built integrity of the surface. The same process was performed for DMLS Inconel 718 specimens manufactured along the (X), (Y) and (Z) orientations.

The experimental setup for surface roughness analysis of these specimens is as shown in Figure 13. Scans were taken using a 5 micron diamond stylus tip, with care taken to scan in the center of the specimen to limit edge effects in surface roughness readings. Surface roughness measurements are determined by vertical variations in the stylus movement, which are recorded as an analog electric signal that is representative of the change in the core position of the linear variable differential transformer (LVDT), and converted to a digital signal that is outputted as a line plot by the computer [Veeco]. Prior to taking roughness measurements on AM specimens, the system was calibrated using a control chromo-glass specimen. Three measurements were taken on each AM specimen, which were averaged to yield the roughness values presented in Chapter 4 for DMLS SS GP1 and Chapter 5 for DMLS Inconel 718. Scans were taken at room temperature, and covered a scan length of 500µm, incorporating 1000 data points, for a horizontal scan resolution of 0.5µm/sample. The scan profile mode was set to "Hill," and the scan speed was kept at medium settings.

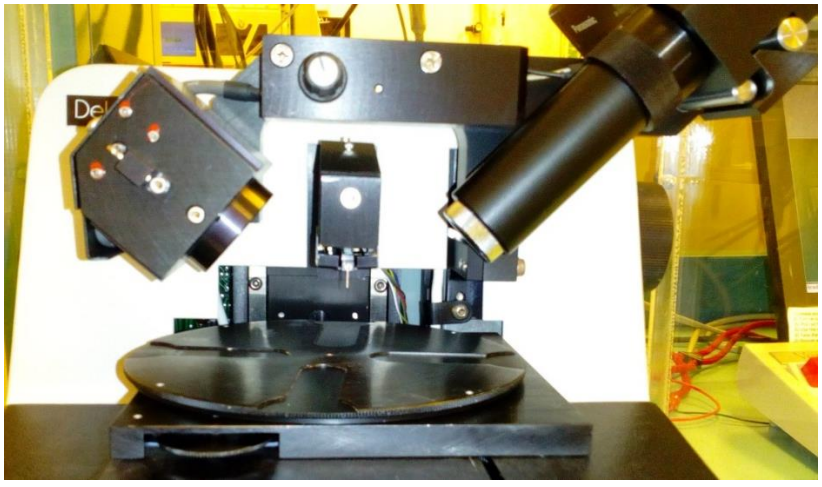

Figure 13: Veeco Dektak^{3}ST surface profilometer in MicroDevice Prototyping Facility

The resulting quantitative surface roughness results with build orientation are presented in Chapters 4 and 5 respectively, in addition to qualitative images of surface roughness, which have been captured using the Phenom Scanning Electron Microscope in Chapter 4. Specific analysis regarding each specimen data is presented in Appendix B.

3.5 Tension Testing

Strain controlled tension testing was performed on DMLS SS GP1 at a strain rate of $1x10^{-3}$ (mm/mm/sec) and a sampling rate of 25Hz. Tension tests were performed using the servo-hydraulic MTS LandMark 793 test system, and a clip on extensometer, MTS 647.11E25, was used to record strain measurements up to a strain value of 0.2mm/mm, after which measurements were recorded in displacement control until sample fracture. The experimental setup is as shown in Figure 14.

$$\boldsymbol{\varepsilon} = \frac{\left((\boldsymbol{D}-\boldsymbol{Dp})\times\left(\frac{\boldsymbol{L_E}}{\boldsymbol{L_0}}\right)\right)+(\boldsymbol{\varepsilon_p}\times\boldsymbol{L_E})}{\boldsymbol{L_E}} \qquad (18)$$

After 0.2mm/mm strain, displacement values were used to calculate the average strain to fracture, through application of Equation (18), as done in a previous study on DMLS Inconel 718 [Kelley, 2016]. In Equation (18), the average strain, ε, is a function of the displacement, D, displacement of the crosshead after the 0.2mm/mm strain point is reached, Dp, average strain at ε_p, length for zero strain in the extensometer, L_E, and the gauge length of the sample, L_0. For the tension specimens, L_E of 24.7mm and L_0 of 25.4mm were used.

Figure 14: Experimental setup for strain-control tension and fatigue experiments using the MTS LandMark 793 servo hydraulic test system [Siddiqui, 2017]

Reproducibility in monotonic response of each build orientation was verified with first cycle response of low cycle fatigue (LCF) tests. Tension testing was used to provide the following mechanical properties for each build orientation: Young's Modulus (*E*), 0.2% Yield Strength (*0.2% YS*), Lower Yield Strength (*LYS*), Upper Yield Strength (*UYS*), and Ultimate Tensile Strength (*UTS*) in addition to the monotonic behavior (tensile stress-strain curve) of these materials along each build orientation. This data will be used determine the anisotropic monotonic material response (e.g. orthotropic, transversely isotropic, tetragonal, etc.) discussed in Chapter 4, and be used for constitutively modeling failure surfaces through application of Hill's failure criterion, monotonic stress-strain behavior through application of a strain-hardening

model (i.e. Ramberg-Osgood, Hahn), and Young's Modulus variation with build orientation in Chapter 6. The fracture response and microstructure will be observed through optical and scanning electron microscopy, and presented in Chapter 4, revealing presence of voids, un-melted powder, and other internal defects intrinsic to the AM process.

3.6 Low Cycle Fatigue (LCF) Testing

Strain-controlled completely reversible (R = -1) fatigue tests were performed using the servo hydraulic MTS Landmark 793, to quantify the life of these as-built materials when subjected to a plastic strain range of 1.4%. The servo hydraulic MTS Landmark 793 used for LCF testing was conducted at a strain rate of 0.001mm/mm/s and a frequency of 25Hz. Tests were run until fracture occurred or tensile stress dropped to approximately 50% of its stabilized value. Each constant amplitude fatigue test was repeated for each build orientation to determine if any scatter in life is observed for each orientation. Anisotropy with respect to the hardening and softening behavior exhibited by these materials was found from the stress history data collected and fatigue crack initiation and propagation were observed through optical and/or scanning electron microscopy imaging from which it can be determined if these fatigue cracks initiated at the surface or from internal voids within the material. Mechanical properties such as the stress range, $\Delta\sigma$, total strain range, $\Delta\varepsilon$, plastic strain range, $\Delta\varepsilon_p$, elastic strain range, $\Delta\varepsilon_e$, mean stress σ_m, and Young's modulus, E, will be assessed for first cycle and stabilized cycle as well as the overall number of cycles to failure, N_f, for each sample. An progressive variation in the hysteresis behavior from the first cycle to the last cycle will be presented. These set of experiments will also be used to determine if existing tensile-fatigue properties can be applied for additively manufactured materials, in addition to the applicability of viscoplasticity models

(i.e. Chaboche) in simulating the hysteresis response of these materials, taking into account the kinematic and isotropic hardening behavior.

3.7 Progressive Amplitude Fatigue Testing

In order to determine the complete cyclic behavior of DMLS SS GP1, progressive amplitude, completely reversible (R= -1) strain-controlled fatigue testing will be performed at elastic and plastic strain ranges from 0.6% to 1.4% for a set number of cycles to achieve stabilization of hysteresis loops at each strain range. A schematic of the strain variation over time for these progressive amplitude fatigue tests is presented in Figure 15.

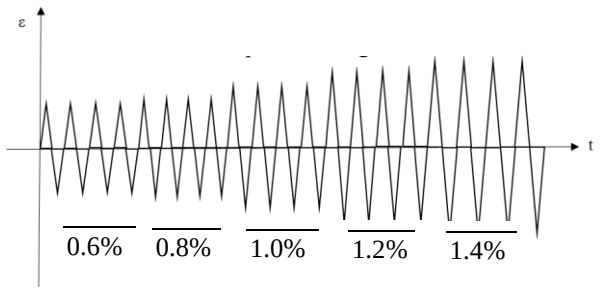

Figure 15: Schematic of progressive amplitude strain control fatigue test study, with 100 cycles set at each strain range

Anisotropic variation in hardening/softening behavior of these materials will be observed from stress history data collected during this test for each strain range tested. Stabilized hysteresis loops at each strain range will be used to develop cyclic stress-strain curve for each build orientation. These tests will be completely reversible tests with cycling from tension to compression. Furthermore, the stress range, $\Delta\sigma$, total strain range, $\Delta\varepsilon$, plastic strain range, $\Delta\varepsilon_p$, elastic strain range, $\Delta\varepsilon_e$, mean stress σ_m, and Young's Modulus, E, will be assessed for stabilized cycle at each strain range.

3.8 Pulsating Tension Fatigue Testing

The impact of mean tensile stress on fatigue life plays a considerable role in many engineering applications. To this effect, this study has performed strain control pulsating tension fatigue tests at a strain rate of 0.001mm/mm/sec, a sampling frequency of 25Hz, and a strain range between 0 mm/mm to +0.007 mm/mm on as-built DMLS SS GP1 samples manufactured along varying build orientations. The cyclic hysteresis response from these findings are modeled through application of the Chaboche model in Chapter 6, from which optimized Chaboche material constants are presented.

3.9 Torsion Testing

In order to assess the impact of twisting/shear on additively manufactured specimens, samples were subject to monotonic torsion testing using the MTS EM Bionix at room temperature. An image of the experimental setup for torsion testing of samples are as shown in Figure 16. Prior to experimental testing, the support structure was removed from the specimens using hand tools. Sandpaper of grit 3M was used to remove any support structure remnants from the sample, as depicted in Figure 17. The resulting shear stress/strain curves for each build orientation were used to determine shear mechanical properties such as the shear modulus, *G*, and the ultimate shear strength. Monotonic torsion tests were performed at an angular twist rate of 1.654 deg/sec and data acquisition rate of 25 Hz. Each monotonic torsion test results will be compared with first cycle response from completely reversible torsion fatigue tests, to determine reproducibility in the cyclic response of each build orientation. Fracture response under monotonic torsion fatigue conditions will be assessed.

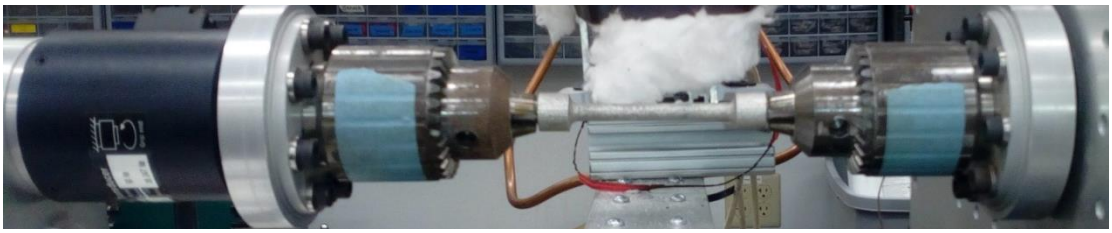

Figure 16: Experimental setup for torsion experiments of DMLS SS GP1 using the MTS EM Bionix test system [Siddiqui, 2018]

Completely reversible (R_ϕ = -1) torsion fatigue tests were performed at an angular twist rate of 1.654 deg/sec, with angular twist control between +15° and -15°, for a total angular twist range of 30°. Sampling frequency was kept at 10Hz and failure detection was set at a drop of 20% in maximum torque. These tests were performed in order to assess the fatigue life, hardening/softening response, and fracture response of as-built DMLS SS GP1 and DMLS Inconel 718 when subject to cyclic shear stresses. Torsional fatigue response variation with build orientation for each specimen is also assessed, providing insight into material behavior classification (i.e., orthotropic, transversely isotropic).

a.)

b.)

c.)

Figure 17: DMLS SS GP1 torsion sample: a.) as-built with support structure attached, b.) after removal of support structure and filed, c.) after machining down gripping section [Siddiqui, 2018].

3.10 Reduced Specimen Geometry

Additive manufacturing of metal components is currently a highly costly manufacturing process, hence the necessity for smaller test specimens to assess the mechanical response of these materials for destructive testing methods (i.e., tensile, fatigue, torsion etc.). Powder-bed additive manufacturing of metal parts can be tailored to limit the expense and production time of components, while at the same time, meeting ASTM Standards for sample size requirements and mechanical testing. In order to develop a comprehensive understanding of these materials and limit the cost associated with part manufacturing, a reduction in test specimen size to determine mechanical response (i.e., anisotropy) is necessary, while at the same time ensuring that experimental findings from reduced test specimens compares with that found for conventional test specimens.

With these considerations, a reduced specimen was developed, that not only meets ASTM standards, but allows for reduction in the amount of powder used for specimen development. These specimens were subjected to similar experimental conditions as the conventional test specimens, from which experimental findings were compared for both cases.

A reduced specimen size was designed that meets ASTM Standards for tensile testing, and allows for a reduction in production cost of AM parts. The geometric dimensions of the reduced specimen developed is presented in Figure 18a, with a total length of 3.2 inches and an inner gauge diameter of 0.2 inches. This is a reduction of 0.8 inches and 0.05 inches in the total length and inner gauge diameter, when compared with the conventional size samples used for part of this study. Also presented in Figure 18b, is the 3D geometry of the reduced test specimen. A discussion on the similarities and differences in mechanical testing results of reduced test specimens versus conventional test specimens is presented in Chapter 4.

a.)

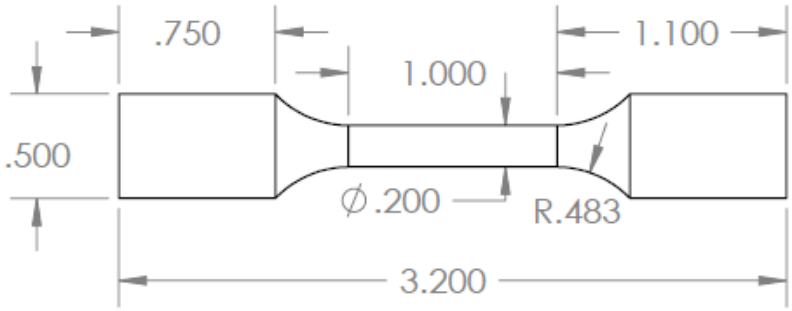

b.)

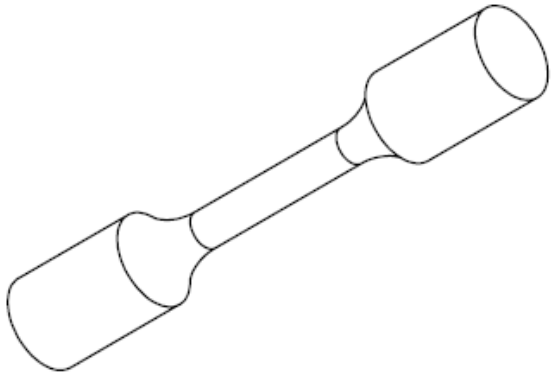

Figure 18: a.) Geometric dimensions of reduced test specimen in inches, b.) 3D image of reduced test

3.11 Fracture Analysis

The additive manufacturing process yields inherent defects, such as surface roughness and internal voids, in as-built specimens that limits the durability of these materials and serves as initiation sites for cracks to develop. Fracture surfaces provide vital information on the location of crack initiation, propagation and final fracture. They further serves as a correlation between the resulting mechanical behavior observed through tensile, torsion and fatigue testing, and the fracture response exhibited at the microstructural level. To observe the impact of build orientation on the resulting fracture surface of DMLS as-built samples subject to tension, torsion and fatigue testing, fracture surfaces of the samples were taken using the DinoLite microscope. It

is important to note that not all samples subjected to LCF fatigue testing fractured, but instead the test was stopped during crack propagation when the tensile stress dropped to approximately 50% of its stabilized stress value. To further assess the fracture response, including the presence of un-melted powder, presence of pores/voids and crack initiation and propagation, the Phenom Scanning Electron Microscope (SEM) was used. An image of the SEM system is as shown in Figure 19a. Preliminary 3D surface profiles of crack depths have also been assessed using the Keyence VHX digital microscope depicted in Figure 19b.

a.) b.)

Figure 19: a.) Phenom Scanning Electron Microscope used for microscopic analysis, b.) Keyence VHX digital microscope used for 3D crack depth profiles

3.12 Hardness Testing

The variability in hardness across DMLS SS GP1 samples manufactured in the horizontal build plane were measured using the Buehler Rockwell C hardness tester, shown in Figure 20. Part of the shank/gripping section was sliced from these specimens for hardness testing. A brale diamond tip, with a load of 150kg, was used to take 10 measurements on the as-built surface of each specimen. These results were averaged to yield the hardness findings presented in Chapter 4 and compared with outcomes reported in literature.

Figure 20: Buehler Rockwell C hardness tester

CHAPTER 4: EXPERIMENTAL RESULTS AND DISCUSSION FOR DMLS STAINLESS STEEL 17-4PH/GP1[3]

Previous chapters have presented a comprehensive literature review on conventional and additively manufactured stainless steel 17-4PH/GP1, providing an understanding on areas which need further research in order to contribute to the current state of knowledge on this material's mechanical behavior, and its correlation to the additive manufacturing process used in its development. This chapter is dedicated to presenting the experimental findings for DMLS Stainless Steel GP1, subject to a variety of loading conditions (i.e., tension, low cycle fatigue, pulsating tension fatigue, progressive amplitude fatigue, torsion and torsional fatigue). Also presented are surface roughness, Rockwell C hardness measurements, and fracture surface response with build orientation. Internal defects found through microstructural analysis are correlated with specimen densities. Findings from this chapter are modeled in Chapter 6, and used to provide a first approximation of elastics constants to describe the anisotropic response exhibited by this material in Chapter 7.

4.1 Tension Test Results

Tensile testing of varying build orientations can yield insight into not only the anisotropic/isotropic response of these materials, but mechanical properties that are crucial to the design of components for engineering applications. With this consideration, the stress-strain curves for initial tensile loading of sample 3, manufactured -5° from the x-axis, sample 5, manufactured at 45°, and sample 9, manufactured -5° from the y-axis, all within the xy build plane, is as shown in Figure 21. These results have been overlaid with the monotonic stress-strain curves reported in other studies on additively manufactured Stainless Steel GP1/17-4PH.

[3] Certain figures and excerpts in Chapter 4 are from my publications: Siddiqui, S.F., Fasoro, A.A., Cole, C., & Gordon, A.P. (2017). Mechanical Characterization and Modeling of Direct Metal Laser Sintered Stainless Steel GP1. Manuscript under review in *ASME Journal of Engineering Materials and Technology;* Siddiqui, S.F., Fasoro, A.A., & Gordon, A.P. (2018). Axial and Torsional Response of Additively Manufactured Steel under Monotonic and Cyclic Conditions. GT2018-76831. In *Proceedings of the ASME 2018 Turbo Expo Turbomachinery Technical Conference & Expo.*

The samples presented in this figure were from batch 1. The presence of slight anisotropy is observable from the stress-strain curves, with the tensile response exhibited by sample 9 (Y) yielding slightly improved mechanical performance, as compared with samples 3 (X) and 5 (XY45°). In order to further assess this tensile behavior, 2 specimens manufactured along the (Y) build direction, from batch 2 were subject to tension testing, in which one was a reduced test specimen and the other was a conventionally manufactured test specimen. Plotting the tensile stress-strain curve for these specimens yielded material response similar to that exhibited by the X and XY45° oriented specimens, suggesting that the material response exhibited by sample 9 (Y) may be an outlier. This can be seen by the stress-strain curve for sample 21 (Y) in Figure 21. Further confirmation of this was done by overlaying the first cycle response from low cycle fatigue testing with the tensile response along the (Y) orientation, which further supports that sample 9 (Y) from Batch 1, may be an outlier.

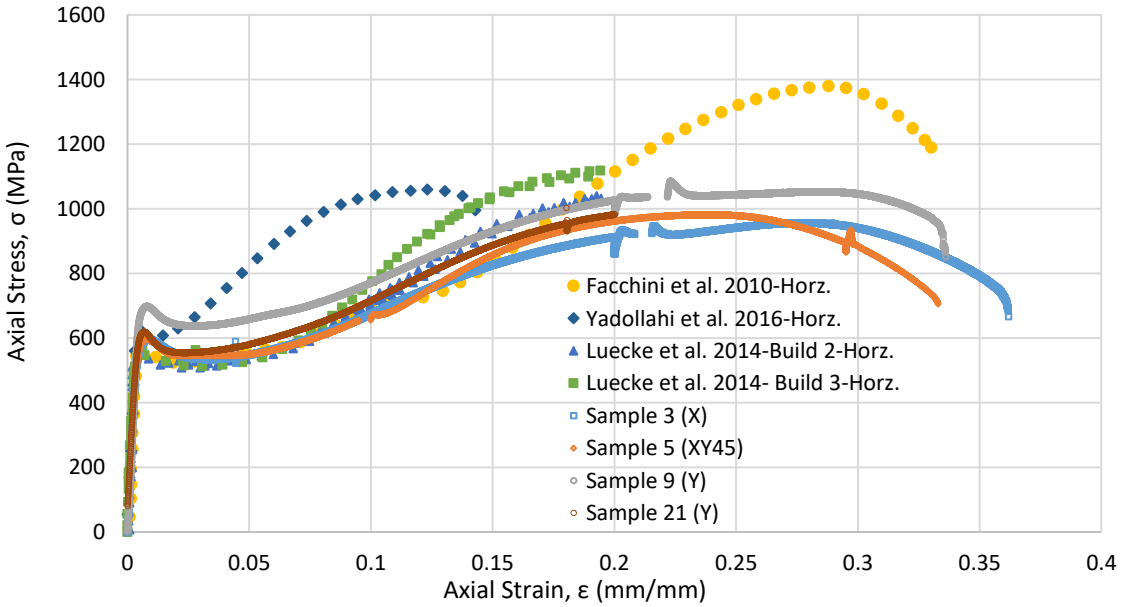

Figure 21: Tensile response of DMLS SS GP1 samples manufactured for varying build orientations within the xy build plane [Siddiqui, 2017]

Table 9 presents a compilation of the tensile properties determined at each of the three build orientations tested. The mechanical properties for the X-oriented and XY45°-oriented samples are very similar, with lower yield strength of 534.1 MPa and 545.7 MPa, upper yield strength of 596.6 MPa, and ultimate tensile strength of 956.4 and 981.9 MPa respectively. A considerable increase in mechanical properties is observed for the Y-oriented sample, with a lower yield strength of 638 MPa, upper yield strength of 698.2 MPa, and ultimate tensile strength of 1086 MPa respectively, for the specimen which has been determined to be an outlier in this study. Nevertheless, analyzing the lower and upper yield strength for the (Y) oriented conventional and reduced test specimens from Batch 2, reveals that the (Y) - oriented specimen yields slightly improved tensile properties as compared with the other build orientations tested in the xy build plane. These findings can be seen in Appendix B for samples 21 and 9 manufactured in batch 2. EOS reported tensile properties also exhibits slight variation in mechanical properties for horizontally manufactured specimens, with lower yield strengths of 586 ± 50 MPa, and upper yield strengths of 645 ± 50 MPa. With these slight variations present in mechanical tensile properties for build orientations in the horizontal build plane, it is suggested that the material behavior in the xy plane is isotropic.

An assessment of tensile properties from this study, with findings from other studies shows agreement. This is further supported by Figure 21, which overlays the tensile response from this study for varying build orientations in the xy build plane (i.e. X, Y and XY45°), with tensile responses observed in other findings on additively manufactured SS 17-4PH/GP1, developed along the horizontal build orientation. Slight variations in the stress-strain response can be observed across literature (i.e. ultimate tensile strength). This can be attributed to the post-

processing conditions and processing parameters used, which vary across studies [Siddiqui, 2018]. A bar chart depiction of tensile properties (lower yield strength, upper yield strength, ultimate tensile strength and 0.2% yield strength) reported across studies on additively manufactured stainless steel 17-4PH has also been used to further validate experimental findings within this study. This is as shown in Figure 22.

Table 9: Comparison of tensile properties (rounded) for 17-4PH and SS GP1* [Siddiqui, 2018]

Reference	**Orientation**	**Elastic Modulus, *E* (GPa)**	**Lower Yield Strength, σ_{lys} (MPa)**	**Upper Yield Strength, σ_{uys} (MPa)**	**0.2% Yield Strength, $\sigma_{0.2ys}$ (MPa)**	**Ultimate Tensile Strength, σ_{UTS} (MPa)**
Current Study	X-Axis*	166.7	534	597	579	956
Current Study	Y-Batch 1*	159.7	638	698	689	1086
Current Study	XY-45°	162.3	546	597	583	982
EOS (Stainless Steel GP1) [1]	Horizontal Direction (XY)	170 ± 30	586 ± 50	645 ± 50	-	930 ± 50
Luecke et al., 2014 [3]	Horizontal (Hp)	-	489	531	531	999
Facchini et al., 2010 [2]	-	-	500	600	-	1300
Yadollahi et al., 2017 [7]	Horizontal	187.3	-	-	650	1060
Mower et al., 2016 [5]	Horizontal	165	-	-	610	1072
17-4PH Wrought**	-	-	-	-	1000	1103

*****Manufactured at -5º from respective axis, as suggested by EOS manufacturer
** Supplied from Mill in Condition A: "Solution Treated at 1038°C ± 14°C, and air cool below 32°C" [9]

These results reveal that additively manufactured SSGP1 mechanical properties are considerably lower than its wrought counterpart, and has been attributed to the phase constituent. Wrought 17-4PH is conventionally in the martensite phase, whereas additively manufactured SS GP1/17-4PH has been found in other studies to exist in the metastable austenite phase [Luecke, 2014; Yadollahi, 2017]. The presence of an upper and lower yield strength can also be observed from the tensile curves, revealing discontinuous yielding/presence of Luder's bands, as observed in other studies [Facchini, 2010; Luecke, 2014]. This material behavior differs from the material

response observed with conventionally manufactured stainless steel 17-4PH, further suggesting that these samples exhibit metastable austenite phase, which is discussed further detail in the microstructural analysis section.

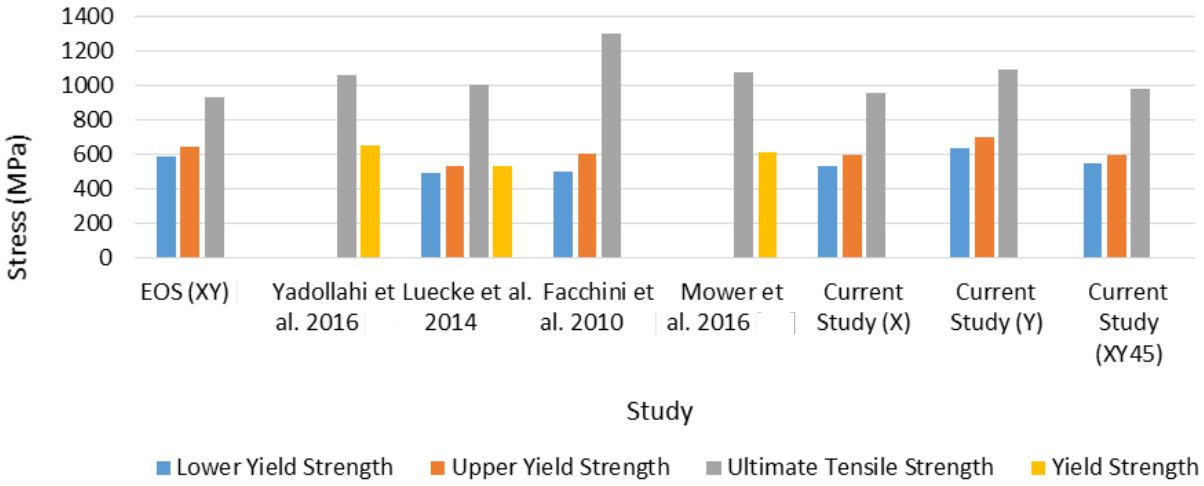

Figure 22: Comparison of tensile properties across literature, determined for additively manufactured stainless steel 17-4PH/GP1 manufactured along the horizontal build orientation [Siddiqui, 2017]

Tensile testing along these build orientations have provided mechanical properties (e.g. E, 0.2% Y.S., LYS, UYS, UTS), from which monotonic strain hardening coefficient 'K' and exponent 'n' can be determined, and first-order approximation of failure surfaces can be generated. Monotonic and cyclic tensile stress-strain curves for each build orientation will be modeled through application of Ramberg-Osgood Model and another appropriate theory (i.e., Hahn's discontinuous yielding model). The constitutive modeling, based upon the experimental behavior described in this section will be presented in Chapter 6.

4.2 Surface Roughness Results

The surface roughness of additively manufactured components contributes to the reduction in fatigue life observed of these components. This study has qualitatively captured the surface roughness (i.e., balling phenomena) of DMLS SS GP1 manufactured along varying build orientations in the *xy* build plane, through SEM imaging, as well as quantitatively through use of the Veeco Dektak^{3}ST surface profilometer. Experimental parameters for quantitative measurements of surface roughness are discussed in Chapter 3. The experimental setup for the specimens is as depicted in Figure 23. The lowering of the stylus onto the specimen can be seen, in addition to an example of the resulting output lineout plot after scan completion. Associated properties corresponding to roughness and waviness are depicted on the left hand side of the lineout plot, in addition to the experimentally set parameters (i.e., scan length, scan speed etc.). Three measurements were taken on the as-built surface of DMLS SS GP1 samples manufactured along varying build orientations, and averaged to yield the roughness values presented in Table 10. A comparison of these average roughness values suggests that an average surface roughness of Ra = 4 to 7 µm is observed for these specimens, for measurements taken at the center of the specimen, when manufactured in the *xy* build plane. The average root mean square roughness is found to be between Rq = 6 to 9 µm. This compares with other reported studies on roughness for as-built DMLS SS 17-4PH, which reported average roughness between 3-5 µm and root mean square roughness between 4-7µm [Mower, 2016], and Ra= 2.5-4.5µm for DMLS SS GP1 after shot-peening [EOS, 2009].

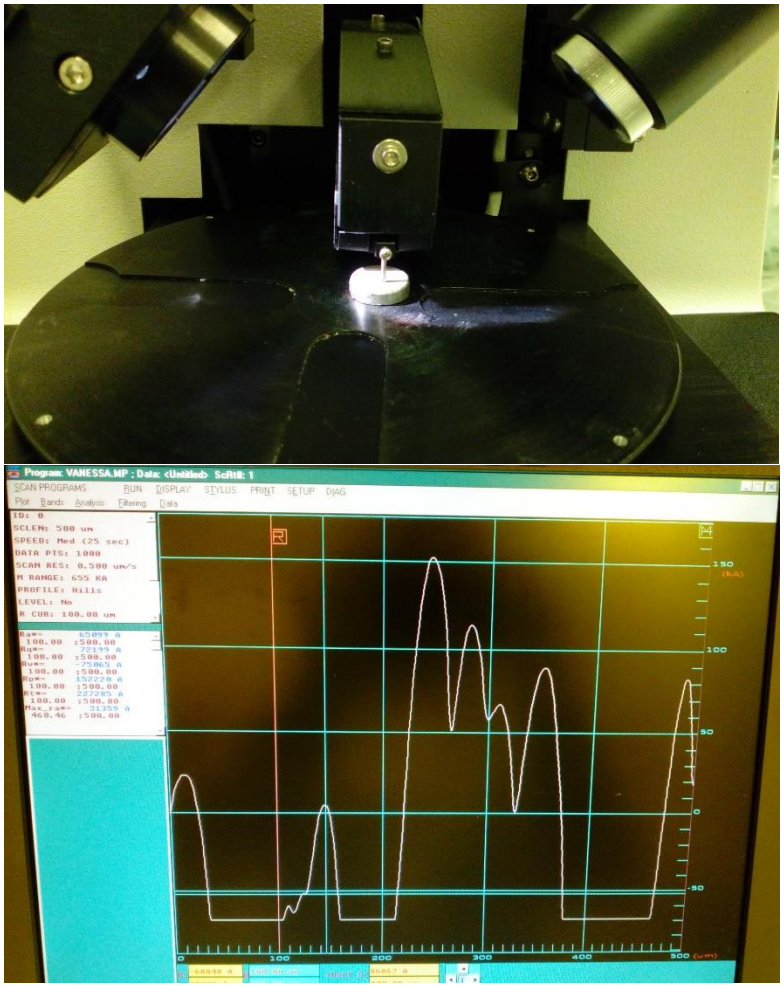

Figure 23: Experimental setup and example of output lineout for surface roughness measurements of AM specimens

Table 10: Summary of surface roughness measurements (rounded) for DMLS SS GP1

Ra (µm), Rq (µm)	(X)	(XY45)	(Y)
Measurement 1	4.305, 5.005	8.102, 8.90	7.270, 8.889
Measurement 2	5.753, 6.655	6.51, 7.22	7.549, 9.3600
Measurement 3	6.551, 7.705	8.649, 9.552	6.304, 8.191
Average ± Standard Deviation	5.536 ± 1.139, 6.455 ± 1.36	7.754 ± 1.11, 8.557 ± 1.203	7.0407 ± 0.653, 8.813 ± 0.588

A summary of these roughness measurements for each specimen is presented in Appendix B. Qualitative images of surface roughness on DMLS SS GP1 specimen, subject to progressive amplitude loading, was captured in Figure 24, using the Phenom SEM. The presence of varying powder particle sizes can be seen at the surface. Also evident is the highly irregular surface caused by the variation in powder particle sizes and voids between powder particles.

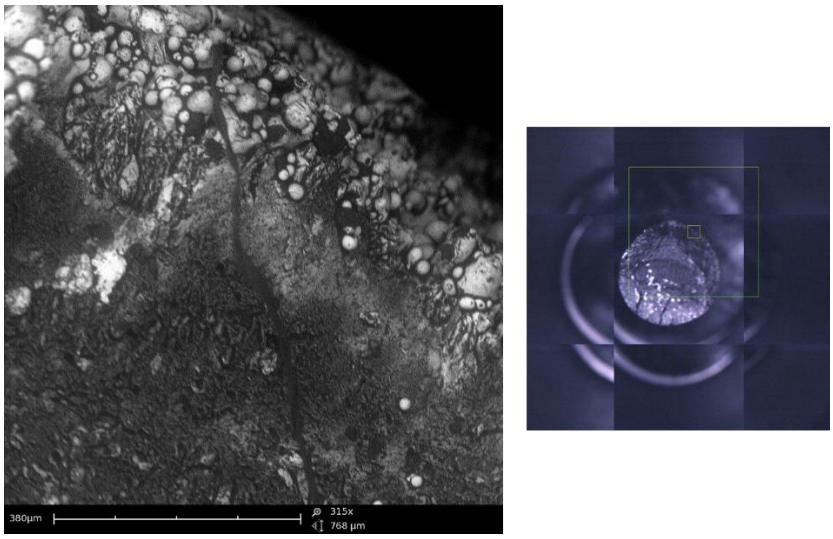

Figure 24: Fracture surfaces of sample subject to progressive amplitude fatigue testing: sample 19 (X), in which a rough surface is observable

4.3 Low Cycle Fatigue Results

In order to assess the impact of plasticity on the life of DMLS SS GP1 manufactured along varying build orientations, samples were subject to strain control LCF test conditions at a strain range of $\Delta\varepsilon = 1.4\%$. A summary of the findings, including the approximate cycles to failure, stress range, $\Delta\sigma$, mean stress, σ_m, elastic, $\Delta\varepsilon_e$, plastic, $\Delta\varepsilon_p$, and total strain ranges, $\Delta\varepsilon$ are presented in Table 11 for the first and stabilized cycles. These results are distinguished by build orientation, and also include the Young's Modulus, E, determined by the ratio of the stress range and elastic strain range. Further detail regarding each specimen is presented in Appendix B in addition to the results found for additional specimens subject to LCF testing in batch 1, which

were manufactured along the XY45° build orientation (i.e., Samples 11 and 12). A comparison across build orientations reveals similarities in the stress and strain ranges, in addition to a decrease observed in Young's modulus between the first and stabilized cycles. There is variation observed in the fatigue life of these specimens that can be attributed to the surface conditions/defects at the microstructural level, but overall the fatigue life for these specimens was found to be less than 200 cycles. This is evident from the plot of stress histories for each specimen presented in Figure 25. Here, the longest life is observed for the Y-oriented sample, with the shortest life seen for the XY45°-oriented sample, followed by the X-oriented sample. It is important to note that approximately 2 axial counts (reversals to failure) is equivalent to 1 cycle. The stress histories from this study were overlaid with the stress history from strain control fatigue tests conducted at a strain amplitude of 0.5%, from an earlier study on as-built SLM SS 17-4PH, manufactured along the horizontal build orientation [Yadollahi, 2017]. It is evident that this material had a longer life when tested at a 0.5% strain amplitude. As this study assessed life performance of as-built specimens at a strain amplitude of 0.7%, there is a reduction in life observed, due to both plasticity effects and surface conditions of these specimens. The average surface roughness for these specimens was found to be Ra = 4 to 7 μm, and was discussed in the previous section. For most samples tested, tests were stopped when a crack was visually detected in the sample and the tensile stress dropped to approximately 50% of the stabilized stress value.

Table 11: LCF test results (rounded) from the present study [Siddiqui, 2018]

Orientation	Sample-Cycle	Approximate Fatigue Life, N_f (cycles)[a]	Young's Modulus, E (GPa)	Stress Range, $\Delta\sigma$ (MPa)	Mean Stress, σ_m (MPa)	Total Strain Range, $\Delta\varepsilon$ (mm/mm)	Plastic Strain Range, $\Delta\varepsilon_{pl}$ (mm/mm)	Elastic Strain Range, $\Delta\varepsilon_{el}$ (mm/mm)
X-Axis	1-First	153	165	1143	27	0.01393	0.0070	0.0069
	1-Stabilized		145	1630	-48	0.01394	0.0027	0.0112
X-Axis	2-First	150	156	1114	52	0.01397	0.0068	0.0071
	2-Stabilized		139	1616	52	0.01394	0.0023	0.0116
Y-Axis	7-First	166	161	1132	34	0.01396	0.0069	0.0070
	7-Stabilized		136	1597	-56	0.01396	0.0022	0.0117
Y-Axis	8-First	192	159	1140	48	0.01396	0.0068	0.0072
	8-Stabilized		138	1593	-41	0.01396	0.0024	0.0116
XY-45°	4-First	151	174	1139	32	0.01384	0.0073	0.0066
	4-Stabilized		144	1631	-38	0.01396	0.0026	0.0113
XY-45°	6-First	126	167	1136	44	0.01396	0.0072	0.0068
	6-Stabilized		140	1580	-51	0.01394	0.0026	0.0113

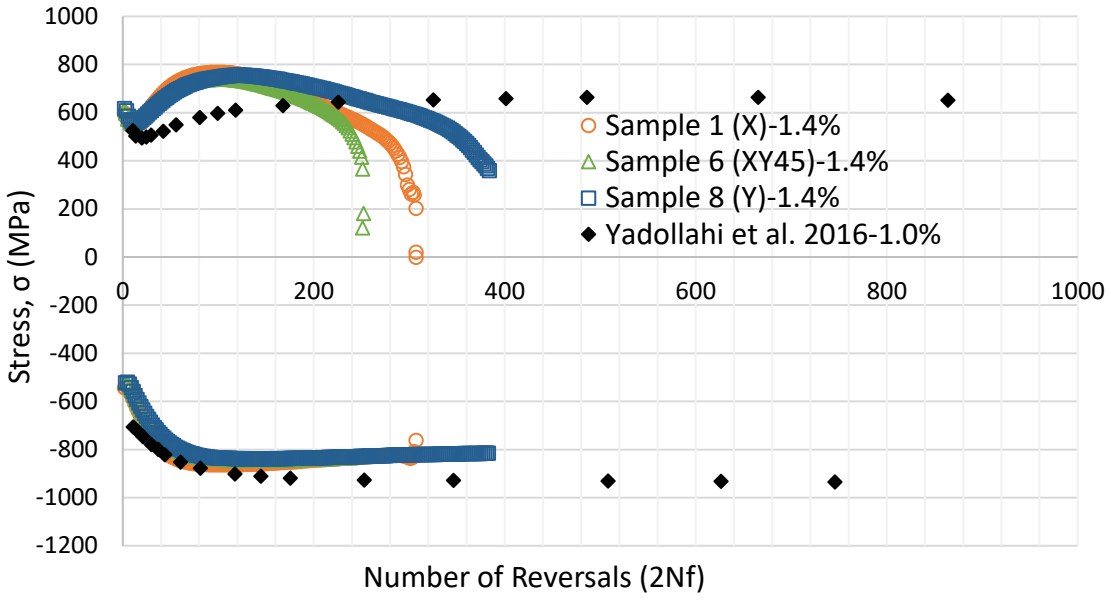

Figure 25: Peak-valley stress history for various orientations for DMLS SS GP1, in which 2 segments ~ 1 cycle [Siddiqui, 2018].

Over a period of time, when subject to repeated cyclic loading, materials tend to either cyclically harden or cyclically soften. Depending upon the application, this can play a considerable role on affecting the performance of a component. Figure 25 is a comparison of the stress-peak variation for samples manufactured along varying build orientations in the xy plane, from which the softening/hardening response of this material can be assessed. The material behavior depicted in Figure 25 suggests that this material initially hardens, followed by a period of stabilization, after which the material begins to soften, until fracture. This is also evident from the increase in stress range values between the first and stabilized cycles for each build orientation, as presented in Table 11. The viability of tensile properties to predict the cyclic hardening and softening material behavior, without the need for fatigue testing, will be explored in Chapter 6 on constitutive modeling.

The level of energy dissipation with cycling, which is evident from analyzing the hysteresis curves, can provide insight into the durability of AM materials to withstand high plastic cyclic loads. Figure 26 provides a representation of this energy dissipation for DMLS SS GP1 samples manufactured along the X-orientation and Y-orientation respectively, when subject to LCF testing at a high plastic strain range of 1.4%.

a.)

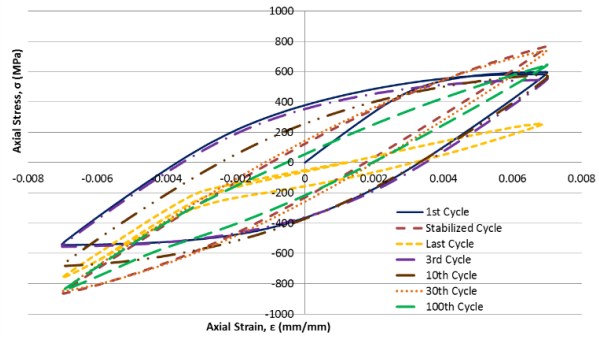

b.)

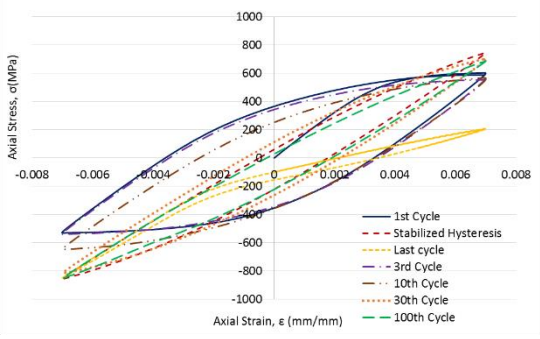

Figure 26: a.) Progression in hysteresis curves for (X)-oriented sample, b.) Progression in hysteresis curves for (Y)-oriented sample [Siddiqui, 2018]

Hysteresis curves are shown during progressive cycling from the 1st cycle to the last cycle (i.e. in most cases, tests were stopped when a crack was detected, and the tensile stress dropped to approximately 50% less than the stabilized tensile stress). Energy dissipation overtime is evident from the hysteresis curves, which is further supported by the reduction in plastic strain range between the first and stabilized cycle for each cycle. These plastic strain ranges are quantified in Table 11. It is evident that the material tolerance to withstand high tensile stress reduces with cycling, as opposed to its tolerance to support compressive stress. As these tests were setup to be completely reversible strain control (R_ε = -1), analysis of these hysteresis curves suggest that slight tensile-compressive asymmetry may exist for this material, since it yields a

greater compressive stress, than tensile stress at the same strain range. This is also evident from Figure 25, which depicts the peak-valley stress history for these build orientations. An analysis of hysteresis curves generated during 1.4% strain range LCF testing of specimens also suggests that a slight tensile compressive asymmetry is present for DMLS SS GP1. Another study [Mahmoudi, 2017] has also shown evidence of slight tensile-compressive asymmetry in SLM SS 17-4PH.

A comparison of the monotonic tension response to the first cycle LCF response can be used to assess the repeatability/quality control in the response of AM materials. Figure 27 overlay the monotonic tension response with the first cycle response for samples manufactured at the same build orientation. For the X-oriented and XY45°-oriented sample, the material response is similar. However, comparing the response for the Y-oriented sample (sample 9 from batch 1), there is a clear variation in the monotonic and first cycle response for this material. To assess this in further detail, Y-oriented specimens (sample 21 and sample 9 from batch 2) were subject to tension testing. The stress-strain response for sample 21 has also been plotted in Figure 27, for qualitative purposes to emphasize the similarity in the tensile response and first cycle response for the Y-oriented specimens, further suggesting that the tensile response observed for sample 9 (Y) may behave as an outlier, as discussed in earlier sections. A comparison of the first cycle Young's moduli with the Young's moduli determined through monotonic tension testing reveals similar results, as presented in Table 9 and Table 11 respectively. In order to assess any anisotropy exhibited in the material response, the first cycle behavior has been plotted for each build orientation, and is also presented in Figure 27. These hysteresis curves suggest minimal variation in material response regardless of build orientation. This would suggest that DMLS SS

GP1 exhibits isotropic behavior, for manufacturing at varying build orientations in the horizontal *xy*-build plane, based upon LCF first cycle results.

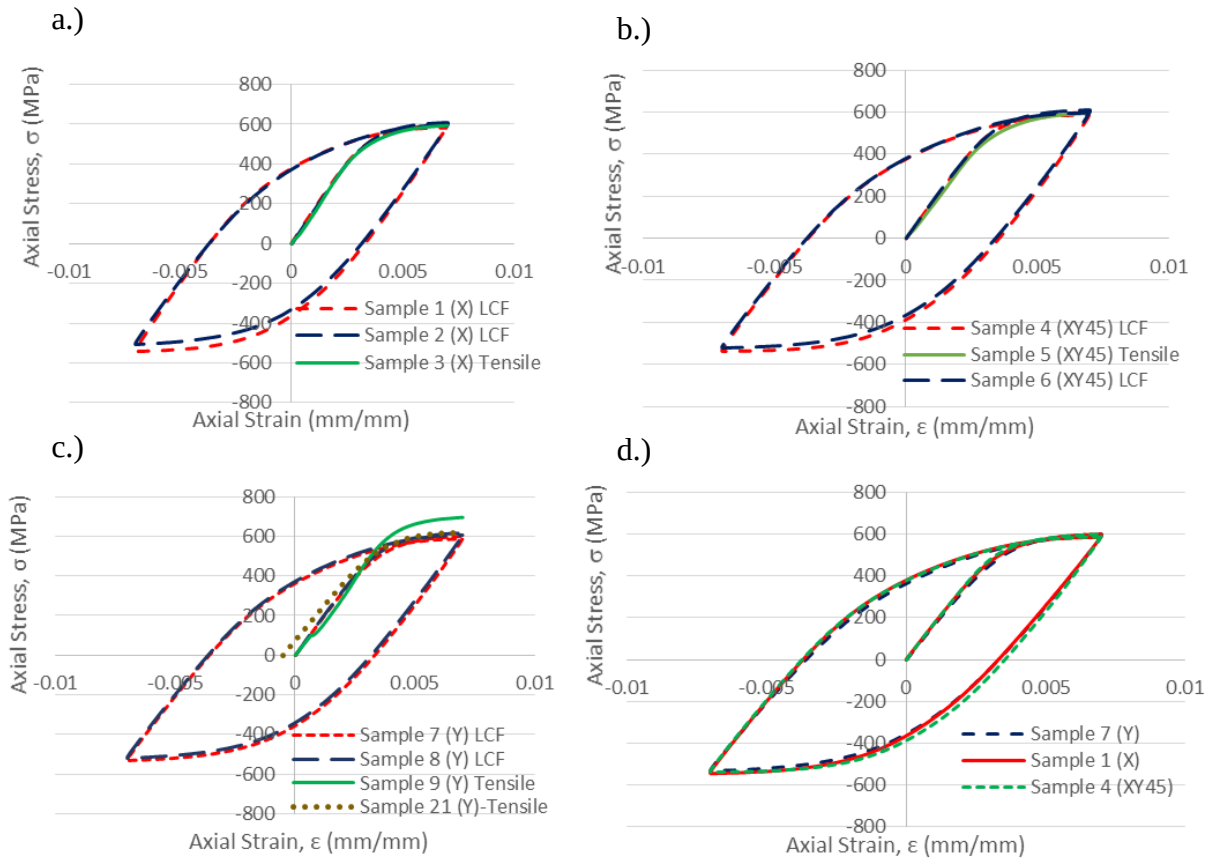

Figure 27: a.) First cycle stress-strain hysteresis curves with tension curves for X-orientation, b.) First cycle stress-strain hysteresis curves with tension curves for XY45°-orientation, c.) First cycle stress-strain hysteresis curves with tension curves for the Y-orientation, d.) First cycle stress-strain hysteresis curves for varying build orientation in the xy build plane [Siddiqui, 2018]

Exploring the variation in the stabilized cyclic response of this material at multiple strain amplitudes can give insight into the onset of plasticity in these additively manufactured materials, which is of import depending upon the application in which these materials are used. To that effect, a comparison of the stabilized hysteresis at the strain amplitude tested in this study of 0.7% for 3 build orientations (i.e. X, Y and XY45°) was plotted in Figure 28, along with the

stabilized hysteresis curves for strain amplitudes ranging from 0.18% to 0.5%, for horizontally built SS 17-4PH, from an earlier study [Yadollahi, 2017]. A significant amount of plasticity can be observed from the stabilized hysteresis curves in this study, with minimal amount of plasticity evident in the hysteresis curves from Yadollahi et al. 2017. There is a variation in the Young's Modulus between the two studies, which is contributing to the differences observed in the slopes of the hysteresis curves. This may be a result of the post-processing condition variation used between the 2 studies prior to experimental testing.

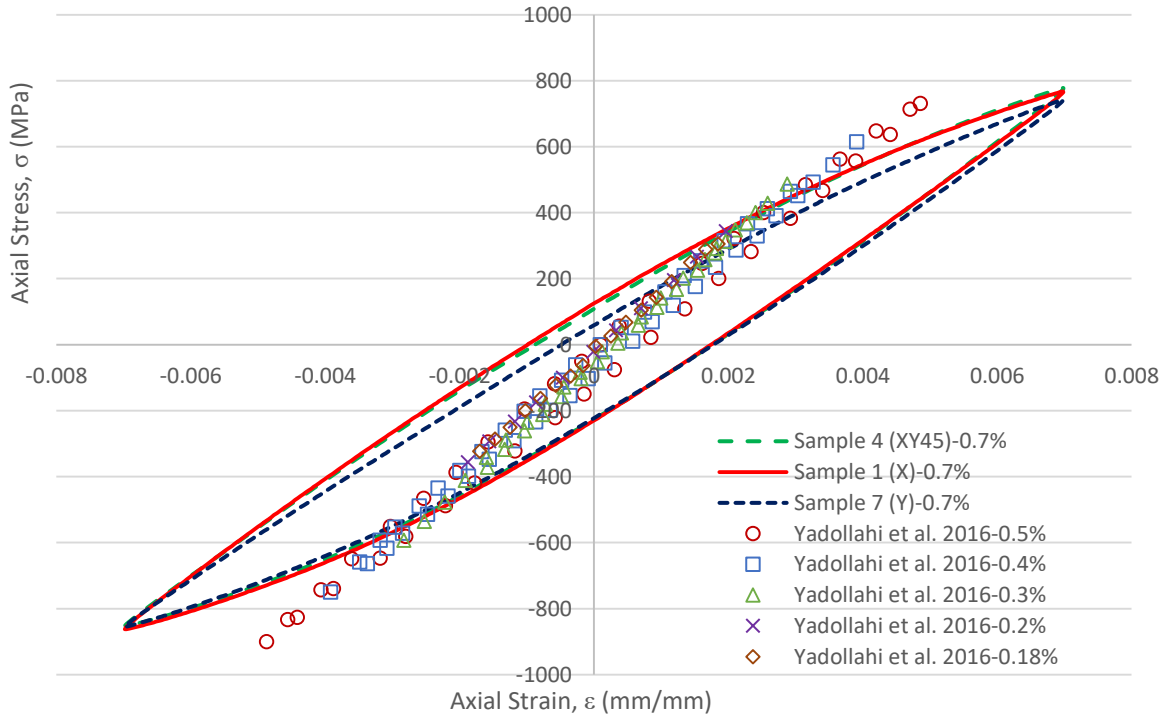

Figure 28: Stabilized hysteresis curves for varying build orientations from this study and Yadollahi et al. 2016 [Siddiqui, 2018]

Resulting first and stabilized hysteresis curves from these constant amplitude fatigue test will be modeled depending upon exhibited anisotropic hardening/softening behavior. The results from these tension and fatigue experiments will be used to determine and identify relations

between tensile and fatigue properties observed for these class of materials and prove whether existing relationships between tensile and fatigue properties for non-additive manufactured materials, discussed in Chapter 2, can be applied towards additively manufactured materials. This is a critical aspect in fatigue analysis, because should connections be found between tensile and fatigue properties, it will lead not only to savings in the additional cost and time associated with fatigue testing and development of additively manufactured specimens for fatigue testing, but also allow for uniaxial tensile testing to provide approximations of the fatigue behavior of these materials. These findings will be further discussed and presented in Chapter 6.

4.4 Progressive Amplitude Fatigue Results

Progressive strain amplitude fatigue testing was performed to assess the increase in strain range on crack initiation/propagation in as-built AM test specimens, as well as to assess the cyclic response of AM materials, from stabilized hysteresis curves. With increase in strain range, the impact of large elasticity, equivalent elasticity and plasticity, and significant amounts of plasticity on failure of DMLS SS GP1 specimens can be assessed. Furthermore, this type of progressive amplitude loading is yet unexplored for this class of AM materials, yet is of critical importance given the service fatigue conditions experienced by these materials used in the gas turbine industry. The stress-life response of these specimens, manufactured along the X and XY45° build orientations, is presented in Figure 29. It is important to note that approximately 2 segments are equivalent to 1 cycle. Cycling was performed at strain ranges of 0.6%, 0.8%, 1.0%, 1.2% and 1.4%, for a set number of 100 cycles at each strain range. This number of cycles for each strain range was set in order to achieve stabilization, before increasing to the next strain range.

a.)

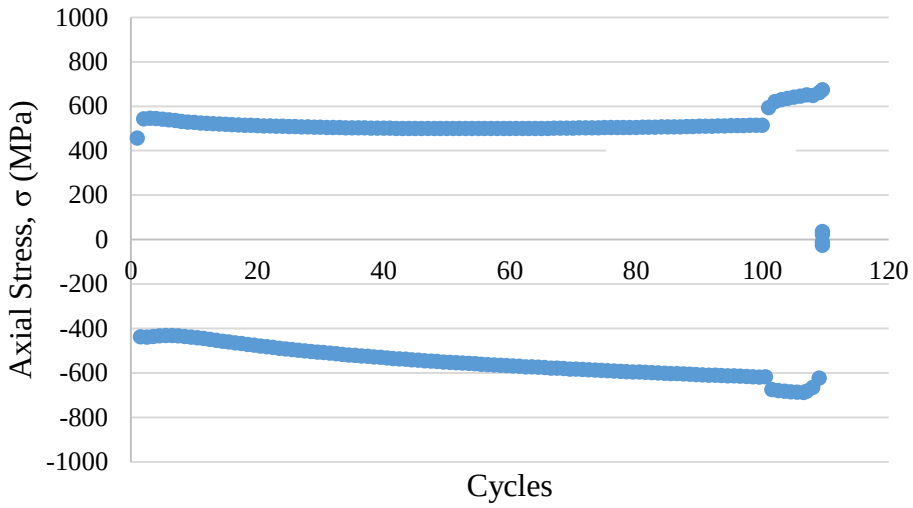

b.)

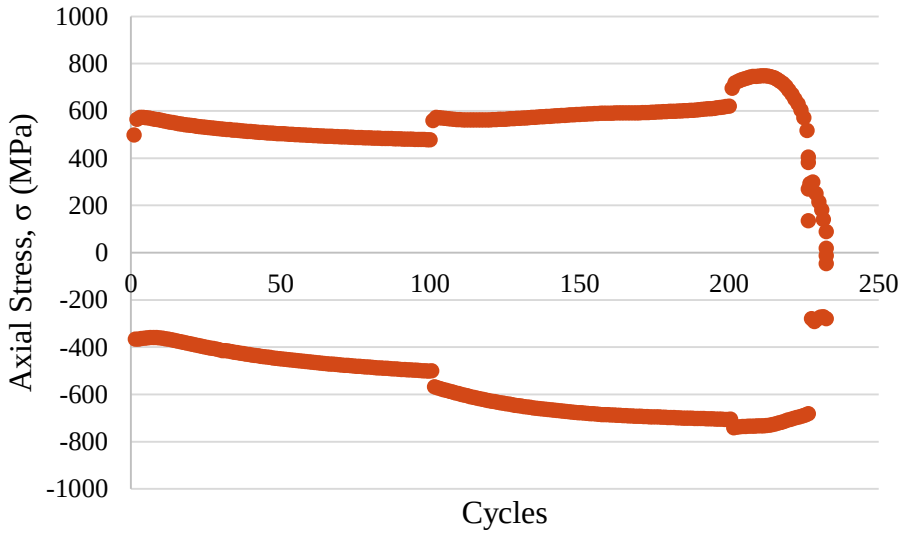

Figure 29: Stress vs. segments for progressive strain amplitude fatigue testing: a.) sample 15 (XY45°-orientation), b.) sample 19 (X-orientation)

From the findings in this study, it is evident that failure occurred in these specimens prior to reaching a strain range of 1.2% and 1.4%, when subjected to progressive amplitude fatigue loading. This would suggest that crack initiation in as-built additively manufactured Stainless Steel GP1 accelerates with an increase in strain range, most especially when the effects of

plasticity become pronounced. While the X-oriented sample did not fail until reaching a strain range of 1.0%, the specimen manufactured along the XY45°-orientation was found to fail upon reaching and cycling at a strain range of 0.8%. This may be a consequence of internal defects (i.e., pores and voids), developed during the AM process and present within these specimens. An analysis of the fracture surfaces obtained for these specimens, and their correlation to this finding is further explored in Section 4.7.

Also evident from the stress-history response presented in Figure 29 is the hardening and softening response of DMLS SS GP1 at each strain range, when subject to proportional amplitude loading conditions. For the specimen manufactured along the XY45° build orientation, which fractured during cycling at a strain range of $\Delta\varepsilon$ = 0.8%, a unique hardening/softening response is observed. The material appears to soften to stabilization, after which it hardens, during testing at a strain range of $\Delta\varepsilon$ = 0.6%, before testing progressed to a strain range of $\Delta\varepsilon$ = 0.8%. A similar phenomena is observed for the specimen manufactured along the X build orientation, in which at a strain range of $\Delta\varepsilon$ = 0.6%, the material appears to soften. However, at a strain range of $\Delta\varepsilon$ =0.8%, the material hardens, and continues to harden at a strain range of $\Delta\varepsilon$ = 1.0%, before fracturing. This would suggest that at a strain range of $\Delta\varepsilon$=0.8% and $\Delta\varepsilon$=1.0%, when plasticity effects become more pronounced, the hardening behavior experienced by this material may be attributed to a strain-induced austenite to martensite phase transformation, as suggested in other studies on additively manufactured stainless steel 17-4PH [Yadollahi, 2016].

To further evaluate the presence of any anisotropic characteristics in the cyclic response of DMLS SS GP1 manufactured at varying build orientations in the *xy* build plane, the first and stabilized cycles at each strain range are presented in Figure 30 and Figure 31 respectively. Overall, it appears that aside from a few slight variations, the initial and stabilized hysteresis

curves suggest that build orientation in the *xy* plane does not contribute to affecting the cyclic response of this material when subject to progressive strain amplitude fatigue testing. However, there is a variation in the Young's Modulus between both build orientations, which would contribute to the shift observed when overlaying the hysteresis curves.

a.)

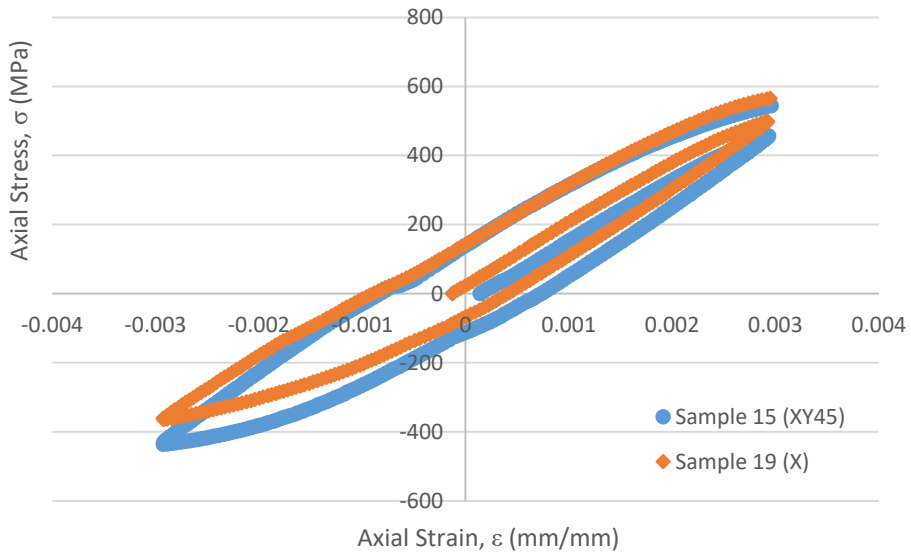

b.)

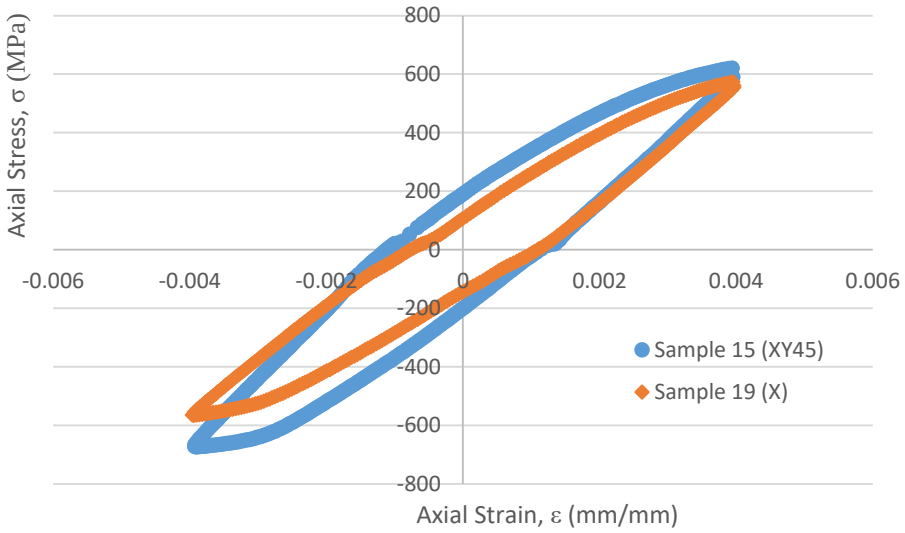

Figure 30: First cycle comparison from progressive amplitude fatigue testing at varying strain ranges: a.) $\Delta\varepsilon$ =0.6%, b.) $\Delta\varepsilon$=0.8%

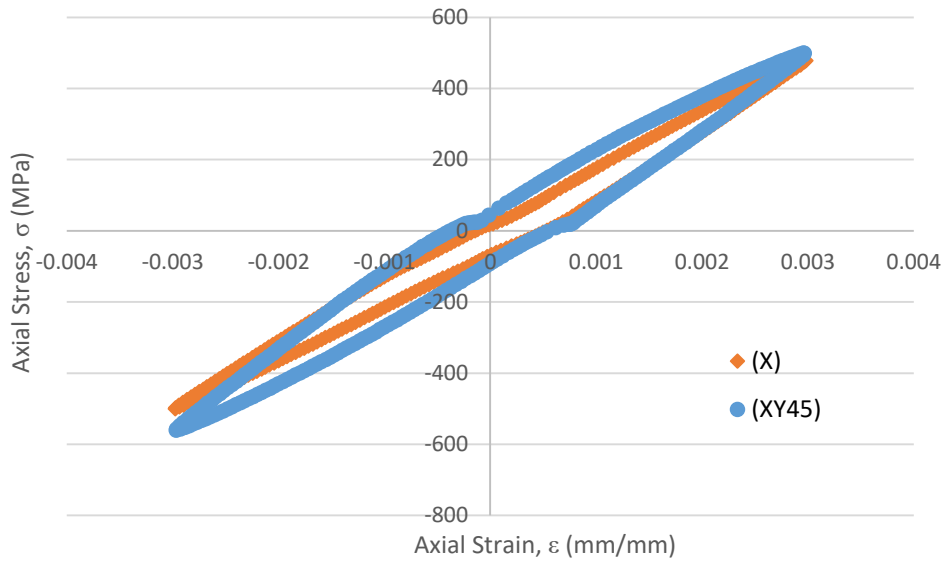

Figure 31: Stabilized cycle comparison from progressive amplitude fatigue testing at strain range of $\Delta\varepsilon$ =0.6%

The fatigue properties obtained for the first and stabilized cycles at strain ranges of $\Delta\varepsilon$ = 0.6% and $\Delta\varepsilon$ = 0.8%, from progressive amplitude fatigue testing, are presented in Table 12 and Table 13 respectively. At these strain ranges, where elasticity effects are more pronounced, it is found that the Young's modulus is considerably larger than that found during LCF testing at a strain range of $\Delta\varepsilon$ = 1.4%. Furthermore, these Young's moduli, determined from the first cycle analysis, are found to be in the range of expected values for conventional stainless steel 17-4PH (E = 190 to 220 GPa). The sample manufactured in the XY45° build orientation was found to have significantly larger Young's Modulus at both strain ranges, as compared with the sample manufactured along the X build orientation. This is also clearly evident from the hysteresis curves, as discussed earlier. While the elastic strain range is predominant during this testing, both specimens were found to fail during strain range testing at $\Delta\varepsilon$ = 0.8% or 1.0%, suggesting that internal defects/voids may have accelerated failure of these specimens, in addition to the sudden

increase in strain range after a fixed number of cycles. This material response is examined further in Section 4.7. Nevertheless, it would appear that progressive amplitude fatigue testing is detrimental to the life of DMLS SS GP1 manufactured in the horizontal build plane, however as these are preliminary experiments, future work will be done to confirm these findings. These findings have been used for cyclic stress-strain curve development presented in Chapter 6, along with reported findings from other studies.

Table 12: Comparison of progressive amplitude fatigue data at Δε = 0.6% for DMLS SS GP1 manufactured along varying build orientations

Orientation	Sample-Cycle	Young's Modulus, E (GPa)	Stress Range, $\Delta\sigma$ (MPa)	Mean Stress, σ_m (MPa)	Total Strain Range, $\Delta\varepsilon$ (mm/mm)	Plastic Strain Range, $\Delta\varepsilon_{pl}$ (mm/mm)	Elastic Strain Range, $\Delta\varepsilon_{el}$ (mm/mm)
X-Axis	19-First	190.266	863.25	66.78	0.0058	0.0013	0.0045
	19-Stabilized	185.495	978.9	-10.86	0.0059	0.0007	0.0053
XY-45°	15-First	207.665	893.135	10.1	0.0059	0.0016	0.0043
	15-Stabilized	211.3857	1059.7	-30.758	0.0059	0.005	0.0054

Table 13: Comparison of progressive amplitude fatigue data at Δε = 0.8% for DMLS SS GP1 manufactured along varying build orientations

Orientation	Sample -Cycle	Young's Modulus, E (GPa)	Stress Range, $\Delta\sigma$ (MPa)	Mean Stress, σ_m (MPa)	Total Strain Range, $\Delta\varepsilon$ (mm/mm)	Plastic Strain Range, $\Delta\varepsilon_{pl}$ (mm/mm)	Elastic Strain Range, $\Delta\varepsilon_{el}$ (mm/mm)
X-Axis	19-First	185.73	1126.53	-3.32	0.0079	0.0018	0.0061
	19-Stabilized	188.34	1322.53	-42.73	0.0079	0.0009	0.0070
XY-45°	15-First	227	1267.51	-40.376	0.0078	0.0023	0.0056

4.5 Pulsating Tension Fatigue Results

For materials used in the gas turbine industry, assessing the impact of pulsating tension (i.e., mean stress) fatigue conditions on the mechanical response, can provide insight into how sudden and repeated tensile stresses can lead to early crack initiation and propagation thus limiting life of these components, and resulting in untimely component failure. With additive manufacturing of these parts on the rise, it is equally important to subject such components to these service conditions in order to assess how manufacturing characteristics contributes to the mechanical performance of these materials. As such, this study has conducted strain-control pulsating tension fatigue experiments, at a strain range of 0.7%, on as-built DMLS SS GP1, manufactured along varying build orientations. The role of specimen size on replicating results observed for conventionally manufactured specimens was also assessed.

The durability of these components when subject to pulsating tension fatigue conditions have been studied. Figure 32 presents a comparison of the stress-life performance of DMLS SS GP1 conventional specimens, manufactured along the XY45° and X build orientations. Failure is defined as complete fracture of specimen or stopping of test, when a surface crack is observed or the tensile stress is observed to drop to ~50% of its stabilized value. The sample manufactured along the XY45° build orientation appears to soften to stabilization, followed by a period of brief hardening to fracture. Similarly, the sample manufactured along the X build orientation softens to a period of brief stabilization. However, after stabilization, it appears that the X-oriented sample softens to fracture. This response is in contrast to that observed during low cycle fatigue testing, in which the specimens exhibited hardening to stabilization, followed by softening to fracture. A comparison of the life of both components reveals that the sample manufactured along the X-orientation exhibits a longer life than that manufactured along the XY45°-

orientation, under pulsating tension fatigue conditions at a highly elastic strain range. As these are preliminary findings, future work will focus on repeat testing to further confirm findings.

Sample 1, from batch 2, which was manufactured along the X-orientation, is a reduced test specimen. A comparison of its stress versus life response shows similarities with regards to the softening and hardening response observed under pulsating tension fatigue conditions, exhibited by sample 14, manufactured along the XY45° orientation. Similarly, it exhibits the characteristic softening to stabilization response observed by sample 20, which was also manufactured along the X-orientation. This confirms that the reduced specimen geometry provides similar findings as compared with conventionally manufactured test specimen size, in addition to yielding savings in the AM process.

As mentioned earlier, LCF tests revealed that DMLS SS GP1 hardens to stabilization, which may be attributed to strain-induced austenite to martensite transformation within the specimen, that gives rise to this hardening phenomenon, as reported in another study [Yadollahi, 2016]. In contract, pulsating tension fatigue tests on DMLS SS GP1 are indicating a softening response up stabilization, which may suggest that mean tensile stresses serve to weaken the material up to stabilization, and perhaps this strain-induced austenite to martensite transformation occurs after stabilization up to the point of fracture, during which the material exhibits cyclic hardening.

a.)

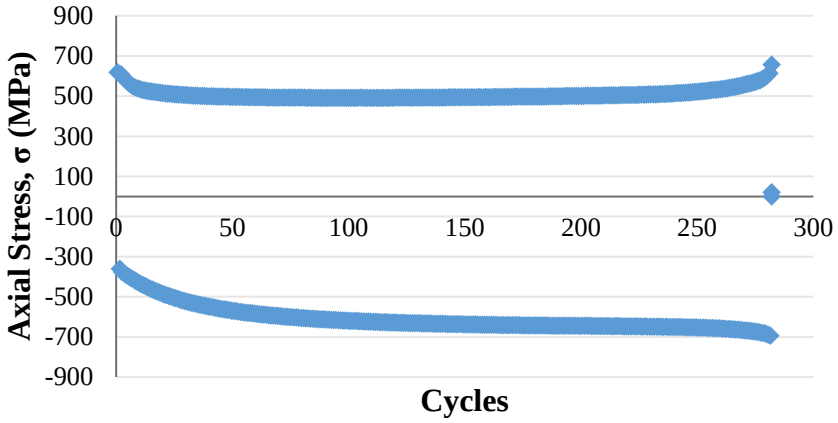

b.)

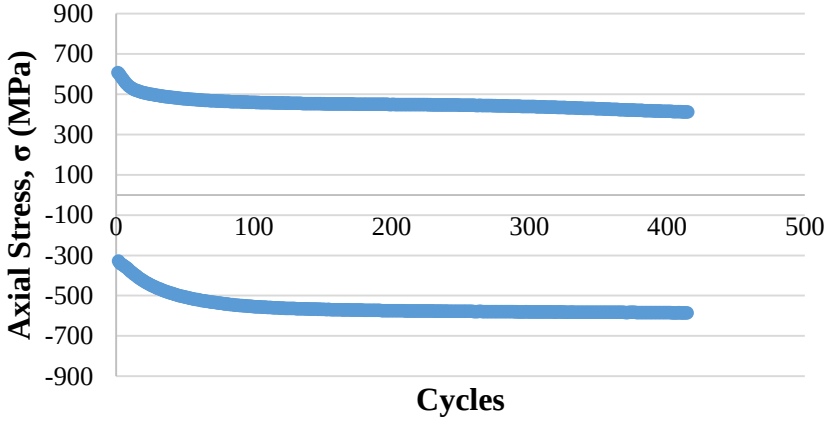

c.)

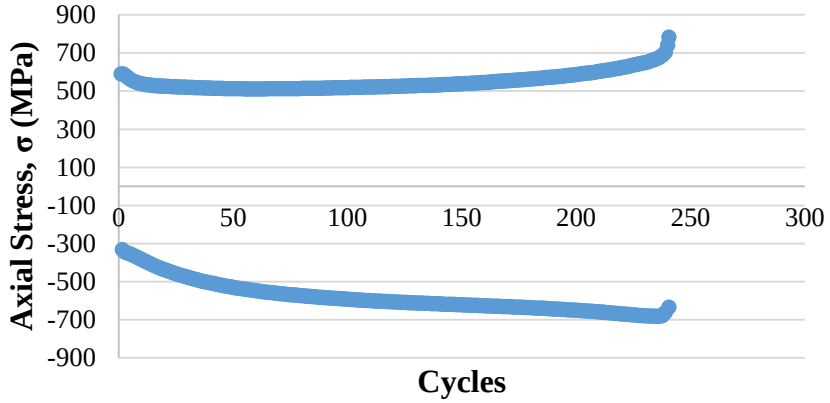

Figure 32: Stress vs. segments for pulsating tension fatigue testing at 0.7% strain range: a.) sample 14 (XY45°-orientation)-conventional specimen, b.) sample 20 (X-orientation)-conventional specimen, c.) sample 1 (X-orientation)-reduced test specimen

An analysis of the first and stabilized cycles from pulsating tension fatigue tests on as-built DMLS SS GP1 samples manufactured along varying build orientations/specimen geometries is presented in Figure 33, Figure 34 and Figure 35. In order to assess the validity of a reduced test specimen in replicating the findings exhibited by conventional test specimens, specimens 1 and 16 from batch 2, manufactured along the X and XY45° orientations, were also subjected to pulsating tension fatigue conditions, and their fatigue properties are presented in Table 14. Analysis of the both the first and stabilized hysteresis curves indicates that the reduced test specimen is able to withstand a greater plasticity range than the conventional test specimens, with the shear stress range being similar between both specimen geometries. Further exploration and modeling of these hysteresis curves is approached in Chapter 6.

The associated fatigue properties from analysis of the first and stabilized cycles, including the stress range, $\Delta\sigma$, mean stress, σ_m, total strain range, $\Delta\varepsilon$, plastic strain range, $\Delta\varepsilon_{pl}$, elastic strain range, $\Delta\varepsilon_{el}$, and Young's Modulus, E, are presented in Table 14. There is considerable variation observed in experimental findings of the Young's Modulus, in which there is a considerable increase found for the XY45° build orientation (E~190 GPa), as opposed to along the X-orientation (E~175 GPa). Clearly evident from all first cycles, is the low plastic strain range (~0.0016 to 0.0018 mm/mm), and large elastic strain range (~0.005), revealing that these pulsating tension fatigue experiments are being conducted under highly elastic strain conditions.

a.)

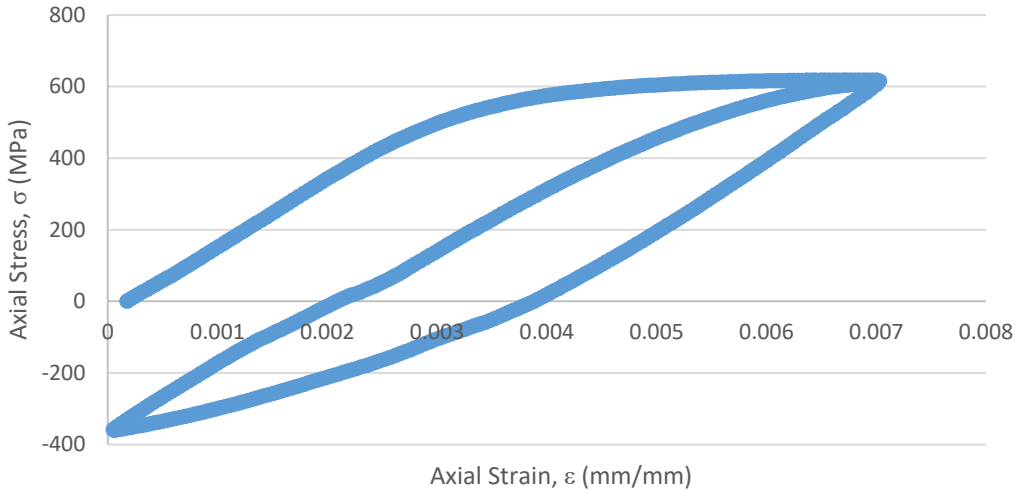

b.)

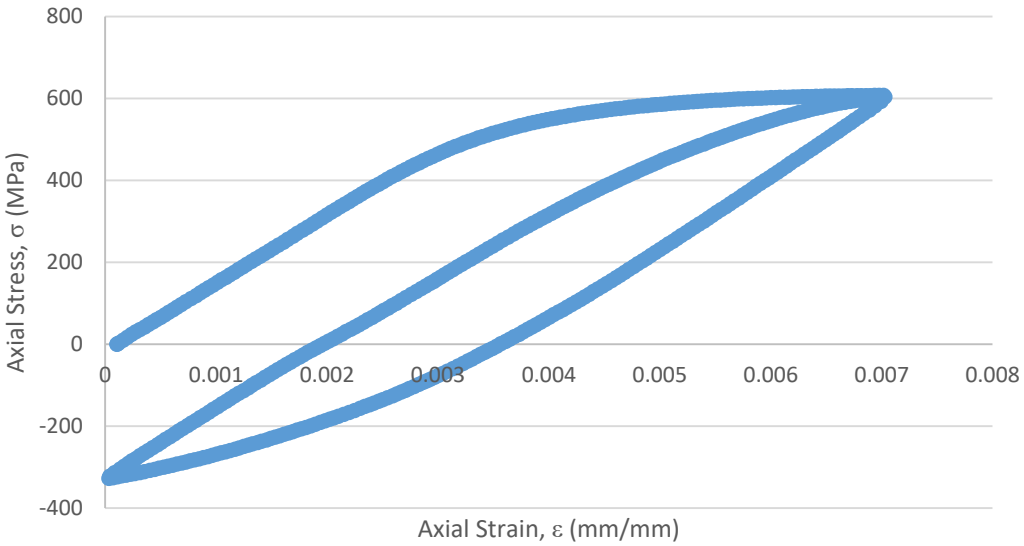

Figure 33: First cycle hysteresis curve pulsating tension fatigue testing at 0.7% strain range for conventionally sized specimens: a.) sample 14 (XY45°-orientation), b.) sample 20 (X-orientation)

a.)

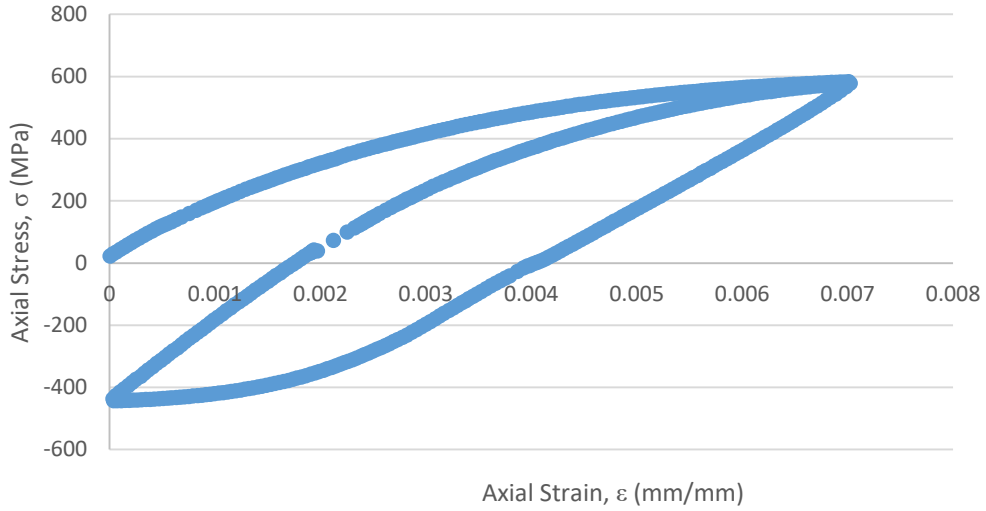

b.)

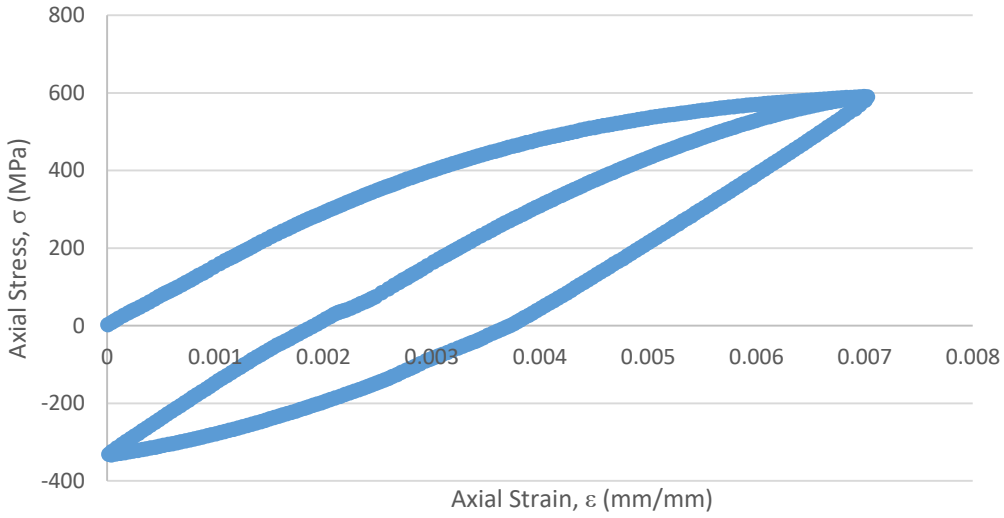

Figure 34: First cycle hysteresis curve from pulsating tension fatigue testing at 0.7% strain range for reduced test specimens: a.) sample 16 (XY45°-orientation), b.) sample 1 (X-orientation),

Table 14: Comparison of pulsating tension fatigue data (rounded) for DMLS SS GP1 manufactured along varying build orientations (conventional and reduced test specimens)

Orientation	Sample-Cycle	Approximate Fatigue Life, N_f (cycles)	Young's Modulus, E (GPa)	Stress Range, $\Delta\sigma$ (MPa)	Mean Stress, σ_m (MPa)	Total Strain Range, $\Delta\varepsilon$ (mm/mm)	Plastic Strain Range, $\Delta\varepsilon_{pl}$ (mm/mm)	Elastic Strain Range, $\Delta\varepsilon_{el}$ (mm/mm)
X-Axis	20-First	~415	174.6	935	140.2	0.00698	0.00163	0.00535
	20-Stabilized		161.4	1020	-65	0.00696	0.00064	0.00632
X-Axis-Reduced Test Specimen	1-First	~241	180.1	923	128.8	0.00695	0.00183	0.00512
	1-Stabilized		179.7	1052	-14.6	0.00696	0.0011	0.00586
XY-45°	14-First	~282	190.3	979	129	0.00694	0.0018	0.00514
	14-Stabilized		181.6	1103	-60	0.00695	0.00088	0.0061
XY-45°-Reduced Test Specimen	16-First	-	219.9	1026	70	0.00697	0.0023	0.00467

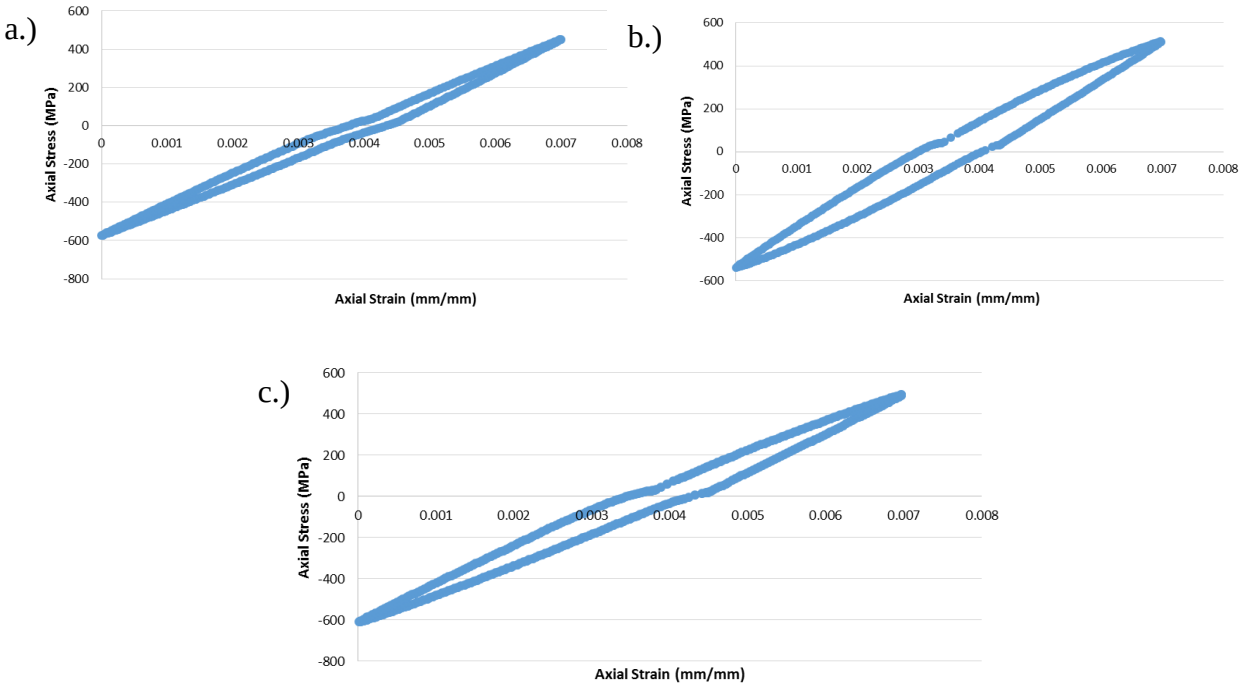

Figure 35: Stabilized cycle hysteresis curve from pulsating tension fatigue testing at 0.7% strain range: a.) sample 20 (X-orientation), b.) sample 1 (X-orientation), c.) sample 14 (XY45°-orientation)

4.6 Torsional Loading Results

An assessment of both the axial and torsional mechanical response of additively manufactured components can provide insight into the durability of these materials under service conditions commonly endured by aerospace components. Although there is a comprehensive understanding of the tensile response of AM materials, few studies have analyzed how these parts behave under monotonic and cyclic shear loading conditions.

Completely reversible (R=-1) torsion fatigue tests, under angle of twist control, with limited plasticity, was performed on DMLS SS GP1 samples, of conventional geometry, manufactured along the (Y) and (XY45°) orientations. The fatigue properties from the first and stabilized cycle (i.e., shear stress range, mean shear stress, shear modulus, plastic, elastic and total shear strain ranges) for each orientation are presented in Table 15. An overlay of the first cycle response for the (Y) and (XY45°) orientations is as seen in Figure 36. While it appears that there is a variation in the first cycle response between both build orientations, this may be a result of the presence of a mean shear stress on the sample, and slight variation in the shear modulus determined for each build orientation (G = 50.7 GPa for (Y)-oriented sample, and G = 49.45 for the (XY45°)-oriented sample). The (Y)-oriented sample has an imparted mean shear stress of 13.8 MPa versus the (XY45°)-oriented sample, which has an imparted mean shear stress of -29.3MPa. For both specimens, the shear strain ranges are within range of one another, indicating that upon initial cycling, the amount of plasticity experienced by each specimen, regardless of build orientation is the same.

The stabilized cyclic response for the (Y) and (XY45°) orientated specimens is as seen in Figure 36. The increase in shear stress range to ~1271 MPa during stabilization for the (Y)-oriented sample, as compared with ~844 MPa for the first cycle reveals that DMLS SS GP1

cyclically hardens to stabilization, under torsional fatigue loading conditions. This hardening response was observed during completely reversible, strain control, low cycle fatigue (LCF) testing as well. A similar increase in the shear stress range is observed for the (XY45°) oriented specimen, revealing cyclic hardening to stabilization. However, the amount of hardening to stabilization, experienced by the (XY45°) orientation is less than for the (Y)-orientation, with a shear stress range of ~818 MPa for the first cycle and ~1087 MPa for the second cycle. This may be a result of slipping encountered by the specimen during torsional fatigue testing or characteristics of the specimen itself. To assess this further, reduced torsion fatigue specimens are developed with a 3 prong gripping design to reduce/eliminate specimen slipping. Discussions on the findings are presented later on in this section.

Overall, an assessment of both specimens reveal hardening to stabilization, followed by softening to fracture. The bar chart presented in Figure 36 reflects the number of cycles before failure of these specimens. Both specimens endured fracture just under 10^4 cycles. While the (XY45°) - oriented specimen endured slightly less than 10^4 cycles before indicating signs of crack propagation along the specimen surface, indicative of a brittle helicoidal fracture, the (Y)-oriented specimen endured a few thousand cycles, before experiencing a complete brittle ‘starry’ spline fracture. Section 4.7 discusses fracture behavior in more detail.

Comparing the fatigue properties for the stabilized curves, shown in Table 15, it is found that there is a reduction in the shear modulus for both specimens at stabilization, as compared with the first cycle. There is also a larger plastic strain range at stabilization observed for the (XY45°) specimen.

a.)

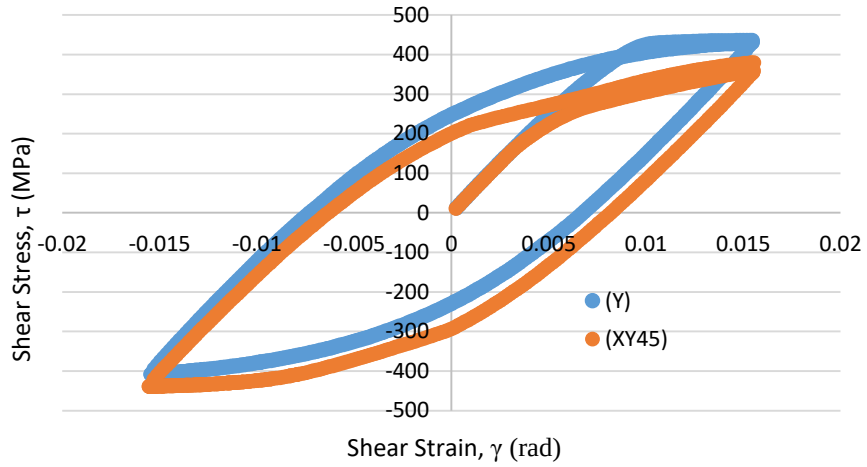

b.)

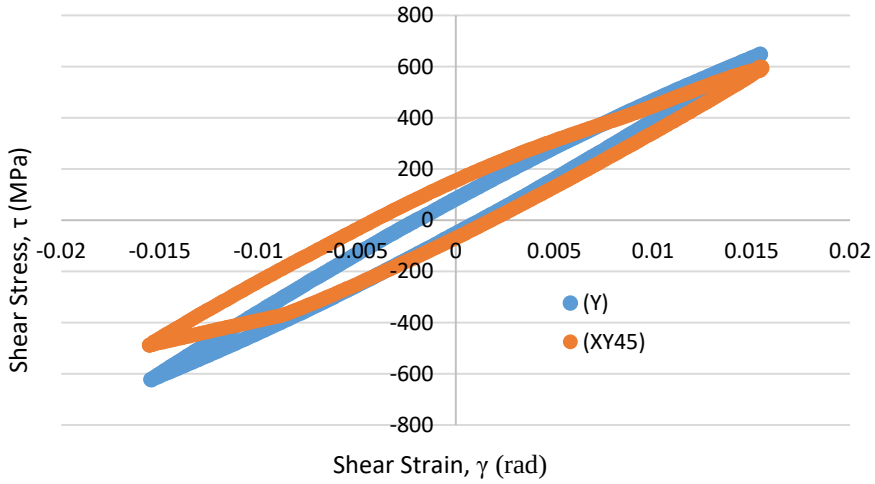

c.)

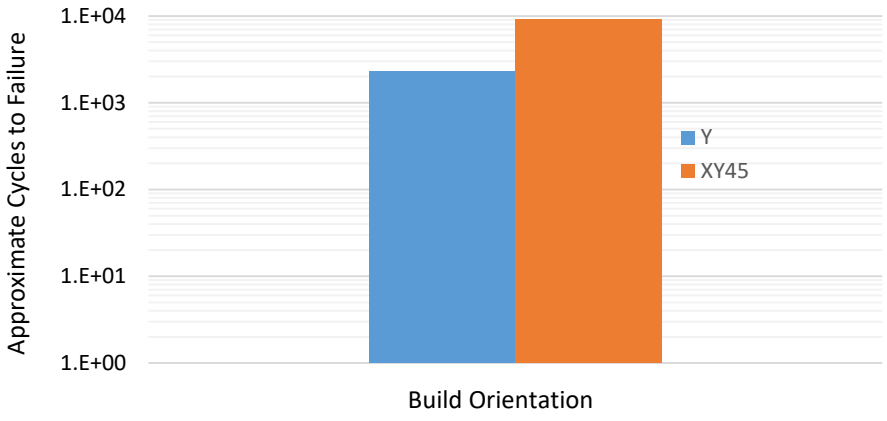

Figure 36: a.) First cycle shear stress versus shear strain hysteresis curves for varying build orientations, b.) Stabilized cycle shear stress versus shear strain hysteresis curves for varying build orientations [Siddiqui, 2018]

Table 15: Cyclic torsional properties (rounded) for DMLS SS GP1 manufactured along varying build orientations, subject to completely reversible (R= -1) torsional fatigue conditions [Siddiqui, 2018]

First Cycle						
Orientation	**Shear Stress Range, $\Delta\tau$ (MPa)**	**Mean Shear Stress, τ_m (MPa)**	**Total Shear Strain Range, Δγ**	**Elastic Shear Strain Range, Δγe**	**Plastic Shear Strain Range, Δγp**	**Shear Modulus (GPa)**
Y (-5° from the y-axis)	843.83	13.85	0.0308	0.0166	0.0142	50.7
XY45° (45° in the xy build plane)	818.24	-29.3	0.031	0.0165	0.0145	49.45
Stabilized Cycle						
Orientation	**Shear Stress Range, $\Delta\tau$ (MPa)**	**Mean Shear Stress, τ_m (MPa)**	**Total Shear Strain Range, Δγ**	**Elastic Shear Strain Range, Δγe**	**Plastic Shear Strain Range, Δγp**	**Shear Modulus (GPa)**
Y (-5° from the y-axis)	1271.15	12.37	0.0309	0.0276	0.0033	46.05
XY45° (45° in the xy build plane)	1086.78	55.03	0.0309	0.025	0.0059	43.51

In addition to assessing the torsional fatigue response of these materials, it is equally important to characterize the monotonic torsional properties of AM materials. To this effect, DMLS SS GP1 specimens manufactured along the (X), (Y) and (XY45°) were subject to monotonic torsion tests at the same angle of twist rate used for torsional fatigue tests, of ϕ_rate = 1.654 deg/sec. As a result of specimen slipping in the grips, a complete shear stress-shear strain curve was unable to be achieved, therefore only the ultimate shear strength was determinable and therefore reported in Table 16. The ultimate shear strength for DMLS SS GP1 was found to be considerably larger than for heat-treated (H900) wrought Stainless Steel 17-4PH. This may suggest that the layer by layer deposition, which is characteristic of the AM process, may allow for improved performance in shear. The resulting fracture surface ductile response observed under monotonic torsion tests were found to be in contrast to those specimens subject to torsional fatigue tests. Section 4.7 discusses this fracture behavior in more detail.

Table 16: Monotonic torsional properties (rounded) of DMLS SS GP1 manufactured along varying build orientations compared with conventional Stainless Steel 17-4PH [Siddiqui, 2018]

Orientation	Shear Strength (MPa)
X (-5° from the *x*-axis)	1011
Y (-5° from the *y*-axis)	1018
XY45° (45° in the *xy* build plane)	1010
H900 SS 17-4PH [MakeItFrom, 2009]	830

During the course of monotonic torsion and torsional fatigue testing on conventionally manufactured specimens, slipping of the specimens within the grips of the MTS EM Bionix system was encountered, and deemed to be attributed to the circular geometry of the gripping section, given that the grips were designed to grip at 3 locations on the specimen ends, 120° apart. To counteract this problem, a new gripping section design was developed, which would allow for firm gripping of the specimens, thereby limiting/eliminating this problem. The new gripping design was applied to reduced test specimens, manufactured along the X, Y and XY45° orientations. The 3 prong gripping design machined for these specimens is as shown in Figure 37. Any remaining machining marks in the radial section of the specimen were removed using a 330M grit sand paper.

Figure 37: Reduced torsion specimen (i.e., sample 2-(X)) after machining 3 prongs in the gripping section to limit slipping of the specimen within the grips

DMLS SS GP1 reduced torsion specimens with the 3 prong gripping section of the following build orientations: (X), (Y) and (XY45°), were subject to completely reversible (R=-1) torsional fatigue tests at an angular rate of 1.654 deg/sec, data acquisition rate of 10 Hz, cycling between +15° and -15°. These tests were performed to not only assess the repeatability in earlier findings, deduce any differences in material behavioral response with change in specimen geometry, but to determine the effectiveness of the 3 prong gripping section in limiting/eliminating slipping within the test device. A superposition of the first cycle and stabilized cycles for each build orientation is presented in Figure 38, from which the following observations were made. First, the amount of plasticity captured during the first and stabilized cycles is significant, as compared with the conventional torsion specimens, which were subjected to the same experimental conditions. This suggests that a reduction in the test specimen size, specifically the inner gauge diameter allows for more pronounced impact of plasticity effects. Second, with the assumption that these materials exhibit isotropic material behavior for build orientations in the *xy* plane, the overlay of cycles across build orientation, depicted in Figure 38, should each capture a similar cyclic response. However, slight variations exist, which may be attributed to an induced slight tensile/compressive mean stress on the specimen under completely reversible (R=-1) torsional fatigue conditions.

a.)

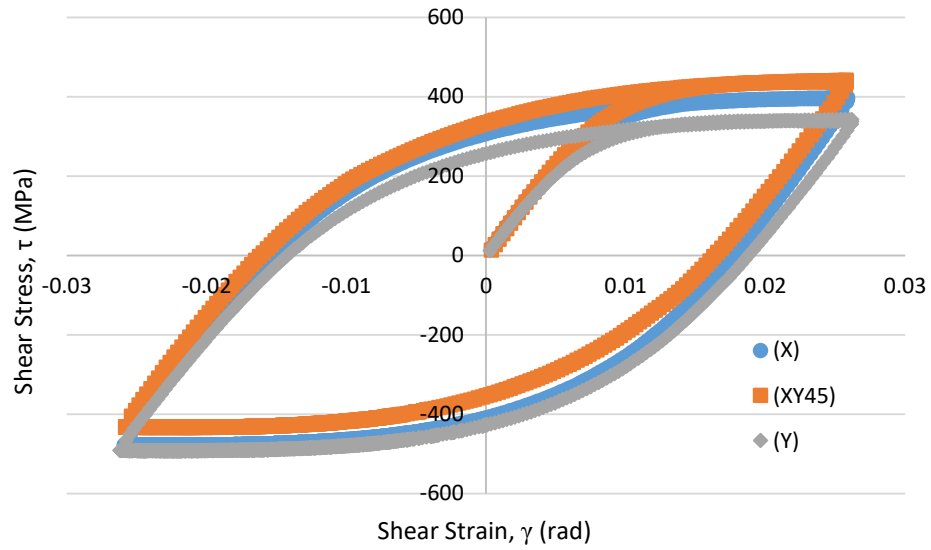

b.)

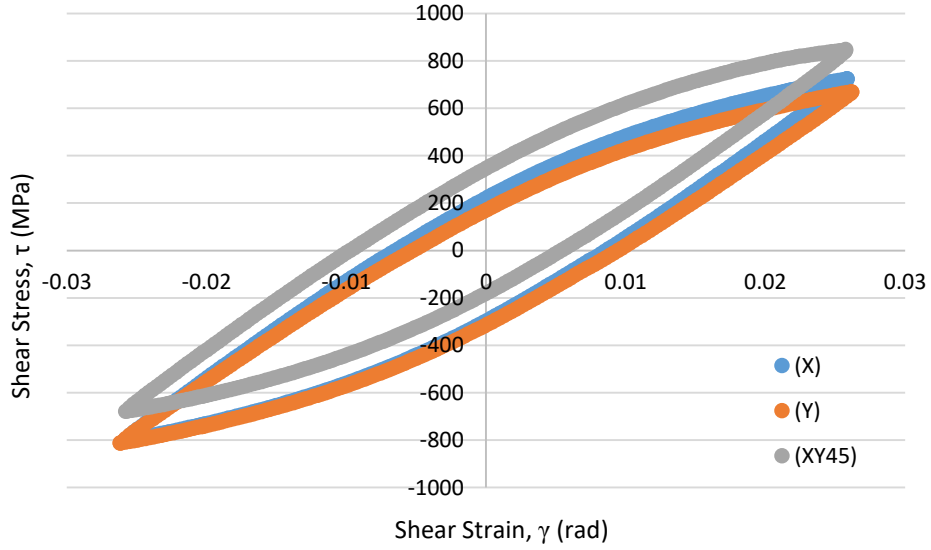

Figure 38: Torsion fatigue testing of reduced test specimens, a.) first cycle shear stress vs. shear strain, b.) stabilized cycle shear stress vs. shear strain

These qualitative observations exhibited by the first and stabilized cyclic responses are explored further through characterization of the torsional properties exhibited by each cycle, based upon build orientation. The torsional properties including the shear modulus, *G*, shear

stress range, $\Delta\tau$, total shear strain range, $\Delta\gamma$, mean shear stress, τ_m, elastic shear strain range, $\Delta\gamma_e$, and plastic shear strain range, $\Delta\gamma_p$ are tabulated in Table 17.

Table 17: Cyclic torsional properties (rounded) for DMLS SS GP1 reduced test specimens manufactured along varying build orientations, subject to completely reversible (R= -1) torsional fatigue conditions

First Cycle-Reduced Test Specimen							
Orientation	**Shear Stress Range, $\Delta\tau$ (MPa)**	**Mean Shear Stress, τ_m (MPa)**	**Plastic Shear Strain Range, Δγp**	**Elastic Shear Strain Range, Δγe**	**Total Shear Strain Range, Δγ**	**Shear Modulus, G (GPa)**	**Approximate Cycles to Failure**
X	872.5	-41.47	0.0332	0.0160	0.0492	54.56	303
Y	830.8	-76.3	0.0331	0.0146	0.0477	56.94	255
XY45°	870.97	2.31	0.0328	0.0141	0.0469	61.68	374
Stabilized Cycle-Reduced Test Specimen							
Orientation	**Shear Stress Range, $\Delta\tau$ (MPa)**	**Mean Shear Stress, τ_m (MPa)**	**Plastic Shear Strain Range, Δγp**	**Elastic Shear Strain Range, Δγe**	**Total Shear Strain Range, Δγ**	**Shear Modulus, G (GPa)**	
X	1525.29	-37.7	0.0150	0.0367	0.0517	41.56	
Y	1481.67	-71.18	0.0147	0.0377	0.0524	39.31	
XY45°	1527.62	85.22	0.0152	0.0363	0.0515	42.03	

A comparison of the shear stress range from the first cycle to the stabilized cycle reveals material hardening during completely reversible torsional fatigue testing. This finding is comparable to the hardening response to stabilization observed in earlier completely reversible LCF tests at a strain range of Δε=1.4%, and the hardening response observed on conventional torsion specimens. Further, this hardening may be attributed to "strain-induced austenite to martensite phase transformation," as found in another study on SS 17-4PH [Yadollahi, 2016]. Also evident, is the large plastic shear strain range within the first cycle, ~0.033, which reduces with cycling to stabilization, to ~0.015. The shear modulus is found to reduce from the initial to stabilized cycles for all build orientations. While stainless steel GP1 has a nominal composition

similar to that of stainless steel 17-4PH, it exhibits material properties that vary from conventionally manufactured martensitic stainless steel 17-4PH. However, as it is closest in chemical composition to SS 17-4PH, a comparison has been done between the shear modulus obtained from first cycle measurements for DMLS SS GP1 and conventionally manufactured, solution annealed and heat-treated SS 17-4PH. The shear modulus reported for solution annealed and heat-treated SS 17-4PH has been reported to be 75GPa [MakeItFrom, 2009]. From Table 17, it is evident that the shear modulus of DMLS SS GP1, for build orientations in the *xy* plane, is considerably less than that reported for conventional martensitic SS 17-4PH. This suggests that under the tested shear fatigue loading conditions, DMLS SS GP1 material performance is limited, and may be attributed to the limited shear stress carrying capacity of the as-built rough surface of DMLS SS GP1, as has been reported by other studies on AM materials [Fatemi, 2017]. Overall, small variations are observed in torsional properties obtained across build orientation, likely attributed to the presence of tensile/compressive mean stresses during completely torsional fatigue testing, thereby supporting the assumption that this material exhibits isotropic material behavior within the *xy* build plane.

$$\boldsymbol{G = \frac{E}{2(1+\vartheta)}} \tag{19}$$

With this assumption, the relationship between Young's modulus, *E*, and shear modulus, *G*, presented in Equation (19), was used to determine the Poisson's ratio, *v*, for DMLS SS GP1 specimens manufactured along the (X), (Y) and (XY45°) build orientations. The Young's Modulus obtained from the first cycle from LCF testing were used to approximate the Poisson ratio for this material. The resulting Poisson's ratio are presented in Table 18.

The Poisson's ratio determined is considerably greater than that reported for conventional martensitic SS 17-4PH of ν = 0.27 to 0.30 [MakeItFrom, 2009]. The average Poisson's ratio within the *xy* plane was determined as 0.393 ± 0.04, based upon 3 measurements, from samples manufactured at varying build orientations in the xy plane.

Table 18: Poisson's ratio determination for DMLS SS GP1 manufactured along varying build orientations, based upon torsional fatigue testing of reduced torsion specimens

Orientation	Young's Modulus, E (GPa)	Shear Modulus, G (GPa)	Poisson's Ratio, ν
X	156	54.56	0.43
Y	159	56.93	0.40
XY45°	167	61.68	0.35
Average ± Standard Deviation	160.67 ± 5.69	57.72 ± 3.63	0.393 ± 0.04

In addition to assessing the Poisson effect exhibited by these specimens, it is critical to determine the durability of such components, when subject to realistic service conditions (i.e. torsional fatigue). Therefore, the shear stress history for reduced torsion specimens manufactured along the (X) and (Y) orientations is as presented in Figure 39, and approximate number of cycles to failure is reported in Table 17. There is considerable reduction in the number of cycles to failure for these specimens, and may be attributed to their reduced geometry (i.e., inner gauge diameter/length), as opposed to conventional torsion specimens. The reduced test specimens, regardless of build orientation fractured after approximately 300 cycles, with actual cycles to failure slightly varying for each specimen. An analysis of the shear stress histories for these specimens reveals hardening to stabilization, followed by softening of the material just before fracture. This characteristic hardening/softening behavior was also observed for DMLS SS GP1 subject to LCF tests at a strain range of $\Delta\varepsilon$ = 1.4%. The fracture response of these specimens, both reduced and conventional torsion specimens, subject to completely reversible torsion

fatigue, will be explored in Section 4.7 in detail. Both specimen types were found to exhibit a brittle fracture response when subject to torsional fatigue testing, as opposed to monotonic torsion testing, in which the characteristic ductile response is observed. Conclusions on this material behavior were further examined in Section 4.7.

a.)

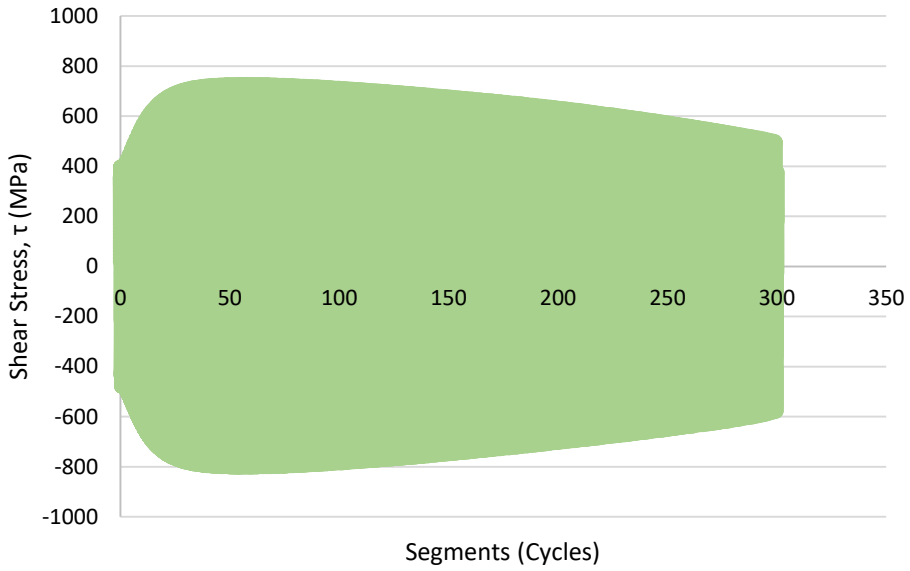

b.)

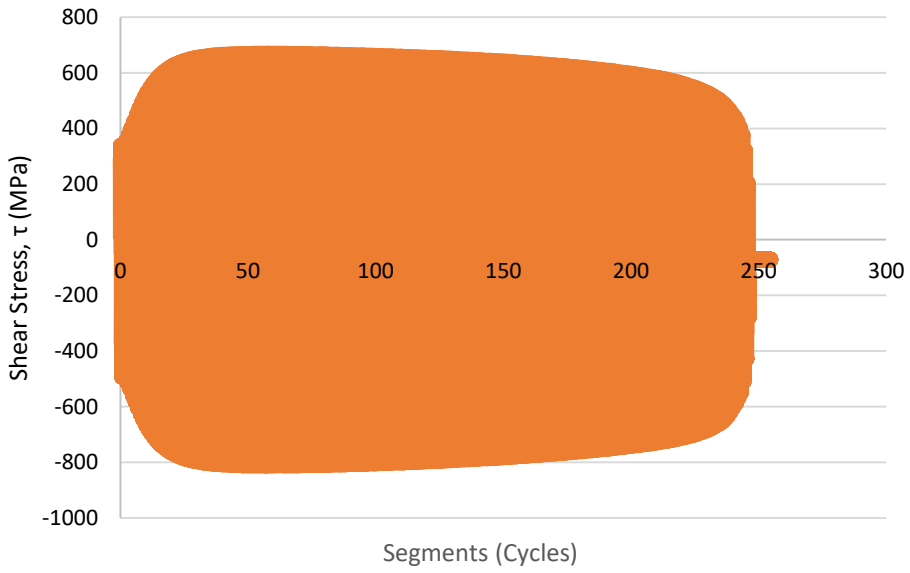

Figure 39: Shear stress history for DMLS SS GP1 reduced torsion specimens, a.) (X) orientation, b.) (Y) orientation

4.7 Fracture Surfaces and Microstructural Observations

Fracture surfaces for samples of varying build orientations, subjected to strain-controlled monotonic tension testing was taken using Dino-Lite Premier Microscope and are shown in Figure 40. Samples 3 (X) and 5 (XY45) from batch 1, exhibited unique fracture surfaces, with variations from the characteristic ductile cup-cone fracture surface. A highly textured and irregular fracture surface is observed, as seen in other studies [LeBrun, 2015]. Sample 9 (Y) from batch 1, exhibited the characteristic ductile cup-cone fracture. Overall, these fracture surfaces were found to exhibit ductile response that was consistent with the σ-ε curves. Crack initiation, crack propagation (i.e. presence of beach marks) and final fracture are evident in all fracture surfaces. The presence of internal voids/pores is also evident from fracture surface images, as well as crack initiation from the surface. Fracture surface images of sample 9 (Y), from batch 1, were also captured using the Phenom Scanning Electron Microscopy, and are presented in Figure 41. The presence of large voids, un-melted powder particles and coalescence of these voids is clearly visible from the SEM images. Also evident are the melt arc pools/scanning tracks during the laser melting and solidification process. Repeat tension testing of a (Y)-oriented specimen from batch 2 revealed a fracture response similar to that observed for specimens 3 (X) and 5 (XY45) from batch 1.

Fracture surfaces for samples manufactured along the X, Y and XY45° orientations, subjected to strain-controlled LCF testing were taken using Dino-Lite Premier Microscope and are shown in Figure 42. The fracture surface for all other specimens subject to LCF testing, not shown in Figure 42 can be found in Appendix B. For majority of the specimens tested, the fatigue crack was found to initiate at the surface, suggesting that surface roughness present in these as-built specimens contributed to crack initiation. Essentially, the failure location of these

samples, which is determined in this study, as the location of crack initiation and propagation, occurred at the extensometer spring attachment to the specimen. Two cracks are clearly evident for sample 6 (XY45°), which initiate at the surface. For sample 1 (X), which fractured completely, a ductile fracture response is observed. An earlier study revealed similar findings, in which fatigue crack initiation was found to initiate at the surface for fatigue testing at high strain amplitudes, up to 0.5% tested [Yadollahi, 2015].

Fracture surfaces for those samples subjected to proportional amplitude fatigue tests are presented in Figure 43, which reveal the presence of large voids that may explain the sudden failure of these specimens during cycling at strain ranges with limited plasticity (i.e., $\Delta\varepsilon$=0.8% and 1.0%). An irregular surface structure is also observable. SEM micrograph images of these specimens are shown in Figure 43 as well. For sample 15 (XY45°) specimen, considerable number of un-melted powder particles can be observed. For sample 19 (X) specimen, the presence of irregular-shaped pores are evident in addition to texturing.

The fracture surfaces for samples subjected to pulsating tension fatigue tests are presented in Figure 44. For those specimens subject to pulsating tension fatigue tests, both conventional and reduced test geometries, the presence of voids, and crack initiation at defects near the surface are evident. In fact, multiple cracks at the surface can be seen for the (X)-oriented specimens.

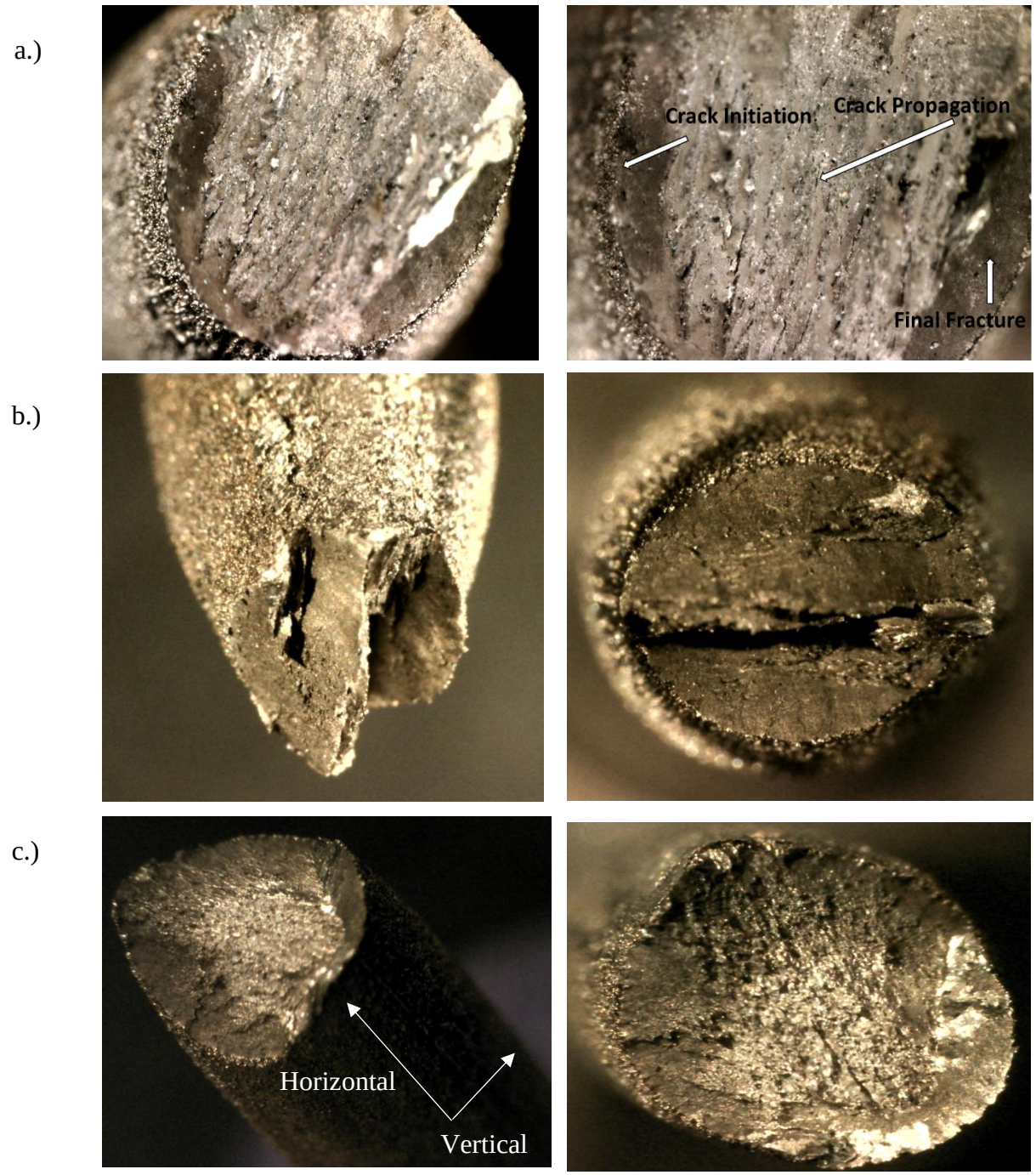

Figure 40: Fracture tensile surfaces: a.) sample 3 (-5° from x-axis), b.) sample 5 manufactured at 45° in the xy build plane, c.) sample 9 (-5° from y-axis) [Siddiqui, 2018]

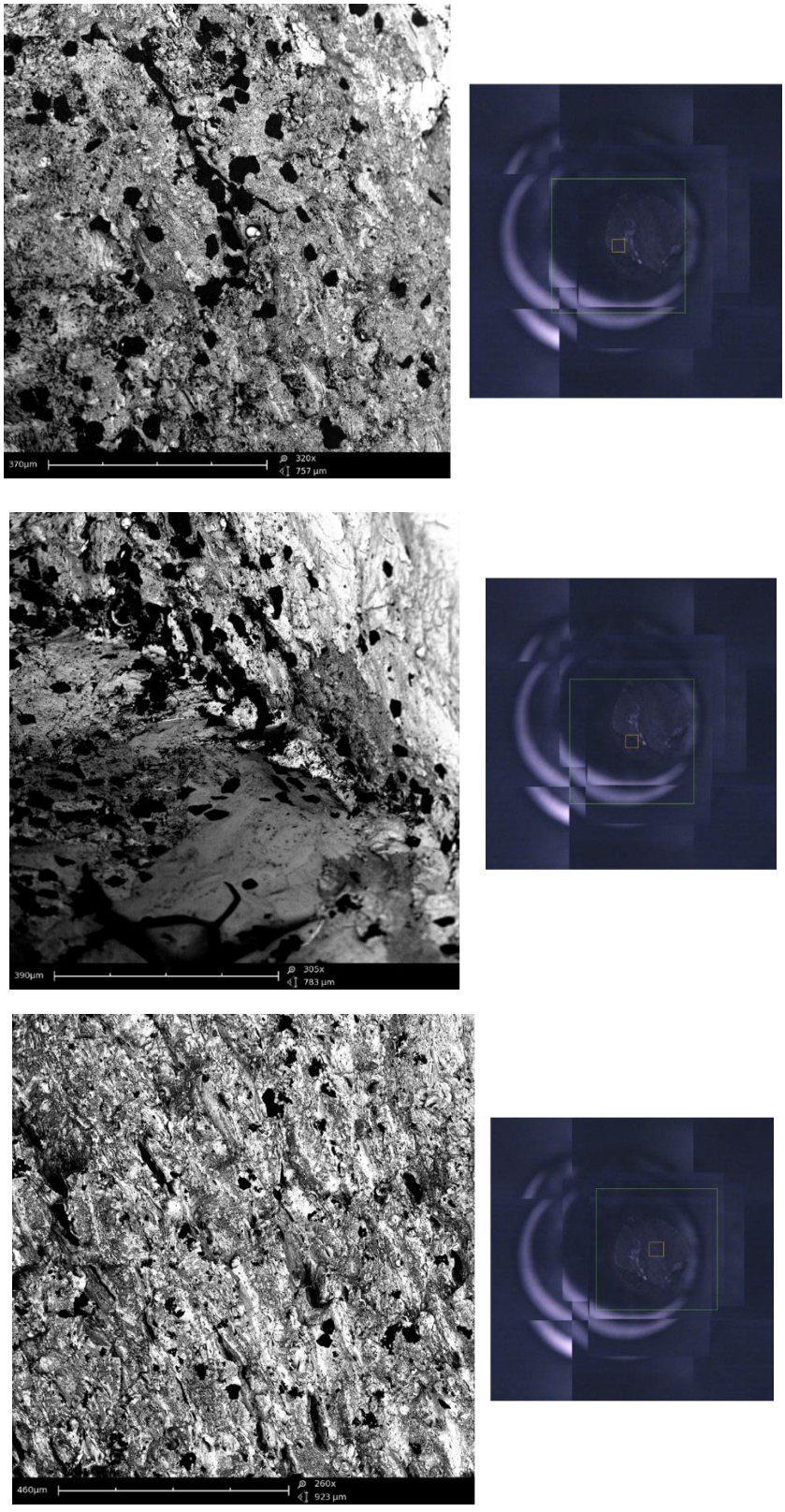

Figure 41: Fracture tensile surfaces taken using SEM: sample 9 (Y)

a.)

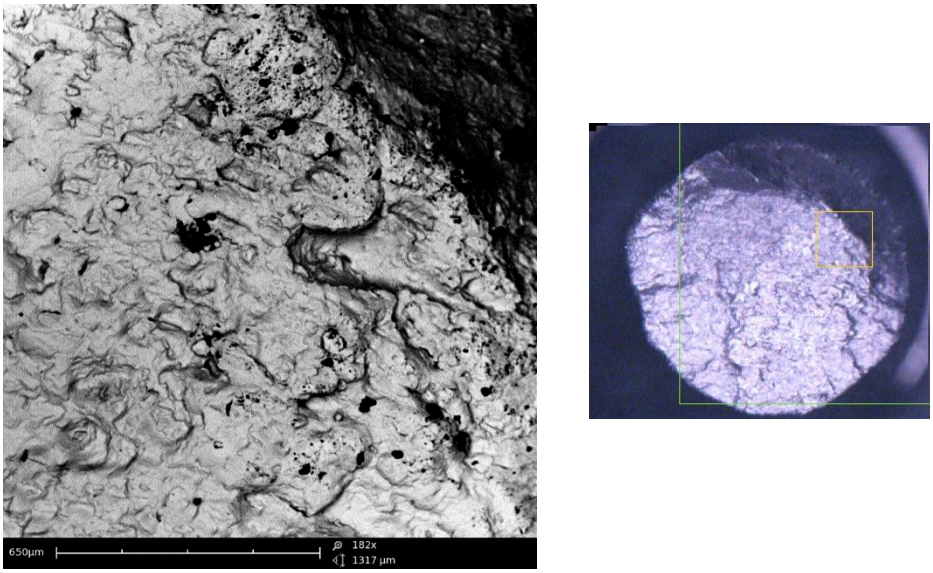

b.)

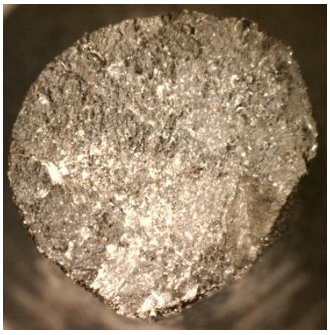

c.)

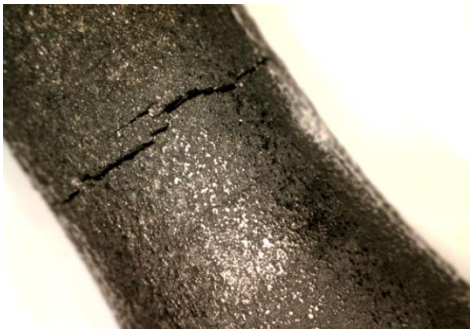

d.)

Figure 42: a.) SEM micrograph image of sample 1 (X), b.) fracture fatigue surface for sample 1 (X), c.) fracture fatigue surface for sample 6 (XY45°), d.) fracture fatigue surface for sample 8 (Y) [Siddiqui, 2018]

a.)

b.)

c.)

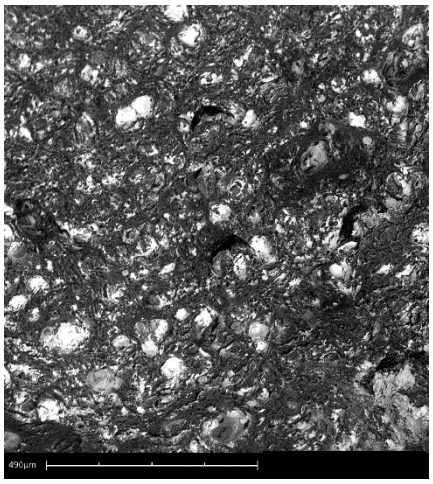

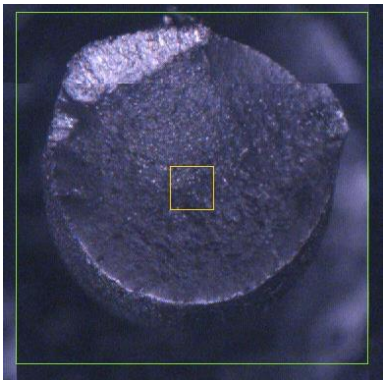

d.)

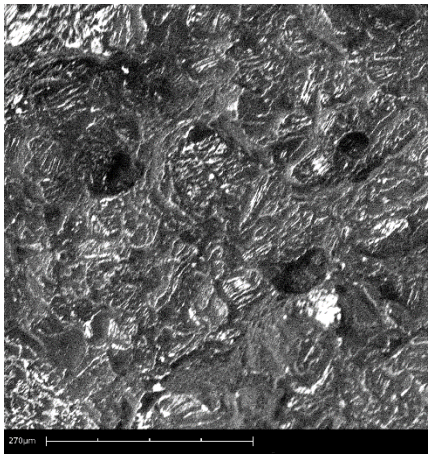

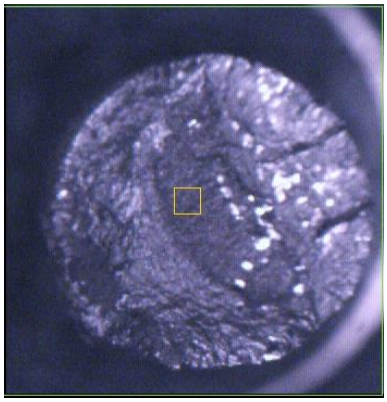

Figure 43: Fracture surfaces for DMLS SS GP1 subject to progressive amplitude fatigue testing: a.) sample 15 (XY45°), b.) sample 19 (X), c.) SEM of sample 15 (XY45°), d.) SEM of sample 19 (X)

a.)

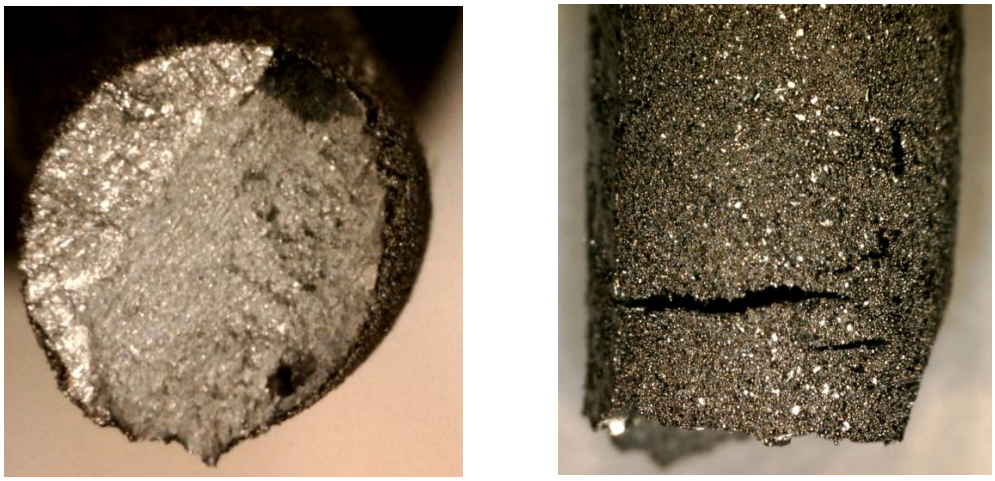

b.)

c.)

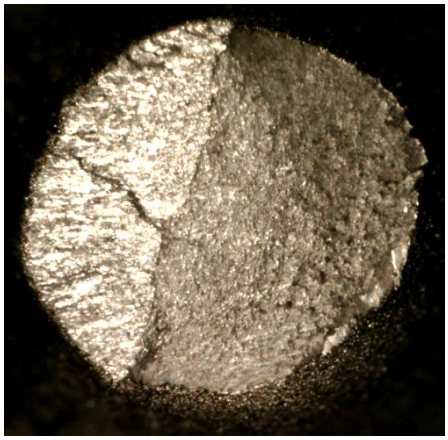

Figure 44: Fracture surfaces for DMLS SS GP1 subject to pulsating tension fatigue at strain range of 0.7%: a.) reduced test specimen, sample 1 (X), b.) conventional test specimen, sample 20 (X), c.) conventional test specimen, sample 14 (XY45°)

Fracture surfaces were taken of conventional and reduced torsion specimens, to assess the loading conditions and consequently material response exhibited under those conditions. The resulting fracture surface for samples of each build orientation, (X), (Y), and (XY45°), subject to monotonic torsion testing, is presented in Figure 45. The fracture surfaces exhibit a ductile fracture, with the characteristic crack initiation, crack propagation, evident through the presence of rotating beach marks, and final fracture. In contrast, however, both conventional and reduced torsion specimens, subject to completely reversible (R = -1) torsional fatigue testing exhibited a brittle fracture response. This may suggest that torsional fatigue loading, which is observed in Section 4.6, to cause cyclic hardening of DMLS SS GP1 during testing, may have resulted in a strain-induced austenite to martensite transformation, as suggested in an earlier study [Yadollahi, 2016]. The introduction of the martensite phase may be the cause for brittle failure response observed during torsional fatigue testing. This finding will be further investigated in future work.

The fracture responses for the (XY45°) and (Y) oriented conventional torsion specimens are exhibited in Figure 46. The (Y)-oriented sample exhibited a star spline type brittle fracture response, whereas the (XY45°)-oriented sample, fractured along and through the build layers, suggesting a brittle helicoidal fracture response. The (XY45°) conventional torsion sample did not completely fracture, but the internal sample structure can be seen in Figure 46b, through which it is evident that crack propagation has occurred through the build layers. Figure 47 captures the fracture response of reduced torsion fatigue specimens, manufactured along the (X), (Y) and (XY45°) build orientations. Here, a star spline brittle fracture response is observed, suggesting unstable crack propagation due to the presence of internal voids/porosity, an outcome of the AM process, resulting in sudden and catastrophic failure of the specimens. As SS 17-4PH

is commonly employed in aerospace-related applications, where these components experience torsional fatigue service conditions, this finding would suggest that such parts may experience sudden failure during operation under these conditions.

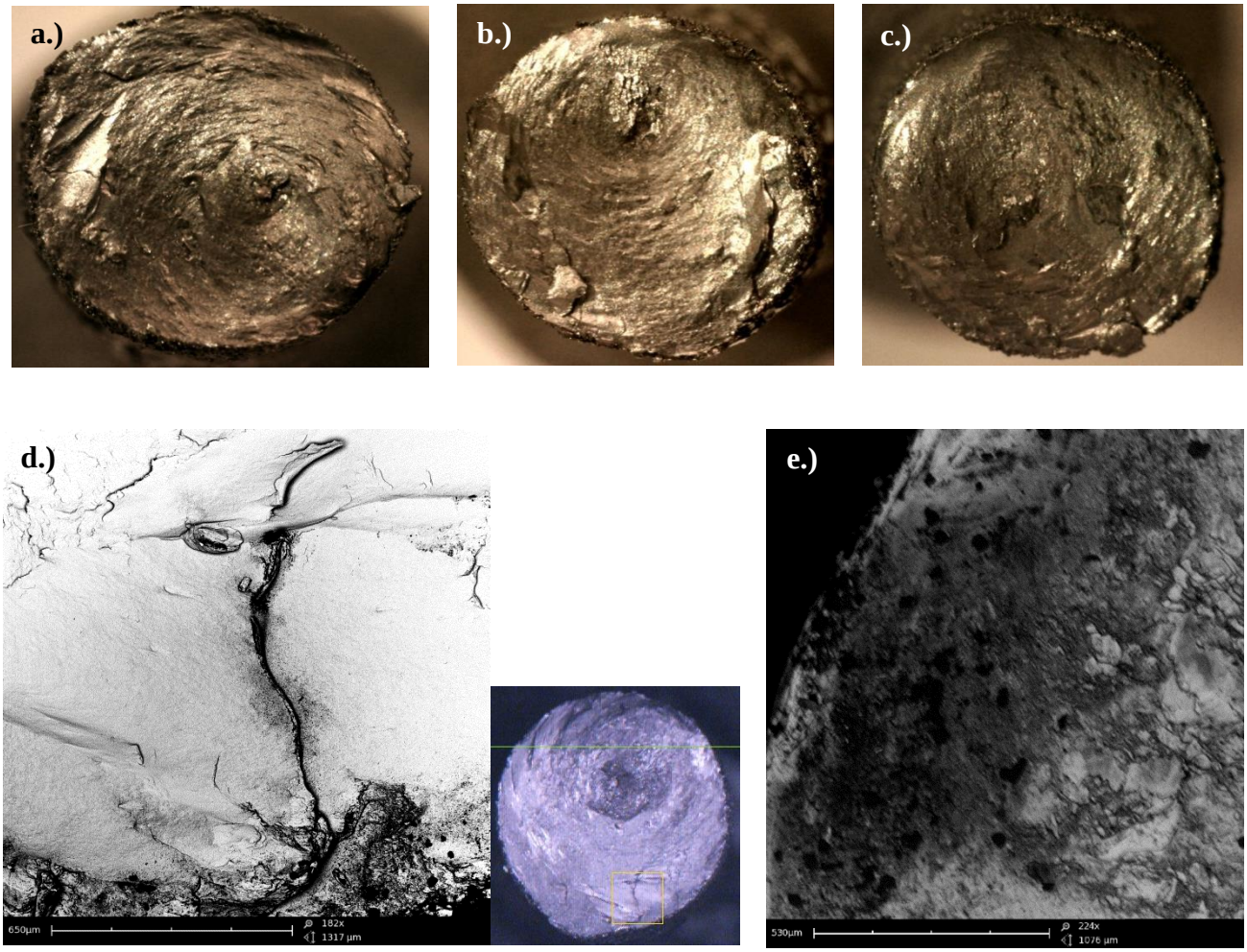

Figure 45: Fracture surfaces of sample after monotonic torsion testing: a.) X-orientation, b.) Y-orientation, c.) XY45° orientation, d.) SEM micrograph image of crack in X-oriented specimen e.) SEM micrograph image of edge of XY45°-oriented specimen [Siddiqui, 2018]

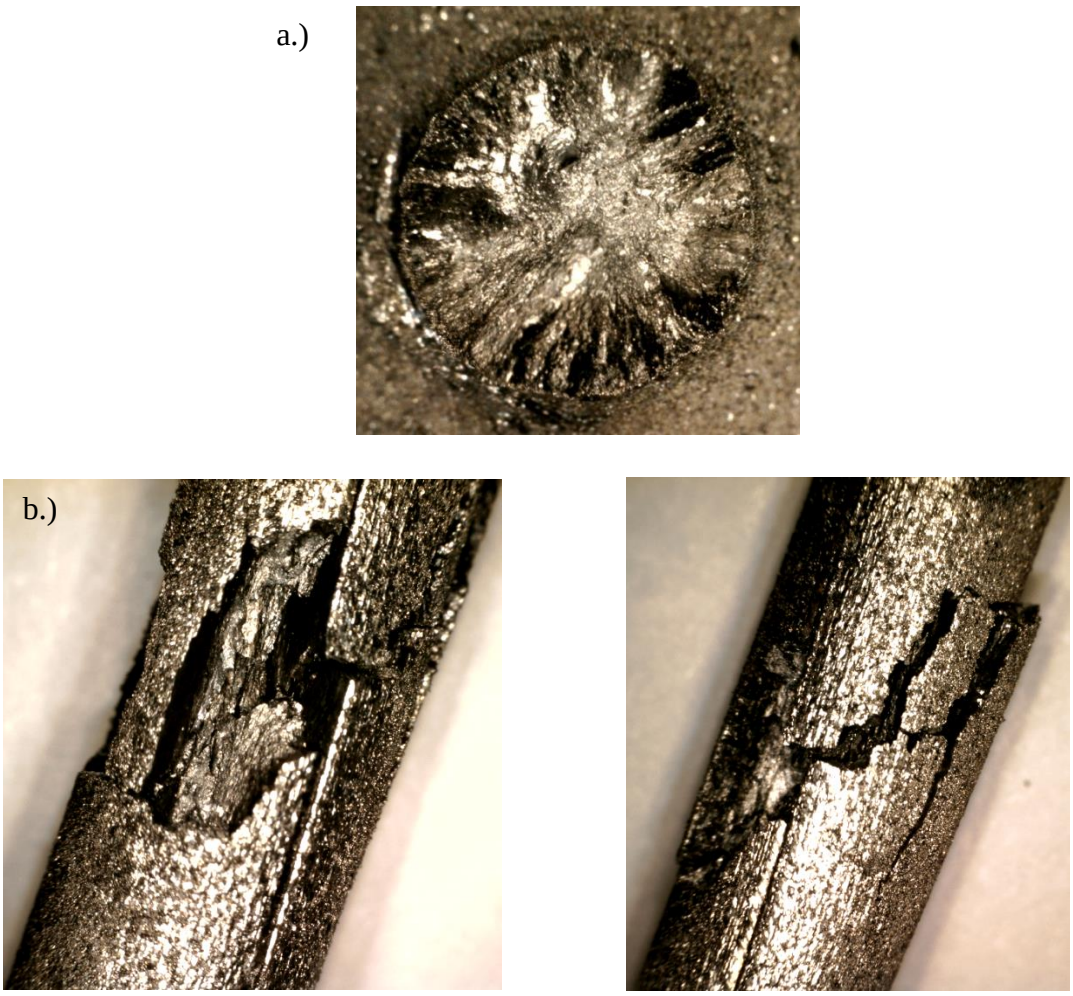

Figure 46: Fracture surfaces of sample after completely reversible (R= -1) torsional fatigue tests on conventional torsion specimens: a.) Y-orientation, b.) XY45° [Siddiqui, 2018]

Figure 47: Fracture surfaces of sample after completely reversible (R= -1) torsional fatigue tests on reduced torsion fatigue specimens: a.) X-orientation, b.) XY45° orientation, c.) Y-orientation

In order to further assess the brittle fracture surface profile of DMLS SS GP1 reduced torsion specimens, the Keyence VHX digital microscope was used to develop preliminary 3D surface profiles of the depth of cracks initiating along the exterior of the specimens, and is as depicted in Figure 48. These preliminary findings reveal considerable variation in crack depth across samples, further suggesting that under torsional fatigue conditions, “as-built” DMLS SS GP1 may be prone to sudden failure, characteristic of brittle fracture, due to the development and coalescence of these fatigue cracks.

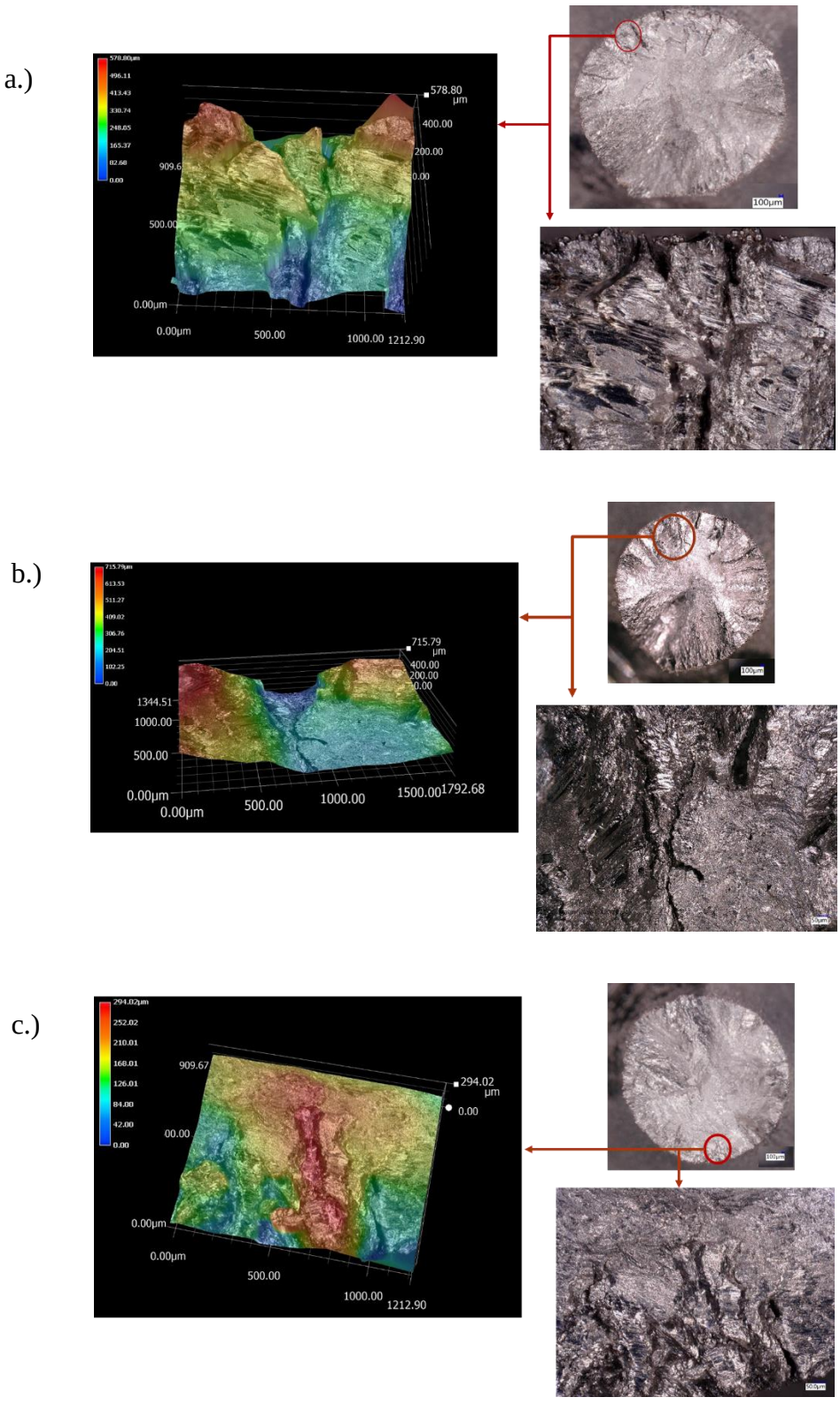

Figure 48: Preliminary 3D surface profile of crack depth in brittle fracture surface response of DMLS SS GP1 reduced torsion specimens: a.) X, b.) XY45, and c.) Y build orientations

4.8 Density and Hardness Results

SEM micrograph images of fracture surfaces presented in the previous section revealed the presence of considerable pores/voids present within these "as-built," DMLS SS GP1 specimens. To further investigate this behavior, density measurements were taken and compared with that reported by EOS for DMLS SS GP1 specimens developed using optimized processing parameters. The shank/gripping section of approximately 9 specimens, manufactured in the horizontal build plane, along the X, Y and XY45° build orientations, were sliced from the specimens. The ratio of the mass to volume of these sections was used to determine the average density. Specimen densities determined are plotted in Figure 49. The density for DMLS SS GP1 has been reported by EOS manufacturer to be 7.8g/cm^3 [EOS, 2009], with the experimental average across these specimens falling slightly below reported literature values for SS GP1, with an experimental average density of 7.71g/cm^3. Specimens 19 and 9, which were shown from fracture images to exhibit the presence of several voids, were also determined to have a specimen density considerably less than 7.8 g/cm^3, thereby further supporting the presented experimental findings.

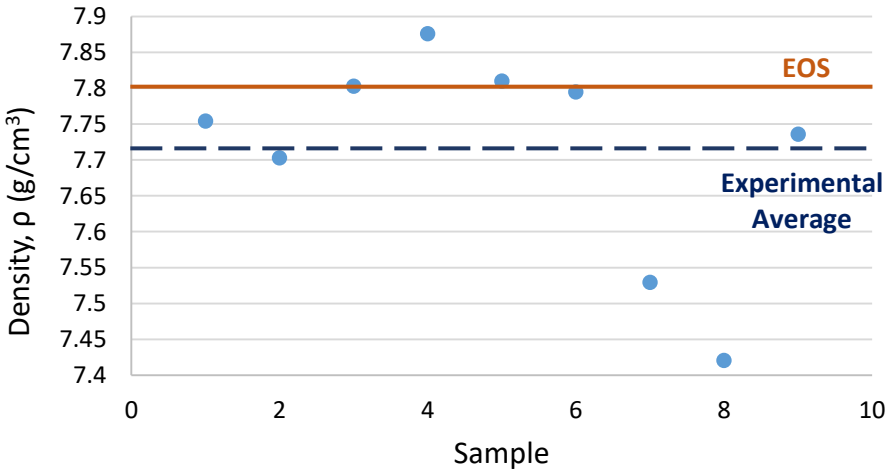

Figure 49: Density measurements of DMLS SS GP1 specimens, manufactured in the *xy* plane. Note: sample does not correspond to sample numbers within each batch

The variability in the Rockwell C hardness across DMLS SS GP1 samples manufactured in the horizontal build plane were measured, and their average is reported in Figure 50, along with the experimental average across all specimens tested. Ten measurements were taken on the as-built surface of each specimen, from which the experimental Rockwell C hardness average of 26.5 ± 0.5 HRC was determined. As evident from Figure 50 however, is the variability in hardness results across specimens tested, with most specimen hardness averages falling at or above the experimental average, and few below the experimental average. The highest hardness average was found to be 28.8 ± 2.4 HRC, and the smallest hardness average was found to be 24.2 ± 1.7 HRC. Hardness of as-built DMLS SS GP1 has been reported by EOS to be approximately 230 ± 20 HV1 (~20 to 23.5 HRC), through Vicker's hardness testing. The experimental hardness values reported in this study are comparable, but slightly higher than the range reported in literature [EOS, 2009].

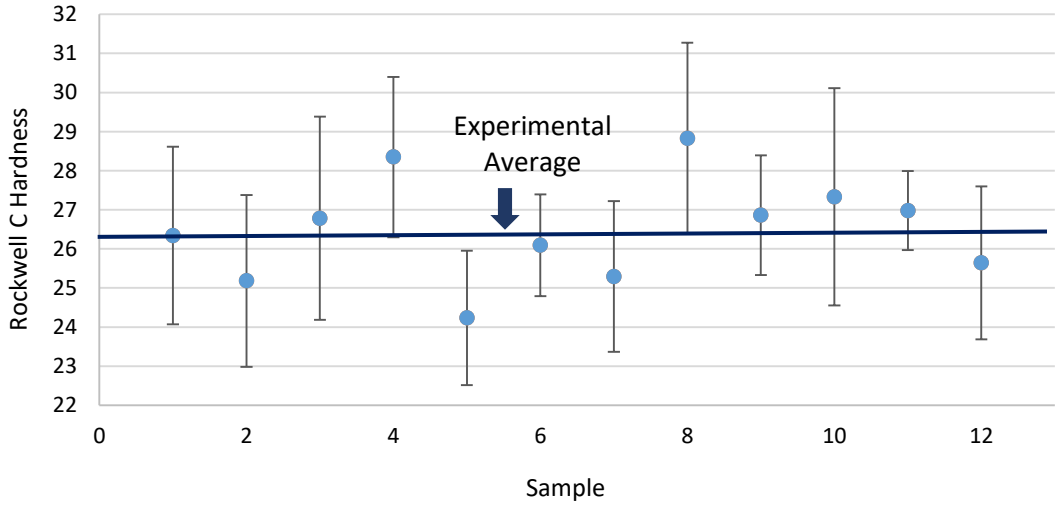

Figure 50: Rockwell C Hardness Testing of DMLS SS GP1 specimens. Note: sample does not correspond to sample batch number

CHAPTER 5: EXPERIMENTAL RESULTS AND DISCUSSION FOR DMLS INCONEL 718

To date, studies have explored both the tensile and fatigue response of additively manufactured Inconel 718, as discussed in Chapter 2. However, it is not known how these materials perform under torsional loading conditions. As Inconel 718 is commonly employed in the turbine blades of gas turbine engines used in the energy propulsion and aerospace industries, the impact of multiaxial loading conditions (i.e., uniaxial tension and shear) on the durability of these components is critical to extending the life of these engines. With additive manufacturing being considered as a replacement/addition to conventional manufacturing techniques, it is important to assess how this manufacturing technique effects overall shear performance of Inconel 718. As such, this study will explore the relation between as-built surface conditions and build orientation on the shear behavioral response of DMLS Inconel 718 under torsional fatigue loading conditions. This chapter presents the torsional monotonic and cyclic response of DMLS Inconel 718 manufactured along 6 build orientations: (100)-X, (010)-Y, (001)-Z, (110)-XY45°, (101)-XZ45° and (011)-YZ45°, as depicted in Figure 51, along with fracture responses and their correlation to build orientation.

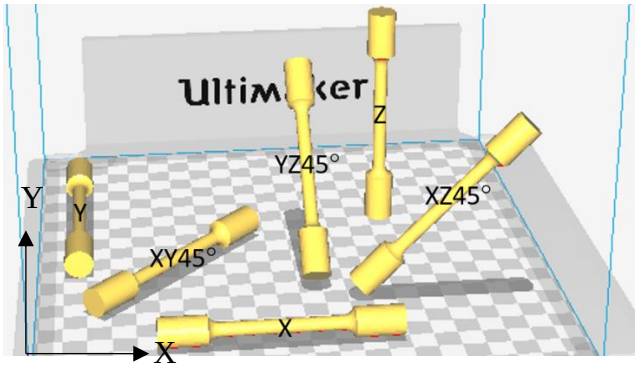

Figure 51: Layout of torsion specimens along varying build orientations for direct metal laser sintering of Inconel 718

The specimen designed for torsional testing is presented in Figure 52, in which the geometric dimensions are presented for a solid torsional test specimen, along with a 3D view of the specimen. These samples were manufactured along 6 build orientations: (100)-X, (010)-Y, (001)-Z, (110)-XY45°, (101)-XZ45° and (011)-YZ45°, through an external vendor, i3DMFG, using the EOS DMLS M290 system. Sample were built using EOS optimized standard processing parameters for Inconel 718, with minimal post-processing to maintain the as-built conditions of the test specimen. A summary of the processing parameters used for manufacturing of DMLS IN718 specimens is as presented in Table 19. The layer thickness was kept at 40µm, and support structure on the specimens were removed through electrical discharge machining (EDM).

Table 19: Summary of DMLS processing parameters used to manufacture Inconel 718

Processing Parameter	
Layer Thickness	40 µm
Gas Chamber Environment	Argon
Power	285 W
Hatch Spacing	0.11 mm
Scan Speed	960 mm/s
Average Size of Powder Particles	15 to 45 µm

For ease of specimen manufacturing and determination of shear properties in the gauge section, the sample geometry was developed with a constant gripping section and no shoulder, in contrast to the specimen design for DMLS SS GP1, presented in Chapter 3. The gripping section of the specimens developed with a support structure attached along one section of the specimen (i.e., X, Y, XY45, YZ45 and XZ45) were machined, prior to testing, to eliminate any slipping effects. Any minor machining marks in the radial section between the inner gauge and gripping sections were removed using a 330M grit sand paper.

a.)

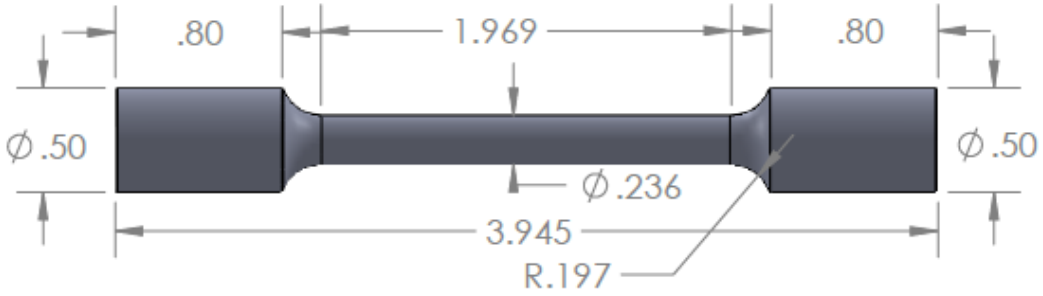

b.)

c.)

Figure 52: Design of specimen for torsion testing of Inconel 718: a.) geometric dimensions of specimen in inches, b.) test specimen (conventionally manufactured (wrought annealed) Inconel 718), c.) experimental setup of DMLS Inconel 718 within torsion test device

5.1 Torsional Fatigue Response

The cyclic response of AM Inconel 718 under shear loading conditions was assessed, and compared with findings on conventionally manufactured (wrought annealed) Inconel 718. A ½" diameter Inconel 718 rod, purchased from McMaster-Carr, was machined based upon the geometric design presented in Figure 52a, and tested using the same experimental torsional fatigue conditions applied to DMLS SS GP1 specimens, with an angle of twist cycling range of $\Delta\phi = \pm 15°$ and twisting rate of 1.654 deg/sec. An image of the conventional Inconel 718 test specimen can be seen in Figure 52b, along with the AM Inconel 718 specimens in Appendix B.

The experimental setup of the specimens is as shown in Figure 52c. Before testing, the specimen inner gauge section was sanded with a 330M grit paper in order to remove any machining marks that could lead to premature failure of the test specimen. A comparison of the first and stabilized cycles/properties obtained from torsion fatigue testing of conventionally manufactured Inconel 718 are presented in Figure 53 and Table 20 respectively. Clearly evident is the hardening behavior from the first cycle to stabilization, with a shear stress range of $\Delta\tau$ = 960 MPa at the first cycle and $\Delta\tau$=1129 MPa at stabilization. Subject to considerable shear plastic strain, the specimen fractured after approximately 1900 cycles near the radial section between the inner gauge diameter and the gripping section. The shear modulus, determined from the first cycle of G = 70 GPa, and from only the initial loading (elastic region) of the first cycle, of G = 73GPa are very close to the reported shear modulus for Inconel 718, of G=77.2 GPa [Maher]. The fracture response exhibited by conventional Inconel 718 test specimen is explored further in Section 5.3.

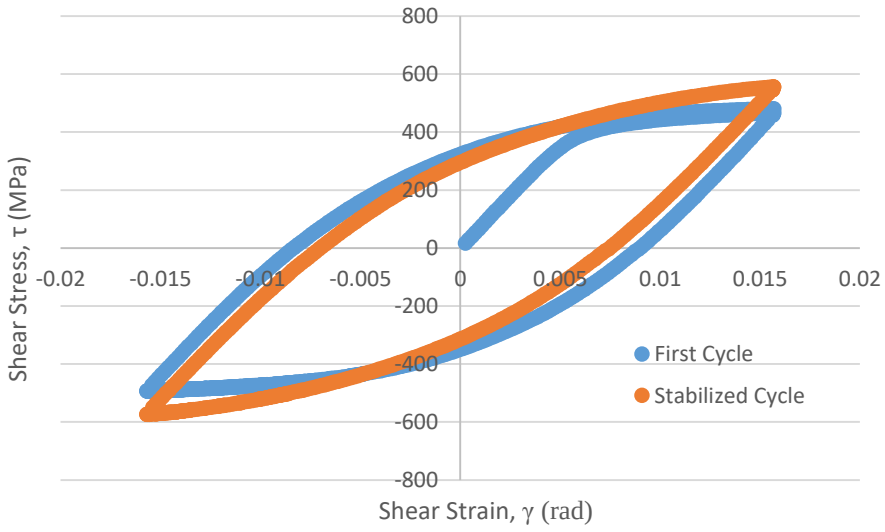

Figure 53: Comparison of first and stabilized cycles for conventionally manufactured Inconel 718

Table 20: Comparison of torsional fatigue properties from the first and stabilized cycles of conventionally manufactured Inconel 718

Cycle	Approximate Cycles to Failure	Shear Stress Range, $\Delta\tau$ (MPa)	Mean Shear Stress, τ_m (MPa)	Plastic Shear Strain Range, $\Delta\gamma_p$	Elastic Shear Strain Range, $\Delta\gamma_e$	Total Shear Strain Range, $\Delta\gamma$	Shear Modulus, G (GPa)
First	~1900	959.89	-14.14	0.0175	0.0138	0.0313	69.5
Stabilized		1129.16	-9.49	0.0145	0.0168	0.0313	67.34

DMLS Inconel 718 specimens, manufactured along each build orientation were subject to room temperature torsional fatigue tests, under the same experimental conditions as its conventionally manufactured counterpart. A comparison of the first and stabilized cycles for all 3 orientations (X, Y and Z) is as present in Figure 54, which reveals that there is a considerable reduction in the shear modulus when manufactured along the X/Y orientation, as opposed to the Z orientation. This may be attributed to the orientation of the build layers, in which twisting is occurring along the build layers for the X or Y-oriented specimen, as opposed to perpendicular to the build layers for the Z-oriented specimen. Furthermore, it is observed that the Z-oriented specimen yields a shear modulus within the same range as conventionally manufactured Inconel 718, but the X and Y-oriented specimen has a reduction of approximately 10 GPa in the shear modulus as compared with conventional Inconel 718. When comparing the shear stress range for the X and Y oriented specimen, it appears that the X-oriented specimen has a larger shear stress range than the Y-oriented specimen, although the plastic shear strain range tolerance is essentially the same for both specimens. As the variations in the torsional fatigue response of the X and Y-oriented specimens are minimal, as compared with the Z-oriented specimen, this would suggest that DMLS Inconel 718 exhibits transversely isotropic material behavior with the xy

plane, being the plane of isotropy. Future repeat experiments will be done to confirm these findings.

a.)

b.)

c.)

Figure 54: Comparison of first and stabilized cycles for DMLS Inconel 718 of varying build orientations: a.) Z-orientation, b) Y-orientation, c.) X-orientation

In order to provide a comprehensive analysis of build orientation variation on the torsional fatigue response of DMLS Inconel 718, the first and stabilized cycles from each of the 6 build orientations ((100), (010), (001), (110), (101), (011)) tested have been overlaid in Figure 55 and Figure 56 respectively. The associated torsional fatigue properties are summarized in Table 21. Most evident from both figures, is the considerably larger plastic shear strain range tolerance exhibited by conventionally manufactured Inconel 718, as opposed to additively manufactured Inconel 718. As this material is used in aerospace applications, this finding is of concern due to the need for these materials to be able to withstand high plastic shear strain. However, in terms of the shear stress range, the additively manufactured specimens yield more improved performance.

The Z-oriented specimen is found to perform similar to the torsional fatigue response exhibited by conventional IN718 and other build orientations testing for DMLS IN718. In contrast, the specimens manufactured along the diagonal orientation (45°) with respect to the build direction (z-axis), XZ45 and YZ45 build specimens, yielded the lowest shear modulus as compared with all other build orientations (X, Y and Z) as well as conventional IN718. The XZ45 and YZ45 build specimens were also observed to have the smallest shear stress range.

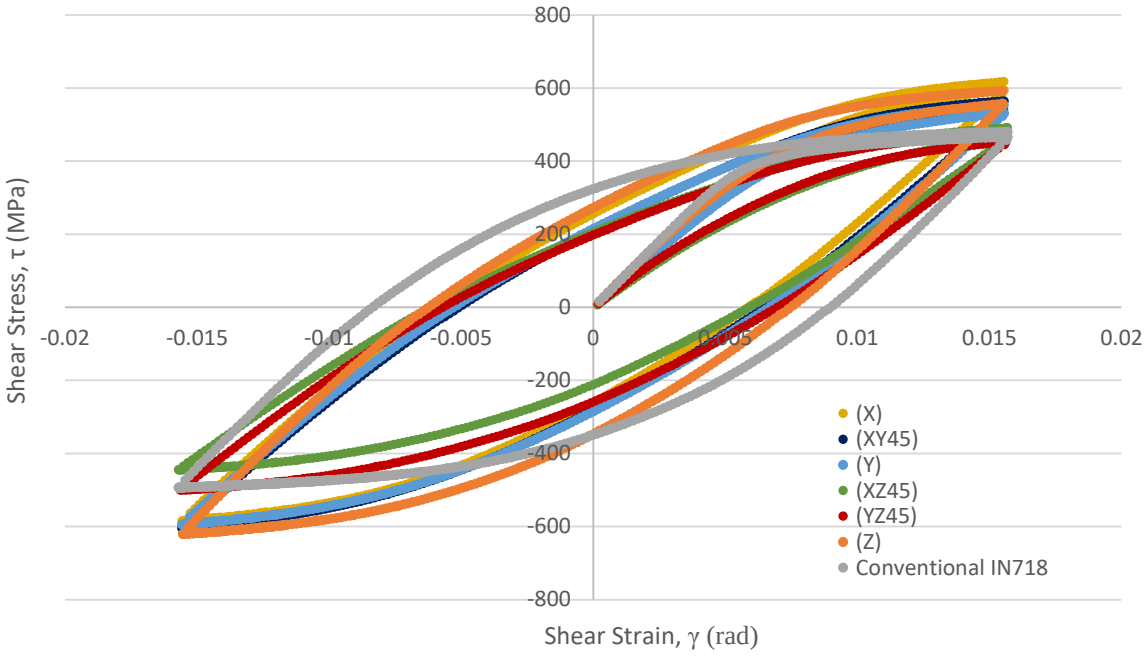

Figure 55: Comparison of first cycles for DMLS Inconel 718 of varying build orientations and conventionally manufactured Inconel 718

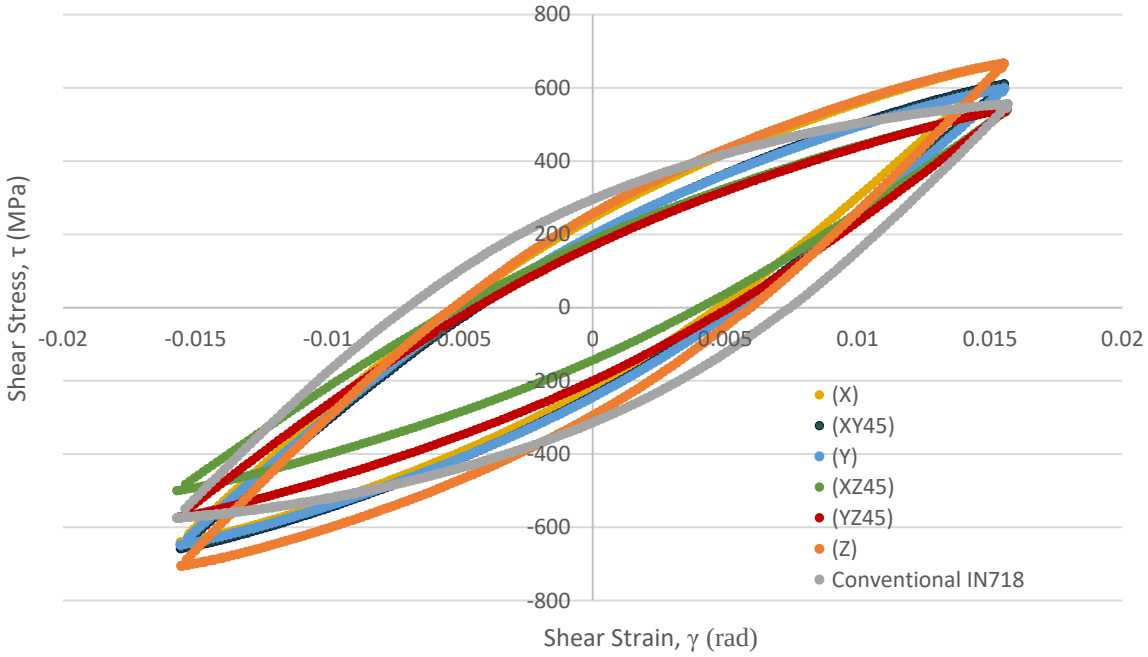

Figure 56: Comparison of stabilized cycles for DMLS Inconel 718 of varying build orientations and conventionally manufactured Inconel 718

Table 21: Comparison of torsional fatigue properties (rounded) from first and stabilized cycles of DMLS Inconel 718 with build orientation

Orientation	Cycle	Shear Stress Range, $\Delta\tau$ (MPa)	Mean Shear Stress, τ_m (MPa)	Plastic Shear Strain Range, $\Delta\gamma_p$	Elastic Shear Strain Range, $\Delta\gamma_e$	Total Shear Strain Range, $\Delta\gamma$	Shear Modulus, G (GPa)
X	First	1178.65	4.48	0.0118	0.0193	0.0311	60.98
	Stabilized	1305.38	12.77	0.0101	0.0210	0.0311	61.99
XY45	First	1147.51	-31.67	0.0116	0.0195	0.0311	58.9
	Stabilized	1268.36	-24.07	0.0096	0.0214	0.031	59.14
Y	First	1124.78	-31.86	0.012	0.019	0.0311	58.88
	Stabilized	1246.44	-24.61	0.0099	0.0211	0.031	59.11
YZ45	First	952.72	-24.23	0.0127	0.0185	0.0312	51.34
	Stabilized	1114	-15.75	0.0095	0.0217	0.0312	51.22
XZ45	First	909.29	9.33	0.01198	0.0194	0.0313	46.91
	Stabilized	1041.98	20.5	0.0093	0.0221	0.0313	47.18
Z	First	1212.7	-14.8	0.0138	0.017	0.0309	70.84
	Stabilized	1371.67	-19.5	0.0113	0.0197	0.0310	69.55

Assessment of the life behavior of these additively manufactured specimens reveals the shortest life for the Z-oriented specimen, followed by the XZ45 and YZ45 oriented specimens. These specimens were found to be exhibit a similar fracture response, with fracture initiating from internal sample defects (i.e., voids etc.). The largest life was observed for the X, Y and XY45 oriented specimens, which experienced multiple cracks at the surface along and through the build layers. The fracture response for all specimens are discussed in further detail in Section 5.3. Life for the X, Y and XY45-oriented specimens are reported based upon the number of cycles at which a crack initiates and causes a reduction of 50% or greater in the stabilized shear stress. Comparison of the shear stress history reveals that Inconel 718, whether additively manufactured or not, cyclically hardens to stabilization, and softens to fracture during completely reversible torsional fatigue test conditions.

A combination of the axial and torsional response of AM materials can provide insight into the Poisson's effect for these materials. With this consideration, Table 22 has been developed, and reports the variation in Poisson's ratio with build orientation. Young's modulus values for DMLS as-built Inconel 718 specimens have been used to provide a first-order approximation of the Poisson's ratio. The shear modulus reported for each build orientation is based on those values determined from the first cycle torsional fatigue response behavior of this material. Based upon torsional fatigue experimental findings from this study, it is suggested that as-built DMLS Inconel 718 exhibits transversely isotropic material behavior with the xy plane being the plane of isotropy. Therefore, the Poisson's ratio for these build orientations are determined based upon Equation (15), presented in Chapter 4. The average Poisson's ratio in the xy build plane is found to be $\nu = 0.343 \pm 0.027$. This is higher than that reported for wrought annealed IN718, of $\nu = 0.294$ [Maher].

Table 22: Poisson's ratio variation with build orientation for DMLS Inconel 718

Orientation	Young's Modulus, E (GPa) [EOS, 2014]	Shear Modulus, G (GPa)	Poisson's Ratio
X	160 ± 20	60.98	0.312
XY45	160 ± 20	58.9	0.358
Y	160 ± 20	58.88	0.359

5.2 Surface Roughness Analysis

In order to assess the relationship between surface roughness, build orientation and the fracture response/life behavior of as-built DMLS IN718, average and root mean square surface roughness measurements were taken using the Veeco Dektak^{3}ST surface profilometer. A slice from the outer gauge section of each specimen was taken using the low speed Isomet cutter, and used to determine the surface profile. Three measurements were taken on each as-built sample,

based upon experimental parameters discussed in Chapter 3, and are presented in Table 23. Measurements were taken towards the center of specimen to reduce edge effects on reported surface roughness values. The average surface roughness and root mean square, along with the standard deviation is reported. The experimental setup for surface profile measurements is as presented in Figure 57.

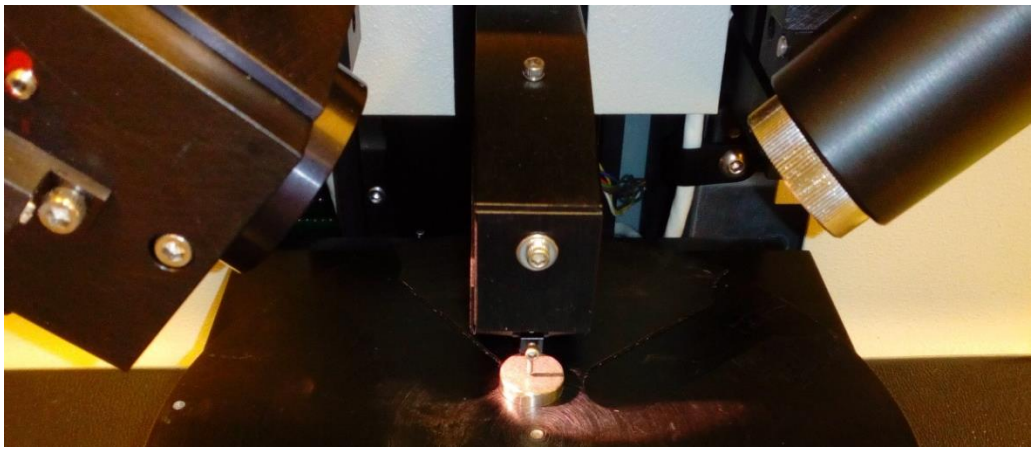

Figure 57: Experimental setup for surface roughness measurements of DMLS Inconel 718 specimens using Veeco Dektak^{3}ST surface roughness profilometer

A comparison across build orientations reveals that the Z-orientation has the lowest average and root mean square surface roughness as compared with the X and Y-oriented specimens. The surface roughness for the X/Y oriented specimens are similar to each other, although the X-oriented specimen yielded a slightly lower average surface roughness. The surface roughness found for the X/Y-oriented specimen is similar to that reported in other studies as Ra = 4 to 6 µm after shot peening [EOS, 2014]. These values support the fracture response observed for these build orientations. The X/Y oriented specimen was found to exhibit multiple cracks at the surface, which may be contributed to the high surface roughness of the as-built surface as well as the impact of the torsional loading direction being parallel to the deposition of

the powder layers. In contrast, the Z-oriented specimen had a considerably lower average surface roughness of Ra = 2.4μm, for which fatigue cracks were not observed to appear at the surface. Rather, crack initiation and propagation occurred at internal defects within the specimen.

Table 23: Surface roughness measurements for DMLS Inconel 718 of varying build orientations

Ra (μm), Rq (μm)	**(X)**	**(Y)**	**(Z)**
Measurement 1	4.789, 7.575	5.715, 7.336	2.498, 2.88
Measurement 2	4.856, 7.673	5.85, 7.519	2.532, 2.863
Measurement 3	4.949, 7.806	5.336, 6.949	2.176, 2.531
Average ± Standard Deviation	4.864 ± 0.080, 7.685 ± 0.116	5.634 ± 0.266, 7.268 ± 0.291	2.402 ± 0.196, 2.758 ± 0.197

5.3 Fracture Surface Observations

In order to assess the fracture response of additively manufactured Inconel 718 and its correlation to build orientation, fracture surface images were taken and are presented in Figure 58. Also presented is the fracture surface for the conventionally manufactured Inconel 718 sample. Torsional fatigue testing on DMLS Inconel 718 test specimen, manufactured along the Z-orientation, XZ45, YZ45, and conventional IN718 reveal a ductile fracture response. Crack initiation, propagation, indicated by rotating beach marks, representative of torsional testing and final fracture can be observed from these fracture surfaces. This is in stark contrast to the brittle fracture response observed for DMLS SS GP1/17-4PH, which would suggest that under the torsional fatigue experimental conditions tested, DMLS IN718, manufactured along the Z, XZ45, and YZ45 orientations, would not encounter sudden failure upon crack initiation, because of the

slow crack propagation rate, exhibited by the ductile fracture response. An analysis of the fracture surface for the YZ45-orientation reveals a significant crack that appears to have initiated at the surface, in addition to minor cracks evident around the perimeter of the fracture surface. The fracture surface for DMLS Inconel 718 manufactured along the X, XY45, and Y-orientations reveals multiple crack initiation/propagation between and within the powder build layers, as evident in Figure 58. This may suggest that manufacturing along the vertical orientation (Z), diagonal (XZ45) orientation, results in improved torsional fatigue fracture response as compared with manufacturing specimens along the horizontal build orientations (X,Y and XY45).

A comparison with DMLS SS GP1 reveals that upon crack initiation, rapid and sudden specimen fracture occurs, for specimens manufactured along the X, Y and XY45° build orientations, may be attributed to a strain/stress-induced austenite to martensite phase transformation. This was seen for reduced test specimens. Future work will focus on assessing the fracture response of other build orientations (YZ45°, XZ45°, Z) for DMLS SS GP1, not yet explored in this study.

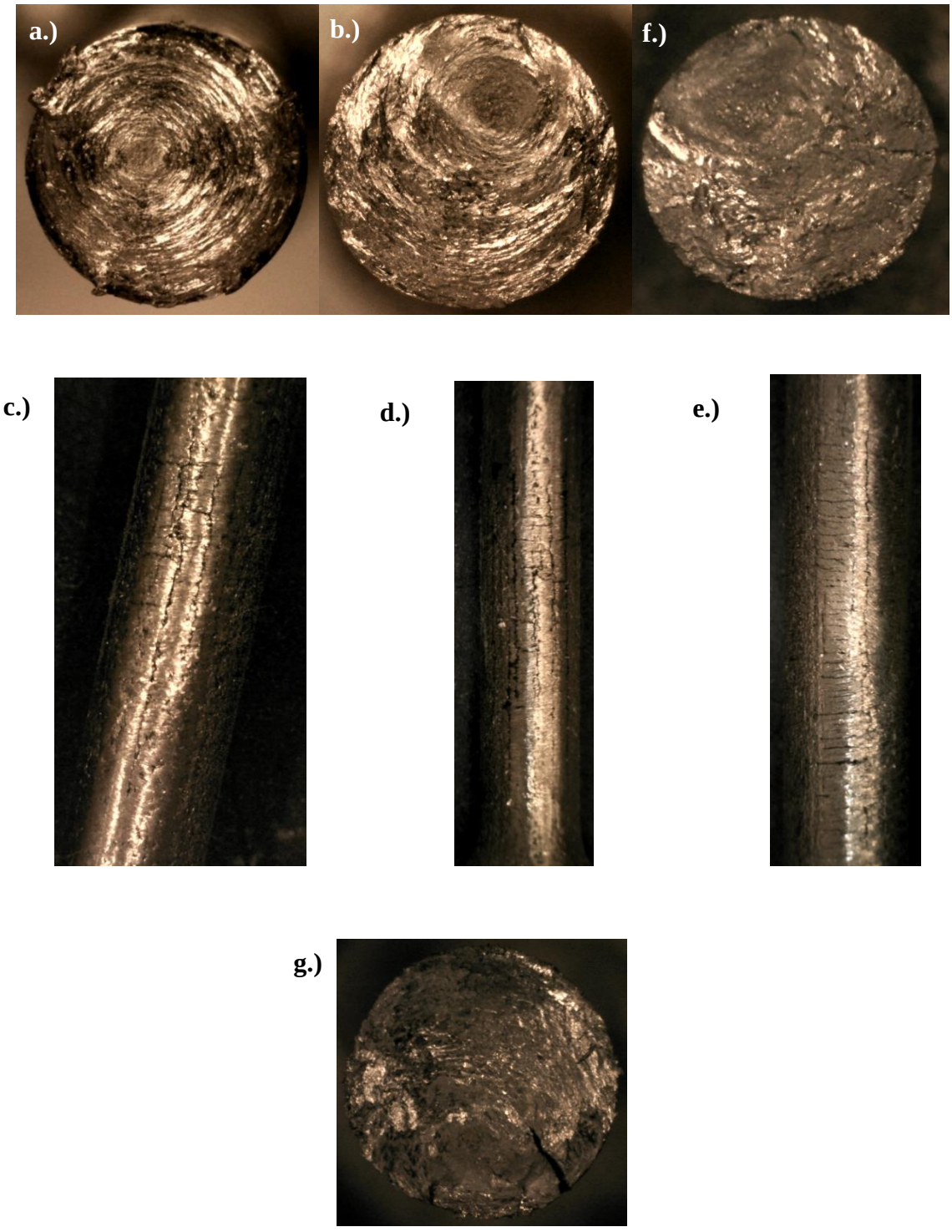

Figure 58: Fracture response of Inconel 718: a.) conventionally manufactured, b.) Z-orientation, c.) Y-orientation, d) X-orientation, e.) XY45°-orientation, f.) XZ45°-orientation, g.) YZ45°-orientation

CHAPTER 6: CONSTITUTIVE MODELING OF ANISOTROPIC BEHAVIOR[4]

With the advances in additive manufacturing and the need to completely characterize the mechanics of materials made through this technology, experimental testing can only provide limited material behavior due to the high cost associated with AM components. As such there is a need for constitutive models to be developed that both simulate experimental behavior and provide an approximation of material response. This chapter has been dedicated to assessing the monotonic and cyclic response of AM metal materials used in this study, as well the development of failure surfaces and mechanical property variation with build orientation for these materials.

6.1 Monotonic Response

6.1.1 Additively Manufactured Stainless Steel 17-4PH/GP1

DMLS SS GP1 has been shown to exhibit discontinuous yielding, with the presence of an upper and lower yield strength, followed by a long period of elongation before fracture. As such, the viability of constitutive models to fit this material behavior was examined. The Ramberg-Osgood model, as depicted in Equation (1) from Chapter 2, is commonly employed to fit a non-linear stress-strain response. Here, E is the Young's Modulus, K, represents the strain-hardening coefficient, and n, represents the strain-hardening exponent.

The model was used to provide a first approximation of the stress-strain response of DMLS SS GP1 samples manufactured along the X, Y and XY45° build orientations, all within the xy

[4] Certain figures and excerpts in Chapter 6 are from my publications: Siddiqui, S.F., Fasoro, A.A., Cole, C., & Gordon, A.P. (2017). Mechanical Characterization and Modeling of Direct Metal Laser Sintered Stainless Steel GP1. Manuscript under review in *ASME Journal of Engineering Materials and Technology;* Siddiqui, S.F., O'Nora, N., Fasoro, A.A., & Gordon, A.P. (2017). Modeling the Influence of build orientation on the monotonic and cyclic response of additively manufactured stainless steel GP1/17-4PH. In *Proceedings of the ASME 2017 International Mechanical Engineering Congress & Exposition*; Siddiqui, S.F., Fasoro, A.A., & Gordon, A.P. (2017). Selective Laser Melting (SLM) of Ni-based Superalloys - A Mechanics of Materials Review. Badiru, A.B., Valencia, V. V., & Liu, D. (Eds.*), Additive Manufacturing Handbook: Product Development for the Defense Industry*. CRC Press.

build plane. In order to determine the monotonic *K* and *n* values, a power law regression was fit between experimentally determined yield strength (i.e. lower yield strength, upper yield strength and 0.2% yield strength) and ultimate tensile strength values for each sample. The resulting Ramberg-Osgood fit to the experimental data, for samples of each build orientation is as shown in Figure 59. *K* and *n* values calculated are presented in Table 24.. However, as depicted in Figure 59, the Ramberg-Osgood model is limited in providing an accurate tensile response when applied to materials that exhibit upper and lower yield strengths. While applying the power law regression fit based upon the upper yield strength, 0.2% yield strength and the ultimate tensile strength, the Ramberg-Osgood model captures the upper yield strength and UTS response, however, it is unable to capture the lower yield strength behavior. Comparison with cyclic *K'* and *n'* from literature is in agreement with the range of monotonic *K* and *n* values determined.

Table 24: Ramberg-Osgood determined constants [Siddiqui, 2018]

	Based upon 0.2% Yield Strength		**Based upon Upper Yield Strength**		**Based upon Lower Yield Strength**		**Yadollahi et al., 2017**	
Orientation	**Strain Hardening Coefficient, *K* (MPa)**	**Strain Hardening Exponent, *n***	**Strain Hardening Coefficient, *K* (MPa)**	**Strain Hardening Exponent, *n***	**Strain Hardening Coefficient, *K* (MPa)**	**Strain Hardening Exponent, *n***	**Cyclic Strain Hardening Coefficient, *K'* (MPa)**	**Cyclic Strain Hardening Exponent, *n'***
X-Axis	1096.3	0.1027	1120.9	0.1193	1370.3	0.27	1567	0.23
Y-Axis	1260.4	0.0972	1281.4	0.108	1573.8	0.2421		
XY-45º	1152.7	0.1097	1178.4	0.1248	1383.4	0.2346		

In order to compare the monotonic and cyclic results obtained in this study, results from Yadollahi and coauthors [Yadollahi, 2017], were overlaid with results from this study, and is as shown in Figure 59c. As evident from the plot, the monotonic response representing the horizontal build orientation from [Yadollahi, 2017], follows the tensile response observed for the

orientations tested in this study. Most especially, it follows the overall tensile response exhibited by the X and XY45° oriented specimens, and the elastic region of the tensile response exhibited by the Y oriented specimen.

The cyclic response from earlier work [Yadollahi, 2017], assessed at varying strain amplitudes ranging from 0.18% to 0.5%, was also plotted in Figure 59c, along with the stabilized cyclic response at a highly plastic strain range of 1.4% (strain amplitude of 0.7%) from this study, to provide an approximate estimation of the complete cyclic response of this material, when manufactured in the horizontal build orientation. A comparison of the stabilized cyclic response for each of the 3 build orientations tested in this study (i.e. X, XY45 and Y) reveal similar cyclic responses at stabilization. When compared with the cyclic response from [Yadollahi, 2017] study, to approximate the complete cyclic response of the material, it is evident that this material cyclically hardens. It is important to point out that the fatigue specimens used in [Yadollahi, 2017] study were polished in the inner gauge section, as opposed to the current study, which assessed fatigue performance of as-built DMLS SS GP1/17-4PH. This could contribute to the lower stabilized stress value observed for the current study at a strain amplitude of 0.7%.

a.)

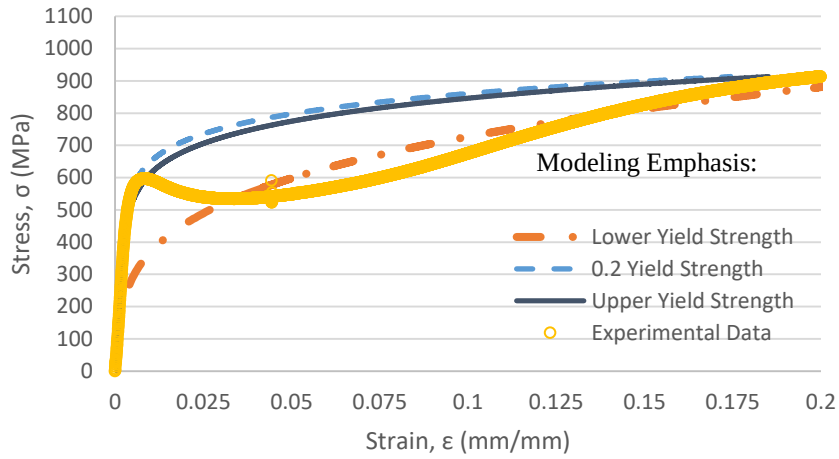

b.)

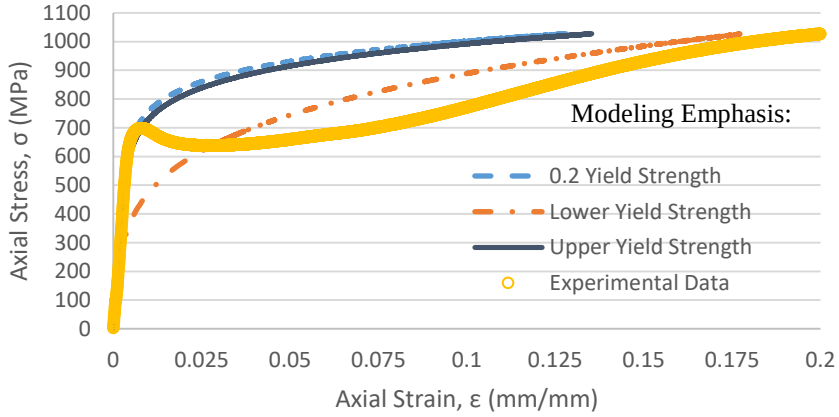

c.)

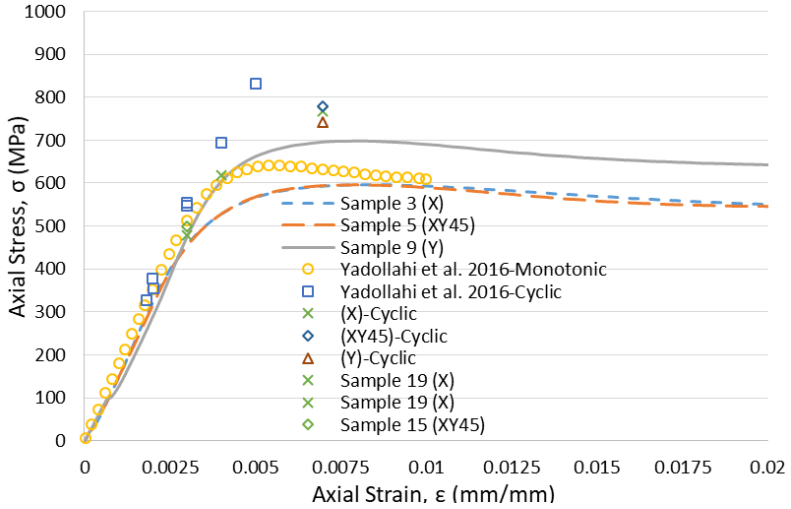

Figure 59: Ramberg-Osgood modeling of tensile response ($\dot{\varepsilon} = \mathbf{0.001}$ mm/mm/sec) of DMLS stainless steel GP1 manufactured: a.) X-orientation, b.) Y-Orientation; c.) Comparison of monotonic and cyclic response from this study and Yadollahi et al. 2016. [Siddiqui, 2018]

Since the Ramberg-Osgood model was shown in Figure 59a and Figure 59b to be limited in capturing the complete tensile response of these materials, (i.e., lower yield strength behavior), the Hahn model was applied to the test data, because it takes into consideration the presence of Lüders bands (i.e., discontinuous yielding).

The Hahns model, which is a plasticity yield-point model, determines the flow stress, σ, as a function of the macroscopic work hardening coefficient, q, plastic strain, ε_p, strain rate, $\dot{\varepsilon}$, resolved shear stress for unit velocity, τ_0, average density of unlocked dislocations, ρ_0, Burger's vector, b, fraction of dislocation density, f, dislocation density parameters, C and a, and a constant related to determining dislocation velocity, n [Hahn, 1962].

This model was applied to simulate the monotonic response of DMLS SS GP1, specifically the upper and lower yield strength phenomena. For the purpose of this study, the strain rate,$\dot{\varepsilon}$ was replaced with the plastic strain rate, $\dot{\varepsilon_{pl}}$ which was determined by assessing the rate of change in the plastic strain for each monotonic tension test. Initial parameters used for fitting the experimental data was referenced from [Hahn, 1962] for mild steel, and optimized to achieve best first-order fit to the monotonic response. The optimized parameters used for fitting the tensile stress-stress curve up to 0.2mm/mm plastic strain, for each build orientation, X, Y and XY45° is as presented in Table 25.

A flow chart depicting the optimization routine in Matlab and associated derived fits given in Figure 61, is as shown in Figure 60. The experimental stress-strain data for the (X), (Y) and (XY45°) oriented specimens were imported and plotted in Matlab through the curve fitting

toolbox. Initial conditions and ranges for Hahn parameters were set based upon reported values in [Hahn, 1962], before running the curve fitting toolbox. Initial parameters used for fitting the experimental data was initially referenced from [Hahn, 1962] for mild steel, and optimized, by trial and error to achieve a relatively good fit to the experimental data. These parameters were then optimized using Matlab's Curve Fitting Toolbox, specifically the Nonlinear Least Squares method and Trust-Region algorithm, to achieve better first-order fits to the monotonic response, after setting the tolerance to $1e^{-06}$ and the number of iterations at 400, conventional standards set in Matlab. To ease the process of optimization, Hahn's 8 constants were simplified to 7 constants, in which *b*, the Burger's vector and *f*, the fraction of dislocation density, were combined. The fraction of dislocation density, *f*, was maintained constant, at 10^{-1}.

As the primary interest was modeling the upper and lower yield strength of this material, the simulated and experimental stress versus plastic strain curve for each build orientation was plotted up to 0.2mm/mm plastic strain, as shown in Figure 61. A comparison of the upper and lower yield strengths between the simulated and experimental findings is presented in Figure 62, in order to assess the durability of the model. As is evident from Figure 62, the model provides a good approximation to the experimental findings, with a variation in values ranging between 6 to 23 MPa. As the experimental upper and lower yield strengths for this material, manufactured in the *xy* plane, are shown by EOS to vary by ± 50MPa, the model fits the experimental results well. Here, it can be seen that the Hahn's model provides a reasonably good fit to the experimental data, as opposed to Figure 59, which depicts the limitation of the Ramberg-Osgood model in capturing this upper/lower yield strength phenomena.

Table 25: Yield point plasticity model (Hahn's) optimized constants [Siddiqui, 2018]

Orientation	Resolved Shear Stress for Unit Velocity, τ_0 (MPa)	Macroscopic Work Hardening Coefficient, q (MPa)	Burger'sVector, b (mm^{-1})	Fraction of Dislocation Density, f	Average density of unlocked dislocations, ρ_0	Dislocation Density Parameter, C (mm^{-2})	Dislocation Density Parameter, a	Constant, n
X-Axis	152.4	3266	3×10^{-7}	10^{-1}	160.9	4.7×10^{5}	1.5	9
Y-Axis	163	3700	2.808×10^{-7}	10^{-1}	255	4.7×10^{5}	1.5	7
XY-45°	124	3813	3×10^{-7}	10^{-1}	288.8	4.7×10^{5}	1.5	6

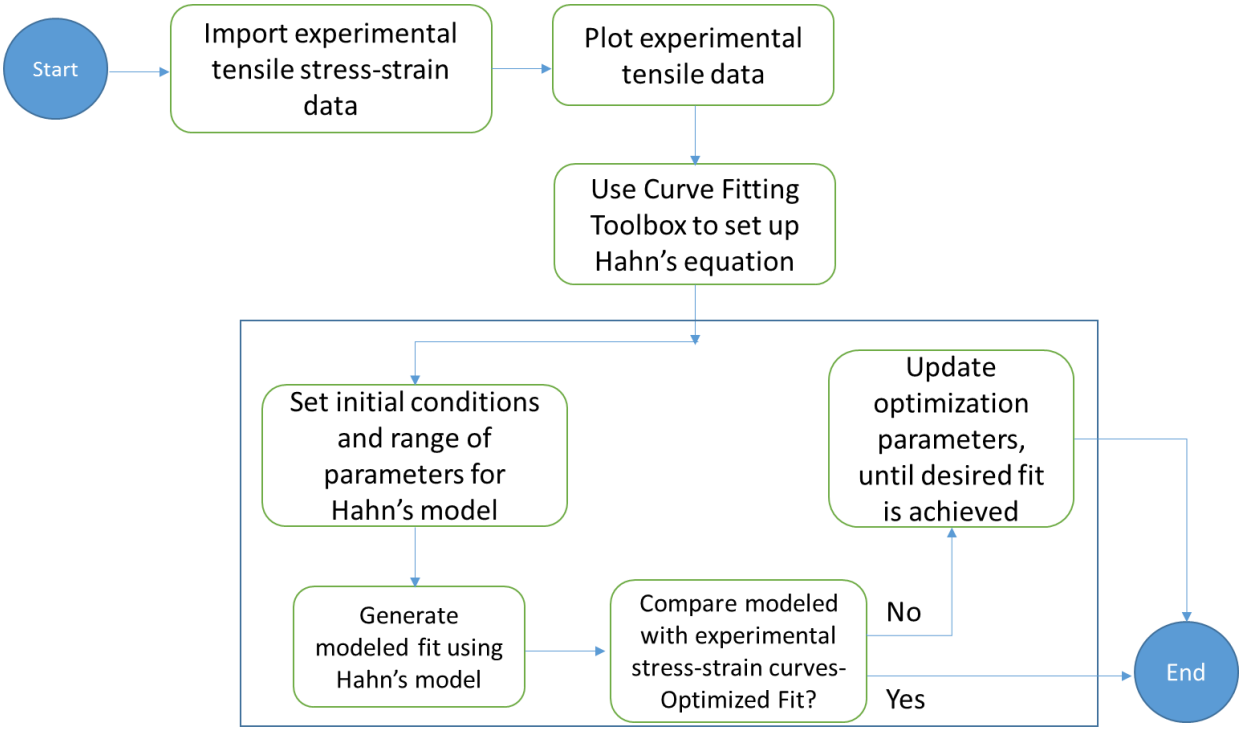

Figure 60: Flow chart of optimization for Hahn constants [Siddiqui, 2018]

As evident in Figure 61, the Hahn plasticity model serves as a relatively good fit to predict the monotonic response exhibited by DMLS SS GP1 along the orientations tested. Unlike the Ramberg-Osgood model, it serves to capture the upper and lower yielding phenomena exhibited by this material. To further analyze the role of key parameters used in the

optimization/fitting routine, the optimized monotonic response of the Y-oriented specimen (i.e., sample 9) was used. Figure 63 through Figure 66 present both the optimized Hahn model response to the experimental data in addition to the impact of increasing or decreasing the associated Hahn parameters. The impact of the macroscopic work hardening coefficient, q, has been assessed in Figure 63, which can be seen to affect the fitting of the lower yield strength and the tail response between the lower yield strength and ε=0.2 of the fitting routine. An increase in q results in the Hahn model over-predicting the lower yield strength/tail response, while a decrease in q results in the Hahn model under-predicting the lower yield strength/tail response.

Figure 64 has explored the role of the resolved shear stress at unit velocity, τ, in predicting the monotonic response exhibited by DMLS SS GP1. It is clearly evident that the value of τ directly affects the entire monotonic response, resulting in an upward shift of the model with an increase in τ, and a downward shift of the model with a decrease in τ.

The value of the material constant, n, in affecting the resulting fit of the model is explored in Figure 65. Here, it can be seen that n directly affects the fitting of the upper yield strength. An increase in n results in a downward shift of the model, thereby under-predicting the upper yield strength; whereas a decrease in n results in an upward shift of the model, thereby over-predicting the upper yield strength response.

Finally, Figure 66, assesses the role of the average density of unlocked dislocations, ρ_0, on the fitted monotonic response. It is evident that ρ_0 contributes to fitting of the upper and lower yield strength, with larger impact seen on fitting of the upper yield strength. A large increase in

ρ_0 results in a slight under-prediction of the upper and lower yield strengths, however a small decrease in ρ_0 is found to cause an over-prediction of the upper yield strength. This small decrease in ρ_0, however, is not found to significantly impact the fit to the lower yield strength. The role of material constants, C and a, in affecting the fitted response has not been assessed, but kept constant.

a.)

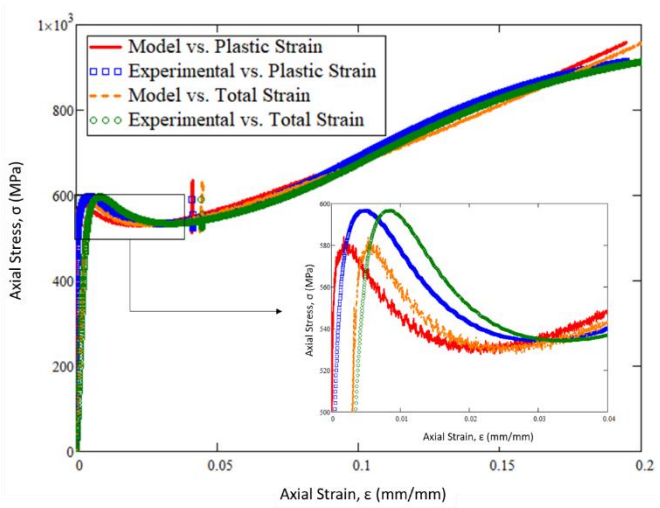

b.)

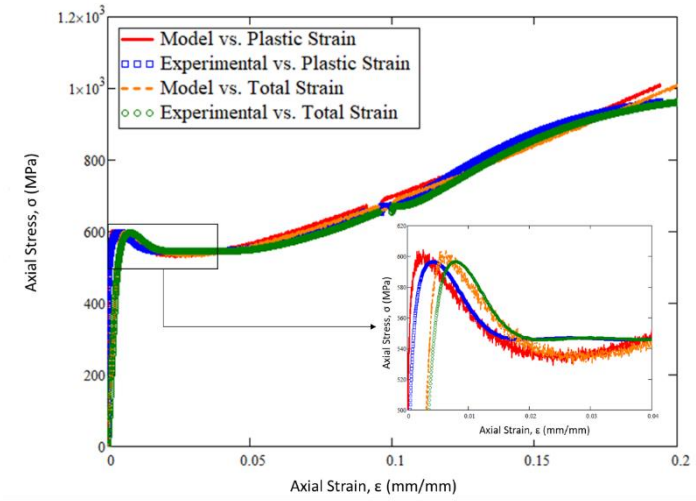

c.)

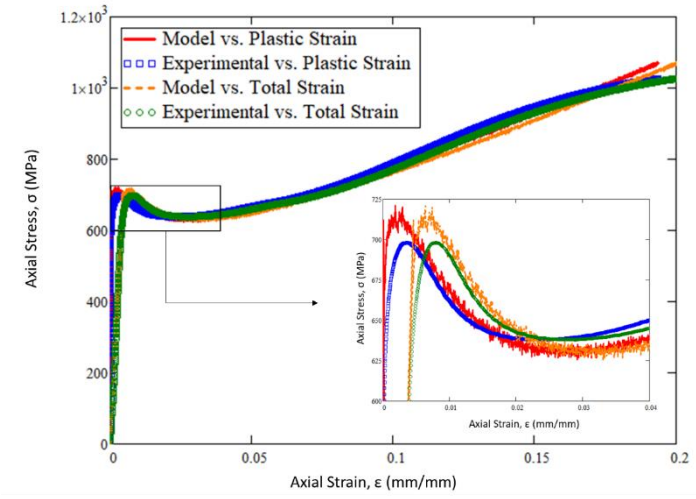

Figure 61: Hahn modeling of tensile response of DMLS stainless steel GP1 manufactured along varying build orientations in the xy build plane for stress versus plastic strain and stress versus total strain: a.) Sample 3 (X), b.) Sample 5 (XY45), c.) Sample 9 (Y) [Siddiqui, 2018]

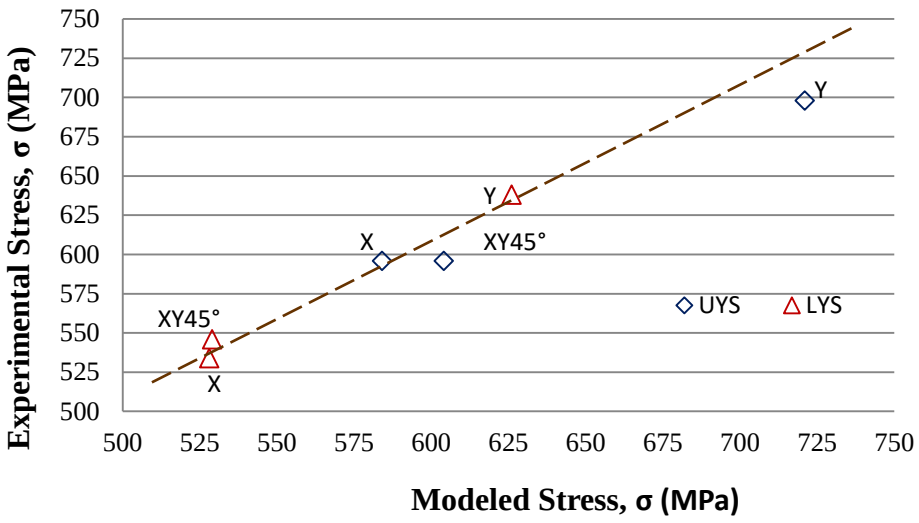

Figure 62: Comparison of actual (experimental) to predicted (modeled) stress (UYS-upper yield strength, LYS-lower yield strength) using the Hahn model, for samples manufactured along the (X), (Y) and (XY45) orientations [Siddiqui, 2018].

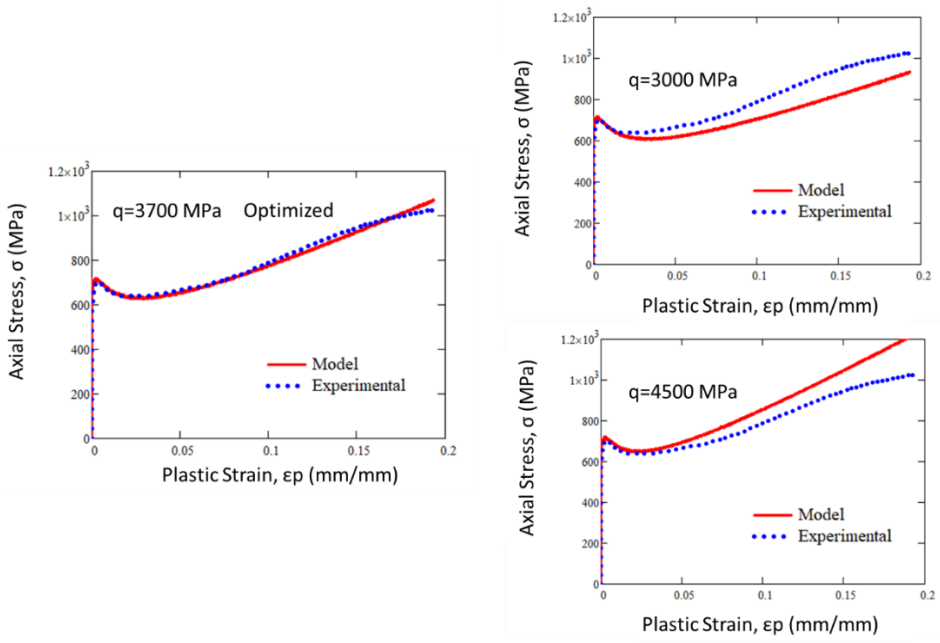

Figure 63: Analysis of macroscopic work hardening coefficient, *q*, on modeling the tensile response of sample 9 (Y)

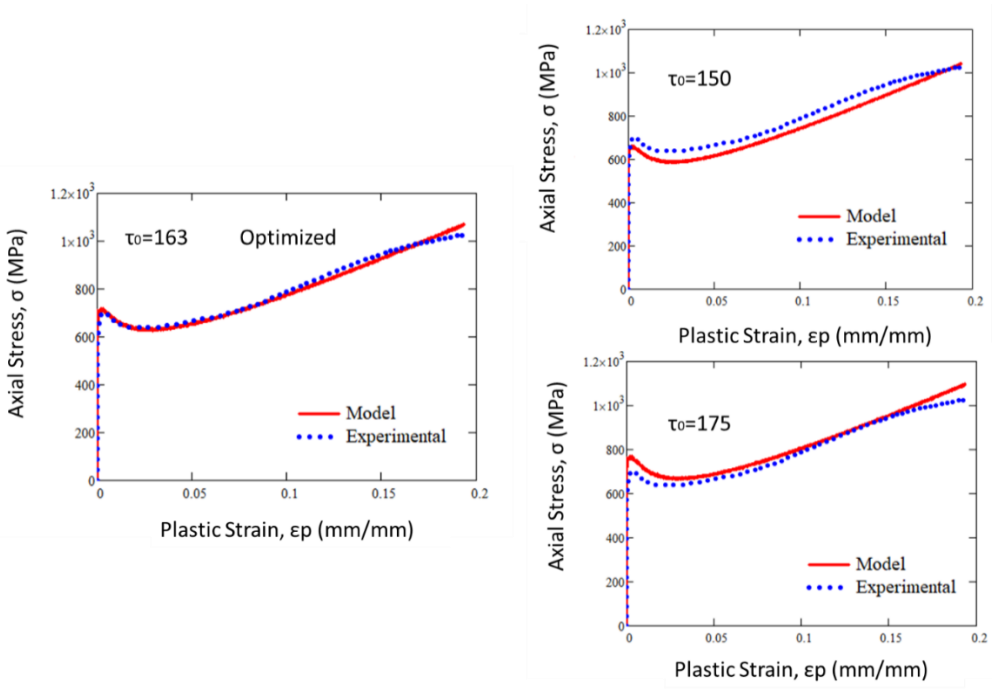

Figure 64: Analysis of resolved shear stress, *τ*, on modeling the tensile response of sample 9 (Y)

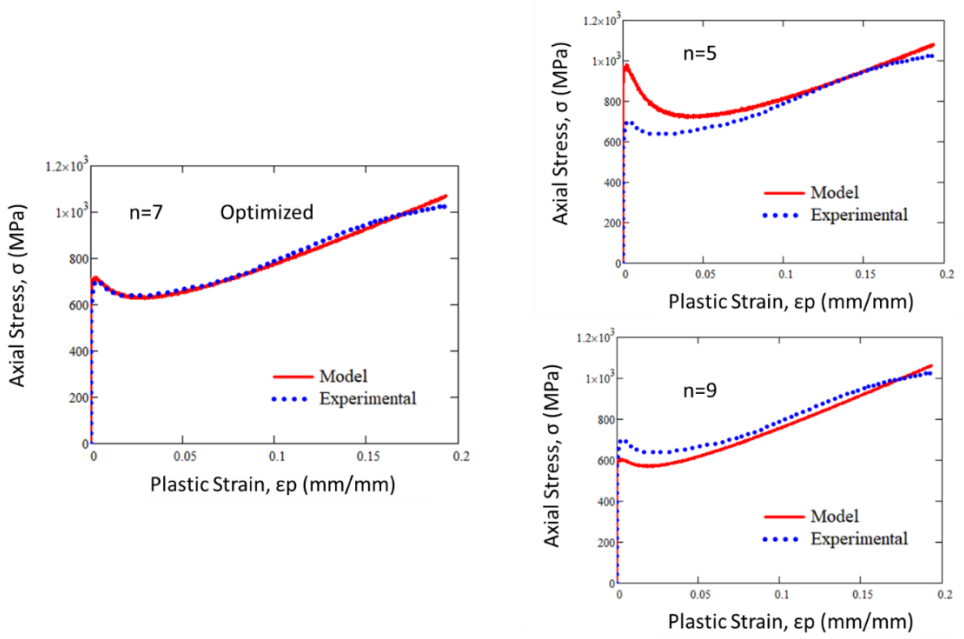

Figure 65: Analysis of constant, *n*, on modeling the tensile response of sample 9 (Y)

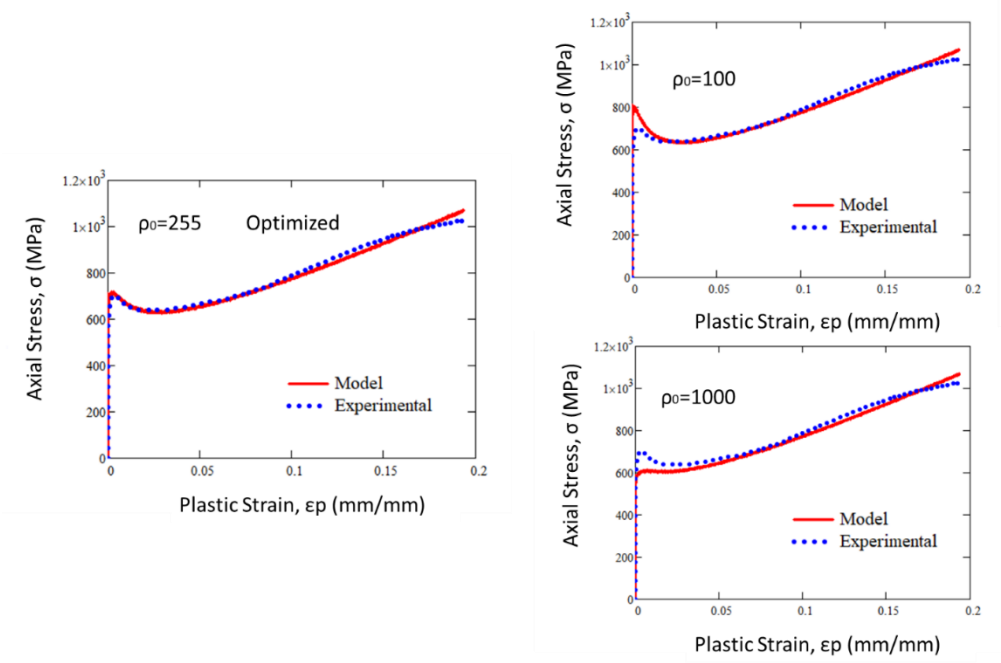

Figure 66: Analysis of average density of unlocked dislocations, ρ_0, on modeling the tensile response of sample 9 (Y)

6.1.2 Additively Manufactured Inconel 718

There have been considerable studies on additively manufactured Inconel 718. A summary of these results can be found in the tables presented in Chapter 2. These results have been used in constitutively modeling the presented results.

First order approximations of fatigue response from basic tensile properties of DMLS IN718 provided by the EOS Manufacturer were calculated using the power law regression in Equation (2) from Chapter 2. Table 26 presents a summary of these tensile properties including Young's Modulus (E), 0.2% Yield Strength (Y.S.), Tensile Strength (U.T.S.), and Elongation % as given by the manufacturer for horizontally built samples (XY) and vertically built samples (Z), since AM materials exhibit anisotropic behavior. The calculated monotonic fatigue constants

(Strain Hardening Coefficient: K, Strain Hardening Exponent: n) are also presented for horizontal and vertically built samples respectively, through use of the Ramberg-Osgood model.

The AM build direction has been shown to affect the tensile properties of "as-built" components. In order to determine its effect on the monotonic response of IN718, a first order approximation of 'K' and 'n' was obtained from basic tensile properties on SLM IN718 built in varying orientations, from a study by [Chlebus, 2015]. Table 27 present the tensile properties in the following orientations, presented in Miller Indices, (001), (010), (011) and (111), in addition to calculated monotonic fatigue constants 'K' and 'n' values. A comparison of "as-built" SLM and DMLS IN718 from these two sources, has shown an increase in the strain hardening coefficient 'K' for specimens manufactured perpendicular to the build direction as opposed to parallel to the build direction. The strength coefficient 'K' for samples oriented 45° from the build direction has been shown to be in between 'K' obtained parallel and perpendicular to the build direction. There is minimal variation in the strain hardening exponent 'n' for (001), (010) and (011) orientations regardless of whether the sample was "heat-treated" or not. This is not the case for (111) orientation, whose 'n' is significantly different than that calculated for (001), (010) and (011) orientations.

Table 26: Experimental tensile data for DMLS IN718 provided by EOS manufacturer & calculated Ramberg-Osgood strain hardening coefficient and exponent

Reference	Orientation	E (GPa)	0.2% Y.S. (MPa)	UTS (MPa)	EL%	K (MPa) Calculated	n Calculated
EOS (IN718)	Vertical Direction (Z)	-	634 ± 50	980 ± 50	31 ± 5	1084.3	0.0864
EOS (IN718)	Horizontal Direction (XY)	160 ± 20	780 ± 50	1060 ± 50	27 ± 5	1150.4	0.0625

Table 27: Experimental tensile data for SLM IN718 “as-built” from Chlebus et al. 2015 & calculated Ramberg-Osgood strain hardening coefficient and exponent [Chlebus, 2015]

Orientation	E (GPa)	0.2 % Y.S. (MPa)	UTS (MPa)	EL%	K (MPa) Calculated	n Calculated
(001)	162 ± 18	572 ± 44	904 ± 22	19 ± 4	1068.2	0.1005
(010)	193 ± 24	643 ± 63	991 ± 62	13 ± 6	1224.3	0.1036
(011)	200 ± 23	590 ± 15	954 ± 10	20 ± 1	1128.5	0.1043
(111)	208 ± 48	723 ± 55	1117 ± 45	16 ± 3	1339.9	0.0993

Table 28: Experimental tensile data for SLM IN718 “heat-treated” from Chlebus et al. 2015 & calculated Ramberg-Osgood strain hardening coefficient and exponent [Chlebus, 2015]

Orientation	E (GPa)	0.2 % Y.S. (MPa)	UTS (MPa)	EL%	K (MPa) Calculated	n Calculated
(001)	163 ± 30	1074 ± 42	1320 ± 6	19 ± 2	1423.1	0.0453
(010)	199 ± 15	1159 ± 32	1377 ± 66	8 ± 6	1549.5	0.0467
(011)	188 ± 19	1152 ± 24	1371 ± 5	15 ± 5	1480	0.0403
(111)	209 ± 44	1241 ± 68	1457 ± 55	14 ± 5	1569.3	0.0378

6.2 Cyclic Response

6.2.1 Additively Manufactured Stainless Steel 17-4PH/GP1

For conventionally manufactured materials, tensile-fatigue relations can be used to predict the hardening/softening response of a material. The ratio of the ultimate tensile strength (UTS) to the yield strength (YS), determined through tension testing, can provide insight into this material behavior, without the need for fatigue testing, consequently leading to time and cost savings. In order to assess the viability of these relationships to the hardening/softening response of an additively manufactured materials, experimentally determined tension data for DMLS SS GP1 tested in this study were used. The ratio of the UTS to the YS can predict whether a material will cyclically harden or soften. If this ratio is greater than 1.4, the material will cyclically harden. If this ratio is less than 1.2, the material will cyclically soften. As this material was unique, in that it exhibited discontinuous yielding (i.e. upper and lower yield strength), the ratio of the UTS to each of these yield strengths was determined and presented in Table 29.

Table 29: Tensile-fatigue relations used to assess cyclic behavior from tensile data, by analysis of ratios of UTS to lower and upper yield strengths [Siddiqui, 2018]

Orientation	$\frac{S_{UTS}}{\sigma_{yL}}$	$\frac{S_{UTS}}{\sigma_{yU}}$	$\frac{S_{UTS}}{\sigma_{y0.2}}$
X-Axis	1.79	1.6	1.65
Y-Axis	1.7	1.55	1.576
XY-45º	1.799	1.64	1.684

Ratios for all build orientations tested were greater than 1.4, suggesting that the material cyclic hardens. When compared with stress histories presented in Chapter 4 of this study, subject to LCF conditions, it was found that DMLS SS GP1 does cyclically harden to stabilization, followed by softening to fracture. As such, these tensile-fatigue relations have successfully

predicted the initial cyclic hardening response exhibited by this additively manufactured material. Further studies can be used to support this finding.

In addition to the fatigue testing experimental results presented in Chapter 4 of this study, the cyclic behavior of specimens subject to low cycle fatigue testing at a strain range of $\Delta\varepsilon$ =1.4% and pulsating tension fatigue tests at a strain range of $\Delta\varepsilon$ = 0.7% were modeled through application of the Chaboche model. Specifications regarding the Chaboche model were presented in Chapter 2. First and stabilized cycle fits, and the associated optimized Chaboche constants used to obtain these fits are as presented later on in this section. The model was developed in Matlab and is comprised of 2 parts, a Chaboche stress calculation routine and the Matlab fitting routine respectively. The elastic modulus and proportional limit for specimens of each build orientation were inputted into the program. The elastic modulus was determined by taking the stress range for the first and stabilized cycle and dividing it by the elastic strain range for those cycles respectively. The 0.01% offset yield stress was chosen for use in the model because, since it acts as the proportional limit, whereas the 0.2% yield stress typically reported for materials has too much plasticity to allow the model to accurately replicate the material behavior.

Initial estimates for kinematic hardening constants were obtained from plots of the plastic strain vs. the amount of hardening the material has experienced in the early, middle, and later plastic portions of the initial quarter cycle for the first, second, and third kinematic hardening terms respectively. Once initial values for all the parameters were obtained, they were run through a numerical optimization process and fit to the initial cycles. The isotropic hardening takes a large amount of plasticity to have a significant effect, so the effect on the first cycle is

negligible. As a result, it was disregarded for this study, and isotropic hardening terms were held at zero.

The resulting Chaboche constants from the numerical optimization of the first cycle and stabilized cycle fits of LCF tests, can be seen in Table 30, and comparisons of the data with the model are presented in Figure 67 and Figure 68. For a first approach, the Chaboche model, while considering isotropic conditions, has served to be a relatively good fit to the experimental data for both the first cycle and stabilized cycle analyses for all build orientations. Improvements in achieving better fits for the peak and valley stresses will be explored in future studies. This has been the first approach to model the cyclic plastic response for DMLS SS GP1, at a significant plastic strain range of 1.4%, and can be used as a first approximation of the material response, with future studies focused on developing a viscoplasticity model that considers the anisotropic material response exhibited by these additively manufactured materials.

Table 30: Chaboche model constants for first and stabilized cycle modeling for varying build orientations [Siddiqui, 2017]

Chaboche Model Constants	(X)-Oriented DMLS SS GP1 Sample		(XY45º)-Oriented DMLS SS GP1 Sample		(Y)-Oriented DMLS SS GP1 Sample	
	First Cycle	Stabilized Cycle	First Cycle	Stabilized Cycle	First Cycle	Stabilized Cycle
k (MPa)	396	97	423	82	443	75
E (MPa)	164571	145316.9	167002.3	139590.6	159170.9	137517.6
a1	10376.4	2629.954	20875.45	338151.1	11120.94	348104.8
C1 (MPa)	1.16E-09	1.88E-02	8.12E-08	3.16E-02	5.67E-09	7.87E-02
a2	1435.41	1155.161	1013.972	1471.332	1101.274	1617.143
C2 (MPa)	151992	848456.1	78427.7	1051637	55808.58	1148033
a3	3.73E-13	1.00E+00	3.42E+00	1.15E+00	8.44E-2	1.15E+00
C3 (MPa)	23822.8	7.58E-10	23829	1.27E-10	28681.57	2.98E-10
Z ($MPaS^{1/n}$)	16.479	80.10113	21.96	204.3426	11.18	207.7998
n	10	10	10	10	10	10

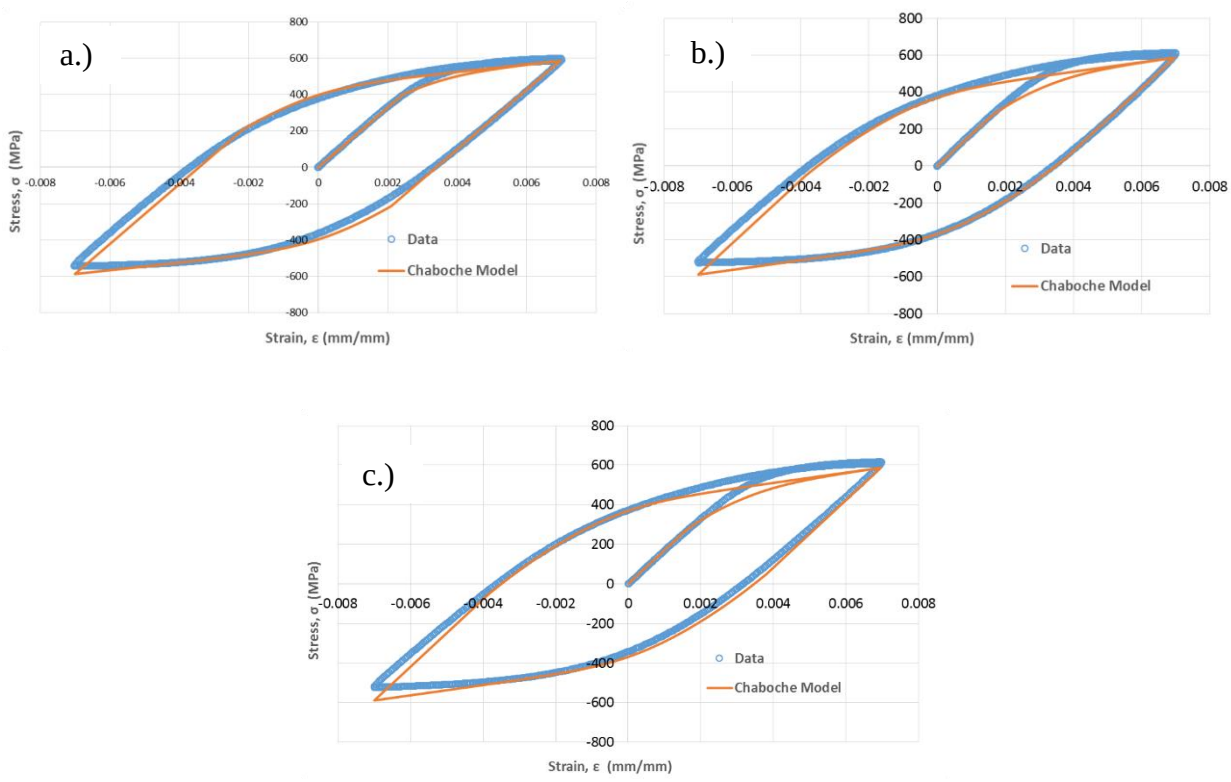

Figure 67: First cycle Chaboche modeling of, a.) sample 1 manufactured at -5° from x-axis in xy build plane, b.) sample 6 manufactured at 45° in xy build plane, c.) sample 8 manufactured at -5° from y-axis in xy build plane [Siddiqui, 2017]

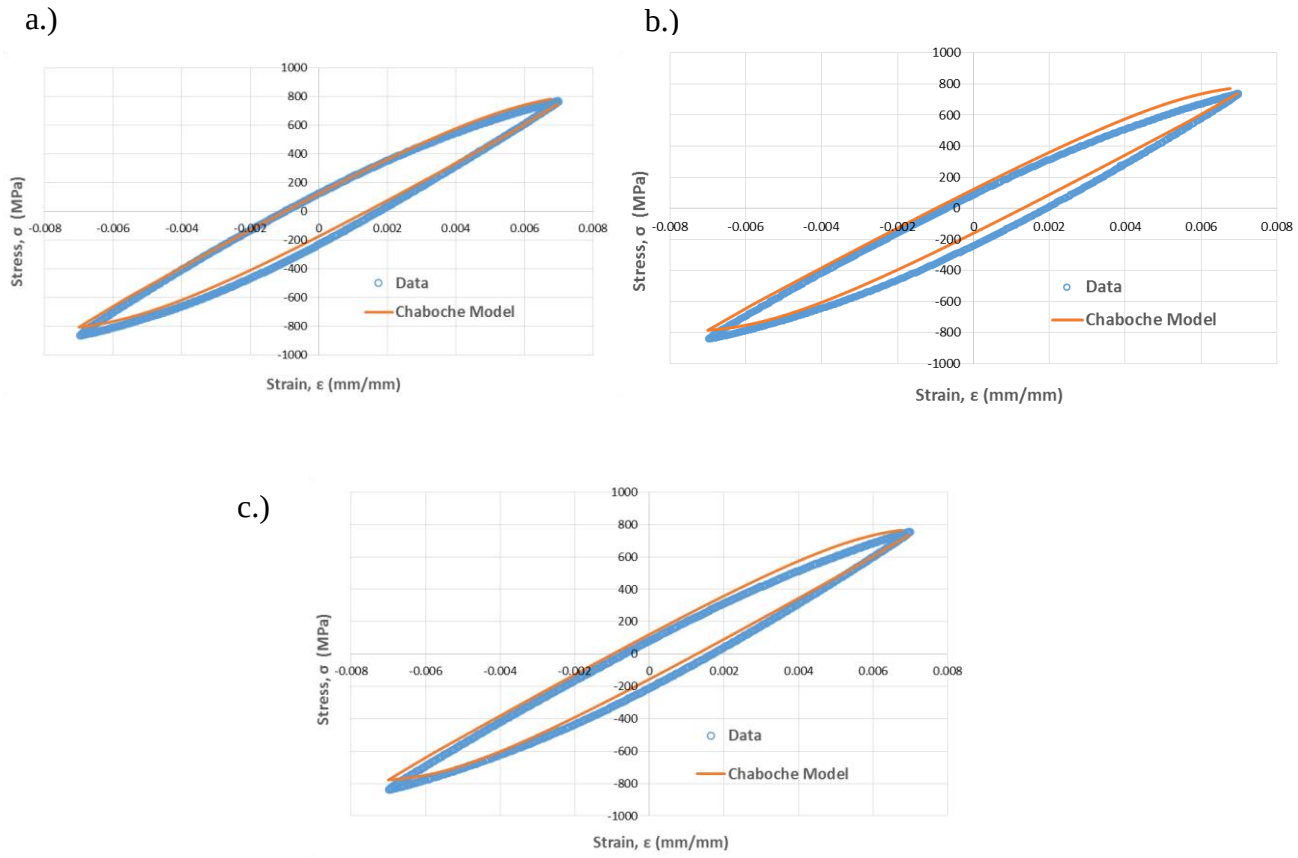

Figure 68: Stabilized cycle Chaboche modeling of, a.) sample 1 manufactured at -5° from x-axis in xy build plane, b.) sample 6 manufactured at 45° in xy build plane, c.) sample 8 manufactured at -5° from y-axis in xy build plane [Siddiqui, 2017]

To explore the effectiveness of the Chaboche model further, it was applied to model the cyclic response of DMLS SS GP1, when subject to pulsating tension fatigue conditions at a strain range of $\Delta\varepsilon = 0.7\%$. Presented in Figure 69 are the fits for the first and stabilized cycle hysteresis response for DMLS SS GP1, manufactured along the (X) and (XY45°) build orientations. This includes results from testing specimens with conventional geometry and reduced geometry. The experimental data and the Chaboche model fitted data are shown, in which it can be seen that the Chaboche model is a relatively good fit to the experimental data.

Slight variations in the model fitting response to the experimental data is most profound, after the elastic linear loading region. A comparison of the optimized Chaboche constants for each build orientation is presented in Table 30. As seen with LCF Chaboche modeling, only kinematic hardening aspects are considered, with isotropic hardening constants (i.e., Q and b) kept at zero.

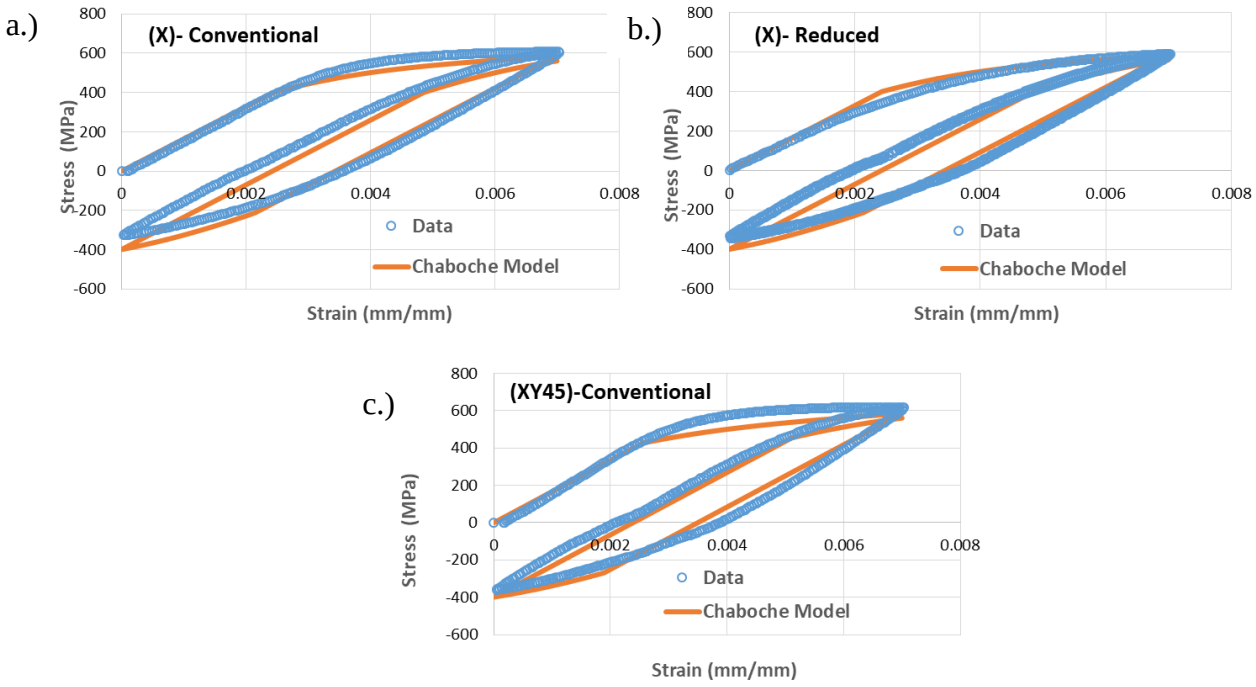

Figure 69: First cycle Chaboche modeling of pulsating tension fatigue data: a.) sample 20, conventional test specimen, manufactured at -5° from x-axis in *xy* build plane, b.) sample 1, reduced test specimen, manufactured at -5° from x-axis in *xy* build plane, c.) sample 14, conventional test specimen, manufactured at 45° in *xy* build plane

6.3 Yield Surfaces

6.3.1 Additively Manufactured Stainless Steel 17-4PH/GP1

Modeling of the failure surfaces can provide insight into the variation in mechanical properties (i.e., lower yield strength, upper yield strength, and ultimate tensile strength) with build orientation in the *xy* plane. In order to assess this behavior for the current study, Hill's

theory was used to develop the failure surfaces presented in Figure 70. Experimentally determined lower yield strength, upper yield strength, and ultimate tensile strength values are plotted for each build orientation tested, as circles, squares and triangle data points respectively. For the purpose of modeling, samples oriented at -5° from the *x*-axis and *y*-axis, were considered to be along the *x*-axis and *y*-axis. The modeled surface for each mechanical property (i.e., lower yield strength, upper yield strength and ultimate tensile strength) is depicted as a dashed/solid line on the polar plot.

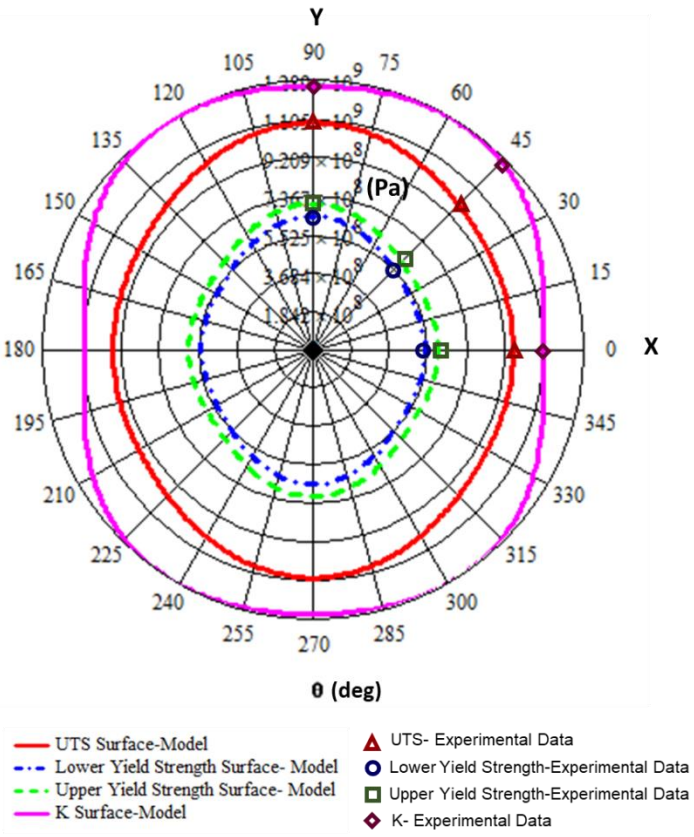

Figure 70: Comparison of failure surfaces for ultimate tensile strength (UTS), lower yield strength, upper yield strength and strength coefficient, K, modeled based on experimental data for as-built DMLS SS GP1 manufactured at varying build orientations in xy build plane [Siddiqui, 2017]

Strength ratios can be used to provide an assessment of the level of variation in mechanical properties for samples manufactured along different build orientations. Experimental tensile properties, presented in Chapter 4, were used to determine strength ratios. For ease of modeling, these tensile properties were rounded. A comparison of the strength ratios for the upper yield strength, lower yield strength and ultimate tensile strength surfaces is presented in Table 31. As these strength ratios were normalized with respect to the *x*-orientation, the strength ratios for R_{xx} for all surfaces is 1. A comparison of the strength ratios, R_{yy} and R_{zz}, when normalized with respect to *x*-orientation, suggests that there is a greater variation in the mechanical strength values when manufacturing this material along the *y*-orientation versus along the *z*-orientation.

Table 31: Strength ratios and Hill's constants determined for failure surface modeling of DMLS SS GP1 [Siddiqui, 2017]

Strength Ratios & Hill's Constants	Upper Yield Strength Surface	Lower Yield Strength Surface	Ultimate Tensile Strength Surface	Strength Coefficient
R_{xx}	1	1	1	1
R_{yy}	1.169	1.195	1.136	1.15
R_{zz}	1.055	1.067	1.004	1.117
F	0.315	0.289	0.383	0.279
G	0.583	0.589	0.608	0.522
H	0.417	0.411	0.392	0.478
N	1.0145	1.024	1.139	1.64

The Hill's constants determined for each failure surface development (i.e., upper yield strength, lower yield strength and ultimate tensile strength) is given in Table 31. As the shear strength in the *xy*-plane was not known, the value for Hill's constant *N* was determined such that the strength value at the 45° build orientation was similar to the experimentally determined strength (i.e., upper yield strength, lower yield strength and ultimate tensile strength) values for DMLS SS GP1 manufactured at 45° in the *xy* build plane.

An analysis of the failure surface for the upper yield strength, depicted by the dashed line, shows that manufacturing along the *x*-axis and 45° in the *xy* build plane does not show a change in upper yield strength. There is also a significant increase in the upper yield strength observed for sample manufactured along the *y*-axis, and for build orientations between 45° in the xy build plane and the y-axis. Also evident, is a slight decrease, followed by an increase in the upper yield strength for build orientations between 0° from the *x*-axis and 45° in the *xy* build plane. This transition is found to occur at 0.55 radians (~31.51°).

An analysis of the failure surface for the lower yield strength, depicted by the dotted-dashed line, also reveals a slight decrease, followed by an increase in the lower yield strength for build orientations between 0° from the *x*-axis and 45° in the *xy* build plane. However, there is a range of build orientations, 0.42 to 0.47 radians, (~24 to 27°) for which the lower yield strength remains the same, based upon the model, before increasing to ~546 MPa at 45° in the xy build plane. This is followed by an increase in the lower yield strength to 638MPa, 90° from the x-axis. This behavior can be attributed to the ~100MPa increase in lower yield strength value observed for the sample manufactured along the *y*-orientation.

An analysis of the failure surface for the ultimate tensile strength, depicted by the solid line, reveals that the UTS varies from ~956 MPa to ~1086MPa from building along the x-orientation versus the y-orientation. Unlike the failure surfaces for the upper and lower yield strength, which appear in a diamond shape, the failure surface for the ultimate tensile strength appears to exhibit more of an elliptical shape. Furthermore, the level of variation in UTS between the x-oriented versus y-oriented sample is greater, ~130MPa. There is an increase in the ultimate tensile

strength for build orientations 45° in the xy build plane and 90° from the x-axis. A slight decrease in UTS is observed up to 0.33 radians (~18.9°), followed by an increase in UTS up to a build orientation of 90° from the x-axis.

The development of these failure surfaces using Hill's theory has allowed for an understanding of how mechanical properties for "as-built" DMLS SS GP1 vary within the xy build plane, while allowing researchers to predict the yielding behavior of this material for build orientations not experimentally tested. Future work will focus on further validating these yield surface, by experimentally testing at intermediary build orientations not explored in this study.

6.3.2 Additively Manufactured Inconel 718

The tensile response is widely reported for additively manufactured Inconel 718, yet no study has applied these mechanical properties towards the development of failure surfaces for this material under a variety of service conditions (i.e., impact of temperature on failure surface, variation in tension and compression on failure surfaces, comparison between as-built and heat-treated AM Inconel 718 surfaces as a function of build orientation, etc.). To further explore the impact of these conditions on the resulting failure surfaces, Hill's failure theory was employed for surface development for manufacturing DMLS/SLM Inconel 718 along the horizontal to the vertical build orientation: Hill's failure theory. This theory, along with the Tsai-Wu theory were introduced in Chapter 2, and have both been used toward the development of failure surfaces for AM Inconel 718. Both theories are used to develop failure surfaces for materials that exhibit anisotropic material behavior, which is well understood to be the response exhibited by AM materials. In addition, certain studies have presented tensile and compressive findings of AM

IN718 that suggest that this material exhibits slight tensile-compressive asymmetry [Smith, 2016; Ghorbanpour, 2017], while others have not presented this finding.

With these considerations, both failure theories were employed in simulating the failure surfaces of DMLS/SLM Inconel 718. As the accuracy of these modeled failure surfaces is dependent upon reported experimental data, a thorough literature review on reported tensile/compressive mechanical properties for AM Inconel 718, manufactured along the horizontal (x,y), vertical (z), and diagonal (45°) build orientations were used to simulate the respective surfaces. These surfaces were designed as 2D models in MathCAD from the build direction (z) to the build plane (x,y), and are presented along with associated constants (Hill's) determined based upon experimentally reported data. Failure surface development through application of Tsai-Wu theory will be pursued in the future work.

It has been clearly exhibited through literature that additively manufactured components exhibit anisotropic behavior, however it is not clearly understood whether these materials exhibit orthotropic or transversely isotropic behavior. Few studies have suggested one or the other as describing the material behavior. A thorough understanding of the mechanics of these materials, with respect to the build direction (z), can provide this needed material behavior. For this analysis, it was assumed that DMLS/SLM IN718 behaves transversely isotropic, with the build platform 'xy' as the plane of isotropy. This suggests that minimal variation in mechanical properties exist for samples built in the xy plane. This assumption was used for simulating the failure surfaces, since most reported literature characterizes manufacturing in the xy plane as the "horizontal" build orientation, and does not disclose an orientation used to manufacture along this build plane. Further, based upon this study's experimental findings, when subjecting DMLS

Inconel 718 to torsional fatigue test conditions, a transversely isotropic material response has been determined for this material, with the *xy* plane being the isotropic plane.

The slight tensile-compressive asymmetry exhibited by DMLS IN718 has been reported [Smith, 2016; Ghorbanpour, 2017] for specimens manufactured along the horizontal, vertical, and diagonal build orientations. This experimental data was used to simulate yield surfaces using both Hill's failure theory. Although Hill's failure theory assumes the same yielding in tension and compression, because of the slight variation in tensile and compressive findings reported in these publications, Hill's model was used to simulate a first approximation of the failure response exhibited by DMLS IN718 in tension and compression. The failure surfaces are presented in Figure 71, in which the solid red surface represents the yielding surface in tension, and the dashed blue surface represents the yield surface in compression. Experimental data provided along each build orientation is plotted as data points, superimposed on the model surface (i.e., red squares for tensile properties and blue circles for compressive properties). Both surfaces are oblong, however it is clearly evident that the failure surface in compression is slightly larger than the failure surface in tension. This variation is greatest along the diagonal (45°) build orientation, and smallest when manufacturing along the build direction (z).

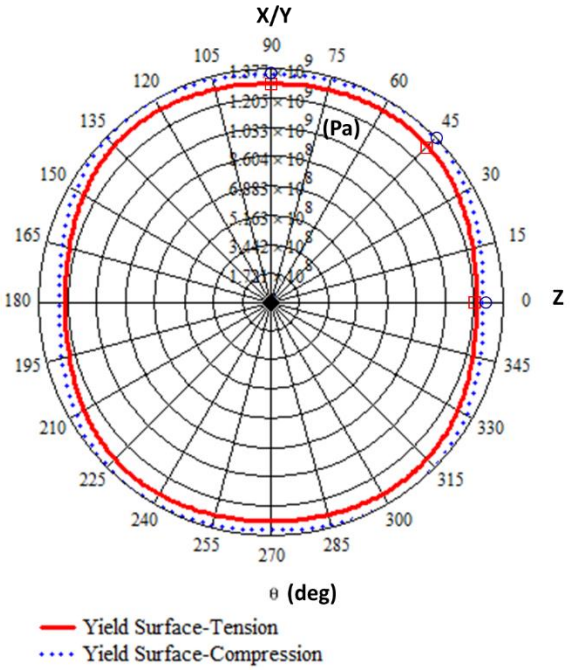

Figure 71: Yield surfaces in the X/Y-Z plane for DMLS Inconel 718 in tension and compression, developed using Hill's theory. Experimental data from D.H. Smith et al., 2016 was used to simulate yield surfaces and are represented as points (squares, and circles) on the plots.

The role of temperature on the mechanical response of AM IN718 manufactured along varying build orientations is also of importance, because of the introduction of phases at this temperature which can contribute to a deterioration in the mechanical properties. This behavior has been explored by Trosch et al., 2016, which reported the tensile properties for SLM Inconel 718, captured at room temperature, 450°C and 650°C. As this study did not explore tensile-compressive response exhibited by SLM IN718 at these temperatures, it was assumed that the yielding response in tension and compression is symmetric for the purpose of failure surface development using Hill's theory. The failure surface for the 0.2% yield strength and ultimate tensile strength developed using Hill's theory is presented in Figure 72. The solid red surface represents the modeled surface at 650°C, the dotted blue surface represents the modeled surface

at 450°C, and the dashed green surface represents the modeled surface at room temperature. The experimental data reported in Trosch et al., 2016 is represented as points (red squares, blue circles and green triangles) on the failure surfaces, at the respective build orientations. It can be seen that an increase in temperature results in a smaller failure surface, and consequently a deterioration in mechanical properties with temperature. For the UTS failure surface, it is also evident that an increase in temperature results in a shape change in the failure surface from circular to oblong. This is not as evident with the yielding failure surface.

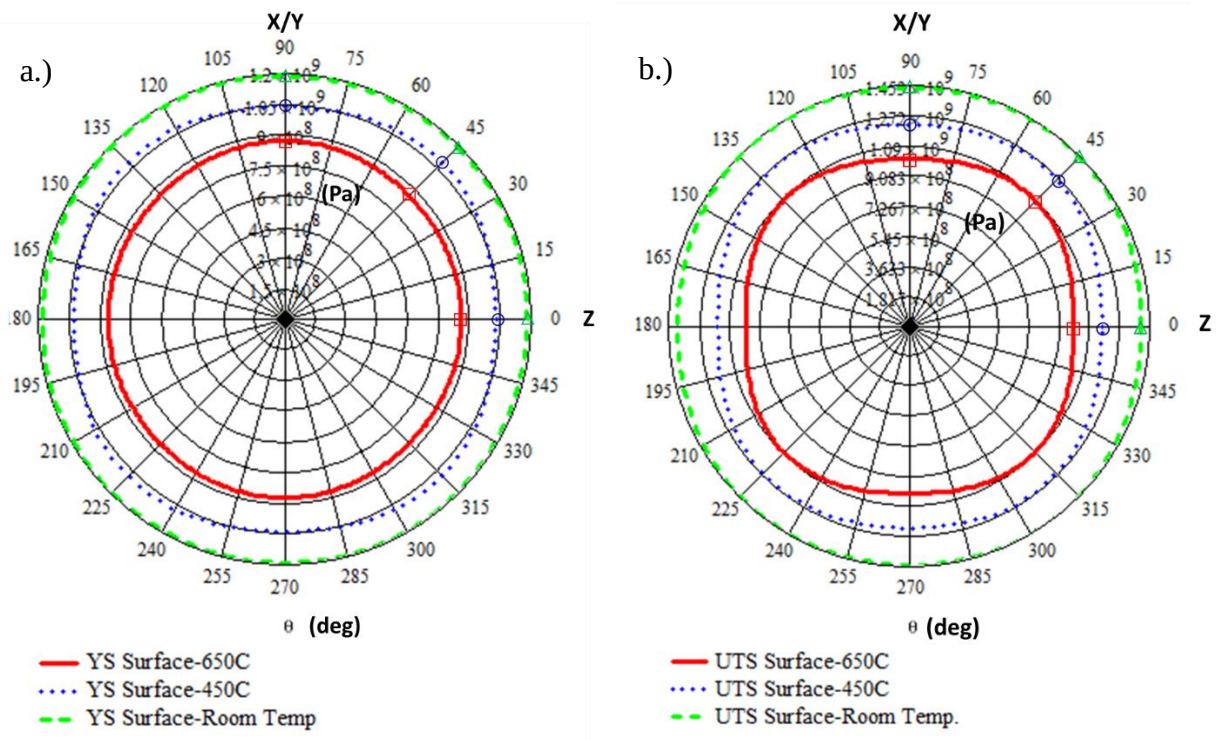

Figure 72: Failure surfaces in the X/Y-Z plane a.) yield surface and b.) ultimate tensile strength surface of SLM IN718 at varying temperatures, developed through Hill's theory. Experimental data from Trosch et al., 2016 was used to simulate yield surfaces and are represented as points (squares, circles, and triangles) on the plots.

Post-processing in the form of heat treatment also impacts the resulting failure response of AM materials. As a study by Chlebus et al., 2015 was found to not only assess multiple build orientations and the impact of heat treatment on SLM IN718, this study was used for failure surface development using Hill's theory. The Tsai-Wu model was not employed for surface modeling, because this study did not report compressive findings, needed for Tsai-Wu failure surface development. Through application of Hill's theory, simplified for conditions of plane stress in the *yz* plane, the failure surface in *yz* plane has been plotted in Figure 73 and Figure 74 for 0.2% yield strength, ultimate tensile strength, and strain hardening coefficient for SLM IN718 "As-Built" and "Heat-Treated." Results for "As-Built" SLM IN718 are depicted by solid red line and results for "Heat-Treated" SLM IN718 are depicted by the dashed blue line. It is important to note that 0° represents the build/z-direction and 90° represents the y-direction. Clearly depicted is that "Heat-Treated" SLM IN718 has a greater region before failure occurs as opposed to "As-Built" SLM IN718 which has a smaller failure surface. Also evident is that 0.2%YS, UTS and K are smallest along the build/z-direction and largest along the y-direction, in addition to the variation in surface shape. For 0.2% YS, UTS, and K, the failure surfaces are essentially oblong.

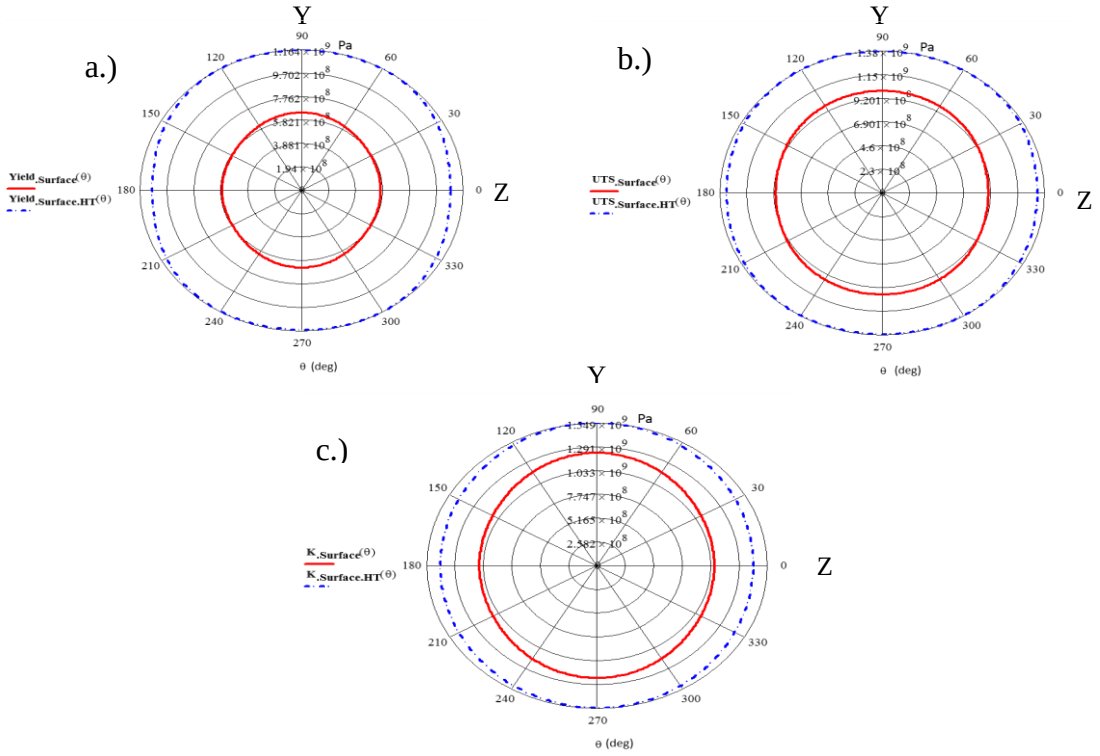

Figure 73: Yield Surfaces for "as-built" and "heat-treated" SLM IN718 developed through Hill's theory: a.) 0.2% yield strength surface b.) ultimate tensile strength surface c.) Ramberg-Osgood strain hardening coefficient 'K' surface

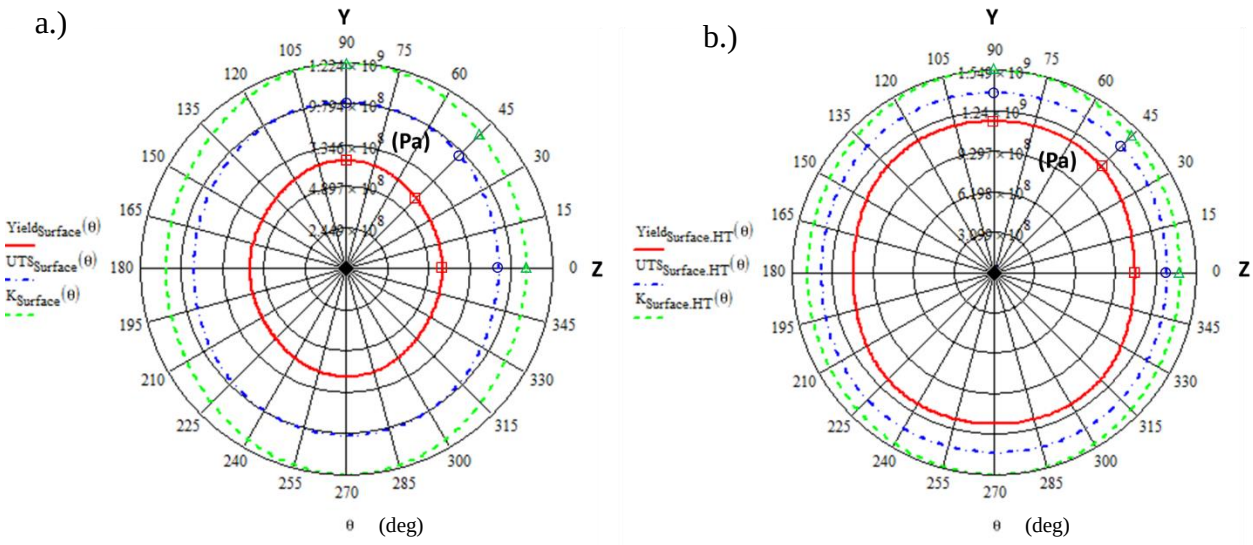

Figure 74: Yield surfaces in the YZ plane for a.) "as-built" and b.) "heat-treated" SLM IN718, developed through Hill's theory. Experimental data (only yield and ultimate tensile strengths) from Chlebus et al., 2015 was used to simulate yield surfaces and are represented as points (squares, and circles) on the plots.

A comparison of Hill's constants calculated for SLM IN718 "As-Built" and "Heat-Treated" failure surface modeling is presented in Table 32. According to R. Hill [Hill, 1998], a "necessary and sufficient condition for anisotropy to be symmetric about the z-axis would be N=F+2H=G+2H, L=M." It can be seen that F=G=0.5 and L=M from all surfaces modeled in the yz plane. The value for 'N' has been determined through both approaches, which yield values within range of each other. For this analysis, however, only the values for F, G, H and L were considered upon simplification of Hill's Equation for the yz plane. A comparison of the strength ratios (e.g. RLL, RTT, RLT) normalized with respect to the build direction are presented in Table 33, for SLM IN718 "As-Built" and "Heat-Treated." RLL is consistently equivalent to 1, which is expected because yield along the build direction has been normalized with respect to the build direction. RTT for 0.2% YS, UTS and K reveals that the strength values along the y-direction are higher than those values found along the build/z-direction in the following order

RTT_K > RTT_0.2%YS > RTT_UTS. A comparison of RTT for SLM IN718 "As-Built" versus "Heat-Treated," shows that RTT reduces for "Heat-Treated" samples, suggesting that the difference in strength (0.2% YS, UTS and K) between samples manufactured along the y-orientation versus samples manufactured along the build/direction reduces with applied heat treatment. Also observable in the "Heat-Treated" condition is RLT_K > RLT_UTS > RLT_0.2%YS whereas in the "As-built" condition, RLT_0.2%YS > RLT_K > RLT_UTS.

Table 32: Hill's constants determined from strength ratio relationships for SLM IN718 modeling based upon experimental data from Chlebus et al. 2015 publication

	"As-Built"				"Heat-Treated"			
Hill's Constants	**0.2% YS**	**UTS**	**K**	**EL%**	**0.2% YS**	**UTS**	**K**	**EL%**
F	0.5	0.5	0.5	0.5	0.5	0.5	0.5	0.5
G	0.5	0.5	0.5	0.5	0.5	0.5	0.5	0.5
H	0.291	0.332	0.261	1.636	0.359	0.419	0.344	5.141
L	1.288	1.438	1.318	3.665	1.546	1.524	1.403	4.207
M	1.288	1.438	1.318	3.665	1.546	1.524	1.403	4.207
N=F+2H	1.083	1.164	1.023	3.772	1.217	1.338	1.187	10.781

Table 33: Strength ratios normalized with respect to build direction 'Z' for SLM IN718 based upon experimental data from Chlebus et al. 2015 publication

	"As-Built"				"Heat-Treated"			
Strength Ratios	**0.2% YS**	**UTS**	**K**	**EL%**	**0.2% YS**	**UTS**	**K**	**EL%**
$\mathbf{R_{LL}}$	1	1	1	1	1	1	1	1
$\mathbf{R_{TT}}$	1.124	1.096	1.146	0.684	1.079	1.043	1.089	0.421
$\mathbf{R_{LT}}$	1.079	1.0215	1.067	0.63975	0.985	0.992	1.034	0.5971

6.4 Young's Modulus with Build Orientation

6.4.1 Additively Manufactured Stainless Steel 17-4PH/GP1

In order to investigate the variation in Young's modulus with build orientation, Equation (9) presented in Chapter 2, was adjusted to characterize this variation across the xy build plane. E_T,

E_L, and E_{45} represent the experimentally determined Young's moduli along the *y*, *x* and 45° orientations, with θ, the build orientation angle, measured from the x-axis. Figure 75 models the variation in Young's Modulus for DMLS SS GP1 as-built samples, based upon experimentally determined Young's Moduli from tension testing of samples built along varying build orientations in the xy build plane. As it is not anticipated that a 5° variation in build orientation for the (X) and (Y) orientations, will impose a significant difference in the Young's modulus, this was not considered in modeling Young's modulus variation with build orientation. As is depicted in Figure 75, there is a slight variation in Young's moduli, even for additively manufactured specimens built in the xy build plane. As this variation is minimal, this study is concluding isotropic behavior for manufacturing in the horizontal build orientation. This is further supported by EOS published Young's moduli for as-manufactured DMLS SS GP1, through which horizontally manufactured specimens in the build plane are expected to exhibit moduli with the range of 170 ± 30 GPa [EOS, 2009], which also does not indicate a variation with mechanical properties at varying build orientations in the *xy* horizontal build plane.

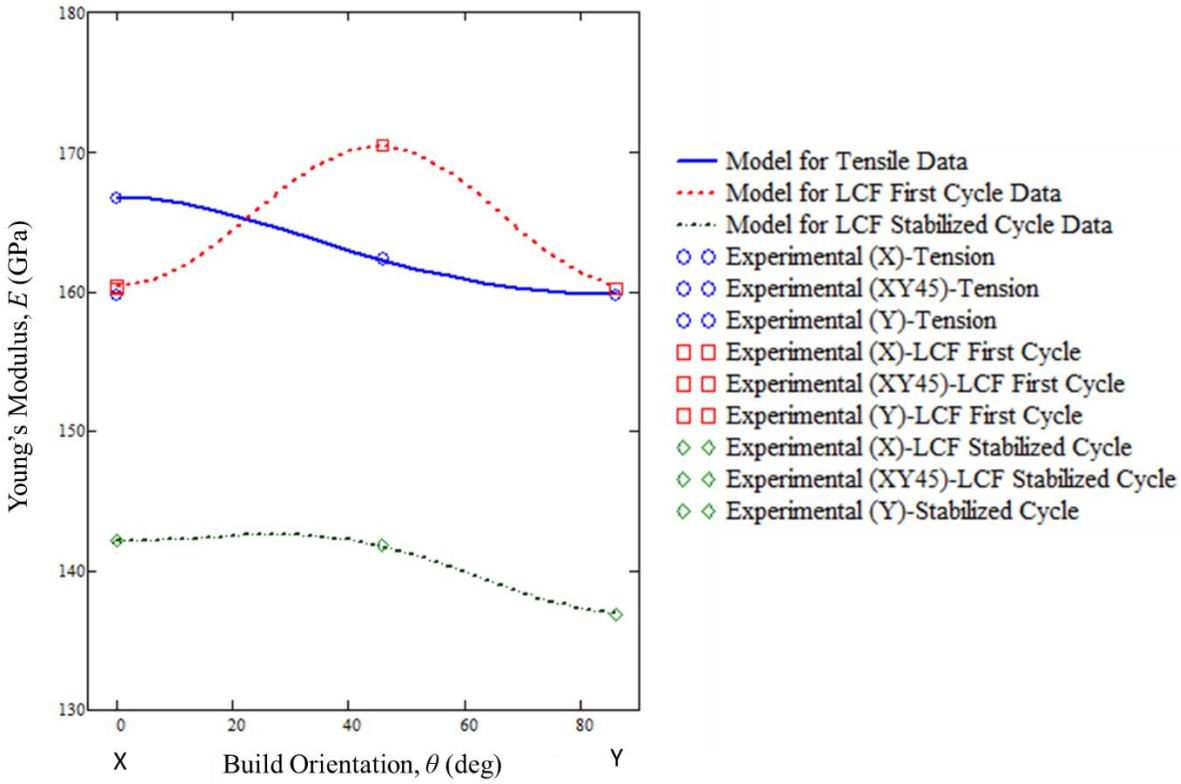

Figure 75: Young's modulus variation with build orientation for DMLS SS GP1 samples manufactured in xy build plane [Siddiqui, 2018]

6.4.2 Additively Manufactured Inconel 718

While several studies have analyzed the tensile properties of additively manufactured Inconel 718, no study to date has assessed the Young's Modulus versus build orientation. The Young's Modulus versus build orientation is presented in Figure 76, and has been developed using Equation (9) presented in Chapter 2, and through use of experimental data presented in [Chlebus, 2015].

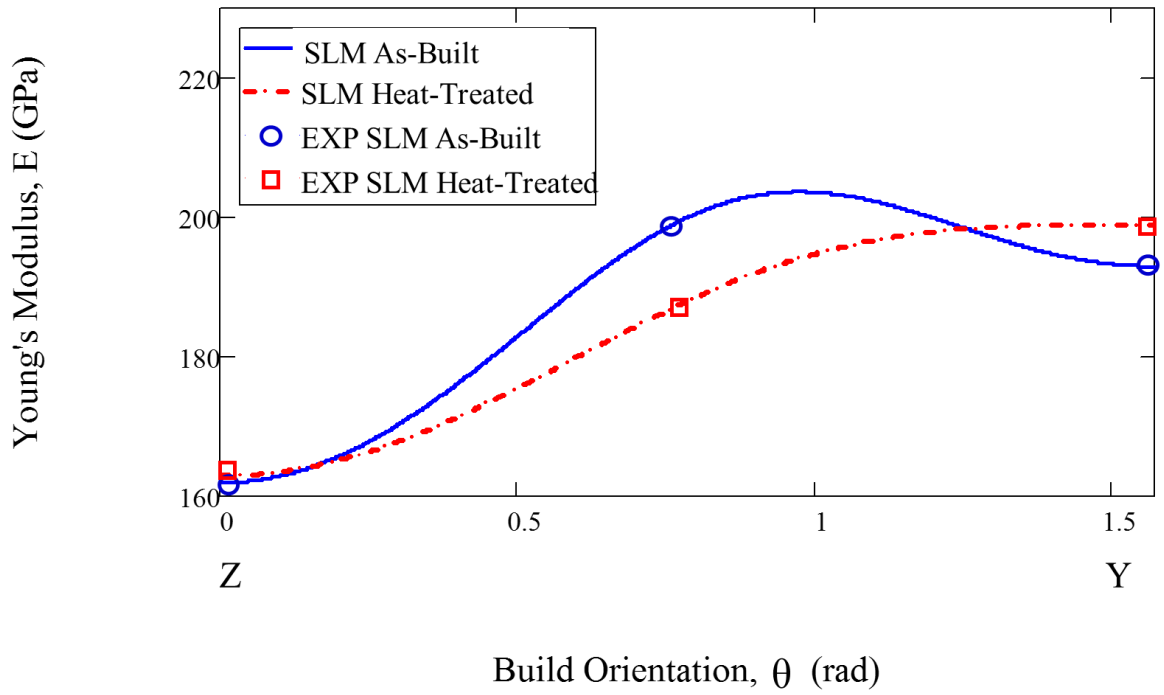

Figure 76: Young's Modulus for varying build orientations for SLM IN718 in the yz plane [Siddiqui, 2017]

For this analysis, E_T is the Young's Modulus in the y-direction (perpendicular to the build axis), and E_{45} is the Young's Modulus 45° from the z-direction (build axis) along the zy plane as provided by Chlebus et al. 2015. Figure 76 is plotted from 0 to $\pi/2$ radians from the z-direction in the *zy* plane and includes both the variation for "as-built" and "heat-treated" SLM IN718. Experimental Young's Modulus values provided in [Chlebus, 2015],

are indicated by 'EXP' for SLM "as-built" and "heat-treated" IN718 in Figure 76. It can be seen that E (0) < E (π/2) < E (π/4) for "as-built" SLM IN718, as previously found by [Chlebus, 2015]. Also evident is the reduction, but not removal, of texture observed for "heat-treated" SLM IN718 as opposed to "as-built" SLM IN718, as discussed in [Chlebus, 2015]. Furthermore, it can be observed that the peak elastic modulus within the *zy* plane varies for "as-built" SLM IN718 and "heat-treated" SLM IN718. For "heat-treated" SLM IN718, the peak elastic modulus of 199 GPa is shown to occur perpendicular to the build direction, for this case, along the y-direction (010). For "as-built" SLM IN718, the peak elastic modulus of 203.696 GPa is found to occur at ~0.97 radians or ~55.5769°, which is approximately 10° above the bias orientation of 45°. Furthermore, there are two observed intersection points for both the "as-built" SLM IN718 and "heat-treated" SLM IN718 Young's Modulus variation with orientation plots. This is found to occur at ~1.257 radians or ~72° from the build direction (z-axis) and ~0.16 radians or ~9.167° from the build direction (z-axis). This suggests that there are two build orientations for which the Young's Modulus in the *zy* plane will not vary regardless of heat-treatment post-processing technique, for the heat treatment applied in this study [Chlebus, 2015] (solution treatment at 1100°C for 1 hr (water cooling) and age hardening at 720°C for 8 hr (furnace cooling at 100°C/h) to 620°C for 10 hr (air cooling)).

CHAPTER 7: CONCLUSIONS AND FUTURE WORK

This study has investigated the impact of build orientation on the anisotropic material response of an additively manufactured stainless steel, through mechanical testing (i.e. tension, torsion and fatigue), which was supported through constitutive modeling, from which a comprehensive framework has been developed to characterize the mechanical response of AM materials under multiple loading conditions. This study has also explored the torsional fatigue response of additively manufactured Inconel 718 manufactured along varying build orientations, and used experimental findings along with literature findings to model material response. The following novel findings were presented.

- DMLS Stainless Steel GP1
    - As-built DMLS SS GP1 has been shown to exhibit slightly orthotropic behavior (i.e., transversely isotropic behavior), with the *xy* plane being the plane of isotropy.
    - First study to investigate the torsional and torsional-fatigue response of as-built DMLS stainless steel (SS) GP1, through monotonic torsion and completely reversed torsional fatigue experiments, for samples built at varying orientations in the horizontal xy build plane, yielding the shear modulus and Poisson's ratio within the xy plane.
    - The ultimate shear strength for DMLS SS GP1, manufactured along the horizontal build orientation was found to be considerably larger than for heat-treated (H900) wrought Stainless Steel 17-4PH. This may suggest that the layer by layer deposition, which is characteristic of the AM process, may allow for improved performance in shear.

- A brittle fracture response was observed for DMLS SS GP1, when manufactured in the horizontal build orientation, and subject to torsional fatigue testing, which may be attributed to a stress-induced austenite to martensite phase transformation.
- First study to contribute to the development of failure surfaces to approximate the yielding response (lower and upper yield strength), ultimate tensile strength response, and Ramberg-Osgood strength coefficient of DMLS SS GP1 through use of Hill's failure criteria.
- Optimized Hahn's plasticity discontinuous yielding model to fit the upper and lower yield strength discontinuous yielding behavior exhibited by DMLS SS GP1.
- Provided an initial start to constitutively modeling the cyclic (LCF and Pulsating Tension Fatigue) hysteresis response of AM materials, through application of the Chaboche Model.
- A reduced specimen size has been developed that yields similar findings to conventional test specimens, while allowing for a reduction in manufacturing cost of test specimens.
- Tensile to fatigue relations were found to be valid in reflecting the initial hardening behavior of this material to stabilization during low cycle fatigue testing at a strain range of $\Delta\varepsilon = 1.4\%$.
- When subject to pulsating tension fatigue conditions at a strain range of $\Delta\varepsilon = 0.7\%$, DMLS SS GP1 is found to soften to stabilization, and harden to fracture.
- When subject to progressive strain amplitude fatigue loading, from $\Delta\varepsilon = 0.6\%$ to $\Delta\varepsilon = 1.4\%$, for 100 cycles at each strain range, DMLS SS GP1 manufactured in

the horizontal build plane is found to fracture at or just before cycling at a strain range of $\Delta\varepsilon = 1.0\%$.

  - The variation in Young's modulus, while minimal in the xy plane, has been modeled with build orientation, thus providing a first approximation of the Young's modulus at intermediary build orientations within the xy plane, for specimens subject to tension testing.
  - Microstructural analysis across mechanical tests performed reveal the presence of internal voids and un-melted powder particles, which are supported by density measurements of specimens.
  - Rockwell C hardness tests reveal slightly improved hardness values, as compared with findings in literature on DMLS SS GP1, but lower than reported for conventional SS 17-4PH (Condition A).

- DMLS Inconel 718
  - First study to investigate the torsional-fatigue response of as-built DMLS Inconel 718, through completely reversed torsional fatigue experiments, for samples manufactured along the (100)-X, (010)-Y, (001)-Z, (101)-XZ45, (011)-YZ45, and (110)-XY45 build orientations, yielding the shear modulus and Poisson's ratio along each build orientation.
  - Findings from torsional fatigue testing of DMLS Inconel 718 along each build orientation suggest that this material may be classified as transversely isotropic, with the xy plane being the plane of symmetry.
  - Ductile fracture response was found for specimens manufactured along the Z, XZ45 and YZ45 build orientations with crack initiation and propagation

emanating from internal defects (i.e., voids). For specimens manufactured along the X, Y and XY45 build orientations, cracks were found to initiate at the surface and propagate between and through the build layers.

- Surface roughness analysis has shown that the Z-oriented specimen has a much lower surface roughness than the X/Y-oriented specimens.
- The plastic shear strain tolerance for additively manufactured specimens were determined to be much lower than for conventional (wrought annealed) Inconel 718. In terms of shear stress range and shear modulus, the Z-orientation exceeded the performance of the horizontally manufactured specimens (X, XY45, Y), with the diagonally manufactured specimens (XZ45, YZ45) yielding the lowest performance when subject to completely reversible torsional fatigue test conditions. The Z-orientation was found to yield a shear modulus closest to that obtained for conventional (wrought annealed) Inconel 718. The variation may likely be due to the fact that conventional Inconel 718 specimens have been annealed, whereas the DMLS specimens were not subject to any form of post-processing heat treatment, in addition to intrinsic defects in the additive manufacturing process that limits performance. These include void/pores and surface roughness.
- Both additively manufactured and wrought annealed Inconel 718 specimens were found to cyclically harden to stabilization, followed by softening to fracture.
- When subject to high plasticity shear strain range, a life assessment of these specimens reveal the shortest life for the Z-oriented specimen, followed by the diagonally-oriented specimens (XZ45, YZ45), with the longest life endured by the

horizontally manufactured specimens (X,XY45,Y). The horizontally manufactured specimens had a fatigue life within range of the fatigue life for the wrought annealed Inconel 718 specimen.

- Failure surfaces have been developed through application of Hill's failure criteria, and reported literature findings on Inconel 718, for heat-treated and as-built Inconel 718, in addition to Young's modulus variation with build orientation. Ramberg-Osgood constants have been determined from literature findings on the monotonic stress-strain response of Inconel 718.

Experimental findings on DMLS SS GP1 and DMLS Inconel 718 suggests that these materials may be classified as transversely isotropic, with the xy plane being the plane of isotropy. With this consideration, a first approximation of the 5 independent elastic constants used to describe this material behavior has been determined for DMLS SS GP1 and DMLS Inconel 718, based upon experimental findings reported in this study and within literature, and are presented in Table 34 . The elastic constants are reported along the 'L' – Longitudinal- (001), and 'T'- Transverse- (100) and (010) build orientations. These elasticity constants were used to generate a first approximation of the 3D elasticity surface of these AM materials, which are depicted in Figure 77. Future experimental testing will be done to further confirm the reported elastic constants, especially G_{LT} and $v_{LT,}$ as those reported within this study are a first approximation.

Table 34: First approximation of elasticity constants for DMLS SS GP1 and DMLS Inconel 718

Elasticity Constants	DMLS Stainless Steel GP1	DMLS Inconel 718
E_T	163 GPa	160 GPa
E_L	170 GPa	170 GPa
G_{TT}	57.7 GPa	59.6 GPa
G_{LT}	60.49 GPa	63.3 GPa
v_{LT}	0.405	0.342

a.)

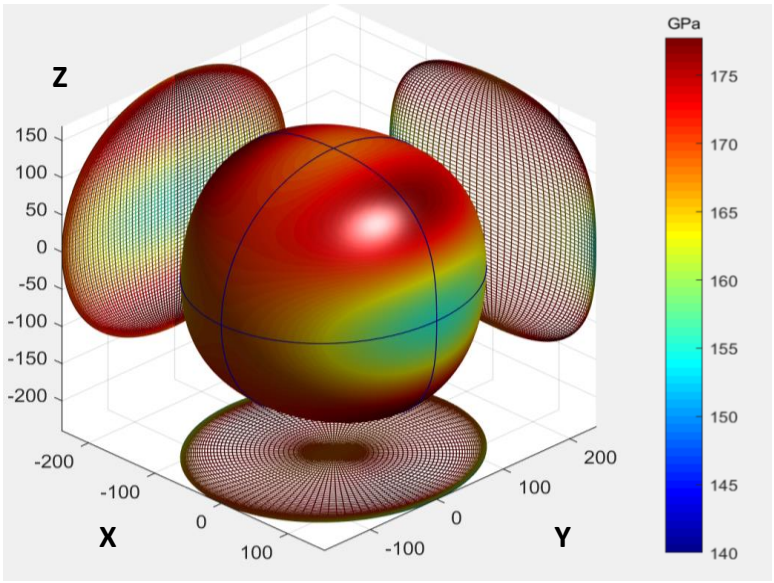

b.)

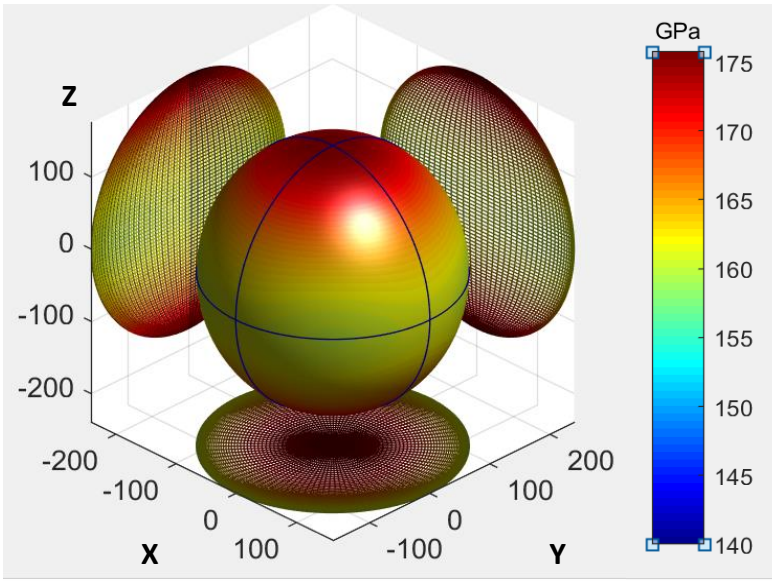

Figure 77: First approximation of 3D elasticity surfaces for a.) DMLS Stainless Steel GP1, and b.) DMLS Inconel 718

Future studies will focus on assessing the best techniques for additively manufacturing stainless steel GP1 specimens along the (101)-XZ45°, (011)-YZ45°, and (001)-Z build orientations, as the current study encountered difficulties in printing of these as-built specimens. For these 3 build orientations, manufacturing of the specimens in the current geometry was found to result in few successfully printed samples. This may be attributed to the sudden change in geometry from the shoulder to gauge section of the test specimens, which resulted in warping of the test specimens, rendering them inadequate for the proposed mechanical testing. This is evident by the image in Appendix A, of the failed DMLS SS GP1 third batch. Also taken into consideration was developing these specimens as cylinders, which could then be machined into test specimens. However, as this study was developing a comprehensive assessment of as-built surface conditions and build orientation on the associated findings, and specimens were printed and tested along the (100)-X, (010)-Y, and (110)-XY45° build orientations using the current geometric configuration, it was not deemed feasible to change the manufacturing conditions since experimental results along all build orientations would no longer be comparable. In addition, manufacturing of these specimens along the (011)-YZ45° and (101)-XZ45° build orientations proved difficult, since the support structure required for these orientations were both difficult to print and not strong enough to prevent warping of the test specimens. Batch 4 specimen testing are underway in not only further confirming findings, but also exploring other mechanical behavior responses of these materials, such as the impact of multiaxial loading conditions (axial and torsional) and temperature on material response and the role of machining and heat-treatment on the material response. This will provide insight into the role of phase change behavior in effecting mechanical response.

APPENDIX A: ADDITIVE MANUFACTURING SPECIMEN LAYOUTS

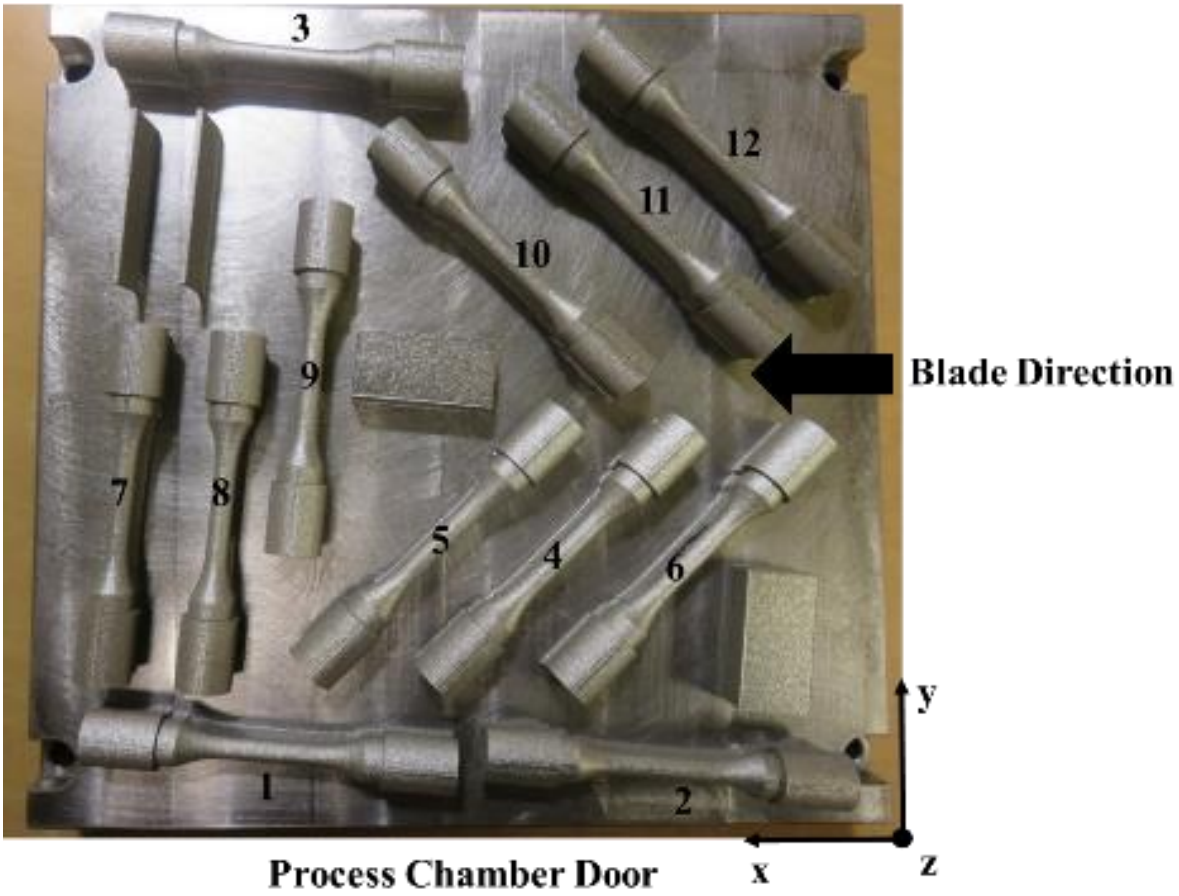

DMLS SS GP1 Batch 1

DMLS SS GP1 Batch 2

DMLS SS GP1 Failed Batch 3

DMLS SS GP1 Batch 4

DMLS Inconel 718 Batch


(Z)


(Y)


(X)


(XY45)


(XZ45)


(YZ45)

APPENDIX B: EXPERIMENTAL SAMPLE DATA

Tensile Specimen

DMLS SS GP1 Batch 1-Specimen 3

Orientation	X-Axis
Elastic Modulus, *E* (GPa)	166.7
Lower Yield Strength, σ_{lys} (MPa)	534
Upper Yield Strength, σ_{uys} (MPa)	597
0.2% Yield Strength, $\sigma_{0.2ys}$ (MPa)	579
Ultimate Tensile Strength, σ_{UTS} (MPa)	956

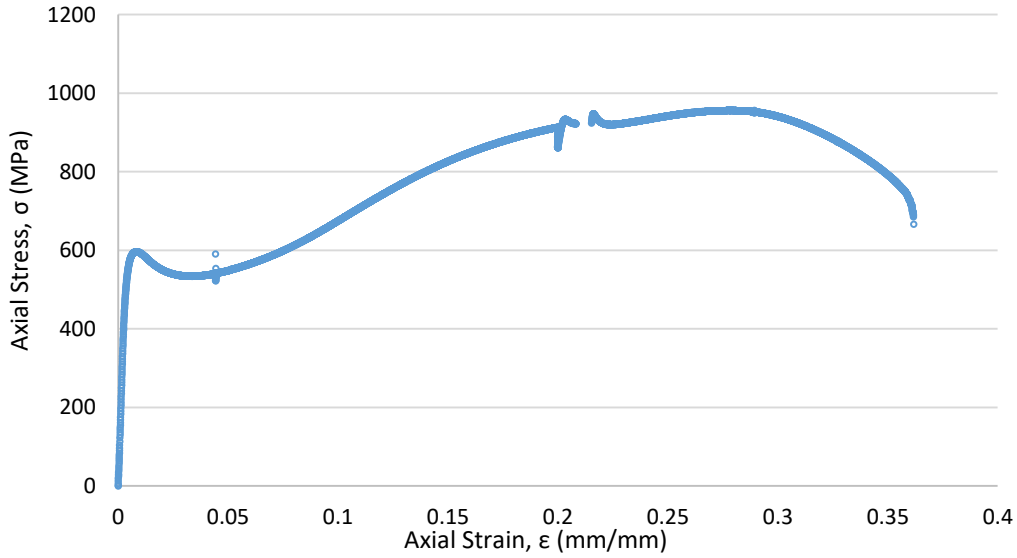

Tensile Specimen

DMLS SS GP1 Batch 1-Specimen 5

Orientation	XY45°
Elastic Modulus, E (GPa)	162.3
Lower Yield Strength, σ_{lys} (MPa)	546
Upper Yield Strength, σ_{uys} (MPa)	597
0.2% Yield Strength, $\sigma_{0.2ys}$ (MPa)	583
Ultimate Tensile Strength, σ_{UTS} (MPa)	982

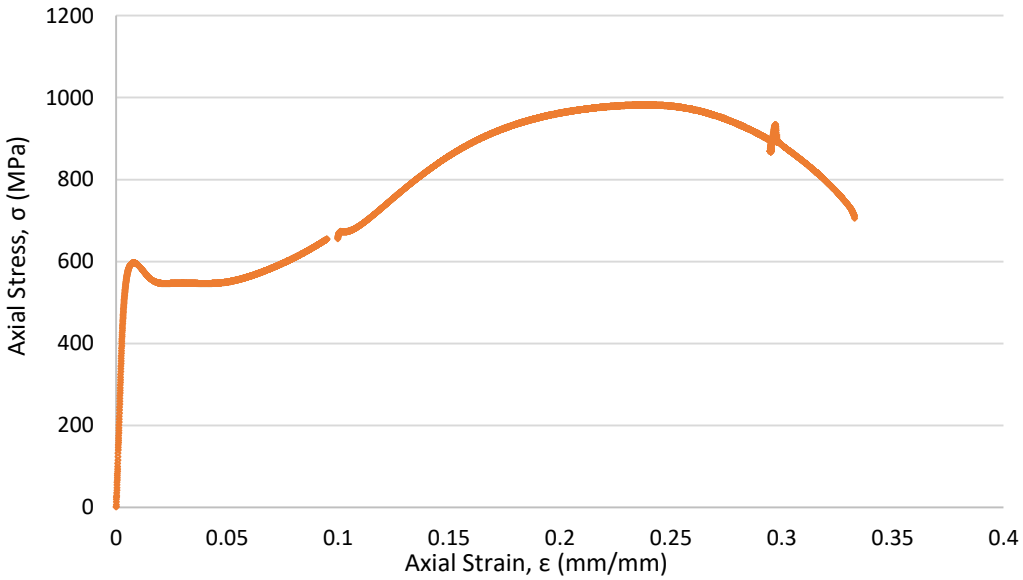

Tensile Specimen

DMLS SS GP1 Batch 1-Specimen 9

Orientation	Y-Axis
Elastic Modulus, *E* (GPa)	159.7
Lower Yield Strength, σ_{lys} (MPa)	638
Upper Yield Strength, σ_{uys} (MPa)	698
0.2% Yield Strength, $\sigma_{0.2ys}$ (MPa)	689
Ultimate Tensile Strength, σ_{UTS} (MPa)	1086

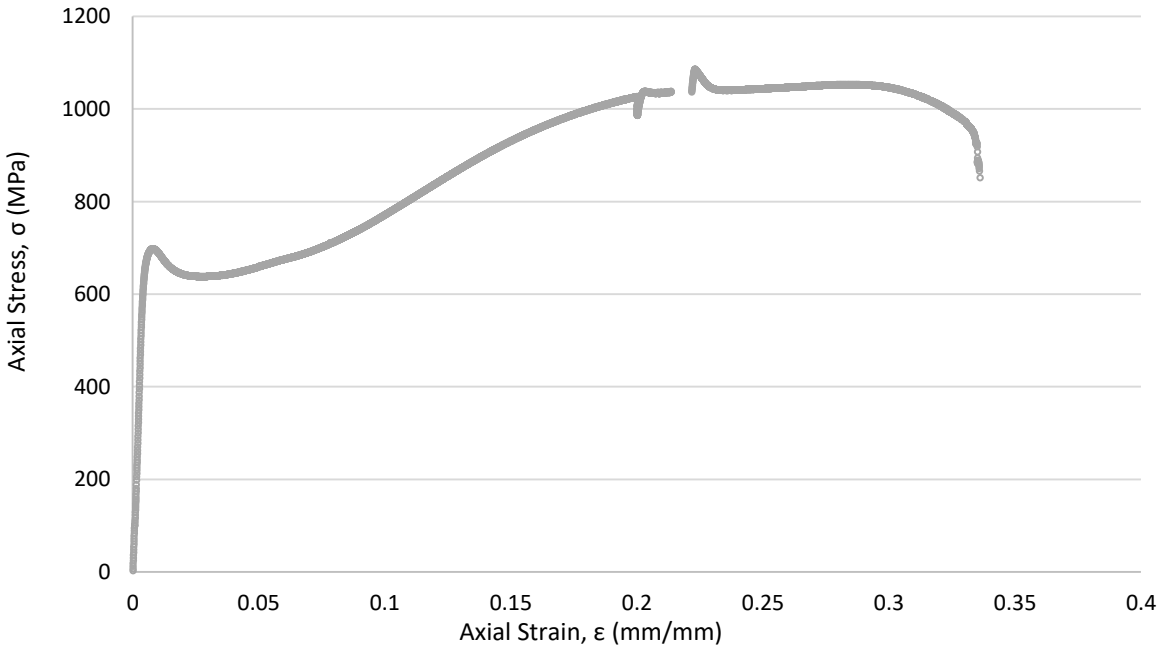

Tensile Specimen

DMLS SS GP1 Batch 2-Specimen 21

Orientation	Y-Axis
Elastic Modulus, *E* (GPa)	145
Lower Yield Strength, σ_{lys} (MPa)	555
Upper Yield Strength, σ_{uys} (MPa)	619

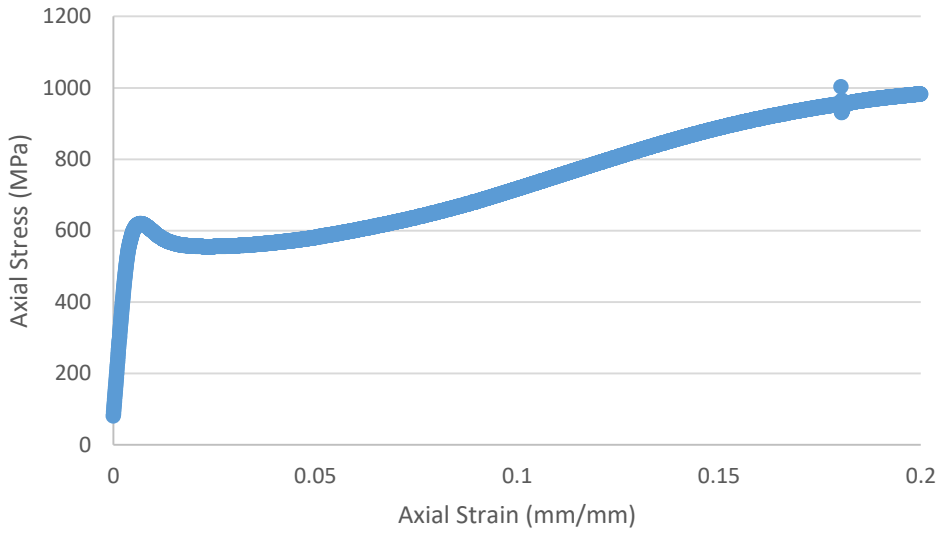

Tensile Specimen

DMLS SS GP1 Batch 2-Specimen 9-Reduced Test Specimen

Orientation	Y-Axis
Lower Yield Strength, σ_{lys} (MPa)	574
Upper Yield Strength, σ_{uys} (MPa)	625

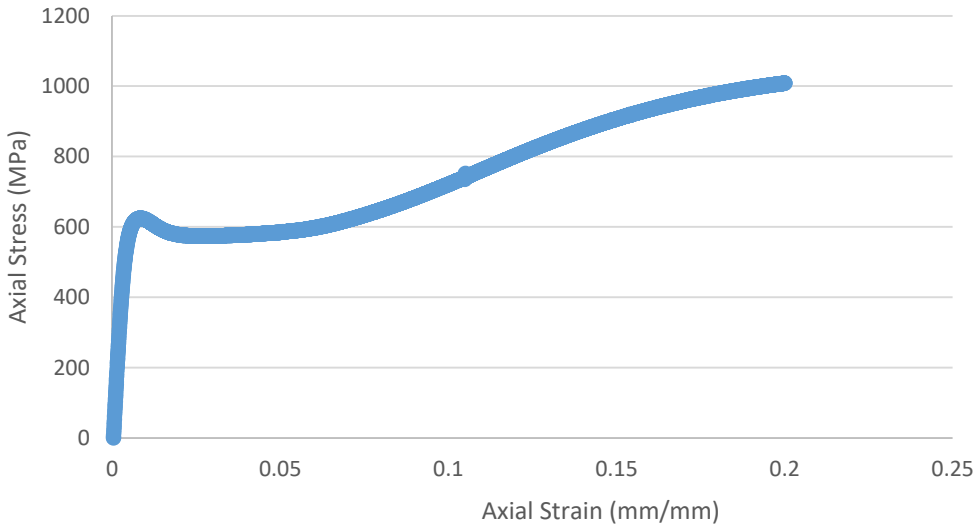

Torsion Specimen

DMLS SS GP1 Batch 2-Specimen 3

Orientation	X
Shear Strength (MPa)	1011

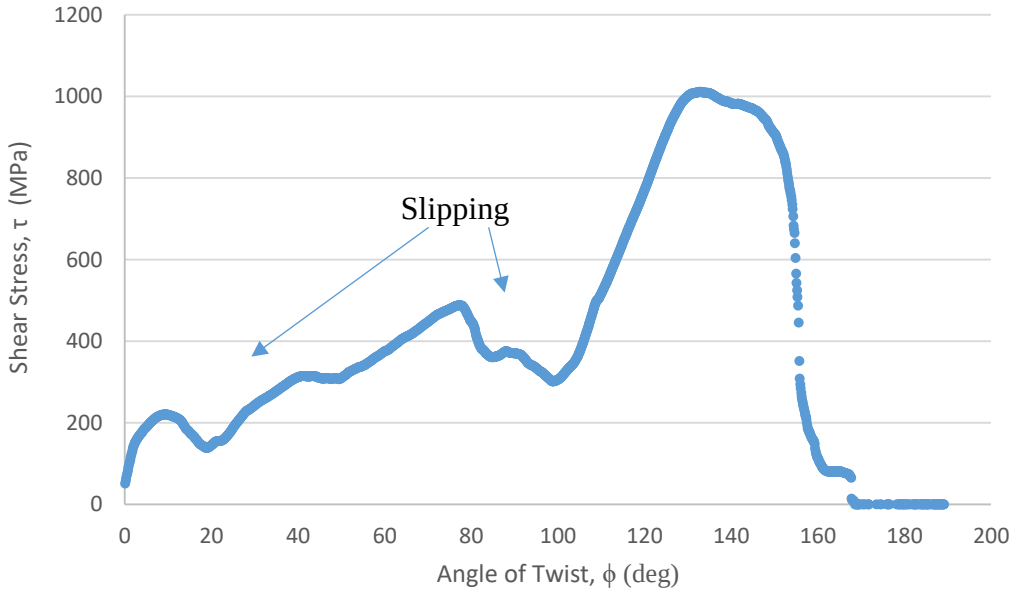

Torsion Specimen

DMLS SS GP1 Batch 2-Specimen 5

Orientation	Y
Shear Strength (MPa)	1018

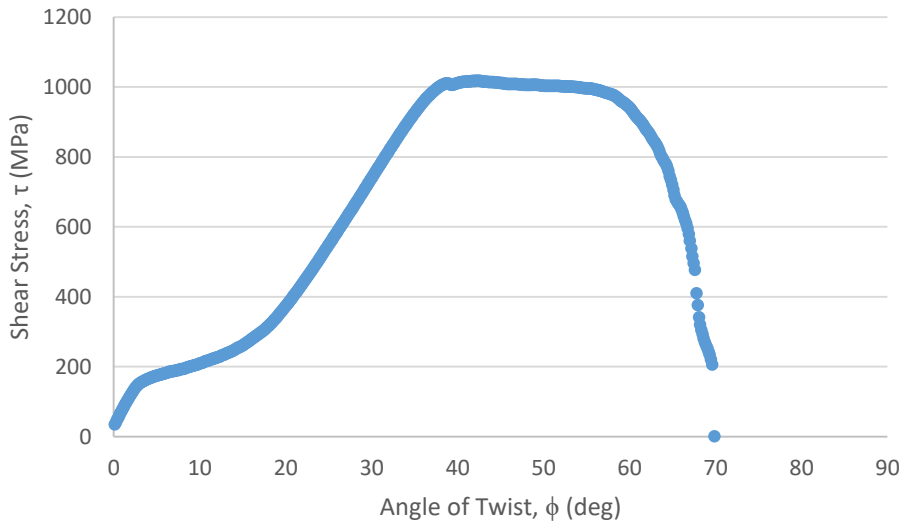

Torsion Specimen

DMLS SS GP1 Batch 2-Specimen 11

Orientation	XY45°
Shear Strength (MPa)	1010

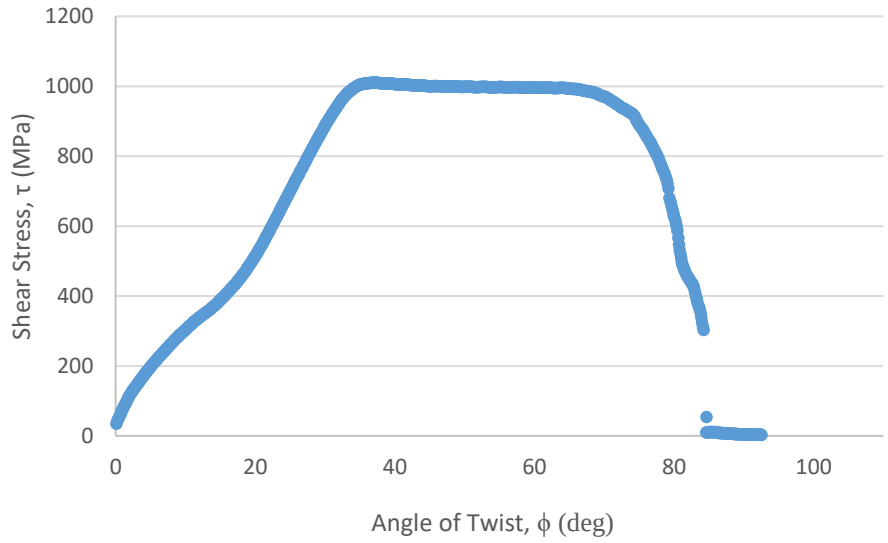

Torsion Specimen

DMLS SS GP1 Batch 2-Specimen 6

Orientation	Y-Axis	
Cycle	**First**	**Stabilized**
Shear Modulus, *G* (GPa)	50.7	46.055
Shear Stress Range, $\Delta\tau$ (MPa)	843.83	1271.15
Mean Shear Stress, τ_m (MPa)	13.8465	12.37
Twist Range, Δϕ (deg)	30.006	29.968
Torque Range, T, (N*m)	34.0488	51.29
Plastic Shear Strain Range, Δγp (mm/mm)	0.014	0.032656
Elastic Shear Strain Range, Δγe (mm/mm)	0.0166	0.0276
Total Shear Strain Range, Δγ (mm/mm)	0.0308	0.030866

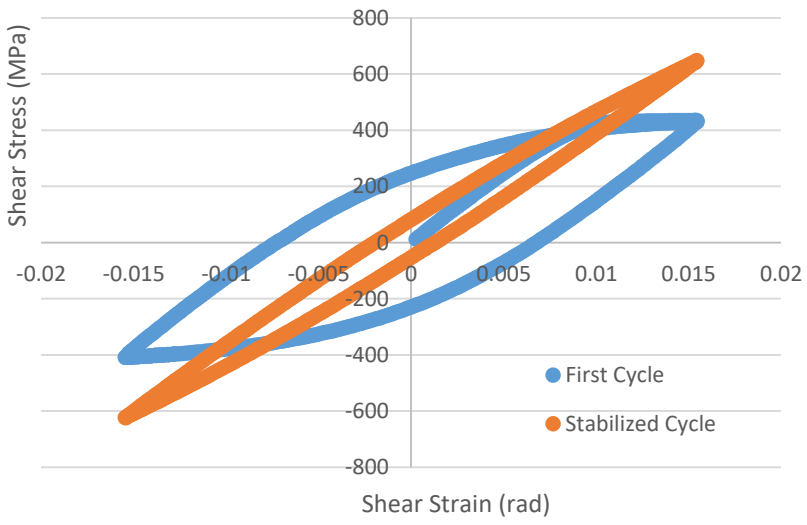

Torsion Specimen

DMLS SS GP1 Batch 2-Specimen 12

Orientation	XY45°	
Cycle	**First**	**Stabilized**
Shear Modulus, *G* (GPa)	49.45	43.51
Shear Stress Range, $\Delta\tau$ (MPa)	818.24	1086.778
Mean Shear Stress, τ_m (MPa)	-29.3	55.03
Twist Range, Δϕ (deg)	29.98	29.86
Torque Range, T, (N*m)	33.5866	44.6
Plastic Shear Strain Range, Δγp (mm/mm)	0.0145	0.00595
Elastic Shear Strain Range, Δγe (mm/mm)	0.0165	0.02497
Total Shear Strain Range, Δγ (mm/mm)	0.031	0.03093

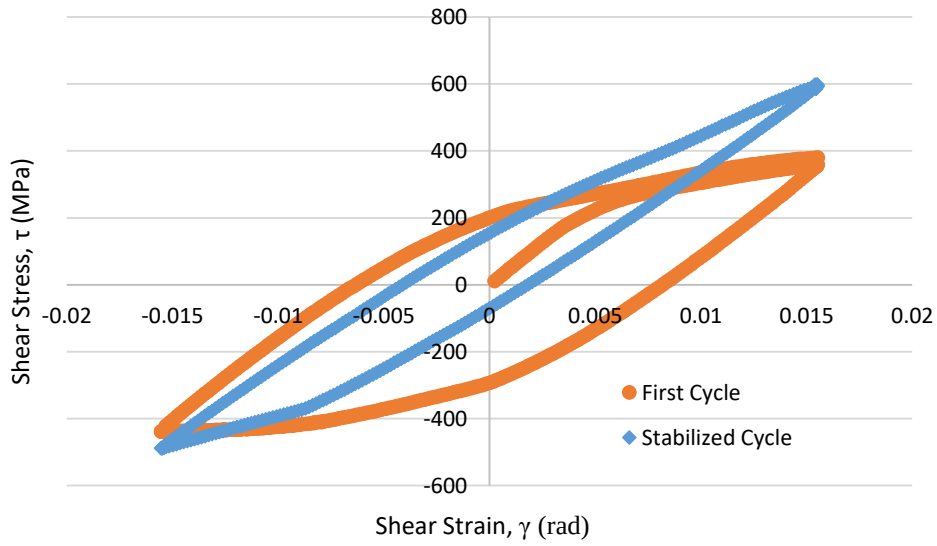

Torsion Reduced Test Specimen

DMLS SS GP1 Batch 2-Specimen 2

Orientation	X	
Cycle	**First**	**Stabilized**
Shear Modulus, G (GPa)	54.561	41.56
Shear Stress Range, $\Delta\tau$ (MPa)	872.488	1525.295
Mean Shear Stress, τ_m (MPa)	-41.47	-37.6957
Twist Range, $\Delta\phi$ (deg)	28.5095	29.9861
Torque Range, ΔT, (N*m)	21.6816	37.904
Plastic Shear Strain Range, $\Delta\gamma p$ (mm/mm)	0.03319	0.01502
Elastic Shear Strain Range, $\Delta\gamma e$ (mm/mm)	0.01599	0.0367
Total Shear Strain Range, $\Delta\gamma$ (mm/mm)	0.04918	0.05172

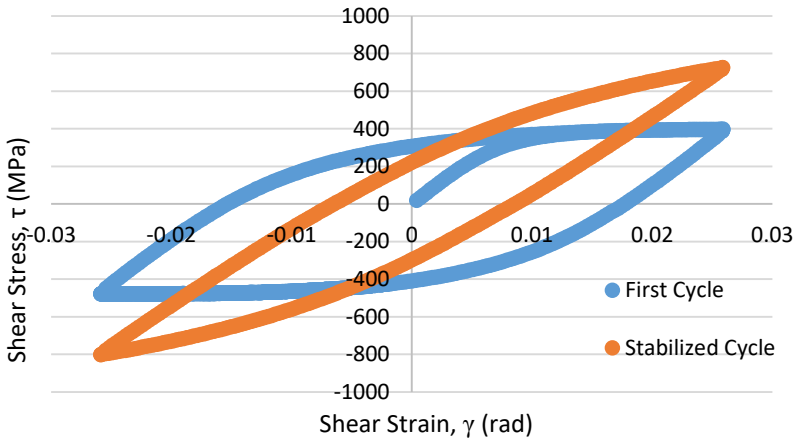

Torsion Reduced Test Specimen

DMLS SS GP1 Batch 2-Specimen 10

Orientation	Y	
Cycle	**First**	**Stabilized**
Shear Modulus, *G* (GPa)	56.935	39.308
Shear Stress Range, $\Delta\tau$ (MPa)	830.8	1481.67
Mean Shear Stress, τ_m (MPa)	-76.288	-71.1778
Twist Range, Δϕ (deg)	27.3164	30.0058
Torque Range, ΔT, (N*m)	21.3856	38.1393
Plastic Shear Strain Range, Δγp (mm/mm)	0.033084	0.014676
Elastic Shear Strain Range, Δγe (mm/mm)	0.01459	0.03769
Total Shear Strain Range, Δγ (mm/mm)	0.047676	0.05237

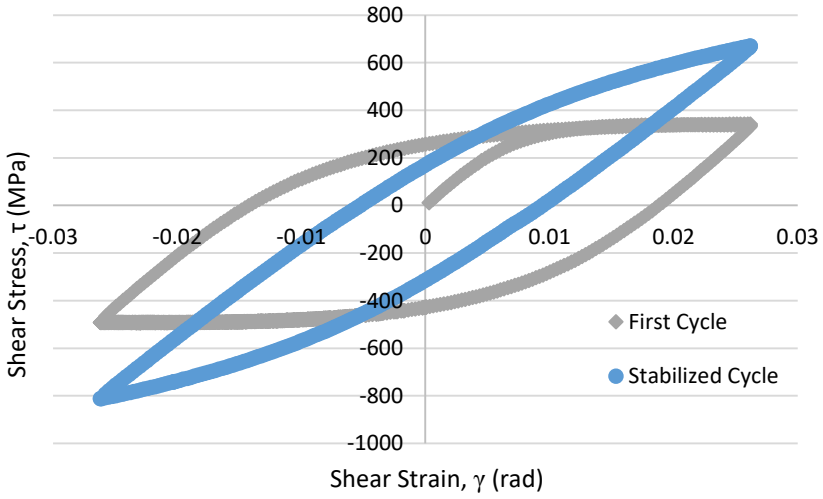

Torsion Reduced Test Specimen

DMLS SS GP1 Batch 2-Specimen 17

Orientation	XY45°	
Cycle	**First**	**Stabilized**
Shear Modulus, *G* (GPa)	61.683	42.031
Shear Stress Range, $\Delta\tau$ (MPa)	870.97	1527.62
Mean Shear Stress, τ_m (MPa)	2.311	85.216
Twist Range, Δϕ (deg)	27.2966	29.977
Torque Range, ΔT, (N*m)	21.425	37.5745
Plastic Shear Strain Range, Δγp (mm/mm)	0.0328	0.015188
Elastic Shear Strain Range, Δγe (mm/mm)	0.01412	0.03634
Total Shear Strain Range, Δγ (mm/mm)	0.0469	0.051533

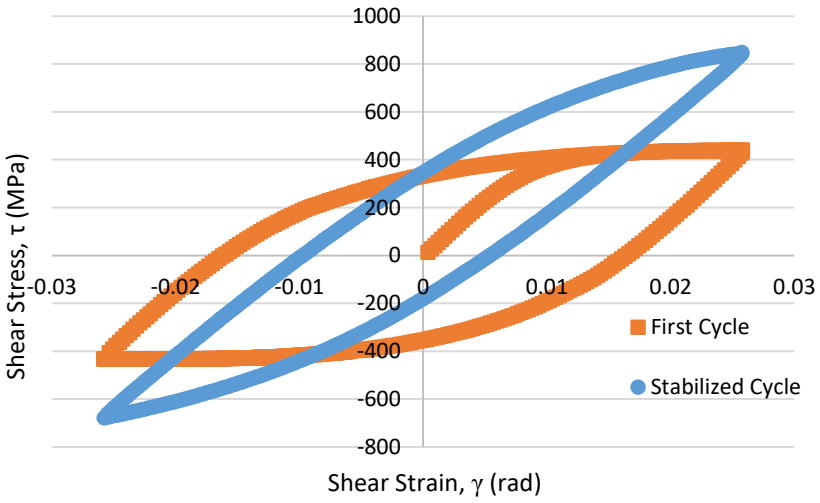

Low Cycle Fatigue Specimen

DMLS SS GP1 Batch 1-Specimen 1

Orientation	X-Axis	
Cycle	**First**	**Stabilized**
Elastic Modulus, *E* (GPa)	165	145
Stress Range, $\Delta\sigma$ (MPa)	1143	1630
Mean Stress, σ_m (MPa)	27	-48
Plastic Strain Range, Δεp (mm/mm)	0.0069837	0.00272
Elastic Strain Range, Δεe (mm/mm)	0.006944	0.01122
Total Strain Range, Δε (mm/mm)	0.013927	0.01394

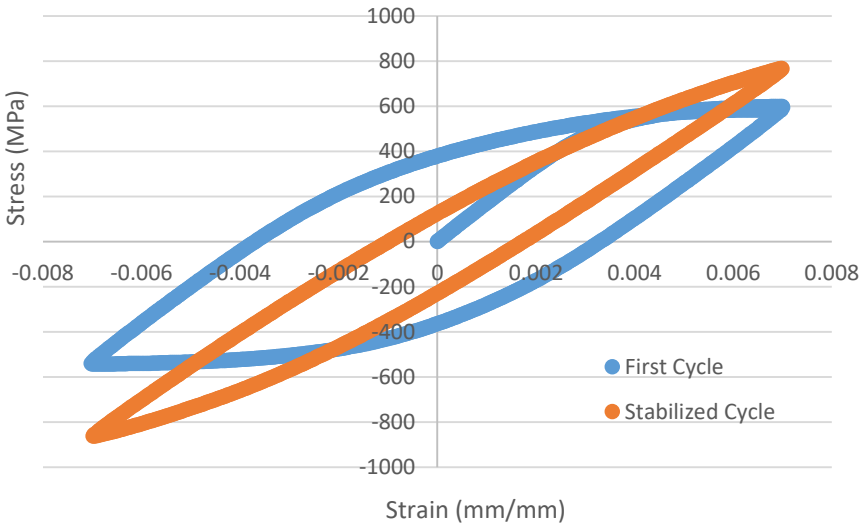

Low Cycle Fatigue Specimen

DMLS SS GP1 Batch 1-Specimen 2

Orientation	X-Axis	
Cycle	**First**	**Stabilized**
Elastic Modulus, *E* (GPa)	156	139
Stress Range, $\Delta\sigma$ (MPa)	1114	1616
Mean Stress, σ_m (MPa)	52	52
Plastic Strain Range, Δεp (mm/mm)	0.00683	0.002294
Elastic Strain Range, Δεe (mm/mm)	0.00713	0.011644
Total Strain Range, Δε (mm/mm)	0.013967	0.013959

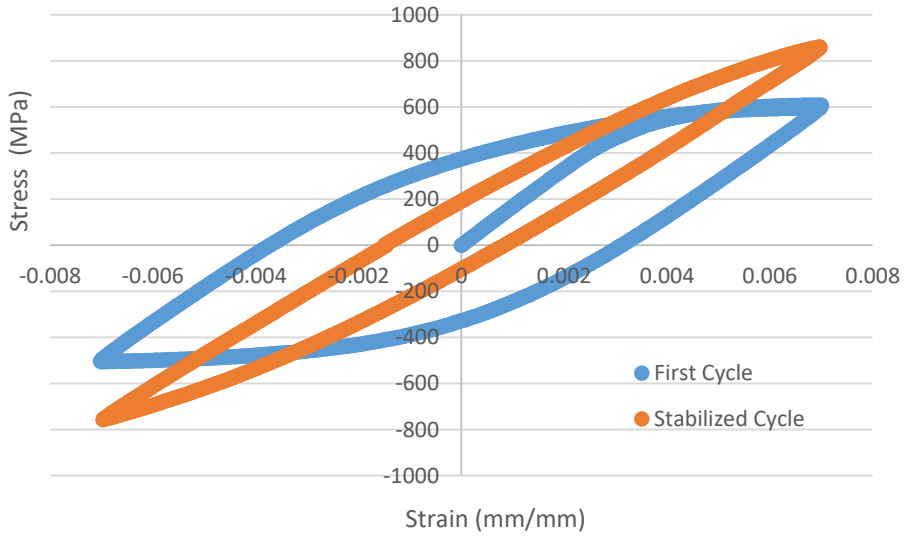

Low Cycle Fatigue Specimen

DMLS SS GP1 Batch 1-Specimen 4

Orientation	XY45°	
Cycle	**First**	**Stabilized**
Elastic Modulus, *E* (GPa)	174	144
Stress Range, $\Delta\sigma$ (MPa)	1139	1631
Mean Stress, σ_m (MPa)	32	-38
Plastic Strain Range, Δεp (mm/mm)	0.00728	0.00263
Elastic Strain Range, Δεe (mm/mm)	0.00655	0.01133
Total Strain Range, Δε (mm/mm)	0.01384	0.01396

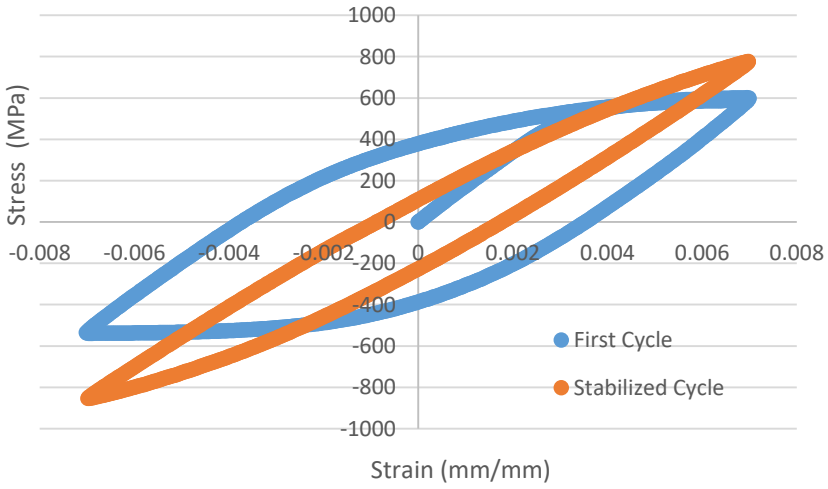

Low Cycle Fatigue Specimen

DMLS SS GP1 Batch 1-Specimen 6

Orientation	XY45°	
Cycle	**First**	**Stabilized**
Elastic Modulus, *E* (GPa)	167	140
Stress Range, $\Delta\sigma$ (MPa)	1136	1580
Mean Stress, σ_m (MPa)	44	-51
Plastic Strain Range, Δεp (mm/mm)	0.00716	0.0026
Elastic Strain Range, Δεe (mm/mm)	0.0068	0.0113
Total Strain Range, Δε (mm/mm)	0.01396	0.01394

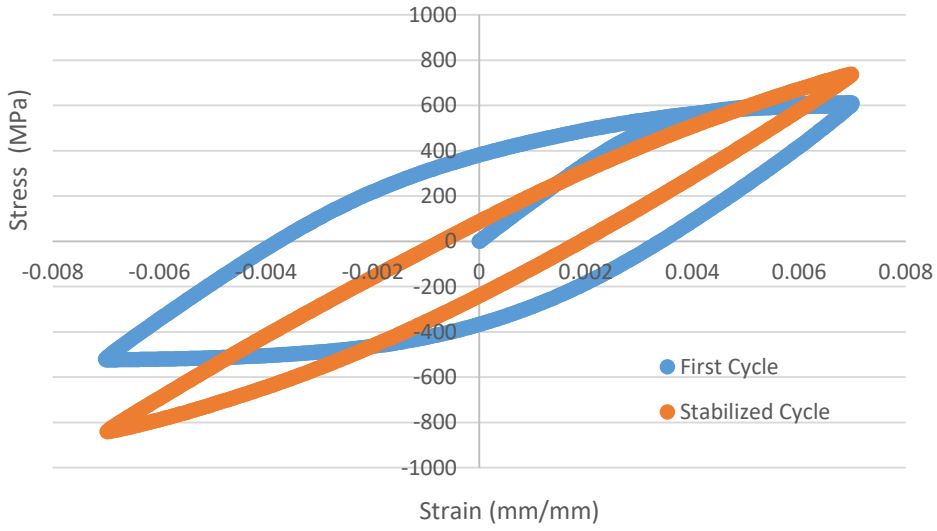

Low Cycle Fatigue Specimen

DMLS SS GP1 Batch 1-Specimen 12

Orientation	XY135°	
Cycle	**First**	**Stabilized**
Elastic Modulus, *E* (GPa)	169.5	152.438
Stress Range, $\Delta\sigma$ (MPa)	1170.23	1715.399
Mean Stress, σ_m (MPa)	36.64	-30.83
Plastic Strain Range, Δεp (mm/mm)	0.007	0.0027
Elastic Strain Range, Δεe (mm/mm)	0.0069	0.01125
Total Strain Range, Δε (mm/mm)	0.01396	0.01395

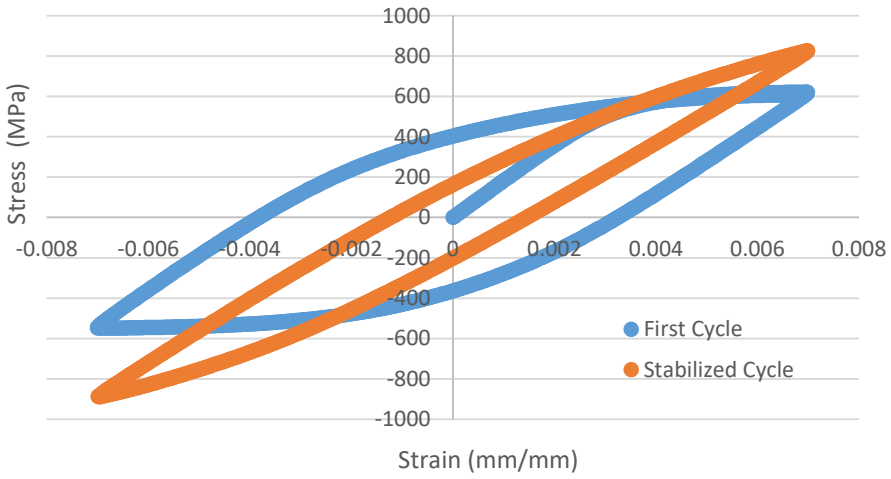

Low Cycle Fatigue Specimen

DMLS SS GP1 Batch 1-Specimen 11

Orientation	XY135°	
Cycle	**First**	**Stabilized**
Elastic Modulus, E (GPa)	179.925	160.093
Stress Range, $\Delta\sigma$ (MPa)	1225.4241	1782.413
Mean Stress, σ_m (MPa)	198.995	152.32
Plastic Strain Range, Δεp (mm/mm)	0.00689	0.002834
Elastic Strain Range, Δεe (mm/mm)	0.006811	0.011134
Total Strain Range, Δε (mm/mm)	0.0137	0.013968

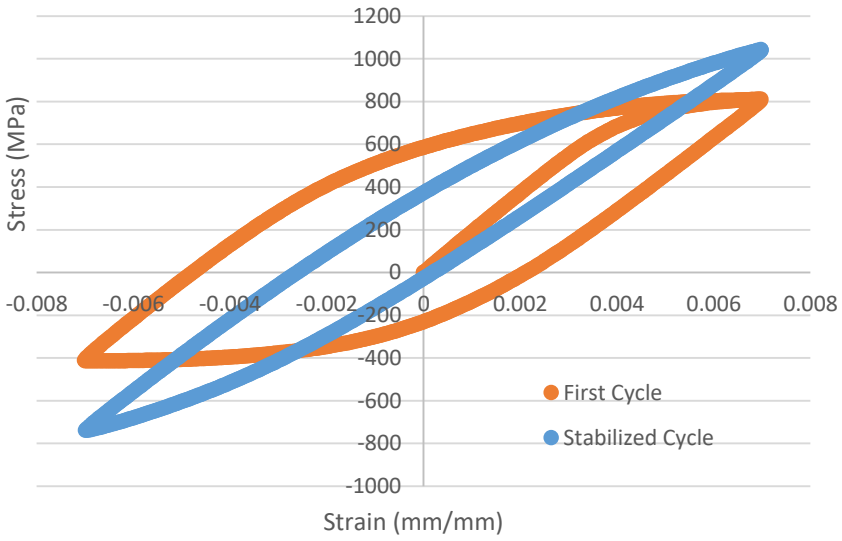

Low Cycle Fatigue Specimen

DMLS SS GP1 Batch 1-Specimen 7

Orientation	Y-Axis	
Cycle	**First**	**Stabilized**
Elastic Modulus, *E* (GPa)	161	136
Stress Range, $\Delta\sigma$ (MPa)	1132	1597
Mean Stress, σ_m (MPa)	34	-56
Plastic Strain Range, Δεp (mm/mm)	0.006935	0.002231
Elastic Strain Range, Δεe (mm/mm)	0.007023	0.011734
Total Strain Range, Δε (mm/mm)	0.013959	0.013964

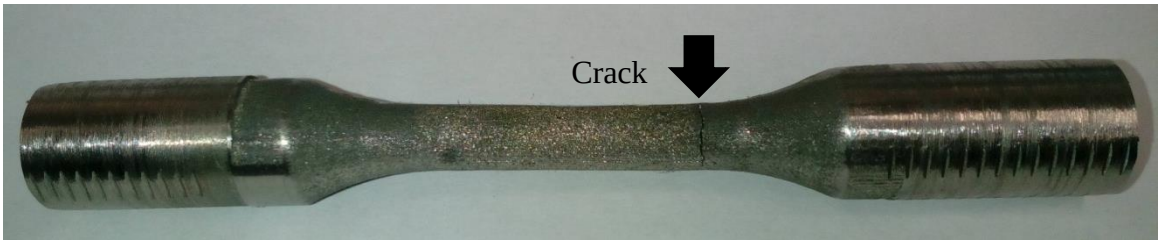

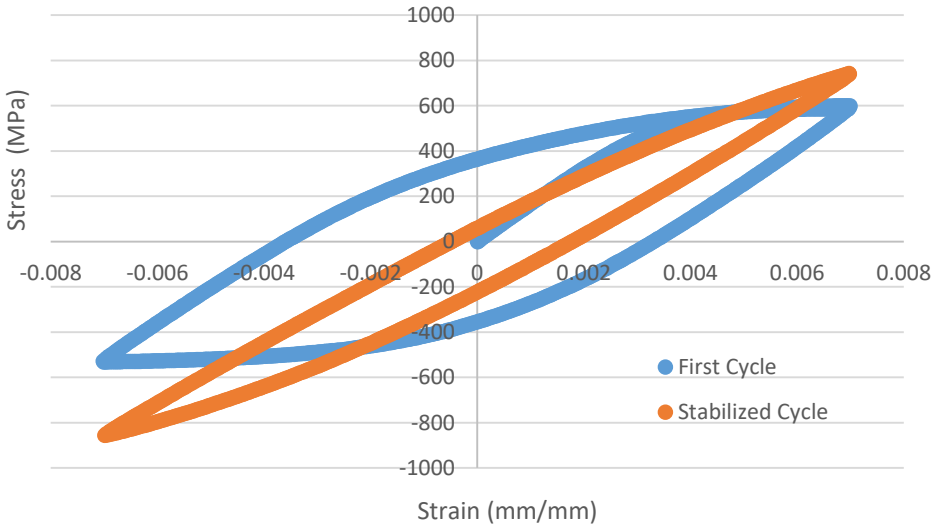

Low Cycle Fatigue Specimen

DMLS SS GP1 Batch 1-Specimen 8

Orientation	Y-Axis	
Cycle	**First**	**Stabilized**
Elastic Modulus, *E* (GPa)	159	138
Stress Range, $\Delta\sigma$ (MPa)	1140	1593
Mean Stress, σ_m (MPa)	48	-41
Plastic Strain Range, Δεp (mm/mm)	0.006803	0.002376
Elastic Strain Range, Δεe (mm/mm)	0.007159	0.011584
Total Strain Range, Δε (mm/mm)	0.01396	0.01396

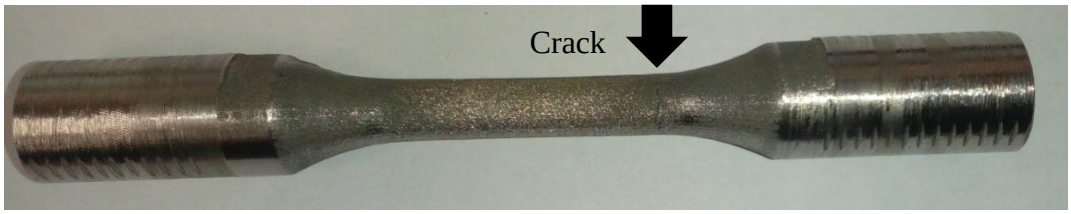

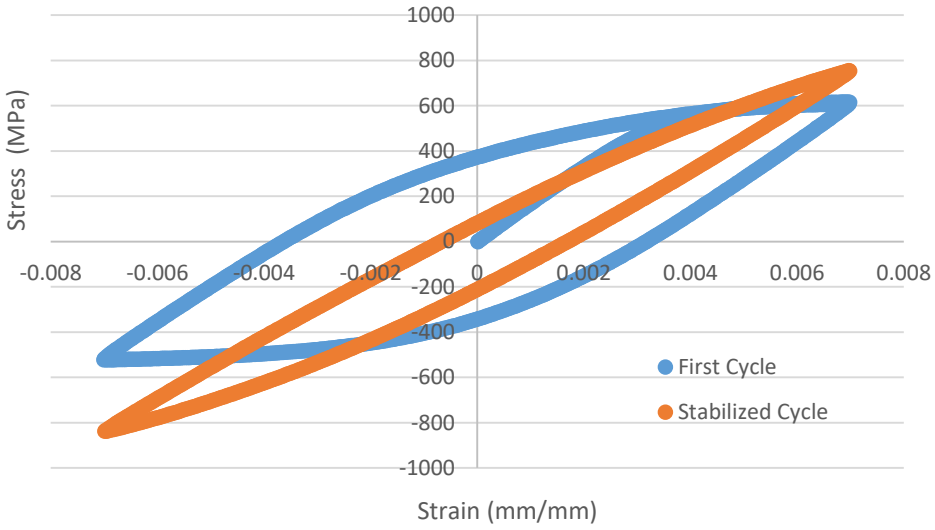

Pulsating Tension Fatigue Specimen

DMLS SS GP1 Batch 2-Specimen 14

Orientation	XY45	
Cycle	**First**	**Stabilized**
Elastic Modulus, *E* (GPa)	190.2796	181.568
Stress Range, $\Delta\sigma$ (MPa)	979.23	1102.66
Mean Stress, σ_m (MPa)	128.97	-59.88
Plastic Strain Range, Δεp (mm/mm)	0.001799	0.0008812
Elastic Strain Range, Δεe (mm/mm)	0.005146	0.00607
Total Strain Range, Δε (mm/mm)	0.0069456	0.006954

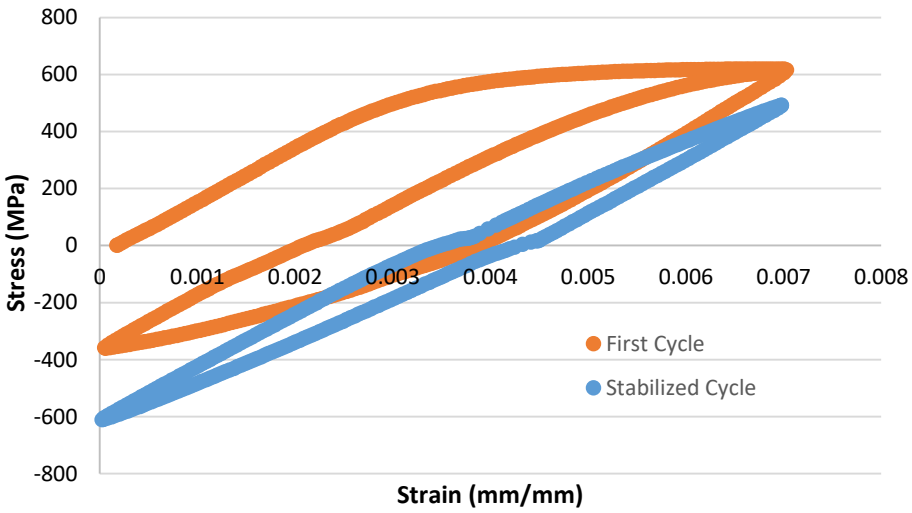

Pulsating Tension Fatigue Specimen

DMLS SS GP1 Batch 2-Specimen 20

Orientation	X-Axis	
Cycle	**First**	**Stabilized**
Elastic Modulus, *E* (GPa)	174.6	161.4
Stress Range, $\Delta\sigma$ (MPa)	934.9696	1019.62
Mean Stress, σ_m (MPa)	140.228	-64.938
Plastic Strain Range, Δεp (mm/mm)	0.001628	0.00064
Elastic Strain Range, Δεe (mm/mm)	0.00535	0.0063
Total Strain Range, Δε (mm/mm)	0.006983	0.00695757

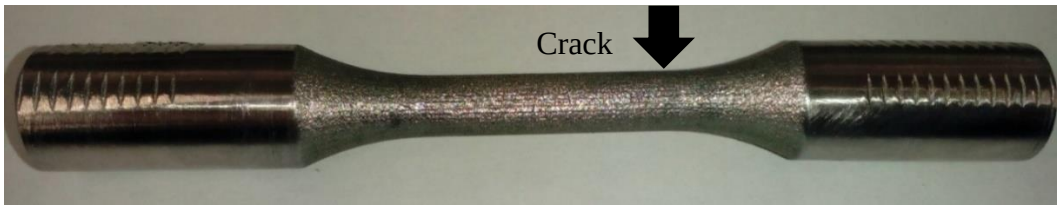

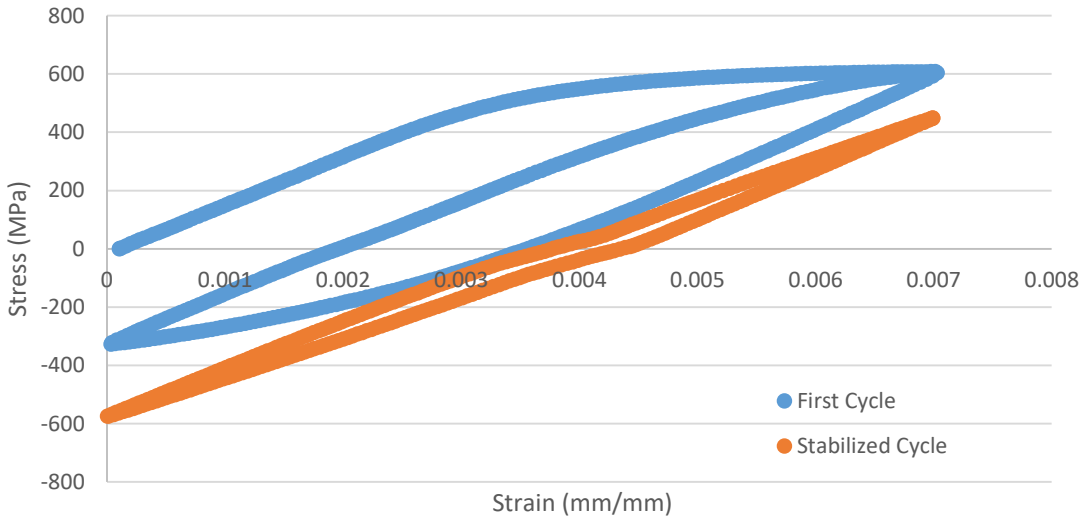

Pulsating Tension Fatigue Specimen

DMLS SS GP1 Batch 2-Specimen 1-Reduced Test Specimen

Orientation	X-Axis	
Cycle	**First**	**Stabilized**
Elastic Modulus, *E* (GPa)	180.118	179.676
Stress Range, $\Delta\sigma$ (MPa)	923	1052.47
Mean Stress, σ_m (MPa)	128.82	-14.5969
Plastic Strain Range, Δεp (mm/mm)	0.001829	0.0011
Elastic Strain Range, Δεe (mm/mm)	0.005124	0.0058576
Total Strain Range, Δε (mm/mm)	0.006953	0.006964

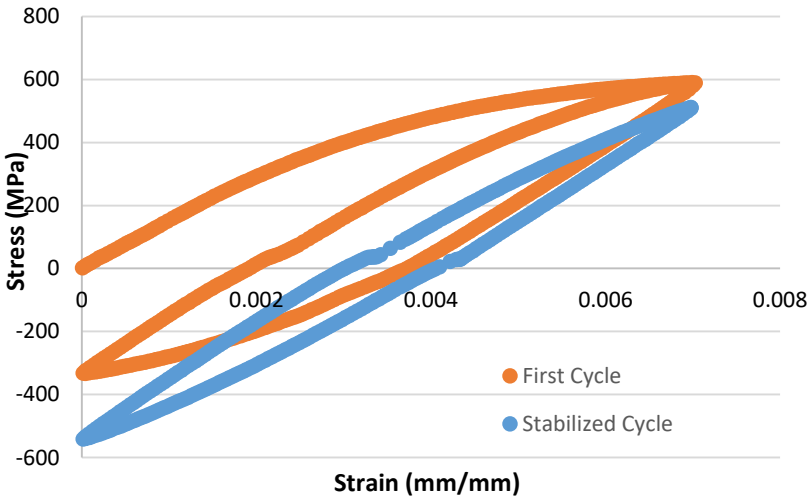

Progressive Amplitude Fatigue Specimen

DMLS SS GP1 Batch 2-Specimen 15

Orientation	XY45		
Cycle	**First (0.6%)**	**First (0.8%)**	**Stabilized (0.6%)**
Elastic Modulus, *E* (GPa)	207.665	227	211.3857
Stress Range, $\Delta\sigma$ (MPa)	893.135	1267.51	1059.7
Mean Stress, σ_m (MPa)	10.1	-40.376	-30.758
Plastic Strain Range, Δεp (mm/mm)	0.001557	0.002265	0.000919
Elastic Strain Range, Δεe (mm/mm)	0.0043	0.0055837	0.005013
Total Strain Range, Δε (mm/mm)	0.0058578	0.007849	0.0059326

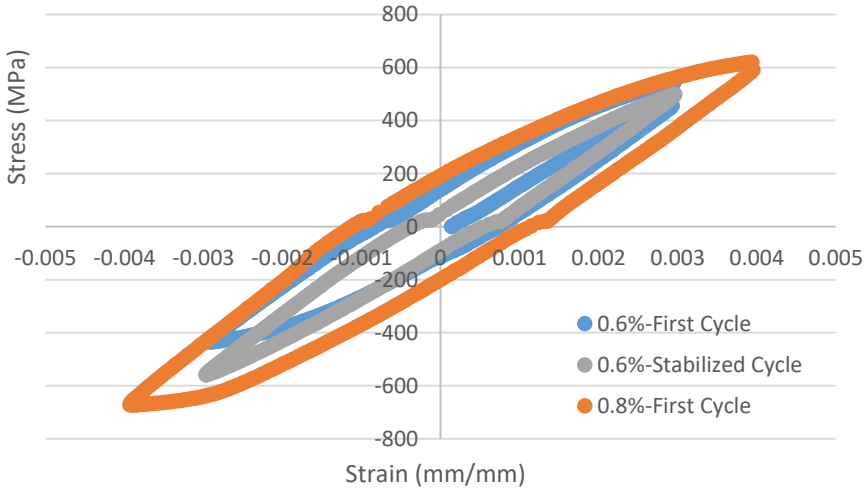

Progressive Amplitude Fatigue Specimen

DMLS SS GP1 Batch 2-Specimen 19

Orientation		X-Axis			
Cycle	**First (0.6%)**	**First (0.8%)**	**First (1.0%)**	**Stabilized (0.6%)**	**Stabilized (0.8%)**
Elastic Modulus, *E* (GPa)	190.266	185.732	189.39	185.495	188.341
Stress Range, $\Delta\sigma$ (MPa)	863.251	1126.53	1436.594	978.9	1322.53
Mean Stress, σ_m (MPa)	66.78	-3.3225	-22.0123	-10.86	-42.73
Plastic Strain Range, Δεp (mm/mm)	0.00131	0.001839	0.0022855	0.00068	0.00092
Elastic Strain Range, Δεe (mm/mm)	0.004537	0.006065	0.007585	0.005277	0.007
Total Strain Range, Δε (mm/mm)	0.005847	0.0079	0.00987	0.005958	0.007942

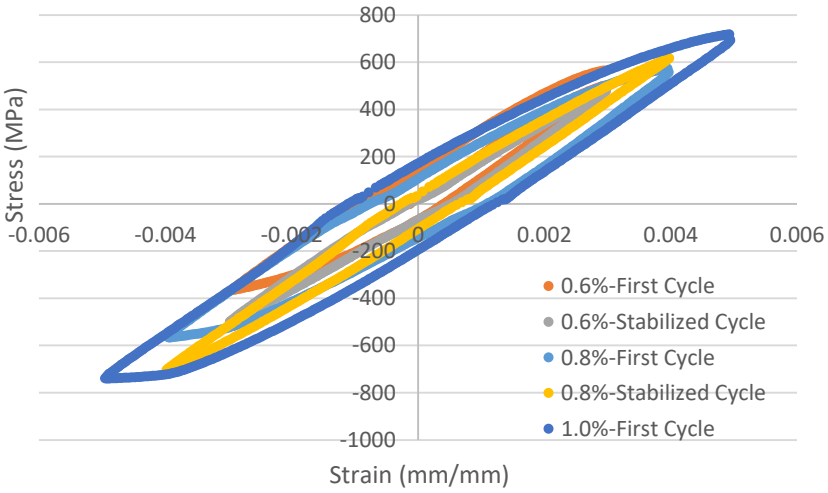

Torsion Specimen

Conventional Inconel 718

Cycle	First	Stabilized
Shear Modulus, *G* (GPa)	69.4596	67.34
Shear Stress Range, $\Delta\tau$ (MPa)	959.886	1129.16
Mean Shear Stress, τ_m (MPa)	-14.137	-9.4905
Twist Range, Δϕ (deg)	29.986	29.8828
Torque Range, ΔT, (N*m)	40.5963	47.7553
Plastic Shear Strain Range, Δγp (mm/mm)	0.01754	0.01449
Elastic Shear Strain Range, Δγe (mm/mm)	0.01382	0.01677
Total Shear Strain Range, Δγ (mm/mm)	0.03136	0.03126

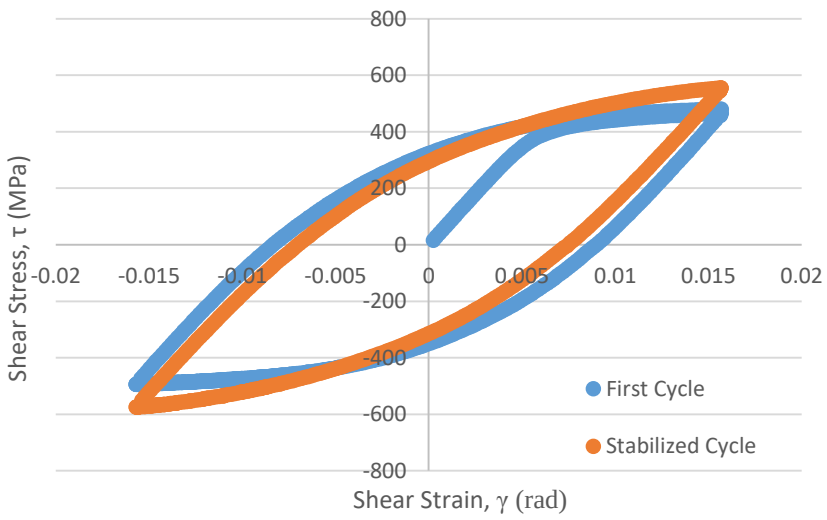

Torsion Specimen

DMLS Inconel 718-Specimen 1 (X)

Cycle	First	Stabilized
Shear Modulus, G (GPa)	60.98	61.99
Shear Stress Range, $\Delta\tau$ (MPa)	1178.65	1305.38
Mean Shear Stress, τ_m (MPa)	4.48	12.77
Twist Range, Δϕ (deg)	30	30
Torque Range, ΔT, (N*m)	48.59	53.81667
Plastic Shear Strain Range, Δγp (mm/mm)	0.01179	0.010058
Elastic Shear Strain Range, Δγe (mm/mm)	0.0193	0.021058
Total Shear Strain Range, Δγ (mm/mm)	0.0311	0.0311

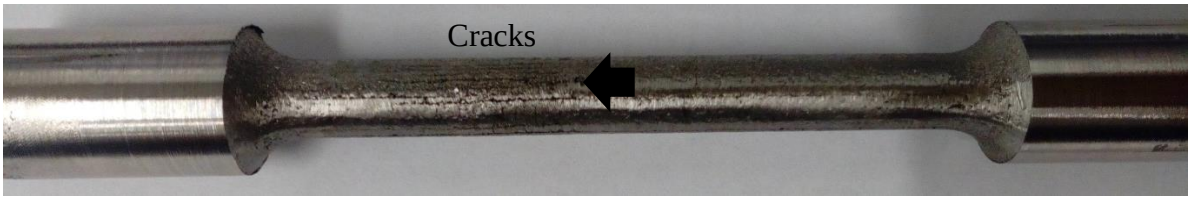

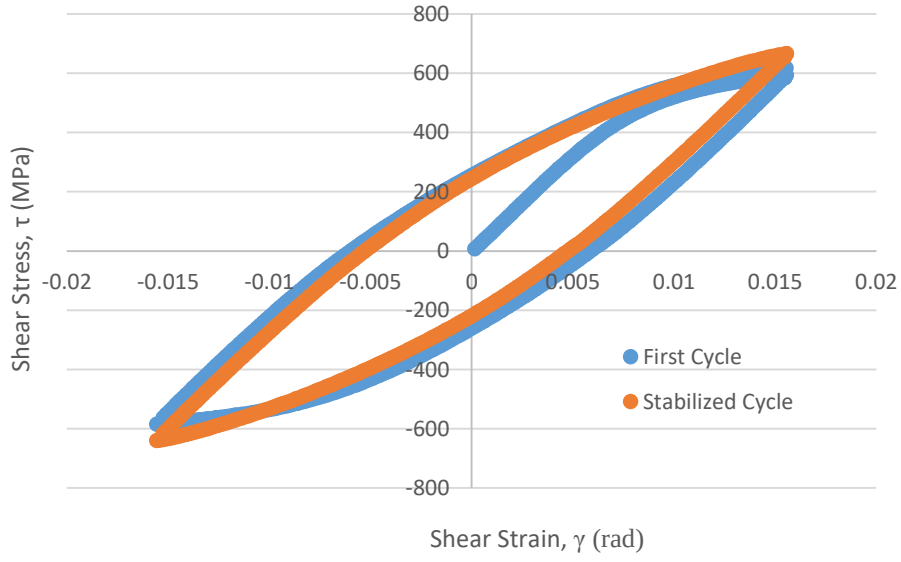

Torsion Specimen

DMLS Inconel 718- Specimen 2 (Y)

Cycle	First	Stabilized
Shear Modulus, G (GPa)	58.88	59.11
Shear Stress Range, $\Delta\tau$ (MPa)	1124.779	1246.44
Mean Shear Stress, τ_m (MPa)	-31.86	-24.61
Twist Range, Δϕ (deg)	30.00365	29.97
Torque Range, ΔT, (N*m)	46.37	51.3866
Plastic Shear Strain Range, Δγp (mm/mm)	0.012	0.009997
Elastic Shear Strain Range, Δγe (mm/mm)	0.0191	0.021085
Total Shear Strain Range, Δγ (mm/mm)	0.0311	0.031082

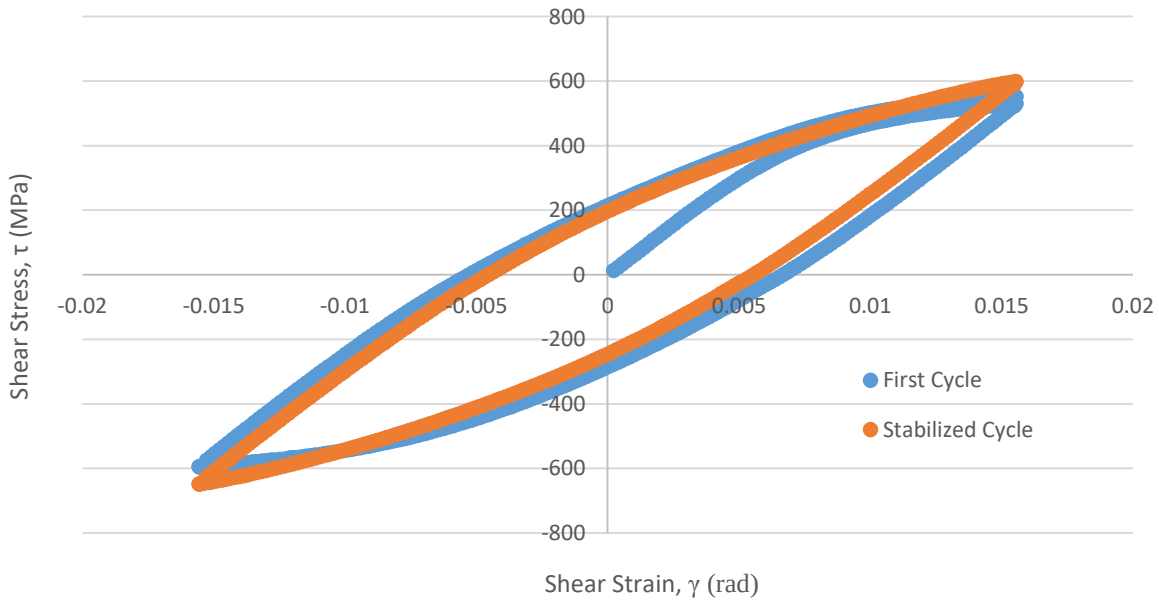

Torsion Specimen

DMLS Inconel 718- Specimen 3 (XY45°)

Cycle	First	Stabilized
Shear Modulus, G (GPa)	58.8966	59.137
Shear Stress Range, $\Delta\tau$ (MPa)	1147.5	1268.36
Mean Shear Stress, τ_m (MPa)	-31.67	-24.07
Twist Range, Δϕ (deg)	29.9795	29.942
Torque Range, ΔT, (N*m)	47.308	52.2904
Plastic Shear Strain Range, Δγp (mm/mm)	0.01161	0.0096
Elastic Shear Strain Range, Δγe (mm/mm)	0.01948	0.02145
Total Shear Strain Range, Δγ (mm/mm)	0.03109	0.03105

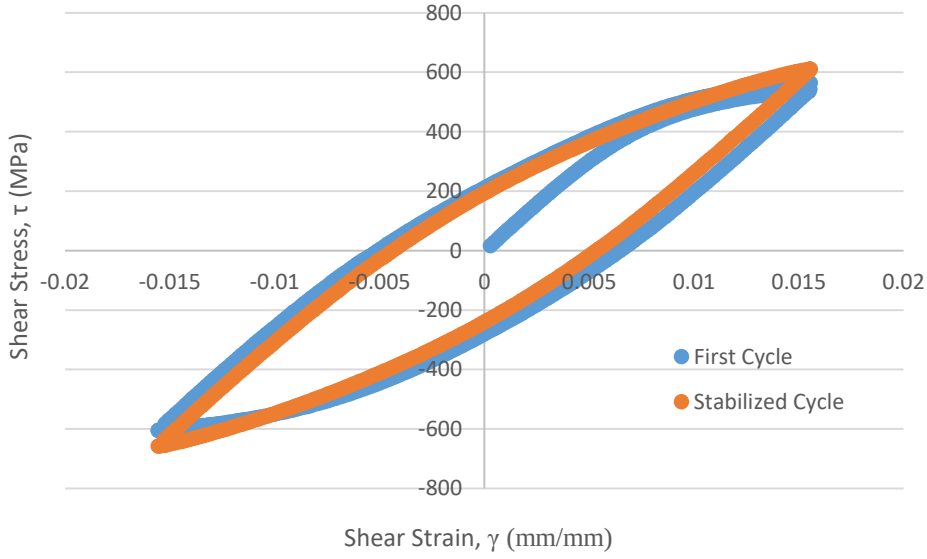

Torsion Specimen

DMLS Inconel 718- Specimen 4 (XZ45°)

Cycle	First	Stabilized
Shear Modulus, *G* (GPa)	46.91	47.1778
Shear Stress Range, $\Delta\tau$ (MPa)	909.29	1041.975
Mean Shear Stress, τ_m (MPa)	9.3298	20.4957
Twist Range, Δϕ (deg)	29.986	29.977
Torque Range, ΔT, (N*m)	38.4566	44.068
Plastic Shear Strain Range, Δγp (mm/mm)	0.01198	0.009269
Elastic Shear Strain Range, Δγe (mm/mm)	0.01938	0.022086
Total Shear Strain Range, Δγ (mm/mm)	0.03136	0.031355

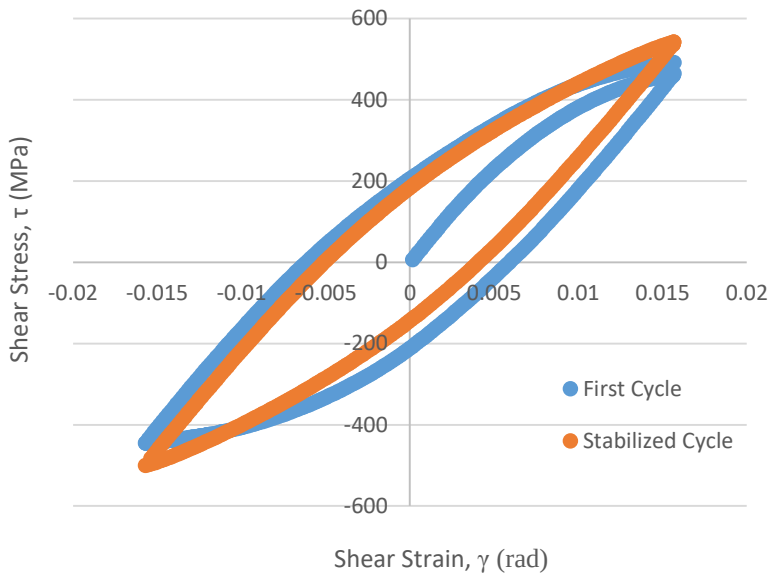

Torsion Specimen

DMLS Inconel 718- Specimen 5 (YZ45°)

Cycle	First	Stabilized
Shear Modulus, G (GPa)	51.34	51.224
Shear Stress Range, $\Delta\tau$ (MPa)	952.72	1114
Mean Shear Stress, τ_m (MPa)	-24.23	-15.7457
Twist Range, $\Delta\phi$ (deg)	29.99	29.99
Torque Range, ΔT, (N*m)	39.783	46.518
Plastic Shear Strain Range, $\Delta\gamma p$ (mm/mm)	0.012687	0.009493
Elastic Shear Strain Range, $\Delta\gamma e$ (mm/mm)	0.018557	0.021748
Total Shear Strain Range, $\Delta\gamma$ (mm/mm)	0.031245	0.03124

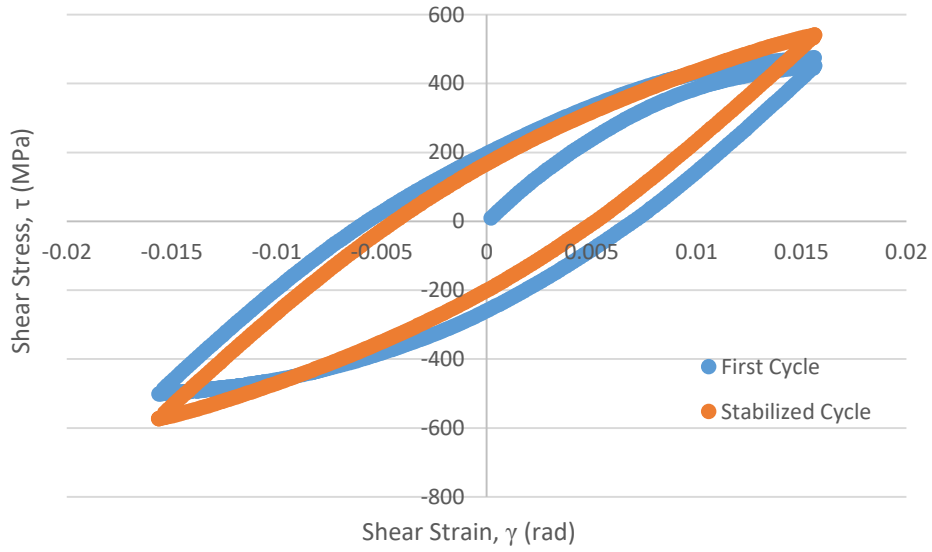

Torsion Specimen

DMLS Inconel 718- Specimen 6 (Z)

Cycle	First	Stabilized
Shear Modulus, *G* (GPa)	70.844	69.552
Shear Stress Range, $\Delta\tau$ (MPa)	1212.7	1371.672
Mean Shear Stress, τ_m (MPa)	-14.8	-19.59
Twist Range, Δϕ (deg)	29.9	29.968
Torque Range, ΔT, (N*m)	49.676	56.187
Plastic Shear Strain Range, Δγp (mm/mm)	0.01383	0.01129
Elastic Shear Strain Range, Δγe (mm/mm)	0.017118	0.01972
Total Shear Strain Range, Δγ (mm/mm)	0.030948	0.031014

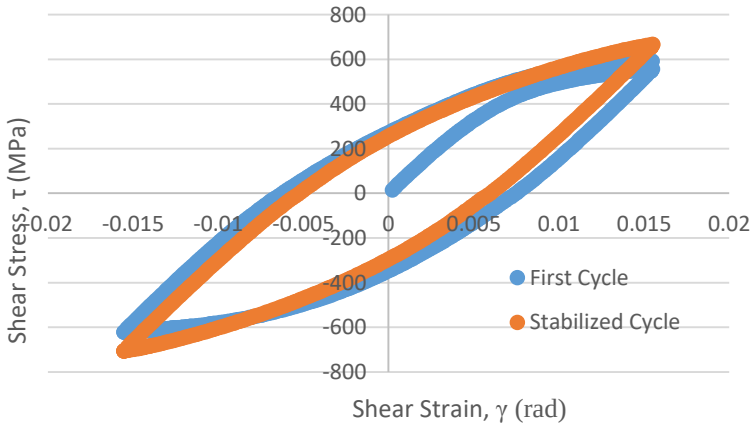

Surface Roughness Data

DMLS Stainless Steel GP1

(Y)

Roughness	Scan 1	Scan 2	Scan 3
Ra (µm)	8.1022	6.5099	8.6489
Rq (µm)	8.9004	7.2199	9.5520

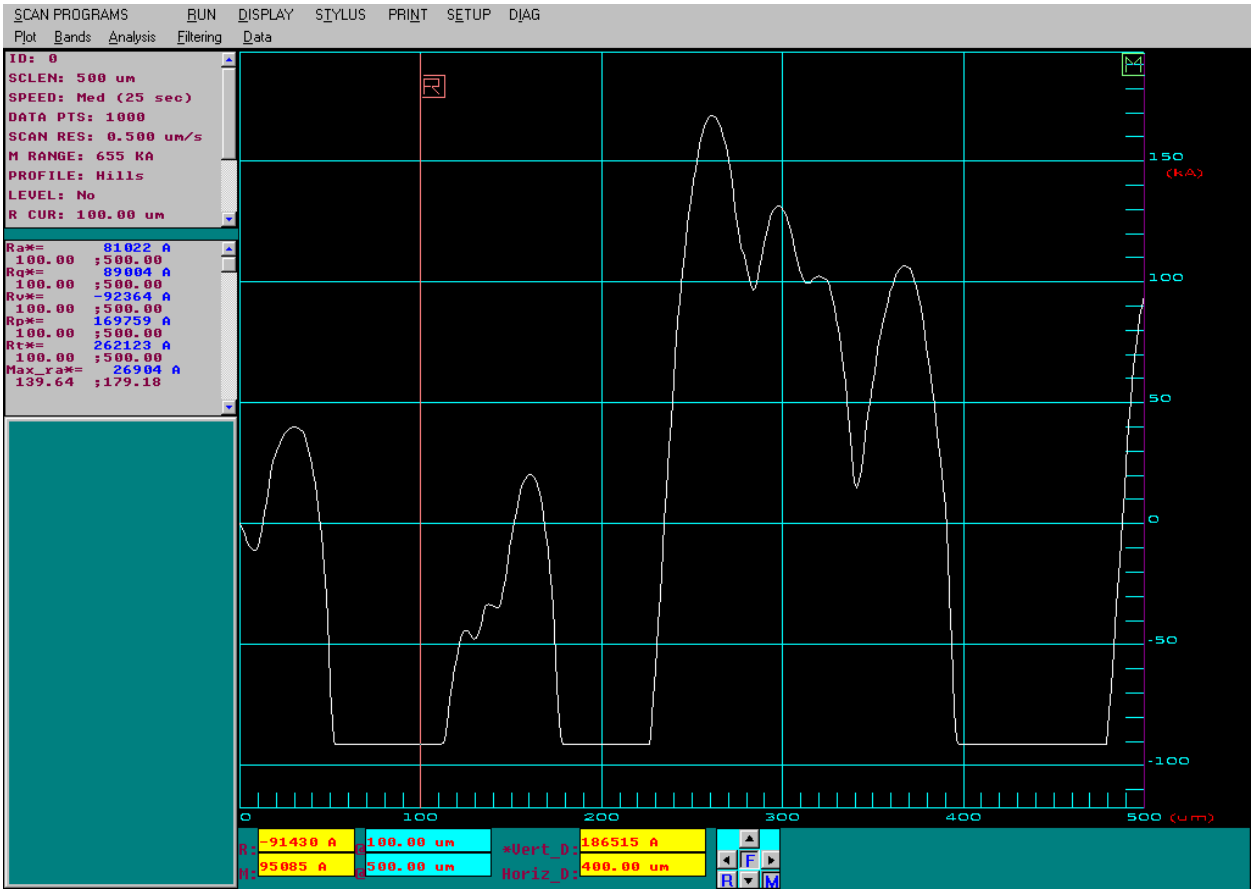

(Note: Image of single roughness measurement, out of combined total of 3 measurements at same location on specimen)

Surface Roughness Data

DMLS Stainless Steel GP1

(XY45)

Roughness	Scan 1	Scan 2	Scan 3
Ra (µm)	7.2699	7.5486	6.3037
Rq (µm)	8.8887	9.3600	8.1908

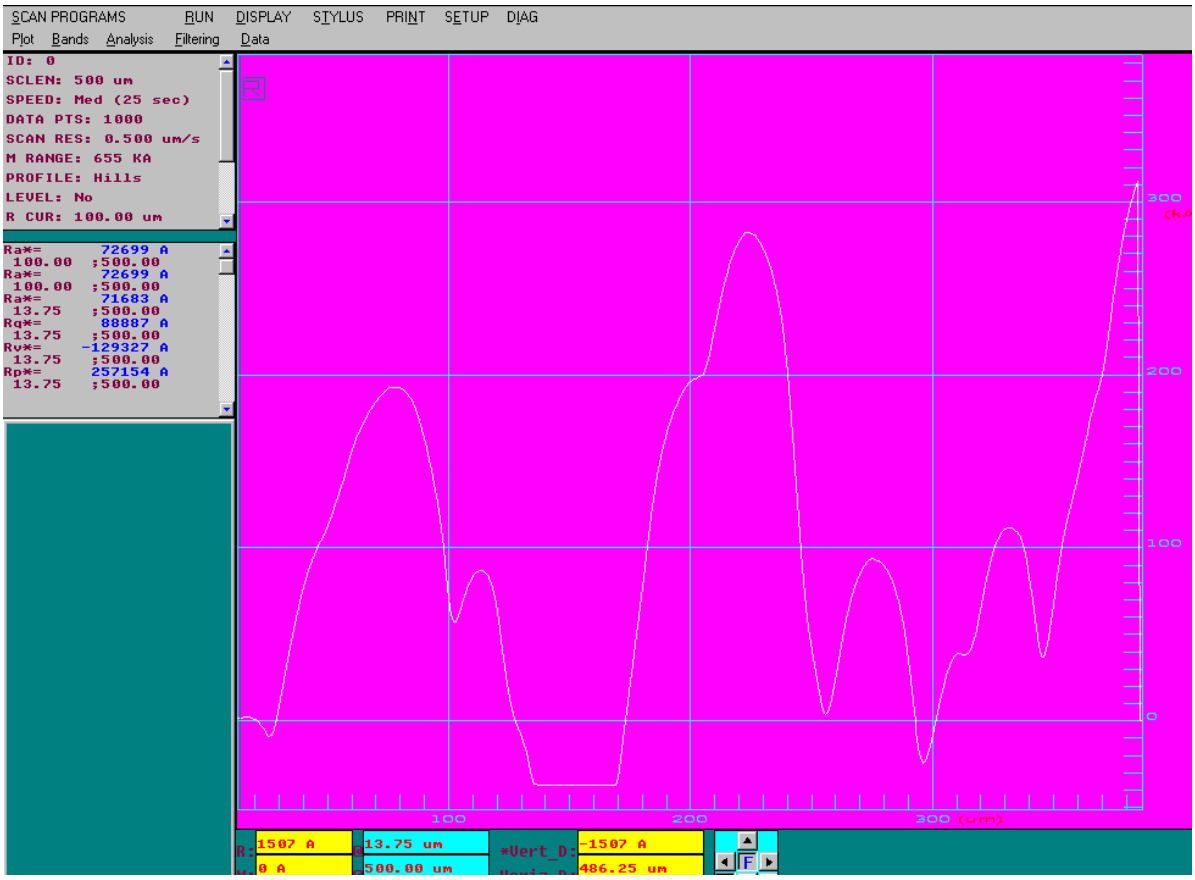

(Note: Image of single roughness measurement, out of combined total of 3 measurements at same location on specimen)

Surface Roughness Data

DMLS Stainless Steel GP1

(X)

Roughness	Scan 1	Scan 2	Scan 3
Ra (µm)	4.3048	5.7527	6.5505
Rq (µm)	5.0054	6.6555	7.7052

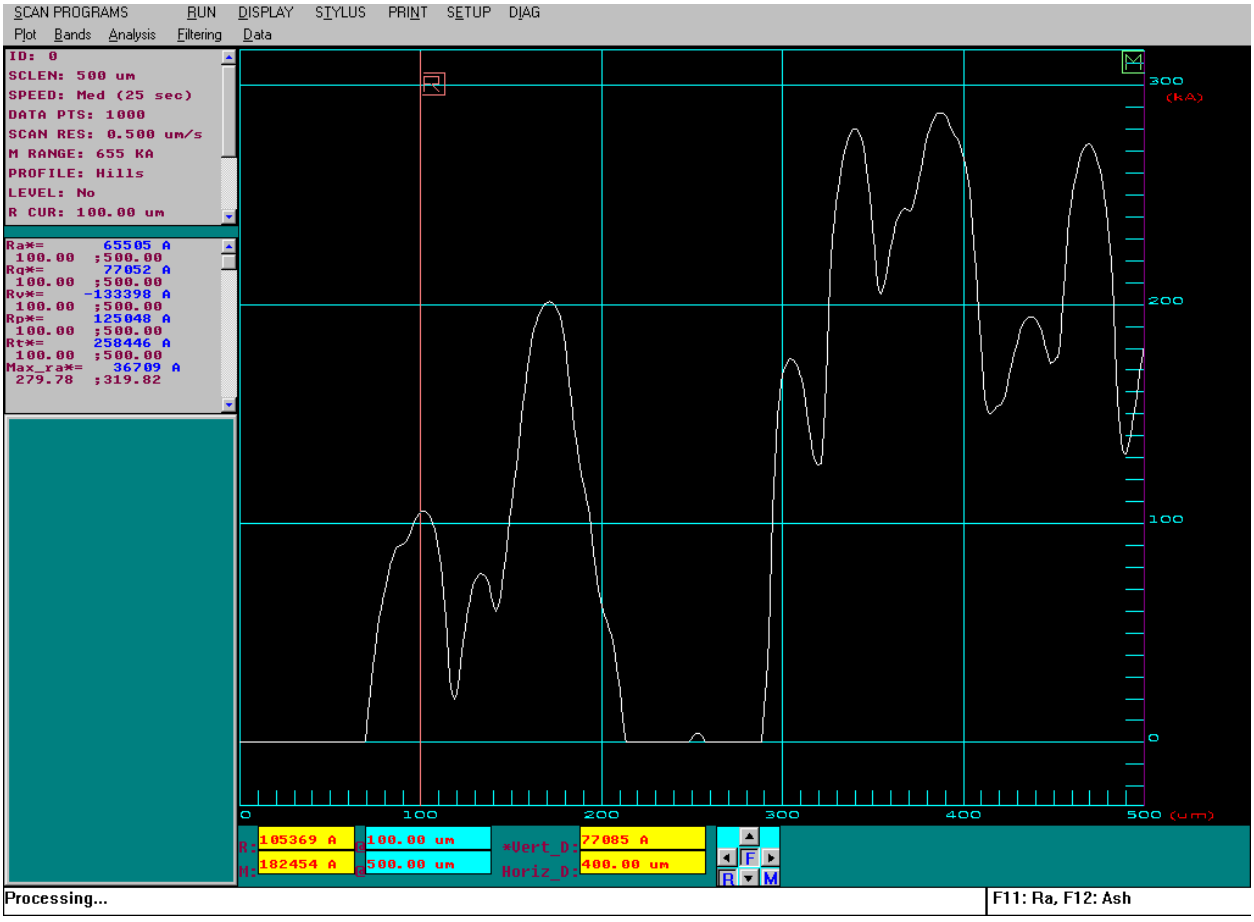

(Note: Image of single roughness measurement, out of combined total of 3 measurements at same location on specimen)

Surface Roughness Data

DMLS Inconel 718

(Z)

Roughness	Scan 1	Scan 2	Scan 3
Ra (µm)	2.4976	2.5318	2.176
Rq (µm)	2.8797	2.863	2.5306

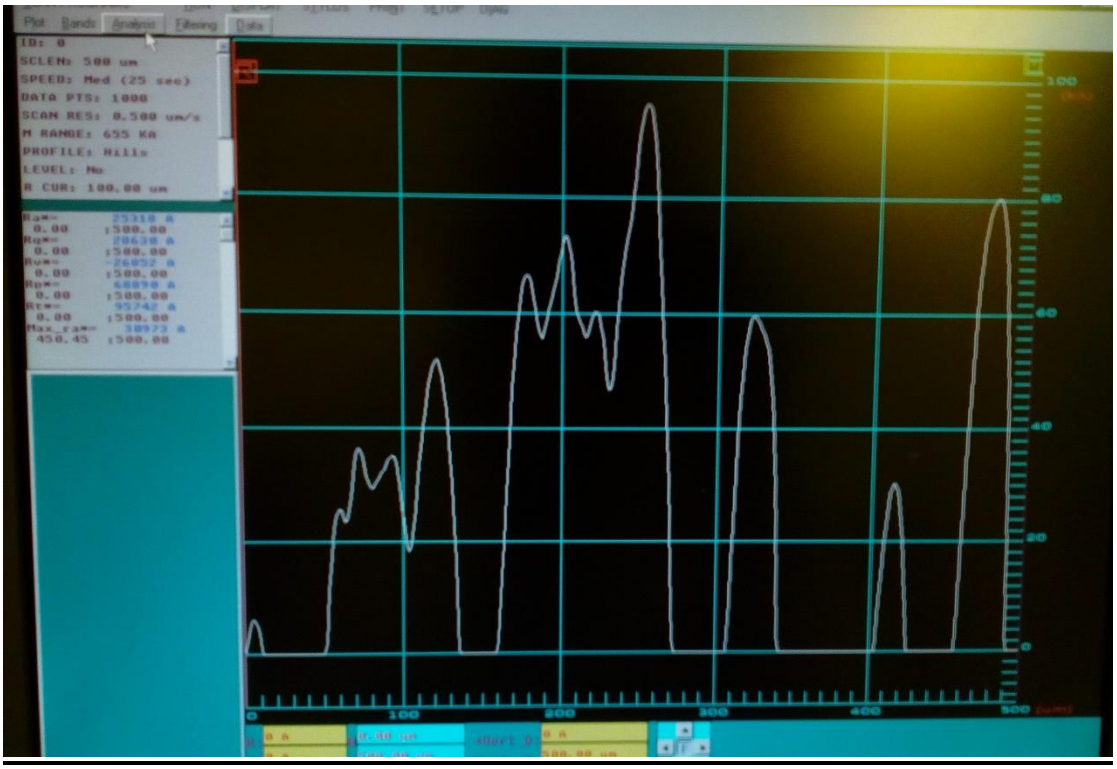

(Note: Image of single roughness measurement, out of combined total of 3 measurements at same location on specimen)

Surface Roughness Data

DMLS Inconel 718

(Y)

Roughness	Scan 1	Scan 2	Scan 3
Ra (µm)	5.7152	5.8499	5.3362
Rq (µm)	7.3356	7.5194	6.9488

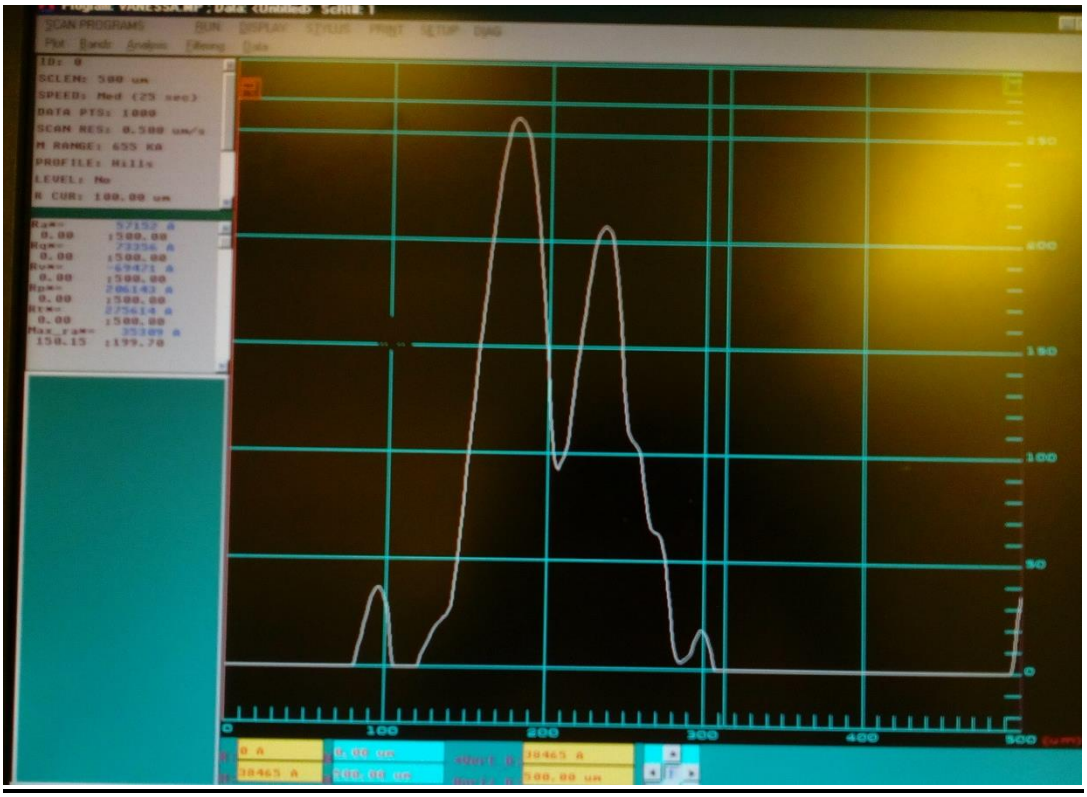

(Note: Image of single roughness measurement, out of combined total of 3 measurements at same location on specimen)

Surface Roughness Data

DMLS Inconel 718

(X)

Roughness	Scan 1	Scan 2	Scan 3
Ra (µm)	4.7886	4.8565	4.9488
Rq (µm)	7.5750	7.6735	7.8059

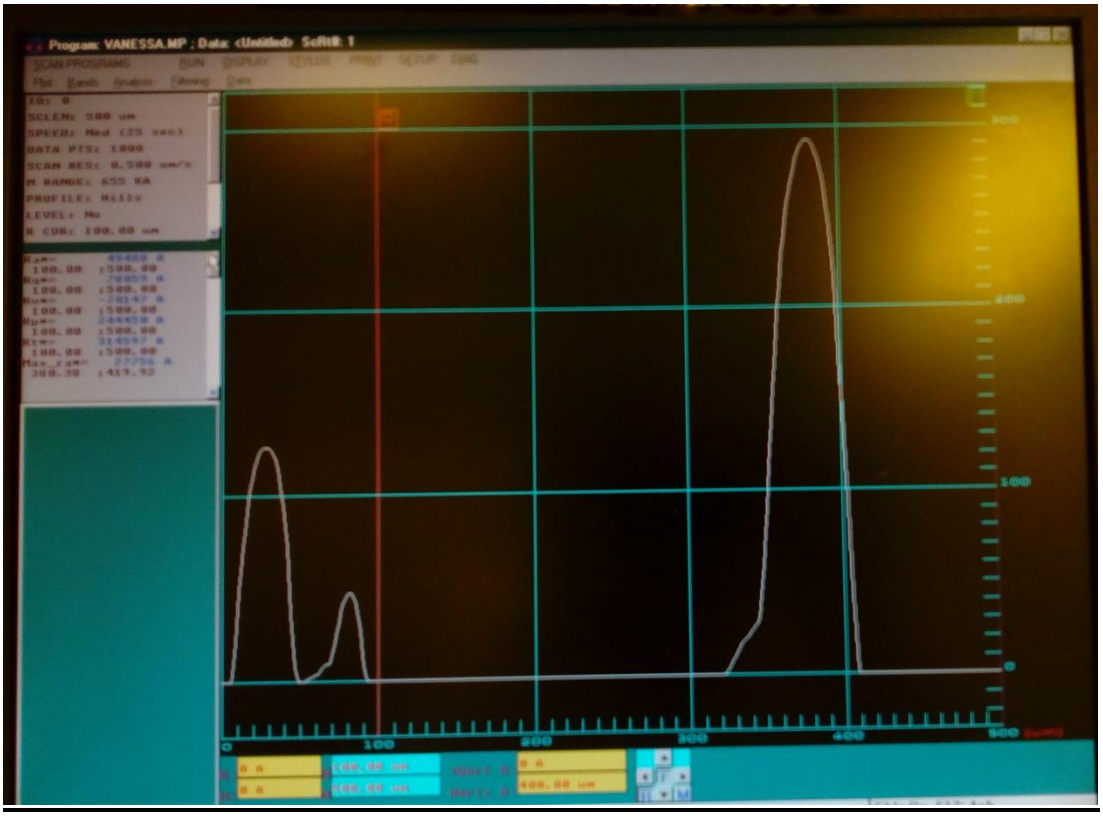

(Note: Image of single roughness measurement, out of combined total of 3 measurements at same location on specimen)

APPENDIX C: CONSTITUITVE MODELING

Hill's Surface Modeling

DMLS SS GP1-(XY) Plane

Upper Yield Strength Surface Determination from Hill's Theory

R values are the strength ratios between a given orientation and reference orientation

T represents the 'y' or (010) direction L represents the 'x' direction or (100).

DMLS SS GP1- "As-Built" Note : Used Main Yield Stress Rounded Values -Does not include error range

$\sigma_L := 597\text{MPa}$ Monotonic Upper Yield Stress in (100) Direction or x-direction

$\sigma_T := 698\text{MPa}$ Monotonic Upper Yield Stress in (010) Direction or y-direction

$\sigma_{45} := 597\text{MPa}$ Monotonic Upper Yield Stress in (110) Direction

$\sigma_0 := 597\text{MPa}$ Reference upper yield stress based upon using x-direction as reference direction, (L)

$\sigma_z := 630\text{MPa}$ Monotonic Typical Upper Yield Stress in (001) Direction given by EOS Stainless Steel GP1 Data Sheet

Strength Ratios

$$R_{LL} := \frac{\sigma_L}{\sigma_0} = 1 \qquad R_{TT} := \frac{\sigma_T}{\sigma_0} = 1.169$$

$$R_{yy} := R_{TT} = 1.169 \qquad R_{xx} := R_{LL} = 1 \qquad R_{zz} := \frac{\sigma_z}{\sigma_0} = 1.055$$

Hill's Constants

$$F := \frac{1}{2}\left(\frac{1}{R_{yy}^2} + \frac{1}{R_{zz}^2} - \frac{1}{R_{xx}^2}\right) = 0.315 \qquad N := 1.0145$$

Value of 'N' gives value expected for 45 deg. orientation on yield surface plot.

$$G := \frac{1}{2}\cdot\left(\frac{1}{R_{zz}^2} + \frac{1}{R_{xx}^2} - \frac{1}{R_{yy}^2}\right) = 0.583$$

$$H := \frac{1}{2}\cdot\left(\frac{1}{R_{xx}^2} + \frac{1}{R_{yy}^2} - \frac{1}{R_{zz}^2}\right) = 0.417$$

Defining General Equations of Plane-Stress Transformation for xy plane

$$S_{yy} := 1 \qquad S_{xy} := 0 \qquad S_{xx} := 0 \qquad \theta := 0, 0.01 .. 2\pi$$

$$\sigma_{y'}(\theta) := \frac{S_{yy} + S_{xx}}{2} + \frac{S_{yy} - S_{xx}}{2} \cdot \cos(2\theta) + S_{xy} \cdot \sin(2\theta)$$

$$\sigma_{x'}(\theta) := \frac{S_{yy} + S_{xx}}{2} - \frac{S_{yy} - S_{xx}}{2} \cdot \cos(2\theta) - S_{xy} \cdot \sin(2\theta)$$

$$\sigma_{x'y'}(\theta) := -\frac{S_{yy} - S_{xx}}{2} \sin(2\theta) + S_{xy} \cdot \cos(2\theta)$$

Defined Hill's Equation for case of plane stress in the xy plane

$$\sigma_{Hill}(\theta) := \sqrt{F \cdot \left(\sigma_{y'}(\theta)\right)^2 + G \cdot \left(-\sigma_{x'}(\theta)\right)^2 + H \cdot \left(\sigma_{x'}(\theta) - \sigma_{y'}(\theta)\right)^2 + 2N \cdot \left(\sigma_{x'y'}(\theta)\right)^2}$$

$$Yield_{Surface}(\theta) := \sigma_{Hill}(\theta) \cdot \sigma_T$$

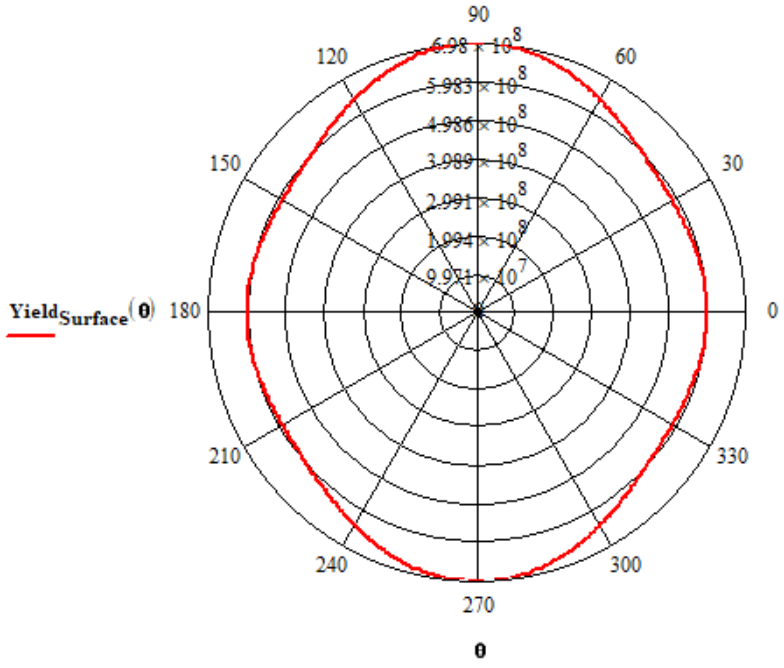

Hahn's Plasticity Modeling of Monotonic Response

DMLS SS GP1 (X)

Fit Options

Method:	NonlinearLeastSquares
Robust:	Off
Algorithm:	Trust-Region
DiffMinChange:	1e-08
DiffMaxChange:	0.1
MaxFunEvals:	600
MaxIter:	400
TolFun:	1e-06
TolX:	1e-06

Coefficients	StartPoint	Lower	Upper
C	470000	-Inf	470000
a	1.5000	0.7000	1.5000
b	3.0000e-08	1.0000e-08	3.0000e-08
n	9.5000	9	35
p	110	100	300
q	3250	2500	4000
t	155	100	250

Results

General model:

f(x,y) = q*x + 2*t*((y)/(0.5*b*(p+C*(x)^(a))))^(1/n)

Coefficients (with 95% confidence bounds):

C = 4.7e+05 (fixed at bound)

a = 1.5 (fixed at bound)

b = 3e-08 (fixed at bound)

n = 9 (fixed at bound)

p = 160.9 (142.6, 179.2)

q = 3266 (3250, 3282)

t = 152.4 (151.6, 153.2)

Hahn's Plasticity Modeling of Monotonic Response

DMLS SS GP1 (Y)

Fit Options

Method:	NonlinearLeastSquares
Robust:	Off
Algorithm:	Trust-Region
DiffMinChange:	1e-08
DiffMaxChange:	0.1
MaxFunEvals:	600
MaxIter:	400
TolFun:	1e-06
TolX:	1e-06

Coefficients	StartPoint	Lower	Upper
C	470000	-Inf	Inf
a	1.5000	0.7000	1.5000
b	2.6940e-08	1.0000e-08	3.0000e-08
n	7	7	35
p	255	100	300
q	3700	2500	4000
t	163	100	250

Results

General model:

f(x,y) = q*x +2*t*((y)/(0.5*b*(p+C*(x)^(a))))^(1/n)

Coefficients (with 95% confidence bounds):

C = 4.7e+05 (-6.65e+10, 6.65e+10)

a = 1.5 (fixed at bound)

b = 2.808e-08 (fixed at bound)

n = 7 (6.731, 7.269)

p = 255 (-3.608e+07, 3.608e+07)

q = 3700 (3660, 3740)

t = 163 (-3.295e+06, 3.295e+06)

Hahn's Plasticity Modeling of Monotonic Response

DMLS SS GP1 (XY45°)

Fit Options

Method:	NonlinearLeastSquares
Robust:	Off
Algorithm:	Trust-Region
DiffMinChange:	1e-08
DiffMaxChange:	0.1
MaxFunEvals:	600
MaxIter:	400
TolFun:	1e-06
TolX:	1e-06

Coefficients	StartPoint	Lower	Upper
C	470000	470000	Inf
a	1.5000	0.7000	1.5000
b	2.9980e-08	1.0000e-08	3.0000e-08
n	6	6	35
p	288.8000	100	300
q	3813	2500	4000
t	124	100	250

Results

General model:

f(x,y) = q*x + 2*t*((y)/(0.5*b*(p+C*(x)^(a))))^(1/n)

Coefficients (with 95% confidence bounds):

C = 4.7e+05 (fixed at bound)

a = 1.5 (1.406, 1.594)

b = 3e-08 (fixed at bound)

n = 6 (5.698, 6.302)

p = 288.8 (180.8, 396.8)

q = 3813 (3780, 3846)

t = 124 (119.3, 128.7)

Hill's Surface Modeling

SLM Inconel 718 (YZ)

Yield Surface Determination from Hill's Theory

R values are the strength ratios between a given orientation and reference orientation

L represents the 'z' or build direction (001)

T represents the 'y' or 'x' direction (010) or (100). Since Chelbus uses the y-direction, assume orientation is (010) for this study.

Reference: Chlebus et al. 2015

SLM IN718- "As-Built" Note : Used Main Yield Stress Value-Does not include error range

$\sigma_L := 572MPa$ Monotonic 0.2% Yield Stress in (001) Direction

$\sigma_T := 643MPa$ Monotonic 0.2% Yield Stress in (010) Direction

$\sigma_{45} := 590MPa$ Monotonic 0.2% Yield Stress in (011) Direction

$\sigma_0 := 572MPa$ Reference yield stress based upon using z-direction as reference direction

Strength Ratios

$R_{LL} := \frac{\sigma_L}{\sigma_0} = 1$ $R_{TT} := \frac{\sigma_T}{\sigma_0} = 1.124$

$R_{zz} := R_{LL} = 1$ $R_{yy} := R_{TT}$

$R_{xx} := R_{yy} = 1.124$

$R_{LT.s} := 1.079$ Need a yield stress in shear of 356.334MPa if we assume that yield stress in shear is 0.6 (Yield stress in tension)

$R_{zx} := R_{LT.s}$ $R_{yz} := R_{zx}$ $R_{xz} := R_{zx}$ $R_{xy} := R_{TT}$

Hill's Constants

$$F := \frac{1}{2}\left(\frac{1}{R_{yy}^{2}} + \frac{1}{R_{zz}^{2}} - \frac{1}{R_{xx}^{2}}\right) = 0.5 \qquad L := \frac{3}{2}\cdot\left(\frac{1}{R_{yz}^{2}}\right) = 1.288$$

$$G := \frac{1}{2}\cdot\left(\frac{1}{R_{zz}^{2}} + \frac{1}{R_{xx}^{2}} - \frac{1}{R_{yy}^{2}}\right) = 0.5 \qquad M := \frac{3}{2}\cdot\left(\frac{1}{R_{xz}^{2}}\right) = 1.288$$

$$H := \frac{1}{2}\cdot\left(\frac{1}{R_{xx}^{2}} + \frac{1}{R_{yy}^{2}} - \frac{1}{R_{zz}^{2}}\right) = 0.291 \qquad N := F + 2H = 1.083$$

Defining General Equations of Plane-Stress Transformation

$$S_{yy} := 1 \qquad S_{yz} := 0 \qquad S_{zz} := 0 \qquad \theta := 0, 0.01 .. 2\pi$$

$$\sigma_{y'}(\theta) := \frac{S_{yy} + S_{zz}}{2} + \frac{S_{yy} - S_{zz}}{2}\cdot\cos(2\theta) + S_{yz}\cdot\sin(2\theta)$$

$$\sigma_{z'}(\theta) := \frac{S_{yy} + S_{zz}}{2} - \frac{S_{yy} - S_{zz}}{2}\cdot\cos(2\theta) - S_{yz}\cdot\sin(2\theta)$$

$$\sigma_{y'z'}(\theta) := -\frac{S_{yy} - S_{zz}}{2}\sin(2\theta) + S_{yz}\cdot\cos(2\theta)$$

$$\sigma_{Hill}(\theta) := \sqrt{F\cdot\left(\sigma_{y'}(\theta) - \sigma_{z'}(\theta)\right)^{2} + G\cdot\left(\sigma_{z'}(\theta)\right)^{2} + H\cdot\left(-\sigma_{y'}(\theta)\right)^{2} + 2L\cdot\left(\sigma_{y'z'}(\theta)\right)^{2}}$$

$$Yield_{Surface}(\theta) := \sigma_{Hill}(\theta)\cdot\sigma_{T}$$

LIST OF REFERENCES

Ahn, D., Kweon, J. H., Kwon, S., Song, J., & Lee, S. (2009). Representation of surface roughness in fused deposition modeling. *Journal of Materials Processing Technology*, *209* (15), 5593-5600.

Amato, K. N., Gaytan, S., Murr, L., Martinez, E., Shindo, P., Hernandez, J., Collins, S. & Medina, F. (2012). Microstructures and mechanical behavior of Inconel 718 fabricated by selective laser melting. *Acta Materialia*, *60*, 2229-2239.

Anitha, R., Arunachalam, S., & Radhakrishan, P. (2001). Critical parameters influencing the quality of prototypes in fused deposition modelling. *Journal of Materials Processing Technology*, *118*(1), 385-388.

AK Steel Corporation. (2007). Product Data Sheet 17-4PH Stainless Steel.

Armillotta, A. (2006). Assessment of surface quality on textured FDM prototypes. *Rapid Prototyping Journal*, *12*(1), 35-41.

ASTM Standard. (2012). Designation: F2792-12a: Standard Terminology for Additive Manufacturing Technologies.

ASTM Standard. (2013). Designation: E2714-13: Standard Test Method for Creep-Fatigue Testing.

ASTM Standard. (2015). Designation: E8/E8M-15a: Standard Test Methods for Tension Testing of Metallic Materials.

ASTM Standard. (2015). Designation: E407-07. Standard Practice for Microetching Metals and Alloys.

Averyanova, M., Betrand, P., & Verquin, B. (2010). Effect of initial power properties on final microstructure and mechanical properties of parts manufactured by selective laser

melting. *Annals of DAAAM for 2010 & Proceedings of the 21st International DAAAM Symposium*, *21*(1), 1-2.

Aydinoz, M. E., Brenne, F., Schaper, M., Schaak, C., Tillmann, W., Nellesen, J., & Niendorf, T. (2016). On the microstructural and mechanical properties of post-treated additively manufactured Inconel 718 superalloy under quasi-static and cyclic loading. *Materials Science & Engineering A*, *669*, 246-258.

Bakar, N. S. A., Alkahari, M. R., & Boejang, H. (2010) Analysis of fused deposition modelling performance. *Journal of Zhejiang University-Science A*, *11*(12), 972-977.

Brodin, H., Andersson, O., & Johansson, S. (2013). Mechanical Behavior and Microstructure Correlation in a Selective Laser Melted Superalloy. *Proceedings of ASME Turbo Expo 2013: Turbine Technical Conference and Exposition*, San Antonio, Texas, USA, 1-7.

Bouchenot, T., Gordon, A.P., Shinde, S., & Gravett, P. (2014). Approach for Stabilized Peak/Valley Stress Modeling of Non-Isothermal Fatigue of a DS Ni-Base Superalloy. *Materials Performance and Characterization*, *3*(2), 16-43.

BUEHLER SUM-MET The Science Behind Materials Preparation. (2007). A Guide to Materials Preparation and Analysis, BUEHLER LTD.

Cao, J., Liu, F., Lin, X., Huang, C., Chen, J., & Huang, W. (2013). Effect of overlap rate on recrystallization behaviors of Laser Solid Formed Inconel 718 superalloy. *Optics & Laser Technology*, *45*, 228-235.

Carter, L. N., Essa, K., & Attallah, M. M. (2015). Optimisation of selective laser melting for a high temperature Ni-superalloy. *Rapid Prototyping Journal*, *21*(4), 423-432.

Carter, L. N., Wang, X., Read, N., Khan, R., Segerra, M. A., Essa, K., & Attallah, M. M. (2015). Process Optimisation of Selective Laser Melting using Energy Density Model for Nickel-based Superalloys. *Materials Science and Technology*, *32*(7), 657-661.

Carter, L.N., Martin, C., Withers, P.J., & Attallah, M.M. (2014). The influence of the laser scan strategy on grain structure and cracking behavior in SLM powder-bed fabricated nickel superalloy. *Journal of Alloys and Compounds, 615,* 338-347.

Chaboche, J. L., & Rousselier, G. (1983). On the Plastic and Viscoplastic Constitutive Equations- Part 1: Rules Developed with Internal Variable Concept. *Journal of Pressure Vessel Technology*, *105,* 153-158.

Chaboche, J. L. (1989). Constitutive Equations for Cyclic Plasticity Viscoplasticity. *International Journal of Plasticity*, *5*(3), 247-302.

Chen, R., Ramachandran, A., Liu, C., Chang, F.K., & Senesky, D. (2017). Tsai-Wu Analysis of a Thin-Walled 3D-Printed Polylactic Acid (PLA) Structural Bracket. *58th AIAA/ASCE/AHS/ASC Structures, Structural Dynamics, and Materials Conference, AIAA SciTech Forum, (AIAA 2017-0567)*, http://dx.doi.org/10.2514/6.2017-0567.

Cheruvathur, S., Lass, E. A., & Campbell, C.E. (2015). Additive manufacturing of 17-4pH stainless steel: post-processing heat treatment to achieve uniform reproducible microstructure. *Journal of Materials, 68*(3), 930-942.

Chlebus, E., Gruber, K., Kuznicka, B., Kurzac, J., & Kurzynowski, T. (2015). Effect of heat treatment on microstructure and mechanical properties of Inconel 718 processed by selective laser melting. *Materials Science & Engineering*, *639,* 647-655.

Clausen, B., Brown, D.W., Carpenter, J.S., Clarke, K.D., Clarke, A.J., Vogel, S.C., Bernardin, J.D., Spernjak, D., & Thompson, J.M. (2017). Deformation behavior of additively manufactured GP1 stainless steel. *Materials Science & Engineering A, 696,* 331-340.

Deng, D., Peng, R.L., Brodin, H., & Moverare, J. (2017). Microstructure and mechanical properties of Inconel 718 produced by selective laser melting: sample orientation dependence and effects of post heat treatments. *Materials Science & Engineering A,* https://doi.org/10.1016/j.msea.2017.12.043.

Dunne, F., & Petrinic, N. (2005). Introduction to Computational Plasticity. New York: Oxford.

EOS GmbH- Electro Optical Systems. (2009). EOS StainlessSteel GP1 for EOSINT M 270 Material Data Sheet, 1-5.

EOS GmbH-Electro Optical Systems. (2014). EOS NickelAlloy IN718 Material Data Sheet, 1-7.

ES Laboratory LLC. (2016). Safety Data Sheet: Kalling's 2 Reagent.

ES Laboratory LLC Etchant Store Website. (2016). Kalling's 2 Reagent, 250mL. http://www.etchantstore.com/Kallings-2-Reagent-250-mL-151.htm

Everhart, W., Sawyer, E., Neidt, T., Dinardo, J., & Brown, B. (2016). The effect of surface finish on tensile behavior of additively manufactured tensile bars. *Journal of Materials Science*, *51*(8), 3836-3845.

Facchini, L., Vicente, N., Lonardelli, I., Magalini, E., Robotti, P., & Molinari, A. (2010). Metastable austenite in 17-4 precipitation-hardening stainless steel produced by selective laser melting. *Advanced Engineering Materials*, *12* (3), 184-188.

Fatemi, A., Molaei, R., Sharifimehr, S., Phan, N., & Shamsaei, N. (2017). Multiaxial fatigue behavior of wrought and additive manufactured Ti-6Al-4V including surface finish effect. *International Journal of Fatigue, 100,* 347-366.

Fatemi, A., Molaei, R., Sharifimehr, S., Shamsaei, N., Phan, N. (2017). Torsional fatigue behavior of wrought and selective laser melted Ti-6Al-4V including as-built and machined surface finish effects. *17th Australian International Aerospace Congress: AIAC 2017*, 121-128.

Fatemi, A., Molaei, R., Sharifimehr,S., Shamsaei, N., and Phan, N. (2017). Torsional fatigue behavior of wrought and additive manufactured Ti-6Al-4V by powder bed fusion including surface finish effect. *International Journal of Fatigue*, *99* (1), 187-201.

Feleman,B., Gordon, A.P., Irmak, F. (2017). 2.25Cr-1Mo Steel under Multiaxial Loading with Creep and Plasticity, *(In Progress).*

Frazier, W. E. (2014). Metal Additive Manufacturing: A Review. *Journal of Materials Engineering and Performance, 23*(6), 1917-1928.

Ghorbanpour, S., Zecevic, M., Kumar, A., Jahedi, M., Bicknell, J., Jorgensen, L., Beyerlein, I. J., & Knezevic, M. (2017). A crystal plasticity model incorporating the effects of precipitates in superalloys: Application to tensile, compressive, and cyclic deformation of Inconel 718. *International Journal of Plasticity, 99,* 162-185.

Gibson, R.F., "Principles of Composite Material Mechanics," CRC Press USA.

Girden, E.R. (1992). ANOVA Repeated Measures. *Sage Publications Inc.*

Gong, Y.P., Hyde, C.J., Sun, W., & Hyde, T.H. (2009). Determination of material properties in the Chaboche unified viscoplasticity model. *Journal of Materials: Design and Application, 224*, 19-29.

Gratton, A. (2012). Comparison of Mechanical, Metallurgical Properties of 17-4PH Stainless Steel between Direct Metal Laser Sintering (DMLS) and Traditional Manufacturing Methods. *Proceedings of the National Conference on Undergraduate Research (NCUR).*

Gribbin, S., Bicknell, J., Jorgensen, L., Tsukrov, I., & Knezevic, M. (2016). Low cycle fatigue behavior of direct metal laser sintered Inconel alloy 718. *International Journal of Fatigue, 93,* 156-167.

Gu, D. D., Meiners, W., Wissenbach, K. & Poprawe, R. (2012). Laser additive manufacturing of metallic components: materials, processes and mechanisms. *International Materials Reviews, 57*(3), 133-164.

Gu, H., Gong, H., Pal, D., Rafi, K., Starr, T., & Stucker, B. (2013, August). Influences of energy density on porosity and microstructure of selective laser melted 17-4PH stainless steel. In *2013 Solid Freeform Fabrication Symposium,* 474.

Hahn, G.T. (1962). A model for yielding with special reference to the yield-point phenomena of iron and related bcc metals. *Acta Metallurgica, 10,* 727-738.

Hill, R. (1998). The Mathematical Theory of Plasticity. Oxford Classic Texts in the Physical Sciences.

Hitzler, L., Hirsch, J., Heine, B., Merkel, M., Hall, W., & Oschner, A. (2017). On the Anisotropic Mechanical Properties of Selective Laser-Melted Stainless Steel. *Materials, 10*(1136), 1-19.

Hitzler, L., Hirsch, J., Tomas, J., Merkel, M., Hall, W., & Öchsner, A. (2018). In-plane anisotropy of selective laser-melted stainless steel: The importance of the rotation angle increment and the limitation window. Proceedings of the Institution of Mechanical Engineers, Part L: Journal of Materials: Design and Applications, 1464420718757068.

Hu, Z., Zhu, H., Zhang, H. & Zeng, X. (2017). Experimental investigation on selective laser melting of 17-4PH stainless steel. *Optics & Laser Technology, 87,* 17-25.

Huang, Y., & Leu, M. C. (2013). Frontiers of Additive Manufacturing Research and Education.

Hyde, C. J., Sun, W., & Leen, S. B. (2010). Cyclic Thermo-Mechanical Material Modeling and Testing of 316 Stainless Steel. *International Journal of Pressure Vessels and Piping, 87*(6), 365-372.

ISO/ASTM International. (2013). ISO/ASTM 52921:2013(E)-Standard terminology for additive manufacturing-coordinate systems and test methodologies. 1-13.

Irrinki, H. (2016). Mechanical Properties and Microstructure Evolution of 17-4PH Stainless Steel Processed by Laser-Powder Bed Fusion. Master's Thesis, University of Louisville, 1-124.

Jia, Q., & Gu, D. (2014). Selective laser melting additive manufacturing of Inconel 718 superalloy parts: Densification, microstructure and properties. *Journal of Alloys and Compounds, 585,* 713-721.

Kanagarajah, P., Brenne, F., Niendorf, T., & Maier, H. J. (2013). Inconel 939 processed by selective laser melting: Effect of microstructure and temperature on the mechanical properties under static and cyclic loading. *Materials Science & Engineering A, 588,* 188-195.

Kelley, P.F. (2016). Fatigue Behavior of Direct Metal Laser Sintered (DMLS) Inconel 718. Master's Thesis in Tufts University.

Khan, A.S., & Jackson, K.M. (1999). On the evolution of isotropic and kinematic hardening with finite plastic deformation Part 1: compression/tension loading of OFHC copper cylinders, International Journal of Plasticity, 15(12), 1265-1275.

Kirka, M.M., Greelay, D.A., Hawkins, C., & Dehoff, R. (2017). Effect of anisotropy and texture on the low cycle fatigue behavior of Inconel 718 processed via electron beam melting. *International Journal of Fatigue, 105,* 235-243.

Konecna, R., Kunz, L., Nicoletto, G., & Baca, A. (2016). Fatigue crack growth behavior of Inconel 718 produced by selective laser melting. *Fracturra ed Integrita Strutturale, 35*, 31-40.

Kraft, S.M., & Gordon, A.P. (2011). Characterization of the tensile behavior of a metallic fiber woven structure. *Textile Research Journal, 81*(12), 1249-1272.

Kruth, J.P., Badrossamay, M., Yasa, E., Deckers, J., Thijs, L., & Humbeeck, J.V. (2010, April). Part and material properties in selective laser melting of metals. In *Proceedings of the 16th International Symposium on Electromachining (ISEM XV1)*.

Kruth, J. P., Froyen, L., Vaerenbergh, J. V., Mercelis, P., Rombouts, M., & Lauwers, B. (2004). Selective laser melting of iron-based powder. *Journal of Materials Processing Technology*, *149*, 616-622.

Kunze, K., Etter, T., Grasslin, J., & Shklover, V. (2015). Texture, anisotropy in microstructure and mechanical properties of IN738LC alloy processed by selective laser melting (SLM). *Materials Science & Engineering A*, *620*, 213-222.

Kudzal, A., McWilliams, B., Hofmeister, C., Kellogg, F., Yu, J., Taggart-Scarff, J., & Liang, J. (2017). Effect of scan pattern on the microstructure and mechanical properties of Powder Bed Fusion additive manufactured 17-4 stainless steel. *Materials and Design*, doi: 10.1016/j.matdes.2017.07.047.

Lambert, D.M. (2015). IN718 Additive Manufacturing Properties and Influences. *Presented at JANNAF Conference*, Nashville, TN, 1-14.

Lambert, D.M. (2016). Evaluation of the Effect of Surface Finish on High-Cycle Fatigue of SLM-IN718.

LeBrun, T., Nakamoto, T., Horikawa, K., & Kobayashi, H. (2015). Effect of retained austenite on subsequent thermal processing and resultant mechanical properties of selective laser melted 17-4PH stainless steel. *Materials and Design, 81*, 44-53.

Liu, B., Wildman, R., Tuck, C., Ashcroft, I., & Hague, R. (2011). Investigation the effect of particle size distribution on processing parameters optimization in selective laser melting process. *Additive Manufacturing Research Group, Loughborough University*, 227-238

Liu, F., Lin, X., Yang, G., Song, M., Chen, J., & Huang, W. (2011). Microstructure and residual stress of laser rapid formed Inconel 718 nickel-base superalloy. *Opt. Laser Technology*, *43*, 208-213.

Liu, F., Lin, X., Huang, C., Song, M., Chen, J., & Huang, W. (2011). The effect of laser scanning path on microstructures and mechanical properties of laser solid formed nickel-base superalloy Inconel 718. *Journal of Alloys and Compounds*, *509*, 4505-4509.

Lu, Y., Wu, S., Gan, Y., Huang, T., Yang, C., Junjie, L., & Lin, J. (2015). Study on the microstructure, mechanical property and residual stress of SLM Inconel-718 alloy manufactured by differing island scanning strategy. *Optics and Laser Technology, 75*, 197-206.

Luecke, W.E., & Slotwinski, J.A. (2014). Mechanical properties of austenitic stainless steel made by additive manufacturing. *Journal of Research of the National Institute of Standards and Technology*, *119*, 398-418.

Mahmoudi, M., Elwany, A., Yadollahi, A., Thompson, S.M., Bian, L., & Shamsaei, N. (2017). Mechanical properties and microstructural characterization of selective laser melted 17-4 PH stainless steel. *Rapid Prototyping Journal, 23*(2), doi: 10.1108/RPJ-12-2015-0192.

MakeItFrom. (2009). UNS S17400 (17-4PH, Alloy 630, 1.4542) Stainless Steel, from https://www.makeitfrom.com/material-properties/UNS-S17400-17-4-PH-Alloy-630-1.4542-Stainless-Steel.

Maher. Alloy 718 Data Sheet, from http://www.maher.com/media/pdfs/718-datasheet.pdf.

Mercelis, P., & Kruth, J.P. (2006). Residual stresses in selective laser sintering and selective laser melting. *Rapid Prototyping Journal*, *12*(5), 254-265.

Moore, Z. J., & Neu, R.W. (2011). Fatigue Life Modeling of Anisotropic Materials Using a Multiaxial Notch Analysis, *Journal of Engineering Materials and Technology*, *133*(3), 031001-1 – 031001-11.

Mower, T. M., & Long, M.J (2016). Mechanical behavior of additive manufactured, powder-bed laser-fused materials. *Materials Science & Engineering A*, *651*, 198-213.

Mucke, R., & Bernhardi, O.E. (2003). A constitutive model for anisotropic materials based on Neuber's rule. *Computer methods in applied mechanics and engineering*, *192*(37), 4237-4255.

Mumtaz, K., & Hopkinson, N. (2008). Top surface and side roughness of Inconel 625 parts processed using selective laser melting. *Rapid Prototyping Journal*, *15*(2), 96-103.

Murr, L.E., Martinez, E., Hernandez, J., Collins, S., Amato, K.N., Gaytan, S.M., & Shindo, P.W. (2012). Microstructures and Properties of 17-4PH Stainless Steel Fabricated by Selective Laser Melting. *Journal of Materials Research and Technology*, *1*(3): 167-177.

MTS Systems Corporation. (2015). MTS Landmark Testing Solutions Brochure.

MTS Systems Corporation. (1997). MTS 634.11 Axial Extensometers Brochure.

MTS Systems Corporation. (2013). Series 647 Hydraulic Wedge Grips Reference Manual.

O'Nora, N. R. (2015). Compendium of Thermoviscoplasticity Modeling Parameters for Materials Under Non-Isothermal Fatigue. Honors in the Major in Mechanical Engineering Bachelors Thesis. University of Central Florida.

Oradei-Basile, A., & Radavich, J. F. (1991). A current TTT diagram for wrought alloy 718. *Superalloys*, *718*(625), 325-335.

Perkowski, C. (2017). Tensile-Compressive Asymmetry and Anisotropy of Fused Deposition Modeling PLA under Monotonic Conditions. *Master's Thesis*, University of Central Florida.

Popovich, A. A., Sufiiarov, V. Sh., Polozov, I. A., & Borisov, E. V. (2015). Microstructure and mechanical properties of Inconel 718 produced by SLM and subsequent heat treatment. *Key Engineering Materials*, 665-670.

Qi, H., Azer, M., & Ritter, A. (2009). Studies of Standard Heat Treatment Effects on Microstructure and Mechanical Properties of Laser Net Shape Manufactured Inconel 718. *Metallurgical and Materials Transactions A*, 2410-2422.

Rack, H. J., & Kalish, D. (1974). The Strength, Fracture Toughness, and Low Cycle Fatigue Behavior of 17-4 PH Stainless Steel. *Metallurgical Transactions, 5*, 1595-1605.

Rafi, H. K., Pal, D., Patil, N., Starr, T. L., & Stucker, B. E. (2014). Microstructure and mechanical behavior of 17-4 precipitation hardenable steel processed by selective laser melting. *Journal of materials engineering and performance*, *23*(12), 4421-4428.

Rashid, R., Masood, S.H., Ruan, D., Palanisamy, S., Rahman Rashid, R.A., & Brandt, M. (2017). Effect of scan strategy on density and metallurgical properties of 17-4PH parts printed by Selective Laser Melting (SLM). *Journal of Materials Processing Technology*, http://dx.doi.org/10.1016/j.jmatprotec.2017.06.023.

Sadowski, M., Ladani, L., Brindley, W., & Romano, J. (2016). Optimizing quality of additively manufactured Inconel 718 using power bed laser melting process. *Additive Manufacturing, 11*, 60-70.

Sarkar, S., Kumar, C.S., & Nath, A.K. (2017). Effect of mean stresses on mode of failures and fatigue melted stainless steel. *Materials Science & Engineering A, 700*, 92-106.

Schonbauer, B.M., Yanase, K., and Endo, M. (2017). Influences of small defects on torsional fatigue limit of 17-4PH stainless steel. *International Journal of Fatigue, 100* (2), 540-548.

Scott-Emuakpor, O., Schwartz, J., George, T., Holycross, C., Cross, C., & Slater, J. (2015). Bending fatigue life characterisation of direct metal laser sintering nickel alloy 718. *Fatigue & Fracture of Engineering Materials & Structures, 38*(9), 1105-1117.

Sehrt, J.T., & Witt, G. (2010). Dynamic Strength and fracture toughness analysis of beam melted parts. *Proceedings of the 36th International MATADOR Conference*, 385-388.

Shioya, T. & Shioiri, J. (1976). Elastic-plastic analysis of the yield process in mild steel. *J. Mech. Phys. Solids, 24*, 187-204.

Siddiqui, S.F., Fasoro, A.A., Cole, C., & Gordon, A.P. (2017). Mechanical Characterization and Modeling of Direct Metal Laser Sintered Stainless Steel GP1. Manuscript under review. Submitted to the *ASME Journal of Engineering Materials and Technology*.

Siddiqui, S.F., Fasoro, A.A., & Gordon, A.P. (2017). Selective Laser Melting (SLM) of Ni-based Superalloys - A Mechanics of Materials Review. Badiru, A.B., Valencia, V. V., & Liu, D. (Eds.), *Additive Manufacturing Handbook: Product Development for the Defense Industry*. CRC Press.

Siddiqui, S.F., O'Nora, N., Fasoro, A.A., & Gordon, A.P. (2017). Modeling the Influence of build orientation on the monotonic and cyclic response of additively manufactured stainless steel GP1/17-4PH. In *Proceedings of the ASME 2017 International Mechanical Engineering Congress & Exposition.*

Siddiqui, S.F., Fasoro, A.A., & Gordon, A.P. (2018). Axial and Torsional Response of Additively Manufactured Steel under Monotonic and Cyclic Conditions. GT2018-76831. In *Proceedings of the ASME 2018 Turbo Expo Turbomachinery Technical Conference & Expo*.

Siddiqui, S.F., Fasoro, A.A., & Gordon, A.P. (2018). Assessment of Progressive Amplitude and Pulsating Tension Fatigue Conditions on Additively Manufactured Stainless Steel. Manuscript in Preparation- To be submitted to the *International Journal of Fatigue*.

Siddiqui, S.F., & Gordon, A.P. (2018). Influence of Build Orientation on the Cyclic Shear Response of Additively Manufactured Inconel 718. To be submitted to the *Rapid Prototyping Journal.*

Siddiqui, S.F., & Gordon, A.P. (2018). Modeling the Tensile and Fatigue Response of Additively Manufactured Inconel 718- A Review. To be submitted to the *International Journal of Plasticity*.

Sing, S. L., An, J., Yeong, W. Y., Wiria, F. E. (2015). Laser and electron-beam powder-bed additive manufacturing of metallic implants: A review on processes, materials and designs. *Journal of Orthopaedic Research*. doi:10.1002/jor.23075.

Smith, D. H., Bicknell, J., Jorgensen, L., Patterson, B. M., Cordes, N.L., Tsukrov, I., & Knezevic, M. (2016). Microstructure and mechanical behavior of direct metal laser sintered Inconel 718. *Materials Characterization*, doi: 10.1016/j.matchar.2016.01.003.

Sochalski-Kolbus, L. M., Payzant, E. A., Cornwell, P. A., Watkins, T. R., Babu, S. S., Dehoff, R. R., Lorenz, M., Ovchinnikova, O., & Duty, C. (2015). Comparison of Residual Stresses in Inconel 718 Simple Parts Made by Electron Beam Melting and Direct Laser Metal Sintering. *Metallurgical and Materials Transactions A*, *46A*, 1419-1432.

Song, B., Zhao, X., Li, S., Han, C., Wei, Q., Wen, S., Liu, J., & Shi, Y. (2015). Differences in microstructure and properties between selective laser melting and traditional manufacturing for fabrication of metal parts: A review. *Frontiers of Mechanical Engineering*, *10*(2), 111-125.

Song, B., Dong, S., Liu, Q., Liao, H., & Coddet, C. (2014). Vacuum heat treatment of iron parts produced by selective laser melting: Microstructure, residual stress and tensile behavior. *Materials and Design*, *54*, 727-733.

Song, X., Xie, M., Hofmann, F., Illston, T., Connolley, T., Reinhard, C., Atwood, R. C., Conner, L., Drakopoulos, M., Frampton, L., & Korsunsky, A. M. (2015). Residual stresses and microstructure in Powder Bed Direct Laser Deposition (PB DLD) Samples. *International Journal of Material Forming*, *8*(2), 245-254.

Song, Y., Li, Y., Song, W., Yee, K., Lee, K.Y., & Tagarielli, V.L. (2017). Measurements of the mechanical response of unidirectional 3D-printed PLA. *Materials and Design*, *123*, 154-164.

Special Metals Corporation. (2013). Inconel alloy 625. 1-18.

Starr, T., Scherzer, C., & Smith, A. (2011). Tensile and Fatigue Performance of Laser Sintered Stainless Steels. *SAMPE Direct Part Manufacturing Workshop*, Dayton, OH, USA.

Starr, T., Rafi, K., Stucker, B., & Scherzer, C. (2012). Controlling Phase Composition in Selective Laser Melted Stainless Steels. *Power (W)*, *195*, 195.

Stephens, R. I., Fatemi, A., Stephens, R. R., & Fuchs, H. O. (2001). Metal Fatigue in Engineering. *John Wiley & Sons Inc*.

Strano, G., Hao, L., Everson, R. M., & Evans, K. E. (2013). Surface roughness analysis, modelling and prediction in selective laser melting. *Journal of Materials Processing Technology*, *213*, 589-597.

Strøßner, J., Terock, M, & Glatzel, U. (2015). Mechanical and Microstructural Investigation of Nickel-Based Superalloy IN718 Manufactured by Selective Laser Melting (SLM). *Advanced Engineering Materials*, 1-7.

Stoffregen, H. A., Butterweck, K., & Abele, E. (2014). Fatigue Analysis in Selective Laser Melting: Review and Investigation of Thin-Walled Actuator Housings. In *25th Solid Freeform Fabrication Symposium*, 635-650.

Tong, J., Zhan, Z. L., & Vermeulen, B. (2004). Modeling of Cyclic Plasticity and Viscoplasticity of a Nickel-Based Alloy Using Chaboche Constitutive Equations. *International Journal of Fatigue*, *26*(8), 829-835.

Torres, J., Cotelo, J., Karl, J., & Gordon, A.P. (2015). Mechanical Property Optimization of FDM PLA in Shear with Multiple Objectives. *Journal of Materials*, *67*(5). 1183-1193.

Trosch, T., Stobner, J., Volkl, R., & Glatzel, U. (2015). Microstructure and mechanical properties of selective laser melted Inconel 718 compared to forging and casting. *Materials Letters*, http://dx.doi.org/10.1016/j.matlet.2015.10.136.

Tsai, S.W., & Wu, E.M. (1971). A General Theory of Strength of Anisotropic Materials. *Journal of Composite Materials*, *5*(1), 58-80.

Turner, B. N., & Gold, S. A. (2015). A review of melt extrusion additive manufacturing processes: II. Materials, dimensional accuracy, and surface roughness. *Rapid Prototyping Journal*, *21*(3), 250-261.

Vasudevarao, B., Natarajan, D. P., Henderson, M., & Razdan, A. (2000). High spatial resolution, high energy synchrotron x-ray diffraction characterization of residual strains and stresses in laser shock peened Inconel 718SPF alloy. *Solid Freeform Fabrication Proceedings,* 251-258.

Veeco Process Metrology. Installation, Operation and Maintenance Manual Dektak^{3}ST Surface Profile Measuring System, 1-148.

Wang, X., Gong, X., & Chou, K. (2015). Review on Powder-Bed Laser Additive Manufacturing of Inconel 718 Parts. *Proceedings of the ASME 2015 International Manufacturing Science and Engineering Conference (MSEC2015-9322)*, 1-9.

Wang, Z., Guan, K., Gao, M., Li, X., Chen, X., & Zeng, X. (2012). The microstructure and mechanical properties of deposited-IN718 by selective laser melting. *Journal of Alloys and Compounds, 513*, 518-523.

Watkins, T., Bilheux, H., An, K, Payzant, A., Dehoff, R., Duty, C., Peter, W., Blue, C., & Brice, C. (2013). Neutron Characterization for Additive Manufacturing.

Wohlers, T., and Gornet, T. (2014). History of additive manufacturing. *Wohlers Report*, 1–34, Wohlers Associates, Inc., Fort Collins, CO.

Wu, A.S., Brown, D.W., Kumar, M., Gallegos, G.F., & King, W.E. (2014). An Experimental Investigation into Additive Manufacturing-Induced Residual Stresses in 316L Stainless Steel. *Metallurgical and Materials Transactions A, 45A*, 6260-6270.

Wu, J., & Lin, C. (2003). Influence of Frequency on High-Temperature Fatigue Behavior of 17-4pH Stainless Steels. *Materials Transactions*, *44*(4), 713-721.

Yadollahi, A., Shamsaei, N., Thompson, S.M., Elwany, A., & Bian, L. (2017). Effects of building orientation and heat treatment on fatigue behavior of selective laser melted 17-4 PH stainless steel. *International Journal of Fatigue*, *94*, 218-235.

Yadollahi, A., Shamsaei, N., Thompson, S.M., Elwany, A., Bian, L., & Mahmoudi, M. (2015). Fatigue behavior of selective laser melted 17-4pH stainless steel. In *Proceedings of 26th International Solid Freeform Fabrication Symposium*, Austin, TX, 721-731.

Yeh, H.L. and Yeh, H.L. A Dimensionless Analysis of Young's Modulus and Stress Distribution for Orthotropic Materials. *Journal of Aeronautics and Aerospace Engineering*, 3(1), http://dx.doi.org/10.4172/2168-9792.1000128.

Zaeh, M.F., & Branner, G. (2010). Investigations on residual stresses and deformations in selective laser melting. *Production Engineering*, *4*(1), 35-45.

Zhao, X., Chen, J., Lin, X., & Huang, W. (2008). Study on microstructure and mechanical properties of laser rapid forming Inconel 718. *Materials Science and Engineering A*, *478*, 119-124.